Electro-optic modulation measurement technique and enhancement

Jacobsen, Rune Shim

Publication date:
2005

Document Version
Publisher's PDF, also known as Version of record

Electro-optic modulation, measurement technique and enhancement

Ph.D. Thesis
Rune Shim Jacobsen

28/6-2005

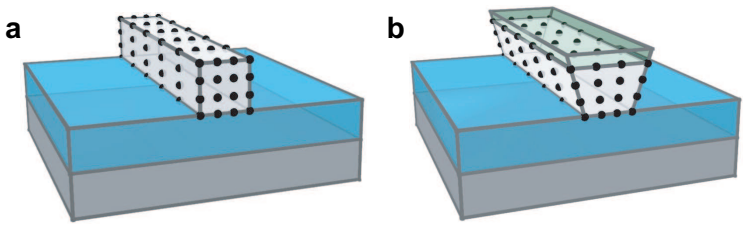

Figure 1: Applying strain to crystalline silicon. a, Waveguide fabricated in the top layer of an SOI wafer. **b**, The same waveguide with a straining layer deposited on top. The straining layer breaks the inversion symmetry and induces a linear electro-optic effect. *This is figure 1 from the article published in* ***Nature*** *based on results from this Ph.D. thesis.*

COM•DTU

Department of Communications, Optics & Materials
Technical University of Denmark
Building 345V
2800 Kgs. Lyngby
DENMARK

The project was supported by the NKT Academy.

Abstract

The goal of this Ph.D. project was to realize a switch in poled silica with a switching voltage below 300V. This goal was *not* accomplished. A possible explanation for the very large, but decaying, poling effects reported during the nineties is found experimentally for a sample with cracks in the topcladding. From this it is concluded that the third-order non-linear coefficient ($\chi^{(3)}$) of silica is a factor of 10 too low for making an interesting switch. To increase the poling induced nonlinearity, the material $\chi^{(3)}$ must be enlarged. A possiblity is to use silicon rich nitride (SRN) as core material, as a 5-fold increase of material non-linearity was found for SRN, relative to the originally used core material $Ge : SiON$

A precision measurement method, which determines both $E_{frozen-in}$, $\chi^{(2)}$ and $\chi^{(3)}$ was developed. The method is applicable to all relevant samples and the uncertainty of the obtained results is $\sim 5\%$.

When investigating photonic crystal (PhC) waveguides it was discovered that stress induces a significant electro-optic (E-O) coefficient in silicon. It was also, for the first time experimentally, verified that the E-O effect scales linearly with the group index, using a developed time-of-flight measurement method. A world record for direct measured group index ($n_g = 220$) was obtained in a $20\mu m$ long symmetric W1 PhC waveguide.

Steps were taken to transfer the discovered stress induced non-linearity to a conventional index-guiding waveguide. When transfered, future measurements will determine how large an E-O coefficient it is possible to achieve in silicon by stress. It will also be determined if the induced E-O coefficient remains at fast electrical modulations.

Resumé

Målet med dette Ph.D. projekt var at realisere en optisk kontakt i polet glas (SiO_2), hvor der skal bruges mindre end 300V til at skifte kontakten. Dette mål blev *ikke* nået. En målig forklaring på de høje, men hurtigt aftagende polingresultater publiceret i halvfemserne er fundet eksperimentelt vha. en prøve med revner i topglasset. Ud fra dette konkluderes, at tredjeordensulineariteten ($\chi^{(3)}$) af glas er en faktor 10 for lav til at opnå en interessant polet kontakt i SiO_2. For at forøge den polinginducerede ulinearitet skal materialekonstanten $\chi^{(3)}$ forøges. En mulighed, som blev fundet, er at anvende silicium rigt nitrid til kerneglasset, da det er 5 gange mere ulineart end det oprindeligt anvendte materiale $Ge:SiON$.

Der blev udviklet en meget præcis målemetode, som kan bestemme både $E_{frozen-in}$, $\chi^{(2)}$ og $\chi^{(3)}$. Metoden kan bruges til måling på alle relevante prøver og usikkerheden af de målte resultater er $\sim 5\%$.

Da fotoniske krystalbølgeledere blev undersøgt, blev der gjort en videnskabelig opdagelse, nemlig at stress inducerer en betydelig elektro-optisk (E-O) koefficient in silicium. Det blev også for første gang eksperimentelt verificeret, at E-O koefficienten forstærkes lineært med gruppeindekset. Til måling af gruppeindekset blev der udviklet en direkte metode baseret på måling af transmissionstiden for en optisk puls. Der blev fundet en verdensrekord for et direkte målt gruppeindeks ($n_g = 220$). Rekorden blev målt for en $20\mu m$ lang symmetrisk W1-bølgeleder.

Overførslen af den stressinducerede E-O koefficient til en konventionel indeks bølgeleder blev påbegyndt. Når en sådan koefficient opnås i en sådan bølgeleder vil fremtidige forsøg kunne fastlægge hvor stor den stressinducerede E-O koefficient i silicium kan blive. Fremtidige forsøg vil også fastlægge om den stressinducerede effekt eksisterer for hurtig elektrisk modulation.

Acknowledgements

Before I started my Ph.D. study I had never done experimental work. It was a fellow Ph.D. student who taught me all about making experiments and for this and much more I would like to thank Carl Johan Marckmann.

In the sample fabrication process I worked together with Carl Johan Marckmann, Yitao Ren, Jacob-Fage Pedersen, Lars Frandsen, Karin Andersen and Haiyan Ou. I am grateful for all the things you helped me with and for a good collaboration.

The PECVD is run and maintained by Roy Cork, Berit Herstrøm, Jonas Jensen and Fadil Karamehmedovic. I would like to thank you all for helping me with and allowing me to run the PECVD with all kind of exotic recipes. I would also like to thank Thøger Eskildsen for valuable help with development of anneal recipes and Peixiong Shi for doing E-beam writing.

I would also like to thank Karin Andersen, Mikael Svalgaard, Thomas Nikolajsen, Niklas Myrén, Lars Frandsen, Anders Harpøth and Peter Borel for providing or helping me to fabricate the variety of different waveguides I investigated during this project.

During the development of the DC-shifted MZI method I got a lot of help from the electronic workshops both at COM and at MIC/Danchip and I would especially like to mention Brian Sørensen at COM and Jan Eriksen who is now with Danchip.

The group index measurements for the PhC waveguides could not have been made without the help and patience of Christophe Peucheret and Beata Zsigri who both helped with the practical setup and assisted with their large insight.

Some of the first samples where made by UV-exposure, for which a laser setup was made available by Jesper Bo Jensen and Hans-Jürgen

Deyerl.

Measurements with an atomic force microscope was made in the Nanotek at DTU, where Jane Nielsen and Jakob Svagin were both very helpful.

For collaboration with theoretical calculations and considerations I would like to thank; J. Lægsgaard, Andrei Lavrinenko, Jørn Hedegaard and Lars Frandsen.

For general collaboration and discussion of results, I would like to thank the following persons; H. R. Sørensen, E. Knudsen, K. G. Hougaard, J. Riishede, T. T. Alkeskjold, T. Sørensen, S. Michelsen, N. Plougmann, A. Boltasseva, A. Bjarklev and K. Rottwitt.

I am also grateful to my supervisors, Mikael Svalgaard, Martin Kristensen and Jacob-Fage Pedersen for their advice. There is especially one advice from Mikael, that I will remember in the future: *Work can be divided into two categories: Nice to do and Need to do - Focus on the last!*

My Ph.D. project was made possible due to funding from the NKT academy for which I am grateful.

Last but not least I would like to thank my understanding wife Veronica Jacobsen for her never ending support, even at the times where I spend too many hours away from my family.

Ph.D. Publications

The work performed during this Ph.D. project have contributed to the following publications

Patents:

[A] R. Jacobsen. "Interferometer based on electro-optic effects in dual-stressed group-iv material", *US Patent Application*

[B] R. Jacobsen (40%), J. Fage-Pedersen (25%), M. Kristensen (20%), P. Borel (5%), L. Frandsen (5%), and O. Hansen (5%). "Phase modulator and interferometer based on electro-optic effects in stressed group-iv material", *US Patent Application*

Journal papers:

[C] R. Jacobsen, K. Andersen, P. Borel, J. Fage-Pedersen, L. Frandsen, O. Hansen, M. Kristensen, A. Lavrinenko, G. Moulin, H. Ou, C. Peucheret, B. Zsigri, and A. Bjarklev. "Strained silicon as a new electro-optic material", *Nature*, vol. 441, no. 11, pp. 199–202, 2006

[D] R. Jacobsen, A. Lavrinenko, L. Frandsen, C. Peucheret, B. Zsigri, G. Moulin, J. Fage-Pedersen, and P. Borel. "Direct experimental and numerical determination of extremely high group indices in photonic crystal waveguides", *Optics Express*, vol. 13, no. 20, pp. 7861–7871, 2005

[E] R. Jacobsen, J. Laegsgaard, A. Bjarklev, and K. Hougaard. "Very low zero-dispersion wavelength predicted for single-mode modified-total-internal-reflection crystal fibre", *Journal of Optics A: Pure and Applied Optics*, vol. 6, no. 6, pp. 604–607, 2004

[F] J. Fage-Pedersen, R. Jacobsen, and M. Kristensen. "Planar glass devices for efficient periodic poling", *Optics Express.*, vol. 13, no. 21, pp. 8514–8519, 2005

[G] Y. Ren, C. Marckmann, R. Jacobsen, and M. Kristensen. "Poling effect of a charge-trapping layer in glass waveguides", *Applied Physics B*, vol. 78, no. 3-4, pp. 371–375, 2004

Conference contributions:

[H] A. V. Lavrinenko, R. S. Jacobsen, J. Fage-Pedersen, L. H. Frandsen, B. Zsigri, C. Peucheret, and P. I. Borel. "Extreme group index measured and calculated in 2d soi-based photonic crystal waveguides.", *LEOS, TuR4*, 2005

[I] A. V. Lavrinenko, R. S. Jacobsen, J. Fage-Pedersen, B. Zsigri, C. Peucheret, L. H. Frandsen, M. Kristensen, and P. I. Borel. "Direct numerical and experimental determination of group index dispersion in photonic crystal waveguides.", *Spie, vol 5950, nr 15*, 2005

[J] J. Fage-Pedersen, R. Jacobsen, and M. Kristensen. "Glass waveguides for periodic poling.", *Paper no. 69, Bragg Gratings, Poling, and Photosensitivity (BGPP), Sydney, Australia, July.*, 2005

[K] J. Fage-Pedersen, R. Jacobsen, and M. Kristensen. "Glass devices for efficient second harmonic generation.", *Paper no. CD4-2, Conference on Lasers and Electro-Optics (CLEO/Europe), Munich, June.*, 2005

[L] J. Fage-Pedersen, Y. Ren, R. Jacobsen, and M. Kristensen. "Thermal poling of silica-based waveguides.", *POWAG, invited presentation at the GLAMOROUS workshop, Bath, UK, July.*, 2004

[M] Y. Ren, C. J. Marckmann, R. Shim, and M. Kristensen. "Electro-optic effect induced in glass waveguides containing a charge-trapping layer.", *Poster at Aphys, Spain*, 2003

[N] P. Borel, L. Frandsen, M. Thorhauge, A. Boltasseva, J. Cheng, M. Kampanis, M. Kristensen, A. Lavrinenko, K. Rechendorff, R. Shim, Y. Zhuang, and H. Chong. "Very low losses for tm polarized light in photonic crystal waveguides", *Lasers and Electro-Optics, 2003. CLEO '03. Conference*, pp. 957–958, 2003

[O] C. Marckmann, R. Shim, Y. Ren, and M. Kristensen. "Interpretation of high poling effects with short lifetimes", *11th European Conference on Integrated Optics. Proceedings*, pp. 301–4 vol.1, 2003

Other publications:

[P] C. Marckmann, R. Jacobsen, Y. Ren, and M. Kristensen. "Correction to "strength and symmetry of the third-order nonlinearity during poling of glass waveguides"", *Photonics Technology Letters, IEEE*, vol. 16, no. 8, p. 1987, 2004

Contents

Chapter 1

Introduction.

The backbone of communication is today comprised by optical signals. The advantage of optical communication is the possibility for transmission of data at very high bit rates over long distances. In the laboratory 40 Gb/s has been transmitted over 160 km [1]. The common modulation format works by turning the light on (1-bit) or off (0-bit), just like blinking with a flashlight. In fast optical communication the light source is not turned on or off but the light is instead sent through an external modulator that either transmits the incident light or prohibits its propagation.

There are several competing methods used for making external modulators. The electro-absorption modulator works by being either transparent or black, depending on the applied current. A more widely used method works by interference. The light is split into two pathways and then recombined after propagating a few centimeters. At recombination, the light can interfere either constructively or destructively depending on the phase difference between the two arms. Constructive interference returns a 1-bit, while destructive interference gives a 0-bit.

The critical point for a modulator, based on the interferometric principle, is how to alter the pathway of the light fast, as a change in the optical length by $\lambda/2$ for one of the two pathways will change the interference from constructive to destructive. The only way for changing the optical pathway fast enough for a telecom system is to make the light propagate in an electro-optic material, i.e. in a material that changes refractive index when a voltage is applied across it.

Materials with high electro-optic coefficient change their refractive indices significantly, when affected by an electric field. The electro-optic material most commonly applied in optical communication is $LiNbO_3$, as it possesses a high electro-optic coefficient. The disadvantage of $LiNbO_3$ is the price and that it cannot be integrated with electronics. I.e. the electrical modulation signal must be made in one component and then transferred through a microwave cable to the $LiNbO_3$ modulator.

The price of $LiNbO_3$ and the lack of integration possibilities makes the search for other material reasonable. One material, which is cheap, transparent and integrable with electronics made in silicon, is silica (SiO_2). The only problem with silica is its lack of a linear electro-optic coefficient. The refractive index of silica is changed quadratic when an electric field is applied and the index change, due to an applied electric field, is therefore 0 to first order. Moving away from the bottom point of the index parabola to a point where the slope is high will induce a electro-optic coefficient, as the index change for an applied electric field scales with the slope.

The moving on the index parabola is done by applying a high voltage electric field. In a device, it is not desirable to include a high voltage generator, both from a security and from a cost perspective. To avoid the high voltage generator, a large electric field is frozen into the glass by poling. Glass is poled by applying high voltage and heating it to $\sim 350^\circ$ for ~ 20 minutes and then maintaining the high voltage while cooling the glass down to room temperature. When the glass is heated, charges will move inside the glass due to the high voltage. These charges are then trapped when the glass is again cooled down, and hence a large permanent electric field is built into the sample.

Poling of glass in this way opens a road for a glass based modulator with all the advantages in terms of price and possible integration with electronics. The scientific goal for this Ph.D. project was to realize a switch or modulator with a switching voltage below 300V in poled glass deposited on top of a 4 inch silicon wafer.

The success of glass poling depends on two parameters, the size of the electric field frozen-in by poling and the curvature of the index parabola ($\chi^{(3)}$). Both parameters are determined for different samples using a precision measurement method developed during this Ph.d. project. From the obtained values and due to the fundamental limitation, that the frozen-in field cannot exceed the breakdown field, it is in chapter (5)

concluded that: *The third-order non-linearity of silica is a factor of 10 too small to be of any interest for making a poling based switch on a 4 inch wafer.*

During the search for an increase in $(\chi^{(3)})$ a discovery was made. In chapter (6) it is described how a significant electro-optic coefficient can be induced in silicon, by applying a stressing layer on top of the structure. The induced effect is significant and by further research it may become possible to make a modulator in silicon that can compete with already existing modulators.

The thesis is organized in the following way:

Chapter 2: The chapter starts with a short introduction to the origin of material non-linearity followed by a description of waveguiding by total internal refraction. The Mach-Zehnder interferometer (MZI) and the connection between material non-linearity and switching voltage is described. The chapter ends with a description of poling.

Chapter 3: This chapter describes in detail the developed non-linear measurement method starting with the derivation of a general equation for the output of a MZI. A measurement method for determining the voltage required to induce a π phase shift using a commercial $LiNbO_3$ phase modulator is then described. This is followed by a description of the measurement method for determining the frozen-in field and the non-linearity $(\chi^{(3)})$ for the investigated samples using the commercial $LiNbO_3$ modulator. Finally, the method is confirmed by measuring on a precharacterized sample and a conclusion based on comparing the developed method with the Bragg grating method is made.

Chapter 4: The standard sample fabrication method is introduced followed by short descriptions for more exotic fabrication methods.

Chapter 5: This chapter starts by evaluating the size of $(\chi^{(3)})$ required to realize an interesting switch. A method for increasing the frozen-in field is then described followed by a measurement that gives a possible explanation of the very large non-linearities reported in the literature [2, 3]. The explanation demonstrates that a $(\chi^{(3)})$ increase is essential to realize an interesting switch and doping of silica is therefore investigated. An increase of $(\chi^{(3)})$ by a factor of 5 is found, but the increase was judged too small for reaching an interesting level. Finally, a totally different waveguiding principle was investigated, i.e. guidance by a surface mode. The result was, however, *not* positive. The chapter ends by concluding

that no more research should be made with the aim of realizing an integrated poled silica switch.

Chapter 6: When photonic crystals (PhC) were investigated, a discovery was made. To give insight into this, the chapter starts with a short introduction to the concept of photonic bandgap guidance, followed by a description of how PhC samples were prepared for non-linearity measurements. The discovery and all the puzzling observations are presented. Most of the puzzling observations are explained by measuring at a higher AC-frequency, but some fast oscillations are first clarified after a method for measuring the group index in PhC waveguides was developed. Finally, the discovery boils down to the existence of a significant $\chi^{(2)}$ value in stressed silicon. The chapter ends with an outlook for future experiments and concludes on the possibility of making an electro-optic modulator in silicon.

Chapter 7 A conclusion on the whole project and the future possibilities.

Appendix A: To process data from the measurements made on the $LiNbO_3$ phase modulator in chapter (3) an ellipsoid must be fitted to measurement points. This is in principle a well known mathematical problem, but as no existing method was found (not even after speaking to the mathematics modeling department, IMM, DTU.), a crude method based on the Montecarlo approach is developed in this appendix. The method can unfortunately introduce a systematic error of up to 1‰ and hence there is room for improvement.

Appendix B: This appendix contains a detailed description of both the systematic and the reproducibility uncertainties for the developed non-linear measurement method. It is also described when and how the uncertainty can be improved.

Appendix C: The Bragg grating measurement method is described in this appendix.

Appendix D: This appendix contains a detailed mathematical description of the $\chi^{(3)}$ tensor and how the index of the light is affected by an electrical field in a $\chi^{(3)}$ material.

Appendix E: The confinement factor of a PhC waveguide is calculated in this appendix. The calculation obviously leaves room for improvement, which does probably require a change of calculation method, e.g. 3D FDTD calculations should be superior.

References to Chapter 1

[1] T. Tokle, Q. Le, C. Peucheret, and P. Jeppesen. "Optimum dispersion map for raman amplified 160 km nzdsf + dcf fibre spans with 40 gbit/s rz signals", *Electronics Letters*, vol. 40, no. 22, pp. 1443–1444, 2004.

[2] R. Myers, N. Mukherjee, and S. Brueck. "Large second-order nonlinearity in poled fused silica", *Optics Letters*, vol. 16, no. 22, pp. 1732–4, 1991.

[3] T. Fujiwara, D. Wong, Y. Zhao, S. Fleming, S. Poole, and M. Sceats. "Electro-optic modulation in germanosilicate fibre with uv-excited poling", *Electronics Letters*, vol. 31, no. 7, pp. 573–575, 1995.

Chapter 2

General Theory.

2.1 Bulk refractive index.

The main scope of this thesis is to use electro-optic modulation to make a switch or an amplitude modulator. The difference between a switch and a modulator is mainly the speed, that is significantly higher for a modulator. A switch is generally more advanced in the sense that a modulator either transmits or blocks the incident light. A switch is capable of transmitting the incident light to a specific output port. Fig. (2.1) shows a picture of a switch and a modulator.
A material with non-zero electro-optic (EO) coefficient is capable of changing refractive index when an electric field is applied over the material. The change in refractive index can be used to make a switch/modulator using an interferometer of the Mach-Zehnder (MZ) type.

The origin of refractive index is the polarization of the material when affected by an electric field. An electromagnetic wave (light) traveling inside a material will polarize the electron orbitals. The polarized orbitals oscillate and emit radiation identical to the incident light except for a phase delay. The transmitted field is the sum of all contributions, i.e. a sum of the remaining part of the original wave plus contributions from all the material oscillators. The outcome of the light-material interaction is an electromagnetic wave that propagates at a slower speed, that is at the speed $c/n_{\phi,bulk}$, where $n_{\phi,bulk}$ is the bulk material's phase refractive index. $n_{\phi,bulk}$ is connected to the electrical susceptibility of the material,

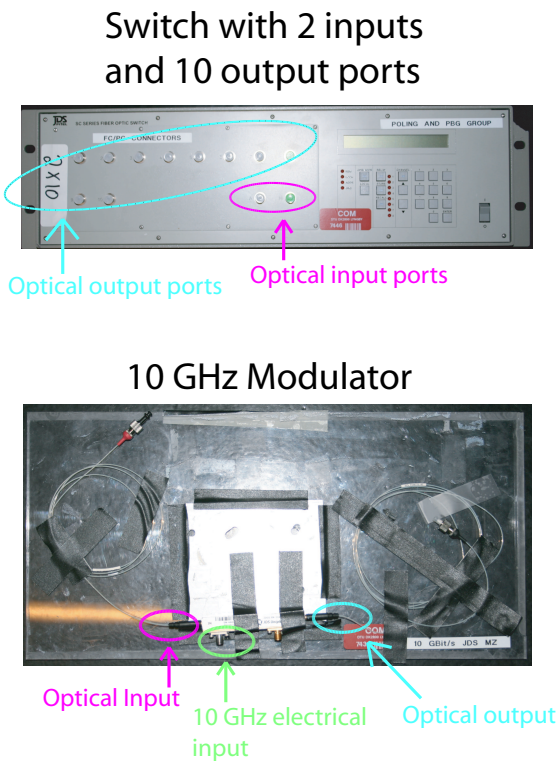

Figure 2.1: Picture of a 2x10 switch and a modulator. The switch is capable of transmitting the input light to any of the 10 output ports. In contrast, the modulator is only capable of either transmitting or absorbing the input light. The advantage of the modulator is the high speed (up to 10 GHz for the shown modulator).

as

$$n_{\phi,bulk} = \sqrt{1+\chi}, \tag{2.1}$$

where χ is the linear term of the susceptibility with respect to the optical field. The electrical susceptibility of a material describes how easy an electric field induces a polarization $\mathbf{P}$ in the material, that is [1]

$$\mathbf{P} = \epsilon_0(\chi^{(1)}\mathbf{E} + \chi^{(2)}\mathbf{E}^2 + \chi^{(3)}\mathbf{E}^3 + \ldots), \tag{2.2}$$

where $\chi^{(n)}$ is a tensor of order $n+1$. Normally χ equals $\chi^{(1)}$, but when

the electric field **E** is a sum of different fields including the optical field, the result is more complicated.

The material susceptibility is wavelength dependent, as the electron orbital distortion depends on the drive frequency. The index of silica is to a good approximation given by the Sellmeier equation, that is

$$(n_{\phi,bulk}(\lambda))^2 = 1 + \sum_{j=1}^{3} A_j \frac{\lambda_0^2}{\lambda_0^2 - \lambda_j^2}, \tag{2.3}$$

where λ_0 is the vacuum wavelength of the propagating light while the material constants A_j and λ_j are experimentally determined [2] to

Sellmeier coefficients for silica

i	A_j	$\lambda_j(\mu m)$
1	0.6961663	0.0684043
2	0.4079426	0.1162414
3	0.897494	9.8961610

Table 2.1: The Sellmeier coefficients found in [2] both describes the place and the strength of the absorption bands in silica.

The wavelengths λ_j correspond to material resonance frequencies. This type of index curve (see fig. 2.2) is common for all materials, as the index is determined by the materials resonance frequencies, where the material is easily polarized by an electric field. This also shows that the material index approaches 1[1] for short wavelengths such as gamma radiation.

2.2 Waveguides.

There exist several methods for guiding light inside a medium. The simplest method applied in this project is to guide the light in a high index material (the core) surrounded by a lower index material (the cladding). This is drawn schematicly in fig. (2.3) below.
In the limit where the wavelength of the light is small compared to the

[1] the index of vacuum, i.e. no wave-material interaction.

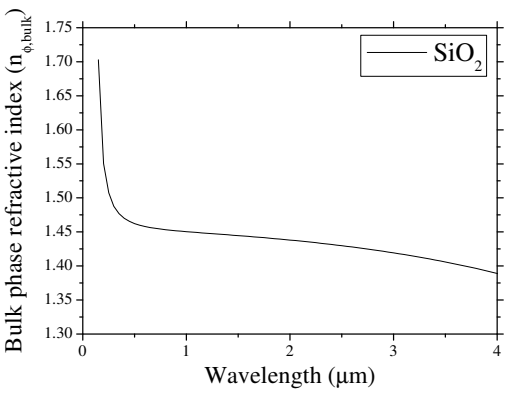

Figure 2.2: The Sellmeier index for SiO_2 vs. wavelength of the light. The index is increasing for small wavelength approaching the resonance wavelength at $\lambda_2 = 0.1162414\mu m$, see table (2.1).

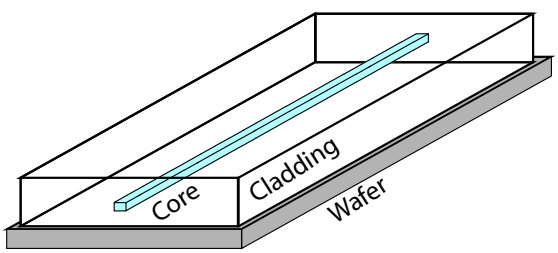

Figure 2.3: A straight planar waveguide. The blue glass (the core) has a higher index than the surrounding cladding. The glass structure is supported by the wafer, a single silicon crystal that is 0.5 mm height.

waveguide dimensions, guiding is due to reflection at the boundary between the materials. If light is incident into the high index (n_1) material it cannot propagate into the low index material (n_2) when the angle (α) of incidence is larger than the critical angle (α_c) found by Snell's law ($\sin(\alpha_c) = n_2/n_1$).
Normally the wavelength of the light is roughly of the same size as the waveguide width and height. In this case the equation for the guided

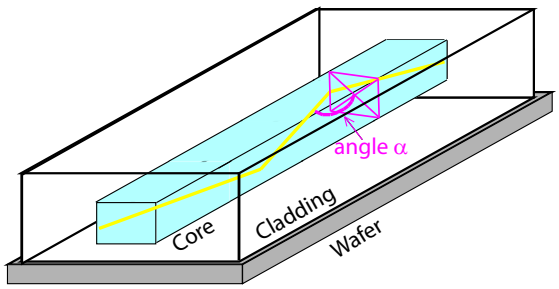

Figure 2.4: A straight planar waveguide with a large core. The yellow line represent light being guided inside the waveguide. The light is reflected at the interface between the high index core (n_1) and the low index cladding (n_2). The angle of incidence is called α and it is illustrated at a waveguide cross section. When the angle is larger than the critical angle ($\sin(\alpha_c) = n_2/n_1$), the light is reflected totally at the interface and is hence guided inside the waveguide.

light (the guided mode) is found by solving Maxwells equations. For a waveguide with dimensions on the wavelength scale there is only a limited number of guided solutions. The number depends on the size of the waveguide. When the waveguide size is small enough only one solution will remain. Such a waveguide is known as a single mode (SM) waveguide. Light in a small waveguide will be propagating partly inside the core and partly in the cladding as shown in fig. (2.5).

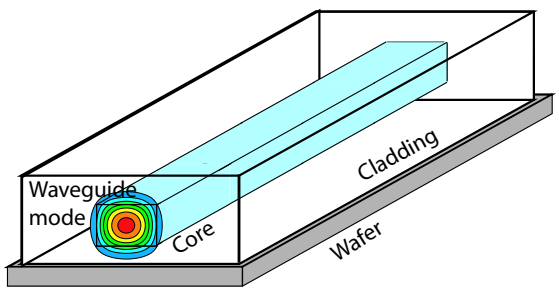

Figure 2.5: A small waveguide. The fundamental mode is illustrated at the waveguide end. The light propagates mostly inside the core with a tail sticking into the cladding. The effective index for the mode is in between the core and cladding index.

The phase propagation constant (β) for light inside a waveguide is some-

where between the bulk phase propagation constant for the cladding and core materials. This phenomenon is described by assigning an effective index to the waveguide, called the effective phase index ($n_{\phi,eff}$). The different modes are numbered by decreasing ($n_{\phi,eff}$) starting from the fundamental mode[2]. The group index[3] is also affected by the waveguide design and it is denoted ($n_{g,eff}$). The group index can in general be determined by the equation [3]

$$n_g = \frac{d\omega}{d\beta_\nu}, \tag{2.4}$$

where ν is the mode index. Even for a single mode waveguide, there are two guided solutions to Maxwell's equations, as the light can be polarized either as a transverse electric (TE) wave or as a transverse magnetic (TM) wave[4]. This is illustrated in fig. (2.6)

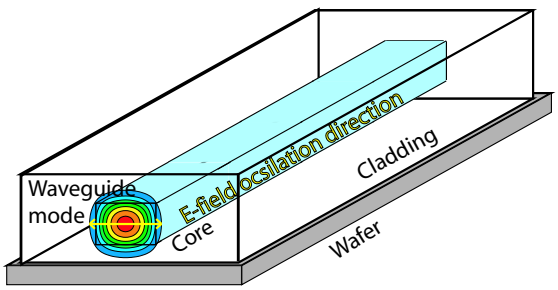

Figure 2.6: The propagating field is transverse electric (TE) polarized. The electric field is oscillating in the horizontal direction and it is perpendicular to the propagation direction.

In the case of TM polarized light, the electrical field is almost vertical, but it has a small component in the propagation direction. The effective index ($n_{\phi,eff}$) depends on the polarization direction, but the modes are degenerate[5] when the waveguide can be rotated into itself around the

[2] the mode that remains when the waveguide becomes single mode.

[3] The group index (n_g) determines the speed (c/n_g) of a light pulse propagating in the waveguide.

[4] The electric field for TM light is *not* perpendicular to the propagation direction. It is however approximately perpendicular and this approximation is used in the derivations of the change in refractive index (Δn_{TM}) due to the nonlinearity $\chi^{(3)}$ in appendix D.

[5] Degenerate modes have equal propagation constants.

waveguides center axis with a turn of 120 degrees or less [4]. This is illustrated in fig. (2.7).

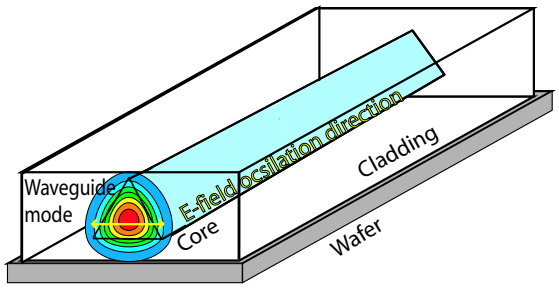

Figure 2.7: A triangular waveguide can be rotated into itself with a rotation of 120°. The TE mode that is illustrated has exactly the same propagation constant as the TM mode.

2.3 Mach-Zehnder interferometer.

The common way to apply EO materials for making an amplitude modulator is to use a Mach-Zehnder interferometer (MZI) configuration. The interferometer works by splitting the incident lights intensity equally into two arms. After some propagation length the two arms are re-combined. The outcome of the re-combined light depends on the phase difference between the two electromagnetic waves at re-combination. When the light is in phase (0 phase difference) the two waves interfere constructively while a π phase difference leads to destructive interference. This is shown schematicly in fig. (2.8).
The phase difference at re-combination is controlled by the optical path length of the two arms. When the arms have equal optical path length the light is in phase at re-combination and light is emitted from the interferometer. To change the output to zero emission, the optical path length of one or both arms must be changed. When the difference in optical path length equals $\lambda/2$ the light will interfere destructively at re-combination. The optical path length l_{opt} is

$$l_{opt} = l_{phy} n_{\phi,eff}, \tag{2.5}$$

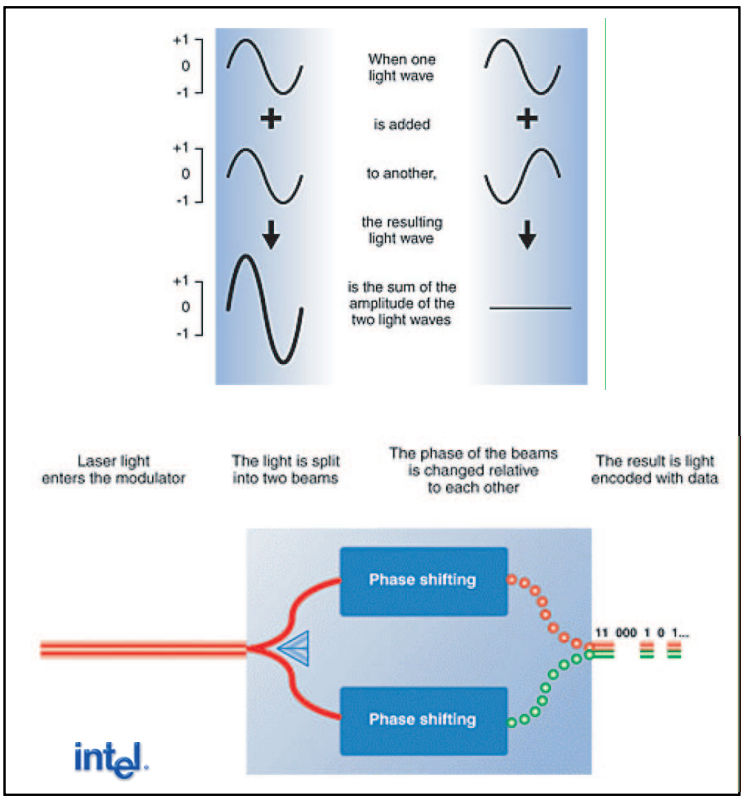

Figure 2.8: A figure from Intel demonstrating a MZI. The light is split into two arms, where the phase of the light can be changed. At re-combination the output depends on the phase difference between the light beams.

where l_{phy} is the physical length of the waveguide. The index $n_{\phi,eff}$ is used, as the relevant parameter for interference at re-combination is the *phase* difference between the two waves.

To change the output of the interferometer, the optical path length must be changed. This can be done by changing either the physical distance and/or $n_{\phi,eff}$. The physical distance is hard to change except when light is propagating in free space and even in free space is difficult to change l_{phy} fast. The index ($n_{\phi,eff}$) can be changed in a number of ways, e.g. the waveguide index is affected by pressure, electric fields, light intensity and numerous other effects. It is convenient to use materials

that change index when affected by an electric field, i.e. materials with a non-zero EO coefficient, as electronics can produce rapid varying electric fields. A material that has a non-zero linear EO coefficient will change its bulk phase index ($n_{\phi,bulk}$), when affected by an electric field E according to the equation [5]

$$\Delta n_{\phi,bulk}(E) = \frac{\chi^{(2)}}{n_{\phi,bulk,0}} E, \tag{2.6}$$

where $n_{\phi,bulk,0}$ is the material phase index when no field is present and $\chi^{(2)}$ is either the materials second order non-linearity or the effective second order non-linearity $\chi^{(2)}_{eff}$ due to $\chi^{(3)}$ combined with a large permanent electric field (E_p). Both $\chi^{(2)}$ and $\chi^{(3)}$ are in general tensors and the derivation of the index change due to a non-zero $\chi^{(2)}$ tensor element can be found in [2]. Due to the nature of the $\chi^{(2)}$ samples investigated in this project, there is only used TE polarized light in the measurement and the tensor element giving an index change is $\chi^{(2)}_{xxz}$. In this thesis $\chi^{(2)}$ is the name of the scalar element $\chi^{(2)}_{xxz}$. For $\chi^{(3)}$ materials eq. (2.6) is derived in appendix D, where it is assumed that the material is isotropic, i.e. that x, y or z direction inversion have no effect on the material. The equation for $\chi^{(2)}_{eff}$ is

$$\chi^{(2)}_{eff} = 3\chi^{(3)} E_p, \tag{2.7}$$

where E_p is the permanent field. The magnitude of $\chi^{(2)}$ and $\chi^{(3)}$ will in general depend on the frequency of the applied electric field (E), that is used to induce $\Delta n_{\phi,bulk}$.

The desired effect in the MZI is to induce a change in the effective refractive index ($\Delta n_{\phi,eff}$). The origin of $\Delta n_{\phi,eff}$ is a change in the bulk materials index $\Delta n_{\phi,bulk}$. Perturbation theory [6] is used to determine the equation for $\Delta n_{\phi,eff}$ as function of $\Delta n_{\phi,bulk}$. The perturbation approach starts with the general differential equation for a propagating wave, i.e. the Helmholtz equation, that is

$$(\nabla^2 + \epsilon(x,y,z)k_0)E(\mathbf{r}) = 0. \tag{2.8}$$

The solution for a waveguide which is uniform along the propagation direction is

$$E_m(\mathbf{r}) = \begin{bmatrix} a_x \\ a_y \end{bmatrix} E_m(x,y)e^{-i\beta_m z}, \tag{2.9}$$

where m is the modal index and $\begin{bmatrix} a_x \\ a_y \end{bmatrix}$ is the normalized Jones vector describing the polarization. When the solution (2.9) is inserted into eq. (2.8), the perturbation approach [6] gives

$$\Delta n_{\phi,eff}(E) = \sum_i \Delta n_{\phi,bulk,i} \Gamma_i, \tag{2.10}$$

where $\Delta n_{\phi,bulk,i}$ is the bulk refractive index change of layer i and Γ_i is the confinement factor to layer i. Notice that the perturbation of the mode shape ($\Delta E_m(x,y)$) to first order has *no* effect on the propagation constant. Eq. (2.10) is normally used for determination of the material non-linearity, even though the perturbation approach is only correct for a waveguide that is uniform along the propagation direction. For other types of waveguides, where the electric field changes significantly along the propagating direction, it has theoretically been shown that [7]

$$\Delta n_{\phi,eff}(E) = \sum_i \Delta n_{\phi,bulk,i} \Gamma_i \frac{n_{g,eff}}{n_{\phi,bulk,i}}, \tag{2.11}$$

where $n_{g,eff}$ is the effective group index of the guided mode. The linear enhancement of $\Delta n_{\phi,eff}(E)$ with the group index $n_{g,eff}$ is demonstrated experimentally in this Ph.D. thesis (see section 6). As eq. (2.10) is the normal equation applied for determination of the material non-linearity, this equation is used through out this thesis, except when explaining the results for photonic crystal (PhC) waveguides.

Combining eq. (2.6) describing the change in $n_{\phi,bulk,i}$ due to an electric field with eq. (2.10) gives

$$\Delta n_{\phi,eff}(E) = \sum_i \frac{\chi_i^{(2)}}{n_{\phi,bulk,0,i}} E_i \Gamma_i, \tag{2.12}$$

where $\chi_i^{(2)}$ is the non-linearity of layer i, $n_{\phi,bulk,0,i}$ is the bulk phase index of layer i when no electric field is applied and E_i is the electric field affecting layer i. The applied measurement technique determines the change in the effective index of the guided mode $\Delta n_{\phi,eff}$ as function of applied voltage across the sample. To determine the individual non-linearities of the core and cladding materials, all the individual terms in eq. (2.12) except one must be known. In the case where the sample

consists of a core material with a non-zero $\chi^{(2)}$ value surrounded by a cladding material with zero $\chi^{(2)}$, eq. (2.12) reduces to

$$\Delta n_{\phi,eff}(E) = \frac{\chi^{(2)}_{core}}{n_{\phi,bulk,0,core}} E_{core} \Gamma_{core}. \tag{2.13}$$

This is the case for PhC waveguides, the only samples investigated in this work, where a $\chi^{(2)}$ value is observed. For samples where $\chi^{(2)}$ is induced by $\chi^{(3)}$ combined with a permanent electric field, both the core and the cladding contribute to the change in $\Delta n_{\phi,eff}$. For $\chi^{(3)}$ materials it is difficult to determine the individual terms and the measured $\Delta n_{\phi,eff}$ is therefore used to interpret an average non-linearity coefficient, i.e.

$$\Delta n_{\phi,eff}(E) = \frac{3\chi^{(3)}_{av} E_p}{n_{\phi,eff,0}} E, \tag{2.14}$$

where $\chi^{(3)}_{av}$ is the average[6] non-linearity of the sample and $n_{\phi,eff,0}$ is the effective phase index of the waveguide when $E = 0$. Eq. (2.14) describes the linear part of the index change for a $\chi^{(3)}$ material where a large permanent field (E_p) is applied together with the switching field (E). In a switch or modulator it is the linear index change with applied field that is useful. In general the requirements for the two fields E_p and E are the same, i.e. a slow variation compared to the optical field. The two fields can therefore *not* be distinguished. The general equation for the index change of a $\chi^{(3)}$ material is therefore

$$\Delta n_{\phi,eff}(E) = \frac{3\chi^{(3)}_{av}}{2n_{\phi,eff,0}} E^2. \tag{2.15}$$

When comparing $\chi^{(3)}_{av}$ values obtained from different samples, the cladding material and the confinement factor to the core is kept approximately identical. The difference in $\chi^{(3)}_{av}$ does then arise from the difference in material $\chi^{(3)}$ for the core material.

The determined equations (eq. 2.13 and eq. 2.14) for the linear change in effective phase index ($\Delta n_{\phi,eff}(E)$) can be used to determine the voltage required to drive a switch. The simplest modulator is a MZI, where only one arm is modulated (see fig. 2.9).

[6] The confinement factor is used as weighting factor for the averaging of the material $\chi^{(3)}$ values.

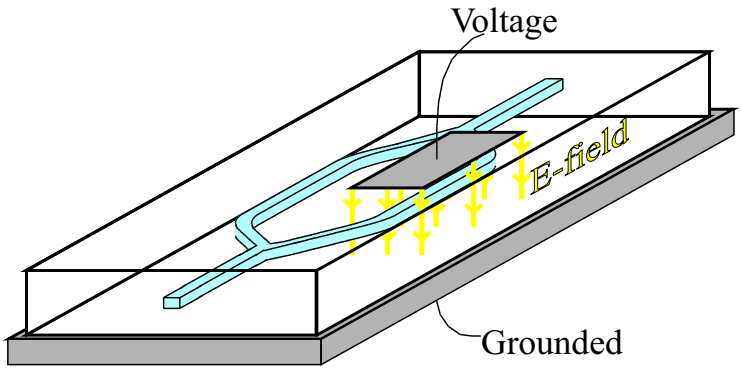

Figure 2.9: A MZI where the phase is modulated in one arm. The switching voltage is applied to the top electrode and the bottom electrode is grounded.

The light will interfere constructively when the two arms are identical, i.e. when no voltage is applied to the electrode. To change the output of the modulator, the voltage V_π is applied. This voltage alters the refractive index of one arm and when the optical path length is changed by $\lambda/2$ the interference becomes destructive when the two waves are re-combined as shown in fig. (2.8). To determine the required voltage V_π for changing the optical path length by $\lambda/2$, eq. (2.5) for the optical path length is combined with either eq. (2.13) or eq. (2.14) describing the change in effective refractive index, that is

$$\lambda/2 = l_{sample}\frac{\chi^{(2)}_{core}\Gamma_{core}}{n_{\phi,bulk,0,core}}\frac{V_\pi \varsigma}{d} \tag{2.16}$$

$$\lambda/2 = l_{sample}\frac{3\chi^{(3)}_{av}E_p}{n_{\phi,eff,0}}\frac{V_\pi}{d}, \tag{2.17}$$

where the electric field E has been replaced by $V_\pi\varsigma/d$ (the factor ς is properly introduced after deriving eq. 2.19) in the case of a $\chi^{(2)}$ material sandwiched between two dielectric medium (see fig. 2.10) and V_π/d for a $\chi^{(3)}$ material.
The strength of the electric field in a specific layer depends on the variation of dielectric constant between the materials[7]. The electric flux

[7] A dielectric constant depends on the frequency of the applied field and is in general different for the slow varying voltage applied and for the optical field.

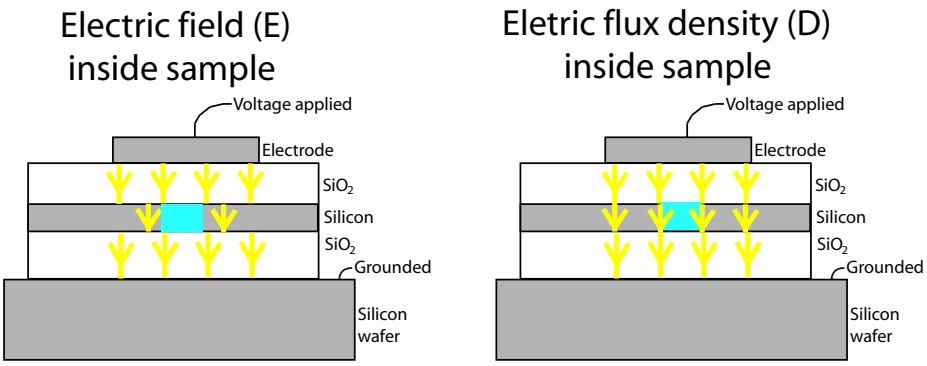

Figure 2.10: A sample where the core layer (Silicon) has a higher dielectric constant ϵ_r than the cladding layer (Silica). The electric field (E) is lower in the high index layer, while the electric flux density (D) is constant [8].

density field $D = \epsilon_r \epsilon_0 E$ is constant between the electrodes and the field in each layer can therefore be determined. The voltage over the sample is

$$V = E_1 d_1 + E_2 d_2, \tag{2.18}$$

where E_1 is the field inside the silicon, d_1 is the thickness of the silicon layer, E_2 is the field inside the silica and d_2 is the total thickness of the silica layers. Writing the equation using the D gives

$$\begin{aligned} V\epsilon_0 &= \frac{D_1 d_1}{\epsilon_{r,1}} + \frac{D_2 d_2}{\epsilon_{r,2}} \Leftrightarrow \quad \text{(as } D \text{ constant)} \\ V\epsilon_0 &= \frac{D d_1}{\epsilon_{r,1}} + \frac{D d_2}{\epsilon_{r,2}} \Leftrightarrow \\ E_1 &= \underbrace{\frac{\epsilon_{r,2}(d_1 + d_2)}{d_1 \epsilon_{r,2} + d_2 \epsilon_{r,1}}}_{=\varsigma} \frac{V}{d}. \end{aligned} \tag{2.19}$$

The determined electric field depends linearly on the applied voltage and the factor ς in eq. (2.16) represents the linear correction factor. An example of ς is plotted in fig. (2.11).
In eq. (2.17) for a $\chi^{(3)}$ material the correction factor is omitted, as the three layers are very similar and hence also have similar ϵ_r values. The

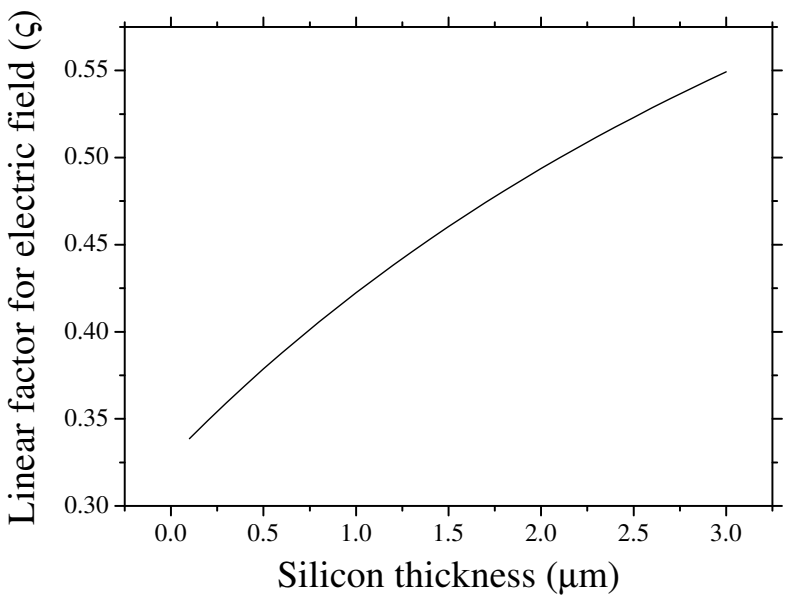

Figure 2.11: The linear factor ς between the naive field V/d and the field inside the silicon for a sample with $2\mu m$ of SiO_2.

difference in dielectric constant is therefore ignored. The switching voltages for the two cases are

$$V_\pi = \frac{\lambda d n_{\phi,bulk,0,core}}{2 l_{sample} \varsigma \chi^{(2)}_{core} \Gamma_{core}} \tag{2.20}$$

$$V_\pi = \frac{\lambda d n_{\phi,bulk,0,eff}}{6 l_{sample} \chi^{(3)}_{av} E_p}. \tag{2.21}$$

The shift in optical path length needed to change the output of the switch is always $\lambda/2$. The absolute value of the required voltage can be reduced by a factor of two by introducing a permanent optical path length increase of $\lambda/4$ in one of the arms (see fig. 2.12). There must then be applied a voltage of $V_\pi/2$ to get constructive interference and a voltage of $-V_\pi/2$ to

get destructive interference. Another way to reduce the absolute voltage by a factor of 2 is by applying electrodes on both sides of the waveguide (see fig. 2.12). The voltage on the bottom electrode must then be the opposite of the voltage on the top electrode. Finally the absolute size of the voltage can be reduced by a factor of 2 by modulating both arms in the MZI at the same time (see fig. 2.12).
By combining all three methods the required voltage is reduced by a factor of 8. This is smart when the challenge is the size of the required voltage, e.g. it is difficult to find an electrical driver that switches 1000 volts fast, while a combination of drivers each producing 125 volts is easier to get. In other cases it might be best only to have one driver, as it is difficult to synchronize fast drivers.

To define a size that is comparable without deciding which electrode configuration is smartest, it is normal to report the total voltage swing required to change the output of the interferometer, multiplied by the total affected length, i.e.

$$V_\pi l_{sample} = \frac{\lambda d n_{\phi,bulk,0,core}}{2\varsigma\chi^{(2)}_{core}\Gamma_{core}} \tag{2.22}$$

$$V_\pi l_{sample} = \frac{\lambda d n_{\phi,bulk,0,core}}{6\chi^{(3)}_{av}E_p\Gamma_{core}}. \tag{2.23}$$

This is a good engineering unit for a device where the waveguide parameters have been optimized, as it includes all the compromises like weighting the desire for a small electrode-electrode distance against the requirement of not loosing light from leakage to the electrode (see fig. 2.13). The other nice feature about the unit $V_\pi l_{sample}$ (normally measured in $V * cm$) is that this is the size directly determined by the non-linear measurement method.

When making material development, it is better to determine the constants $\chi^{(2)}_{core}$ or $\chi^{(3)}_{av}$, as the optimal waveguide design for a certain material is not trivial to determine.
The material non-linearities can alternatively to eq. (2.2) be described as a Taylor expansion of the material impermeability (η). In the alternative expansion, the bulk refractive index change is written [5]

$$\Delta n_{\phi,bulk}(E) = n_{\phi,bulk,0} - \frac{1}{2}\mathfrak{r}n^3_{\phi,bulk,0}E - \frac{1}{2}\mathfrak{s}n^3_{\phi,bulk,0}E^2 \tag{2.24}$$

where $\mathfrak{r}$ is called the Pockels coefficient and $\mathfrak{s}$ is called the Kerr coefficient. The equations connecting the two ways of expressing material non-linearity are

$$\mathfrak{r} = -\frac{2\chi^{(2)}}{n_{\phi,bulk,0}^4} \tag{2.25}$$

$$\mathfrak{s} = -\frac{3\chi^{(3)}}{n_{\phi,bulk,0}^4}. \tag{2.26}$$

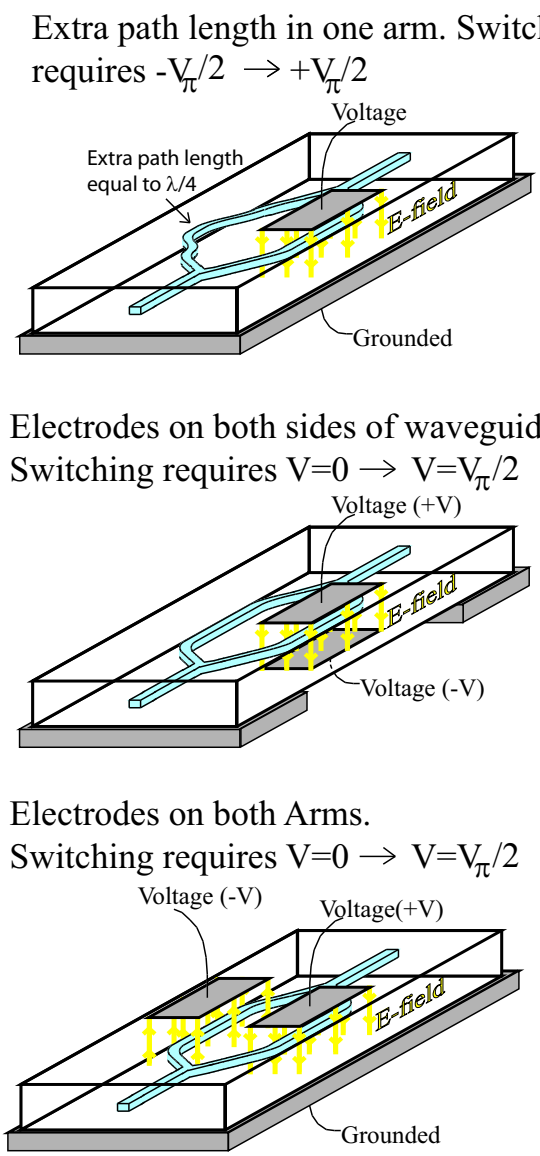

Figure 2.12: There exist three ways for reducing the required voltage. The first way is to increase the optical path length of one arm by $\lambda/4$. Switching is then done by changing the applied voltage from $-V_\pi/2$ to $+V_\pi/2$. The optical path length is normally adjusted by applying a DC-electric field over the arm. The second possibility is to apply electrodes on both sides of the waveguide. Switching is then obtained by applying $+V_\pi/2$ to the top electrode and $-V_\pi/2$ to the bottom electrode. The third possibility is to modulate both arms simultaneously, i.e. switching is obtained by applying $+V_\pi/2$ to one arm and $-V_\pi/2$ to the other arm.

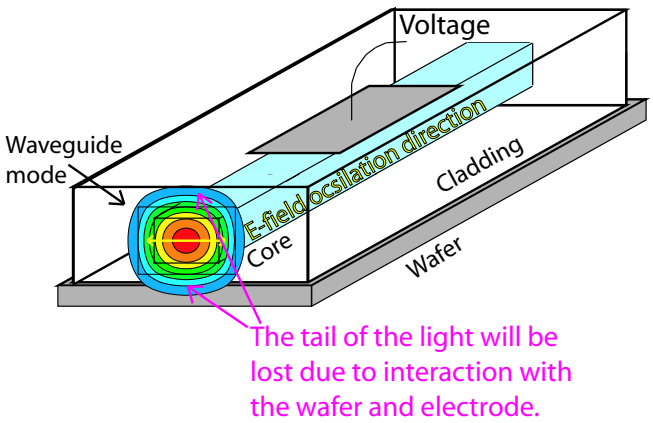

Figure 2.13: Waveguide where the distance between the electrodes is too small. The tail of the optical field sees both the top and bottom electrode. The field reaching the electrodes is lost due to the high optical loss in the conducting materials.

2.4 Poling.

In eq. (2.7) and effective $\chi^{(2)}$ value is introduced by combining the material $\chi^{(3)}$ with a permanent electric field E_p. This section describes how such a permanent field is obtained through the poling process. Poling is done by applying a high voltage field over the sample while it is heated to $\approx 350°C$. The sample is kept at elevated temperature for approximately 20 minutes and then cooled down to room temperature while the high voltage field is maintained over the sample. When the glass is heated charges and/or dipoles inside the glass orient themselves according to the external field (see fig. 2.14). The charges and/or dipoles are trapped, when the glass is cooled back to room temperature.

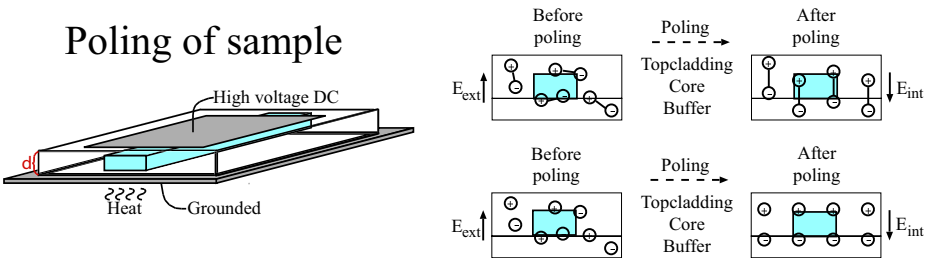

Figure 2.14: Poling is performed by maintaining an electric field over the sample while exciting the glass, e.g. by heating. The top right figures illustrate the dipole model, while the bottom right figures illustrate the charge separation model [9].

Etching results performed in [10] show that charges are moved in poled fibers. The best explanation for the field poled into the samples is therefore the movement of charges, as there is no fundamental difference between our planar samples and the fibers poled in [10]. There is an optimum for both the poling time and temperature as described in [11]. The explanation of this is probably charge depletion of the material as described in [10]. When all movable charges inside the material have migrated to the electrodes, the material is totally depleted. Then there are no charges that can make an internal electric field (see fig. 2.15). The trick of poling is to stop, when the charges have migrated to the optimal

position as shown in fig. (2.15). The poling temperature controls the migration speed of the different types of charges and by choosing the correct temperature the difference in charge migration speed is optimized.

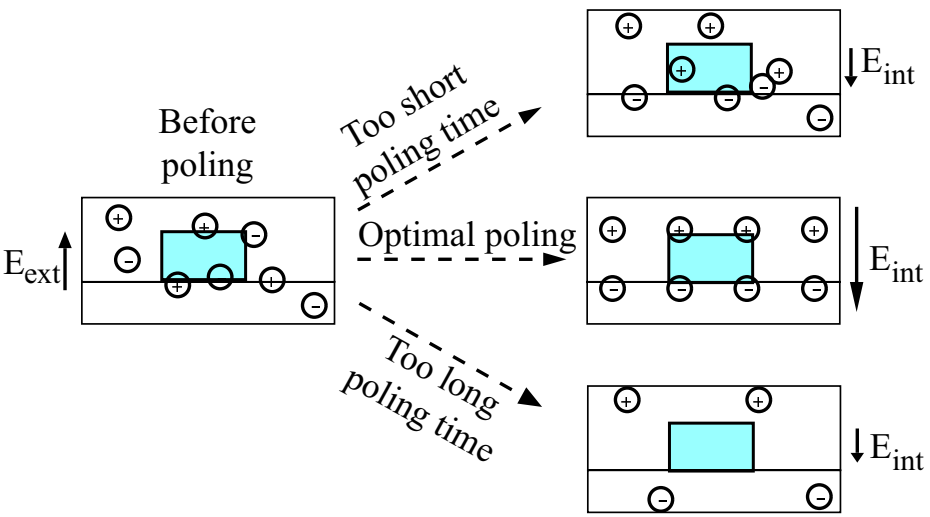

Figure 2.15: When the external field is applied and the sample is heated, i.e. when the sample is poled, charges inside the glass starts to move. If the poling time is to short, the charges will only move a short distance and the build-in electric field is hence small. A very long poling time will on the other hand move the charges out of the sample and the build-in electric field will also be small. The optimal poling time is somewhere in between, at the point where the optical field inside the waveguide is affected in an optimal manor.

The effect of poling can be demonstrated by measuring the Bragg wavelength vs. applied DC-field. In appendix C it is shown that the Bragg wavelength is equal to $n_{\phi,eff}\Lambda$, where Λ is the pitch of the phase mask (i.e. a constant). The Bragg wavelength vs. applied field is shown in fig. (2.16) for a sample before and after poling. The figure shows that the index parabola is shifted due to the frozen-in field ($E_{frozen-in}$). It also shows that the curvature of the parabola is not affected by the poling, i.e. that $\chi^{(3)}_{av}$ is constant.

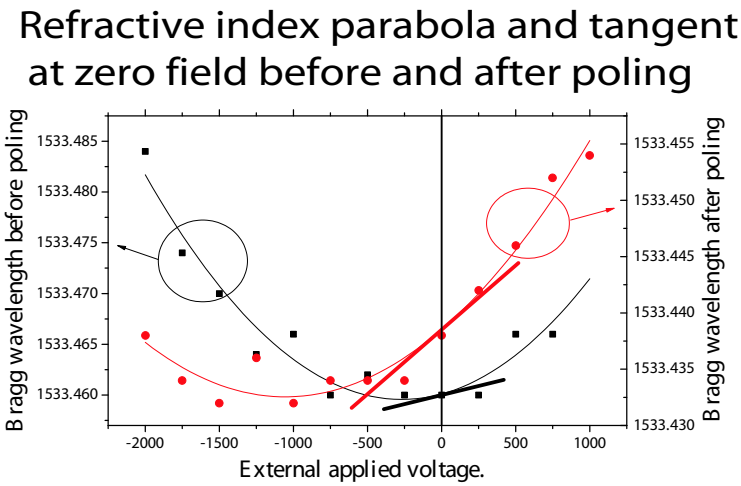

Figure 2.16: Before poling, the index follows the black curve. After poling a field corresponding to $\sim 1050V$ is built into the sample. The tangent at zero field was small before poling, i.e. a small electric field did not have a significant impact at the refractive index of the sample. The tangent at zero field is after poling much higher due to the frozen-in field. A small electric field has a significantly higher impact on the refractive index after poling. Notice that the curvature of the parabola is not changed, i.e. the only significant effect of poling the sample is the creation of a large built-in electric field (E_p).

References to Chapter 2

[1] P. Butcher and D. Cotter. *The elements of nonlinear optics*. Cambridge University Press, 1990. ISBN 0-521-42424-0.

[2] R. Syms and J. Cozens. *Optical guided waves and devices*. McGraw-Hill, 1992. ISBN 0-07-707425-4.

[3] C. Kittel. *Introduction to solid state physics*. Wiley, 1996. ISBN 0-471-11181-3.

[4] M. J. Steel, T. P. White, C. M. de Sterke, R. C. McPhedran, and L. C. Botten. "Symmetry and degeneracy in microstructured optical fibers", *Optics Letters*, vol. 26, pp. 488–90, 2001.

[5] B. Saleh and M. Teich. *Fundamentals of Photonics.* Wiley, 1991. ISBN 0-471-83965-5.

[6] L. Coldren and S. Corzine. *Diode lasers and photonic integrated curcuits.* Wiley, 1995. ISBN 0-471-11875-3.

[7] M. Soljačić, S. Johnson, S. Fan, M. Ibanescu, E. Ippen, and J. Joannopoulos. "Photonic-crystal slow-light enhancement of nonlinear phase sensitivity", *J. Opt. Soc. Am. B.*, vol. 19, no. 9, 2002.

[8] B. Elbek. *Elektomagnetisme.* Niels Bohr Institutet, 1997. ISBN 87-87585-07-3.

[9] P. Kazansky and P. Russel. "Thermally poled glass: Frozen-in electric field or oriented dipoles?", *Opt. Commun.*, vol. 19, pp. 611–614, 1994.

[10] N. Myrén. *Poled fiber devices.* Ph.D. thesis, Department of Physics and Quantum Optics, Royal institute of technolegy, Roslagstullsbacken 21, SE-106 91 Stockholm, Sweden., 2005. ISBN 91-7178-053-x.

[11] Y. Ren, C. Marckmann, J. Arentoft, and M. Kristensen. "Thermally poled channel waveguides with polarization independent electro-optic effect", *IEEE Photon. Technol. Lett.*, vol. 14, no. 5, pp. 639–641, 2002.

Chapter 3

Theory for the DC-shifted Mach-Zehnder interferometer method.

3.1 Introduction to the theory for the measurement method

There exist many methods [1–4] for measuring the frozen-in field $E_{frozen-in}$ and the non-linearity coefficients $\chi^{(2)}$ and $\chi^{(3)}$ for a sample. One method previously used in the group [1] (The Bragg grating method, outlined in appendix C) was discarded due to two aspects. The most severe problem was a reproducibility problem[1]. The measured result for $\chi^{(3)}$ could vary randomly with a factor of 1.5. The other aspect was the requirement of a Bragg grating written into the waveguide. The grating was induced by shining very intense UV-light onto the sample through a phase mask. This only introduces a Bragg grating when the sample is UV-sensitive.

The other method used in the group was based on a Mach-Zehnder interferometer(MZI). It was previously assumed that the phase difference between the two arms in the fiber based MZI was not only constant during

[1] A possible explanation for the reproducibility problem is a communication problem between the laser and optical spectrum analyzer used. The problem was detected by Jesper Bevensee Jensen after I finished the work on *the DC-shifted MZI method*. The communication problem has *not* been intensively investigated.

a measurement but actually equal to $\pi/2$. As shown in fig. (3.6) and (3.7) this was *not* the case when measurements where performed in this Ph.D. project. This chapter about the new **DC-shifted MZI method** is mainly a consequence of the fast random phase drift (severe up to 5 kHz and measurable up to 10 kHz).

The derivation and explanation of the DC-shifted MZI method is divided into 3 sections. Section (3.2) is used to derive a general equation (that is eq. 3.14) for the light intensity output from a MZI. Section (3.3) describes the calibration method used for measuring V_π for the $LiNbO_3$ phase modulator that is used in the experimental DC-shifted MZI setup. The measured $V_\pi(\lambda)$ values are listed in table (3.1) and plotted in fig. (3.13). The measurement method that determines $E_{frozen-in}$ and the non-linearity coefficients $\chi^{(2)}$ and $\chi^{(3)}$ for a sample is described in section (3.4). The goal of the 3 sections is to proof that the measurement can be used to determine the phase shift induced by the sample in an unambiguous way. The chapter ends with a section concerning the accuracy of the method and also a summary of the pros and cons for the developed method.

3.2 General theory for a Mach-Zehnder interferometer.

3.2.1 The optical setup for section (3.2).

A Mach-Zehnder interferometer(MZI) is used for measuring the frozen-in field $E_{frozen-in}$ and the non-linearity coefficients $\chi^{(2)}$ and $\chi^{(3)}$ for the characterized waveguides. The MZI setup has been modified in a number of ways to obtain better accuracy and more information. A detailed description is given first for a general MZI, then for the special MZI setup used to calibrate the $LiNbO_3$ phase modulator and finally for the setup used to measure the samples. A general MZI consists of a light splitter, a propagation distance where both the phase, the polarization and the amplitude are changed and, finally, a coupler that combines the light again. A fiber based interferometer made using two couplers is illustrated in fig.(3.1).

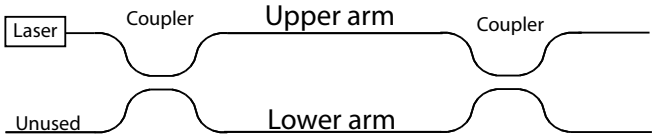

Figure 3.1: A general Mach-Zehnder interferometer(MZI) where light traveling in the upper and lower arms can be influenced by numerous affects.

3.2.2 Derivation of the output from a general MZI

To derive equations describing the intensity output from the two arms to the left in fig.(3.1), the central part of the last coupler is investigated. The central part consist of two straight waveguides of length l_c, where light is coupled from one arm to the other. For a simple case this is sketched in fig. (3.2).

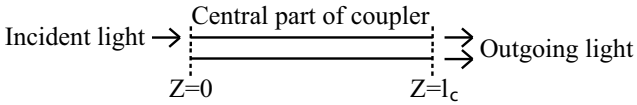

Figure 3.2: Central part of the last coupler. The length of the central part is l. To describe a simple case, light is only incident in the upper arm. The distance between the center of the two waveguides is around $15\mu m$.

To describe the outgoing intensity, it is adequate to look at a simpler case first. In [5] it is described how light in two close lying waveguides couples from one waveguide to the other. Light with unity intensity is incident in the upper arm, while no light is incident in the lower arm (corresponding to fig.(3.2)). The equations for the amplitudes of the light in the upper arm (a_1) and in the lower arm (a_2) after propagating a length z are

$$a_1(z) = e^{\frac{i\Delta\beta z}{2}}\left(\cos(\gamma z) - i\frac{\Delta\beta}{2\gamma}\sin(\gamma z)\right) \tag{3.1}$$

$$a_2(z) = \frac{C_{12}}{i\gamma}e^{\frac{-i\Delta\beta z}{2}}\sin(\gamma z), \tag{3.2}$$

where

$$\gamma^2 = \left(\frac{\Delta\beta}{2}\right)^2 + C_{12}C_{21}. \tag{3.3}$$

The constant $\Delta\beta = \beta_1 - \beta_2$ describes the difference in propagation constants between the two waveguides, the constant C_{12} is the coupling coefficient from the upper arm to the lower arm and C_{21} is the reverse coupling coefficient.

After having presented the simple case, where light is only incident into one arm, the general case can be derived. The coupling for the light incident in the upper arm is not affected by the light incident in the lower arm. The general solution, when light with intensity I_1 and phase ϕ_1 is incident into the upper arm while there is simultaneously incident light into the lower arm with intensity I_2 and phase ϕ_2, is found by adding the outgoing amplitudes. Calling the general amplitude solutions in the upper and lower arm $a_1^g(z)$ and $a_2^g(z)$, respectively, the general solutions are

$$a_1^g(z) = \sqrt{I_1}e^{-i\phi_1}a_1(z)\begin{bmatrix} a_{1x} \\ a_{1y} \end{bmatrix} + \sqrt{I_2}e^{-i\phi_2}a_2(z)\begin{bmatrix} a_{2x} \\ a_{2y} \end{bmatrix} \quad (3.4)$$

$$a_2^g(z) = \sqrt{I_2}e^{-i\phi_2}a_1(z)\begin{bmatrix} a_{2x} \\ a_{2y} \end{bmatrix} + \sqrt{I_1}e^{-i\phi_1}a_2(z)\begin{bmatrix} a_{1x} \\ a_{1y} \end{bmatrix}, \quad (3.5)$$

where $\begin{bmatrix} a_{1x} \\ a_{1y} \end{bmatrix}$ and $\begin{bmatrix} a_{2x} \\ a_{2y} \end{bmatrix}$ are the normalized Jones vectors describing the polarization for the light incident in the upper and in the lower arm. When the two polarizations are orthogonal to each other, there is no interference, and the output power from an arm is found by adding the power contributions from the two arms. On the other hand, when the two polarizations are parallel, there is maximal interference.

To obtain maximal interference a number of parameters must be optimized. A polarization controller is introduced to make the polarization of the light in the two arms parallel. Moreover the coupler must be symmetrical, meaning the propagation constants in the two arms must be equal ($\Delta\beta = 0$) and the coupling coefficients must be equal ($C_{12} = C_{21} \equiv C$). These restrictions are fulfilled if a 3 dB coupler[2] is used as the last coupler. The MZI including the polarization controller and a 3 dB coupler is shown in fig. (3.3). Using a 3 dB coupler also ensures that half of the light incident in one arm is coupled over to the other arm at the output for a certain wavelength. In the experiment the coupler is 3 dB at 1550

[2] A 3 dB coupler distributes light from an input fiber evenly into the two output fibers.

nm. The experiment is made for a number of different wavelengths, and the coupler is not 3 dB for all the wavelengths. In the derivations, it is therefore *not* assumed, that half the light is coupled from one arm to the other.

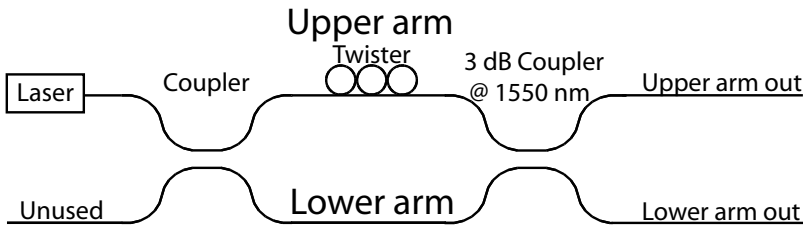

Figure 3.3: MZI where the polarization is adjusted for maximum interference.

With these restrictions on the polarization and the coupler ($\Delta\beta = 0$ and $C_{12} = C_{21} \equiv C$), the equations describing the amplitudes ($a_1^{\max}$) and ($a_2^{\max}$) for the light after propagating through the last coupler are

$$\begin{aligned} a_1^{\max}(l_c) &= \sqrt{I_1}e^{-i\phi_1}a_1(Cl_c)\begin{bmatrix} a_x \\ a_y \end{bmatrix} + \sqrt{I_2}e^{-i\phi_2}a_2(Cl_c)\begin{bmatrix} a_x \\ a_y \end{bmatrix} \\ &= \left(\sqrt{I_1}\cos(Cl_c)e^{-i\phi_1} - i\sqrt{I_2}\sin(Cl_c)e^{-i\phi_2}\right)\begin{bmatrix} a_x \\ a_y \end{bmatrix} \quad (3.6) \\ a_2^{\max}(l_c) &= \sqrt{I_2}e^{-i\phi_2}a_2(Cl_c)\begin{bmatrix} a_x \\ a_y \end{bmatrix} + \sqrt{I_1}e^{-i\phi_1}a_1(Cl_c)\begin{bmatrix} a_x \\ a_y \end{bmatrix} \\ &= \left(\sqrt{I_2}\cos(Cl_c)e^{-i\phi_2} - i\sqrt{I_1}\sin(Cl_c)e^{-i\phi_1}\right)\begin{bmatrix} a_x \\ a_y \end{bmatrix}. \quad (3.7) \end{aligned}$$

Defining the phase difference $\Delta\phi = \phi_2 - \phi_1$, the powers ($P_1^{max}$) and ($P_2^{max}$) in the upper and lower arms after the last coupler are

$$\begin{aligned} P_1^{\max} &= I_1\cos^2(Cl_c) + I_2\sin^2(Cl_c) \\ &\quad -2\sqrt{I_1I_2}\sin(Cl_c)\cos(Cl_c)\sin(\Delta\phi) \quad (3.8) \\ P_2^{\max} &= I_1\sin^2(Cl_c) + I_2\cos^2(Cl_c) \\ &\quad +2\sqrt{I_1I_2}\sin(Cl_c)\cos(Cl_c)\sin(\Delta\phi). \quad (3.9) \end{aligned}$$

As noted, the variation of the power is biggest when $\sin(Cl_c) = \cos(Cl_c) = 1/\sqrt{2}$, i.e. when the last coupler is 3 dB. In the MZI setup the phase ($\Delta\phi$)

is affected by different factors; the length of the two arms, the temperature fluctuations for the arms and the phase change induced actively by phase modulators (see fig.(3.4)).

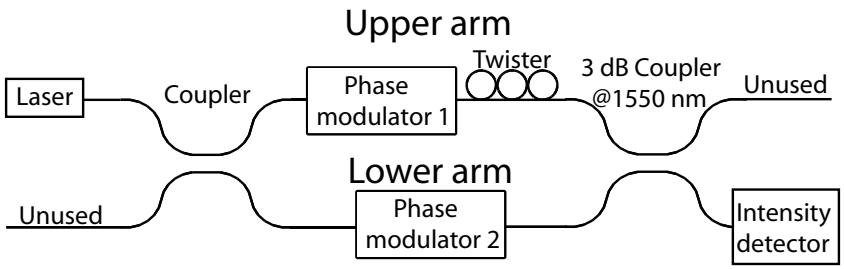

Figure 3.4: MZI where the phases (ϕ_1) and (ϕ_2) of the light are changed actively by phase modulators.

The phase ($\phi_1(t)$) of the light in the upper arm and the phase ($\phi_2(t)$) of the light in the lower arm before entering the last coupler are

$$\phi_1(t) = c_1 + \varphi_1^{noise}(t) + \phi_1(E_{mod,1}) \tag{3.10}$$
$$\phi_2(t) = c_2 + \varphi_2^{noise}(t) + \phi_2(E_{mod,1}), \tag{3.11}$$

where c_1 and c_2 are the phases for $z = 0$ and $t = 0$, $\varphi_1^{noise}(t)$ and $\varphi_2^{noise}(t)$ are the phase changes due to noise and finally $\phi_1(E_{mod,1})$ and $\phi_2(E_{mod,2})$ are the phase changes due to electrical fields $E_{mod,1}$ and $E_{mod,2}$ applied to the phase modulators. The power detected by the intensity detector in the lower arm is

$$\begin{aligned} I(t) &= I_1 \sin^2(Cl_c) + I_2 \cos^2(Cl_c) + 2\sqrt{I_1 I_2} \sin(Cl_c)\cos(Cl_c) \\ &\quad \cdot \sin\left[c_1 + \varphi_1^{noise}(t) + \phi_1(E_{mod,1})\right. \\ &\quad \left. -c_2 - \varphi_2^{noise}(t) - \phi_2(E_{mod,2})\right]. \end{aligned} \tag{3.12}$$

Replacing the phase constants c_1, c_2 and the noise terms $\varphi_1^{noise}(t)$ and $\varphi_2^{noise}(t)$ with a general noise term $\varphi^{noise}(t)$ the equation is

$$\begin{aligned} I(t) &= I_1 \sin^2(Cl_c) + I_2 \cos^2(Cl_c) + 2\sqrt{I_1 I_2} \sin(Cl_c)\cos(Cl_c) \\ &\quad \cdot \sin\left[\varphi^{noise}(t) + \phi_1(E_{mod,1}) - \phi_2(E_{mod,2})\right]. \end{aligned} \tag{3.13}$$

This is the intensity in the lower arm of a general MZI. To ease the later derivations the equation is written as

$$\begin{aligned} I(t) &= I_1 \sin^2(Cl_c) + I_2 \cos^2(Cl_c) \\ &\quad +\eta \sin\left[\varphi^{noise}(t) + \phi_1(E_{mod,1}) - \phi_2(E_{mod,2})\right]. \end{aligned} \tag{3.14}$$

where η is

$$\eta = 2\sqrt{I_1 I_2}\sin(Cl_c)\cos(Cl_c). \tag{3.15}$$

3.3 V_π for the $LiNbO_3$ phase modulator.

3.3.1 The optical setup for section (3.3).

To find V_π, i.e. the voltage required to change the phase by π, for a $LiNbO_3$ phase modulator, a MZI setup is used (see section 3.2.1). The $LiNbO_3$ modulator is placed in the upper arm, while the lower arm is a non-modulated fiber. A polarization controller is placed in front of the $LiNbO_3$ modulator, as the loss in the modulator is polarization dependent. To ensure stable incident polarization throughout the measurement, a polarization controller and a polarizer are placed after the laser (see fig. 3.5). The two new introduced polarization controllers are adjusted to ensure the best transmission through the polarizer and through the $LiNbO_3$ modulator, respectively. There is also inserted a wavemeter for measuring the precise wavelength in the reference arm.

Even though the amplitude modulation of the measured signal is proportional to $2\sqrt{I_1 I_2}$ (see eq.3.14), the dynamic range of the photo detector sets restrictions on the power level. The maximal power detected ($= I_1 + I_2$) should be within the dynamic range for the photo detector. To obtain the largest signal with this restriction on the maximum power, the optical attenuator is adjusted so $I_1 \approx I_2$ [3]. The sum of the intensities $(I_1 + I_2)$ is adjusted by controlling the laser output power.
The intensity $I(t)$ detected by the photo diode is a simpler form of

[3] This is strictly only true when the last coupler is 3dB, that is when $Cl_c = 1/2$. However the last coupler is almost 3dB for the wavelength range used (1270nm to 1620nm) and the attenuator is therefore still adjusted so $I_1 \approx I_2$.

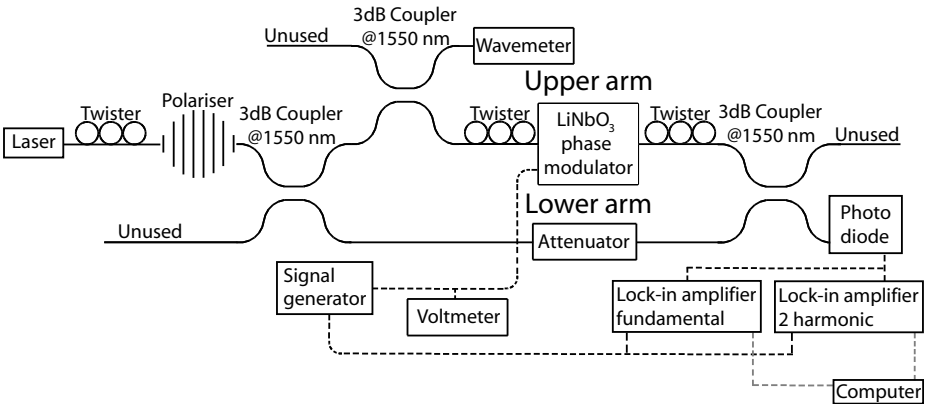

Figure 3.5: The MZI used for measuring V_π of the $LiNbO_3$ modulator. On the optical side there is added two polarization controllers, a polarizer, an attenuator and a wavemeter relative to fig. (3.4). The lower arm is not modulated actively.

eq.(3.14), as only one arm is modulated externally. That is

$$I(t) \quad = \quad I_1 \sin^2(Cl_c) + I_2 \cos^2(Cl_c) + \eta \sin\left[\varphi^{noise}(t) + \phi_1(E_{mod,1})\right]. \tag{3.16}$$

3.3.2 Estimating frequency and amplitude for $\varphi^{noise}(t)$.

To estimate $\varphi^{noise}(t)$, $E_{mod,1}$ is set to 0, i.e. none of the arms are modulated actively. The setup used corresponds to fig. (3.3) where the light intensity in the lower output arm is detected with a photo diode. The measured change in intensity arises solely from noise. To determine the frequency of the noise, the intensity signal from the photo diode is measured with an oscilloscope and the signal is Fourier transformed. The result is plotted in fig.(3.6).
This spectrum reveals that the noise is slower than $\sim 10kHz$. To estimate the amplitude of the noise, a single oscilloscope picture of the intensity is plotted in fig. (3.7).
As shown in fig. (3.7), the intensity varies between 0 and $I_1 + I_2$, i.e. $\varphi^{noise}(t)$ varies between $-\pi/2$ to $\pi/2$ (modulo π). That is, the phase fluctuates with an amplitude that could be bigger than measurable with a MZI setup.

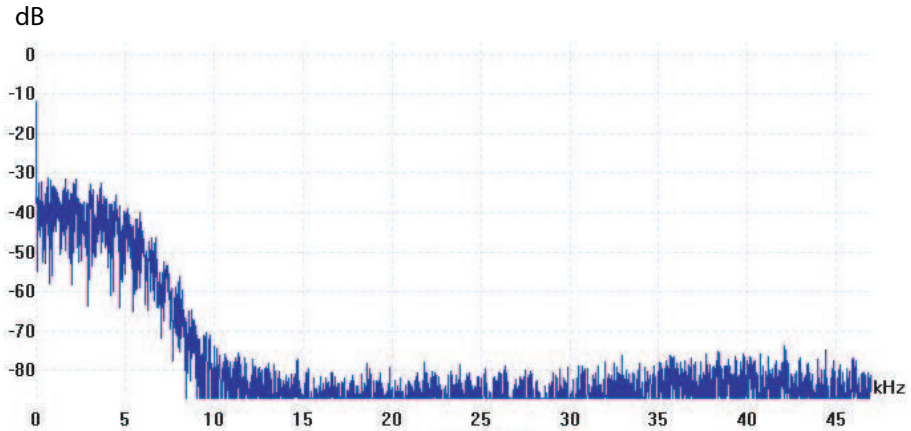

Figure 3.6: Fourier transform of the phase noise signal measured. The noise floor of the used oscilloscope is -80dB. The noise is severe up to 5 kHz and it has measurable frequency components up to 10 kHz.

3.3.3 Measuring V_π using two lock-in amplifiers

With the large and relatively fast oscillating noise in the back of the mind, $E_{mod,1}$ is chosen as a sine function[4]. This choice of electrical modulation function results is eq. (3.19-3.23) in the following and with the final derivation of eq. (3.28) the choice should be self-explaining.

$$E_{mod,1} = A_{electric} * \sin(\omega t + \theta) \tag{3.17}$$

As $LiNbO_3$ is a non-linear material with a $\chi^{(2)}$-value, the phase of the optical signal is modulated by a function proportional (see section 2.3) to the electrical signal. I.e. the phase is also modulated by a sinus function $A * \sin(\omega t + \theta)$. The frequency of the signal $E_{mod,1}$ is chosen to 33.333 kHz. As the noise frequency is lower than 33.333 kHz, it is assumed, that $\varphi^{noise}(t)$ can be replaced by a constant c_φ^{noise} for each oscillation of the electrical 33.333 kHz function. This assumption is justified after the derivation of eq. (3.28). The intensity ($I_{\text{noice constant}}(t)$) with the noise replaced by a constant c_φ^{noise}, is given in the eq.(3.18) below. The constant

[4]Different electrical functions (sinus, square and triangular) and different detection schemes have been tried before a good approach was found.

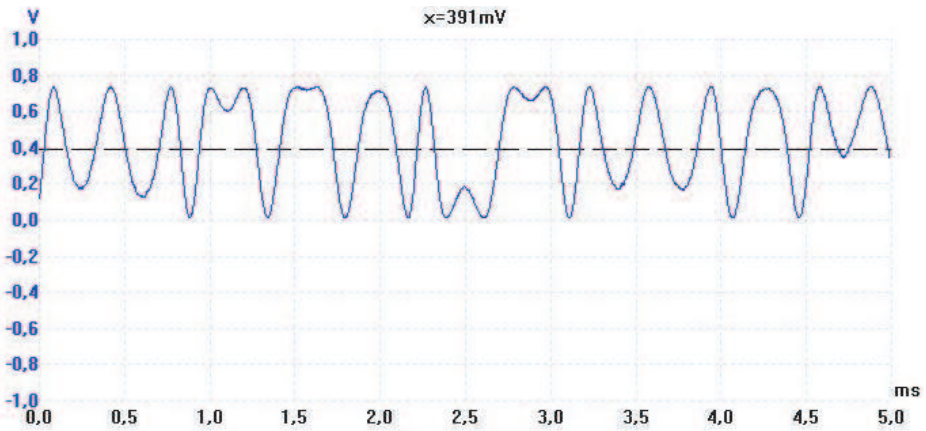

Figure 3.7: The curve is the measured intensity, when the arms of the MZI are *not* modulated actively. The oscillations of the phase noise ($\varphi^{noise}(t)$) makes the signal oscillate between 0 and $I_1 + I_2$. The intensities are almost equal ($I_1 \approx I_2$ and the intensity in one arm corresponds to 391mV on the photo detector.

c_φ^{noise} is different for each oscillation.

$$\begin{aligned} I_{\text{noise constant}}(t) &= I_1 \sin^2(Cl_c) + I_2 \cos^2(Cl_c) + \eta \sin\left(c_\varphi^{noise} + \phi_1(E_{mod,1})\right) \\ &= I_1 \sin^2(Cl_c) + I_2 \cos^2(Cl_c) + \eta \sin\left(A * \sin(\omega t + \theta) + c_\varphi^{noise}\right) \end{aligned} \tag{3.18}$$

To determine the amplitude A as function of $A_{electric}$, i.e. to determine V_π, the signal is detected by a lock-in amplifier. The lock-in amplifier also receives a reference TTL[5] with signal from the signal generator. From the reference signal, the lock-in amplifier generates an internal $\sin(\omega t+\theta+\theta_2)$ function and an internal $\cos(\omega t+\theta+\theta_2)$ function with the same frequency as the reference function but with a different phase $(\theta + \theta_2)$.

The lock-in amplifier works by splitting the input signal in two. One part is multiplied by the reference function $\sin(\omega t + \theta + \theta_2)$ and then integrated over a chosen timeslot. The other part of the input is multiplied by the reference function $\cos(\omega t + \theta + \theta_2)$ and then integrated over the same timeslot. The Lock-in amplifier then measures the DC-value of

[5] A TTL (Transistor-Transistor logic) signal is a square signal oscillating between 0V and + 5V.

the resulting functions. The timeslot is chosen to 30 μs corresponding to integration over one period of a 33.333 kHz function. The signals Lock-in$_{\sin(x)}$ and Lock-in$_{\cos(x)}$, detected by the Lock-in amplifier, with $(\omega t + \theta)$ substituted by (x), are

$$\begin{aligned}
\text{Lock-in}_{\sin(x)} &= \int_0^{2\pi} \left(I_1 \sin^2(Cl_c) + I_2 \cos^2(Cl_c)\right) \sin(x+\theta_2)/(2\pi) dx \\
&\quad + \eta \int_0^{2\pi} \left[\sin\left(A * \sin(x) + c_\varphi^{noise}\right)\right] \sin(x+\theta_2)/(2\pi) dx \\
&= \eta/(2\pi) \int_0^{2\pi} \left[\sin\left(A * \sin(x)\right) \cos\left(c_\varphi^{noise}\right)\right. \\
&\quad \left. + \cos\left(A * \sin(x)\right) \sin\left(c_\varphi^{noise}\right)\right] \\
&\quad \cdot \left(\sin(x)\cos(\theta_2) + \cos(x)\sin(\theta_2)\right) dx \\
&= \eta/(2\pi) \int_0^{2\pi} \sin\left(A * \sin(x)\right) \cos\left(c_\varphi^{noise}\right) \sin(x)\cos(\theta_2) dx \\
&\quad + \eta/(2\pi) \int_0^{2\pi} \cos\left(A * \sin(x)\right) \sin\left(c_\varphi^{noise}\right) \sin(x)\cos(\theta_2) dx \\
&\quad + \eta/(2\pi) \int_0^{2\pi} \sin\left(A * \sin(x)\right) \cos\left(c_\varphi^{noise}\right) \cos(x)\sin(\theta_2) dx \\
&\quad + \eta/(2\pi) \int_0^{2\pi} \cos\left(A * \sin(x)\right) \sin\left(c_\varphi^{noise}\right) \cos(x)\sin(\theta_2) dx \\
&\quad = \eta J_1(A) \cos\left(c_\varphi^{noise}\right) \cos(\theta_2) \\
&\quad + 0 + 0 + 0 \Rightarrow \\
\boxed{\text{Lock-in}_{\sin(x)} &= \eta J_1(A) \cos\left(c_\varphi^{noise}\right) \cos(\theta_2)} \qquad (3.19)
\end{aligned}$$

$$\begin{aligned}
\text{Lock-in}_{\cos(x)} &= \int_0^{2\pi} \left(I_1 \sin^2(Cl_c) + I_2 \cos^2(Cl_c)\right) \cos(x+\theta_2)/(2\pi) dx \\
&\quad + \eta \int_0^{2\pi} \left[\sin\left(A * \sin(x) + c_\varphi^{noise}\right)\right] \cos(x+\theta_2)/(2\pi) dx \\
&= +0 + 0 - \eta J_1(A) \cos\left(c_\varphi^{noise}\right) \sin(\theta_2) - 0 \Rightarrow \\
\boxed{\text{Lock-in}_{\cos(x)} &= -\eta J_1(A) \cos\left(c_\varphi^{noise}\right) \sin(\theta_2)}, \qquad (3.20)
\end{aligned}$$

where $J_1(A)$ is the first kind of Bessel function of order 1. The factor of $1/(2\pi)$ normalizes the integrals to DC level, as the integration interval

is 2π. Even though the equations look complicated, the only thing that varies during an experiment series is $\cos\left(c_\varphi^{noise}\right)$, taking on a new value for each 33.333kHz cycle. The value varies between -1 and 1 depending on the c_φ^{noise} value. Making numerous measurements and plotting Lock-in$_{\sin(x)}$ as function of Lock-in$_{\cos(x)}$ gives a straight line with slope $(-1/\tan(\theta_2) = \tan(90° + \theta_2))$. An example of this is plotted in fig. (3.8).

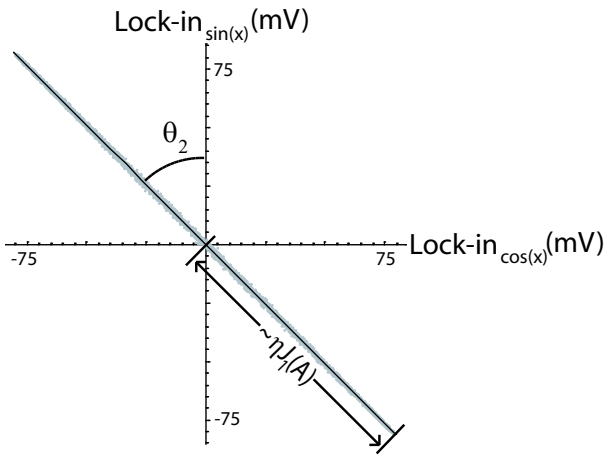

Figure 3.8: Plot of values measured by the lock-in amplifier at the fundamental frequency (33.333 kHz). The position of the measured points on the straight line is determined by the size of $\cos(c_\varphi^{noise})$. The angle θ_2 is an electrical phase chosen by settings on the lock-in amplifier.

The value of

$$\eta J_1(A)\cos\left(c_\varphi^{noise}\right) \tag{3.21}$$

is determined for each measurement point by making a projection onto the straight line. The set of projected values is called $S_{fundamental}$.

While the signal is detected by the lock-in amplifier, a second lock-in amplifier also receives the signal. As the cable length is very small ($\sim 10cm$) compared to the wavelength of the fastest oscillations ($= 66,666kHz \Rightarrow 4.5km$ for the 2-harmonic) both lock-in amplifiers receive the same signal. The second lock-in amplifier is set to detect the 2-harmonic. That is, it

multiplies the input signal with $\sin(2\omega t + \theta + \theta_3)$ and $\cos(2\omega t + \theta + \theta_3)$[6], respectively. The resulting DC-levels are

$$\begin{aligned}
\text{Lock-in}_{\sin(2x)} &= \int_0^{2\pi} \left(I_1 \sin^2(Cl_c) + I_2 \cos^2(Cl_c)\right) \sin(2x + \theta_3)/(2\pi) dx \\
&\quad + \eta \int_0^{2\pi} \left[\sin\left(A * \sin(x) + c_\varphi^{noise}\right)\right] \sin(2x + \theta_3)/(2\pi) dx \\
&= \eta/(2\pi) \int_0^{2\pi} \sin\left(A * \sin(x)\right) \cos\left(c_\varphi^{noise}\right) \sin(2x) \cos(\theta_3) dx \\
&\quad + \eta/(2\pi) \int_0^{2\pi} \cos\left(A * \sin(x)\right) \sin\left(c_\varphi^{noise}\right) \sin(2x) \cos(\theta_3) dx \\
&\quad + \eta/(2\pi) \int_0^{2\pi} \sin\left(A * \sin(x)\right) \cos\left(c_\varphi^{noise}\right) \cos(2x) \sin(\theta_3) dx \\
&\quad + \eta/(2\pi) \int_0^{2\pi} \cos\left(A * \sin(x)\right) \sin\left(c_\varphi^{noise}\right) \cos(2x) \sin(\theta_3) dx \\
&= +0 + 0 + 0 + \eta J_2(A) \sin\left(c_\varphi^{noise}\right) \sin(\theta_3) \Rightarrow \\
&\boxed{\text{Lock-in}_{\sin(2x)} = \eta J_2(A) \sin\left(c_\varphi^{noise}\right) \sin(\theta_3)} \qquad (3.22)
\end{aligned}$$

$$\begin{aligned}
\text{Lock-in}_{\cos(2x)} &= \int_0^{2\pi} \left(I_1 \sin^2(Cl_c) + I_2 \cos^2(Cl_c)\right) \cos(2x + \theta_3)/(2\pi) dx \\
&\quad + \eta \int_0^{2\pi} \left[\sin\left(A * \sin(x) + c_\varphi^{noise}\right)\right] \cos(2x + \theta_3)/(2\pi) dx \\
&= +0 + \eta J_2(A) \sin\left(c_\varphi^{noise}\right) \cos(\theta_3) - 0 - 0, \Rightarrow \\
&\boxed{\text{Lock-in}_{\cos(2x)} = \eta J_2(A) \sin\left(c_\varphi^{noise}\right) \cos(\theta_3)}, \qquad (3.23)
\end{aligned}$$

where $J_2(A)$ is the first kind of Bessel function of order 2. As for the measurements of the fundamental, numerous measurements of the second harmonic are made and a plot of $\text{Lock-in}_{\sin(2x)}$ as function of $\text{Lock-in}_{\cos(2x)}$ is made. This gives a straight line with slope $\tan(\theta_3)$. Projecting the measurement point onto the line gives a set of value for the size

$$\eta J_2(A) \sin\left(c_\varphi^{noise}\right), \qquad (3.24)$$

[6]The different phase θ_3 for the second lock-in amplifier is because the phase of the internal oscillator in the lock-in amplifier can be adjusted compared to the phase of the reference TTL signal the lock-in amplifier receives from the signal generator.

called $S_{2-harmonic}$. As there was made one and only one measurement of the 2-harmonic for each measurement of the fundamental, the two sets $S_{fundamental}$ and $S_{2-harmonic}$ can be combined into a single set S_{total} by setting

$$S_{total,i} = \{S_{fundamental,i}, S_{2-harmonic,i}\} \quad \forall i, \tag{3.25}$$

where i is the index for the measurement. As the measurements of the fundamental and the 2-harmonic where done simultaneously, this set corresponds to values of

$$S_{total,i} = \eta\{J_1(A)\cos\left(c_{\varphi,i}^{noise}\right), J_2(A)\sin\left(c_{\varphi,i}^{noise}\right)\}, \tag{3.26}$$

where the phase noise $c_{\varphi,i}^{noise}$ is a randomly different constant for different values of i. Notice that $c_{\varphi,i}^{noise}$ for a given i is the same for the fundamental and for the 2-harmonic measurement. When the whole set S_{total} is plotted as $\{x, y\}$ values, the result is an ellipse, as

$$\eta^2\left(\frac{\left(J_1(A)\cos\left(c_{\varphi,i}^{noise}\right)\right)^2}{a^2} + \frac{\left(J_2(A)\sin\left(c_{\varphi,i}^{noise}\right)\right)^2}{b^2}\right) = 1, \tag{3.27}$$

when $a = \eta J_1(A)$ and $b = \eta J_2(A)$. An example of S_{total} is plotted as $\{x, y\}$ values in fig. (3.9).
From the plot of the set S_{total} (the ellipsoid) the experimental value of b/a is determined[7] using **the iterative polar fitting procedure**. The constant A is then determined by solving the equation

$$\frac{b}{a} = \frac{J_2(A)}{J_1(A)} \tag{3.28}$$

numerically. Now the basis assumption about c_{φ}^{noise} being a different *constant* for each oscillation of the 33.333 kHz function can be justified. If c_{φ}^{noise} changes during an oscillation, the angle α[8] on fig. (3.9) for the measured point on the ellipsoid will change. But the point will still

[7] The ellipsoid fitting procedure is non-trivial and a description of the procedure is given in appendix A.

[8] The angle α is equal to c_{φ}^{noise} modules 2π if c_{φ}^{noise} is constant during the measurement of a point.

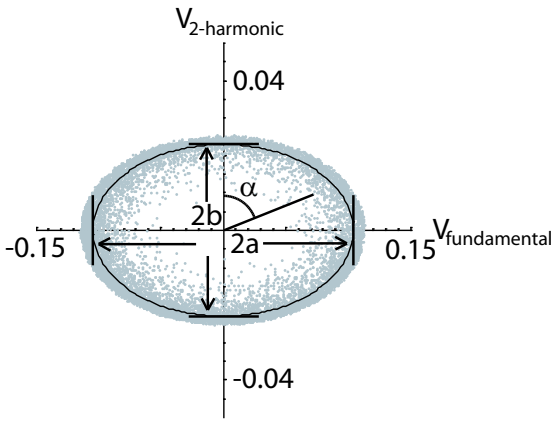

Figure 3.9: Points on a measured ellipsoid with a mathematical ellipsoid fitted onto. The fitting procedure is described in appendix A. The vector pointing to a measured point illustrates the angle (α). When c_φ^{noise} is constant during the measurement of a point, α is equal to c_φ^{noise} modules 2π.

lie on the ellipsoid, unless the change of c_φ^{noise} is significant enough to affect the radial value of the ellipsoid. This seems not to be the case, as the ellipsoids measured looks like mathematical ellipsoids with an added stochastic error.

The mathematical accuracy of determining A by measuring b/a is determined by the variation of $\frac{J_2(A)}{J_1(A)}$ with A. If $\frac{J_2(A)}{J_1(A)}$ was independent of A, it would be impossible to determine A from the measured b/a value. To show that the value of $\frac{J_2(A)}{J_1(A)}$ indeed depends on A (in a one to one manner in the range of interest) a plot of $\frac{J_2(A)}{J_1(A)}$ is made in fig. (3.10). The value of A is varied between 0 and π. This variation of A is larger than the variation obtainable experimentaly[9] and the plot demonstrates both $\frac{J_2(A)}{J_1(A)}$'s strong dependence on A and it demonstrates the function is one to one in the range of interest.

The measurement of an ellipsoid is made for different values of $A_{electric}$. For each $A_{electric}$ value the amplitude A of the induced phase change is

[9]The experimental amplitude of A is limited by the $LiNbO_3$ phase modulator. If a higher electrical modulation voltage is used the switch might be permanently destroyed by a short circuit.

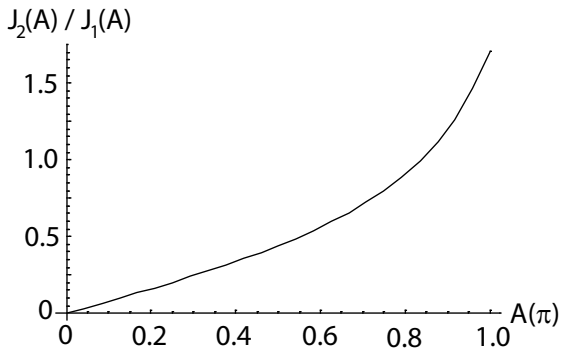

Figure 3.10: The plot shows the value of $\frac{J_2(A)}{J_1(A)}$ depends strongly on the value of A. The plot also shows the function $\frac{J_2(A)}{J_1(A)}$ is one to one for $A \in [0 : \pi]$.

determined by fitting an ellipsoid to the measured points and then solving eq. (3.28) numerically. The value of $2A$ is plotted as function of $2A_{electric}$ in fig (3.11). The factor of 2 converts the amplitude values into peak to peak (P-P) values. As the modulator is made using a Pockels material ($LiNbO_3$) the points $(2A_{electric}, 2A)$ should lie on a straight line going through zero.

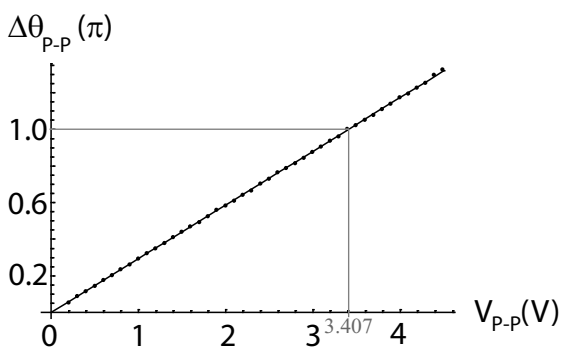

Figure 3.11: Phase shift as function of modulation voltage measured at 1550.009 nm. The points are fitted with a straight line going through (0,0). V_π is the x-coordinate for the point with y-value π. The plot shows $V_\pi = 3.407 \pm 0.006$ at 1550.009 nm.

The value V_π for the $LiNbO_3$ modulator is found as the x-coordinate

of the point (V_π,1) on the straight line. Making the same approach for different wavelength of the optical light, V_π vs. λ has been determined. Even though the value in search is $V_\pi(\lambda)$, a plot of the underlying physical value ($\chi^{(2)}(\lambda)$) is more informative. The connection between $\chi^{(2)}(\lambda)$ and $V_\pi(\lambda)$ is found by rewriting eq. (2.20) into

$$\chi^{(2)}(\lambda) = \frac{d\lambda n_e(\lambda)}{2lV_\pi(\lambda)}, \tag{3.29}$$

where d is the electrode-electrode distance, l is the length of the modulated waveguide and $n_e(\lambda)$ is the extraordinary index for the uniaxial crystal $LiNbO_3$ when no electric field is applied to the crystal. The confinement factor is set to 1, as the waveguide in $LiNbO_3$ is made by proton exchange, i.e. the core and cladding materials are identical for non-linear purposes. The factor ς describing the electric field in the nonlinear region is also equal to 1, as the material between the electrodes is uniform (it is $LiNbO_3$). The formula for $n_e(\lambda)$ is found in [6].

$$n_e(\lambda) = \sqrt{4.5820 + \frac{0.099169}{\lambda^2 - 0.04443} - 0.02195\lambda^2}. \tag{3.30}$$

The refractive index dispersion of $LiNbO_3$ is similar the refractive index dispersion of glass (SiO_2). $n_e(\lambda)$ for $LiNbO_3$ and $n(\lambda)$ for SiO_2 (the Sellmeier equation [7]) are plotted in fig. (3.12).
As the length l and the distance d are unknown (but constant with wavelength), $\chi^{(2)}(\lambda) \cdot l/d$ is found instead of $\chi^{(2)}(\lambda)$. The values are listed in table (3.1).
This data is plotted in fig. (3.13) with a fitted function. The fitted function $(\alpha \left|\lambda - \lambda_c|^P\right|)^{10}$ is used to determine the value of V_π when curves of $\chi^{(2)}(\lambda)$ are made in chapter (6). When measurements are made for a single wavelength, V_π from the table (3.1) is used directly. The values on the right vertical axis on fig. (3.13) are found by assuming $\chi^{(2)}(1550nm) = 359.4pm/V$, as is the case for wafers from [6]. The right vertical scale in only shown to give an easy overview of behaviour of $\chi^{(2)}(\lambda)$ and should *not* be used for anything else.

[10]The function type is chosen as it gives a nice fit. There is no physical reason for the chosen function.

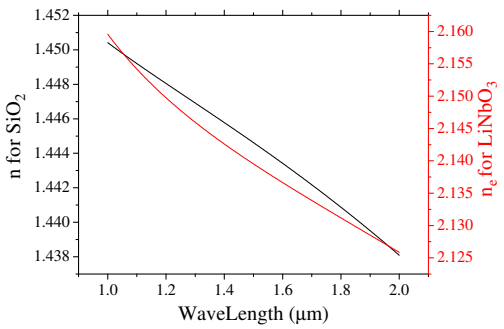

Figure 3.12: The refractive index dispersion for SiO_2 [7] (black curve) and for $LiNbO_3$ [6] (red curve).

V_π for $LiNbO_3$ modulator

Wavelength (nm)	V_π (V)	$\pm^1$	$\chi^{(2)} \cdot l/d$ (nm/V)	$\pm^1$	$\pm^2$
1280.03	2.663	0.016	515.9	2.7	2.2
1300.02	2.714	0.017	514,0	3.4	2.9
1320.03	2.762	0.017	512.6	2.4	1.9
1379.981	2.915	0.018	507.3	1.9	1.4
1399.986	2.965	0.018	505.8	2.4	1.9
1419.994	3.027	0.018	502,4	1.3	0.8
1480.003	3.183	0.019	497.5	1.3	0.8
1530.004	3.341	0.020	489.7	1.2	0.7
1550.009	3.407	0.021	486.4	0.9	0.4
1619.99	3.659	0.022	472.9	1.3	0.8

Table 3.1: The $\pm^1$ error value includes both the reproducibility error and the systematic error (see appendix B.2). The $\pm^2$ error value is only the reproducibility error. The $\pm^1$ uncertainty should *always* be used except in plots of V_π vs. λ, where both $\pm^1$ and $\pm^2$ should be shown.

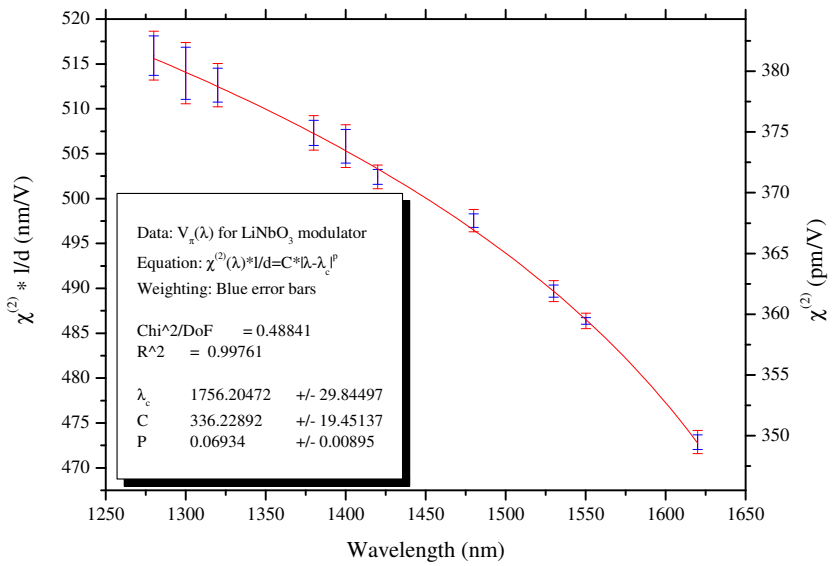

Figure 3.13: The blue bars are the uncertainty directly from the fitting of straight lines like fig. (3.11). The blue bars can *only* be used to evaluate if the fitted line is trustworthy. In *all* other cases the red uncertainty should be used. The red uncertainty takes all uncertainty contributions into account (see appendix B.2). The right vertical axis is *only* included to give an easy overview, as the scale is probably off by a linear factor.

3.4 Measuring on a sample by modulating on both arms.

3.4.1 The optical setup for section (3.4).

The non-linearity of a sample is determined by modulating both arms of the MZI at the same time. The same electrical sinus signal is used for both arms, however it is attenuated, phase adjusted and possibly inverted for the $LiNbO_3$ while it is amplified and possibly combined with a DC level for the sample. The setup is drawn systematically in fig.(3.14). Even though the setup looks complicated, there have only been added two more optical components compared to the setup used to measure V_π for the $LiNbO_3$ phase modulator. The reused optical components are adjusted as for the $LiNbO_3$ calibration experiment described in section (3.3.1). The attenuator has been moved to the other arm, as the loss in a sample is bigger than the loss in the $LiNbO_3$ phase modulator. The sample is a straight buried waveguide covered by an electrode (see fig. 3.15). The sample acts as a Pockels[11] phase modulator in the setup. The polarization controller before the sample adjusts the polarization of the light, such that it is either TE or TM polarized when it propagates through the sample.

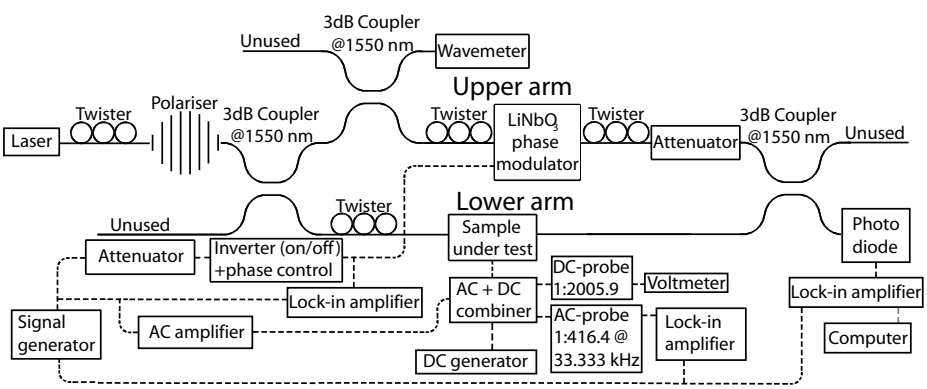

Figure 3.14: The MZI setup used for determining the non-linearity of the glass samples. The phase of both arms in the setup are actively modulated.

[11] Either a pure Pockels effect or a Pockels effect induced by a Kerr effect combined with a high voltage DC-field (See section 2.3).

3.4.2 Modulation signal from the $LiNbO_3$ modulator.

The phase modulation of the upper and lower arm are $\phi_1(E_{mod,1})$ and $\phi_2(E_{mod,2})$, respectively. The phase modulations arise from the non-linearity of the material (se chapter 2), that changes the material refractive index because of the electric field. As $LiNbO_3$ is a Pockels material, the phase change in the upper arm is a linear response to the applied electrical signal. The electrical signal used is a sinus signal. That is

$$\phi_1(A_1^{electric}\sin(wt+\theta_1)) \quad = \quad s_{inv}A_1\sin(wt+\theta_1). \tag{3.31}$$

The s_{inv} is a sign determined by the inverter, i.e. s_{inv} is $+1$ when the inverter is turned off and s_{inv} is -1 when the inverter is turned on. The electrical phase (θ_1) can be adjusted using the phase adjuster. The constant A_1 can be determined, as V_π is known for the $LiNbO_3$ modulator (see table 3.1) and as the amplitude ($A_1^{electric}$) of the modulation voltage is measured. That is

$$A_1 = -\pi \cdot \frac{A_1^{electric}}{V_\pi}. \tag{3.32}$$

The sign of the right hand side of the equation was not determined, when V_π was measured. The sign depends on the orientation of the $LiNbO_3$ crystal inside the phase modulator. The sign is determined by a measurement described in section (3.5.4). When the signal from the signal generator is chosen as $A_1^{electric}\sin(wt+\theta_1)$ the phase modulation (ϕ_1) induced by the $LiNbO_3$ modulator is

$$\phi_1 \quad = \quad -s_{inv}\pi \cdot \frac{A_1^{electric}}{V_\pi}\sin(wt+\theta_1). \tag{3.33}$$

3.4.3 Modulation signal from the sample.

Pockels material.

The sample in the lower arm can be made of either a Pockels or a Kerr material. In both cases the change in phase (ϕ_2) is due to a change in the

effective phase refractive index ($\Delta n_{\phi,eff}$) of the waveguide. The change in phase is

$$\phi_2 = \frac{2 l_{sample} \pi}{\lambda} \Delta n_{\phi,eff}, \tag{3.34}$$

where λ is the wavelength of the light and l_{sample} is the length of the affected waveguide. The formula can be proven by looking at a 2π phase shift. A 2π phase shift occurs when the light is delayed by a wavelength, that is the optical path length ($l_{sample} \cdot (n_{\phi,eff} + \Delta n_{\phi,eff})$) is increased by λ. This is exactly what the formula says, as inserting $\phi_2 = 2\pi$ and $l_{sample} \cdot \Delta n_{\phi,eff} = \lambda$ fulfills the equation. As the phase shift is linear with the change in refractive index, the formula is proved. The refractive index ($n_{\phi,eff}$) is the effective phase refractive index of the waveguide when it is not affected by an electric field.

It is normally[12] assumed that the length (l_{sample}) of the affected waveguide is equal to the length of the top electrode (see fig. 3.15).

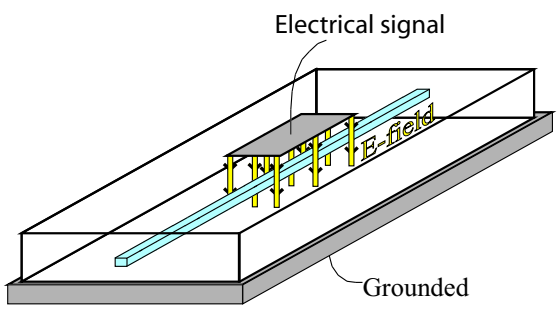

Figure 3.15: Sample with a straight waveguide affected by an electric field. It is assumed that only the waveguide directly under the electrode is affected by the electric field, i.e. rim effects at the electrode edges are ignored. The introduced error is minimal, as the thickness (d_{sample}) of the sample is $\sim 10\mu m$ and the length (l_{sample}) of the sample is $\sim 10mm$ (a factor 1000 bigger).

If the sample is a Pockels material the refractive index change ($\Delta n_{\phi,eff}(E)$) due to an electric field (E) is (see eq. 2.13)

$$\Delta n_{\phi,eff}(E) = \Gamma_{core} \chi^{(2)}_{core} / n_{\phi,bulk,0,core} \cdot E_{core}, \tag{3.35}$$

[12]The assumption is applied for all samples but for photonic crystal (PhC) waveguides (see fig. (B.8) in appendix B.3.

where Γ_{core} is the confinement factor too the non-linear medium, $n_{\phi,bulk,0,core}$ is the bulk phase refractive index of the non-linear medium and $\chi^{(2)}_{core}$ is the second-order nonlinear coefficient. The phase change ($\phi_2^{Pockels}(E)$) induced by the electric field due to the second-order nonlinearity is found by combining eq. (3.34) and eq. (3.35). That is

$$\phi_2^{Pockels}(E) = \frac{2l_{sample}\pi\Gamma_{core}\chi^{(2)}_{core}}{\lambda n_{\phi,bulk,0,core}} \cdot E_{core}. \tag{3.36}$$

When the electric field is a sinus function ($A_2^{electric}/d_{sample}\sin(\omega t + \theta_2)$) the phase change for a Pockels material is

$$\phi_2^{Pockels} = \frac{2l_{sample}\pi\Gamma_{core}\chi^{(2)}_{core}}{\lambda n_{\phi,bulk,0,core}} \cdot A_2^{electric}\varsigma/d_{sample}\sin(\omega t + \theta_2), \tag{3.37}$$

where $A_2^{electric}$ is the amplitude of the AC voltage applied, ς is the linear correlation between applied electric field and the electric field in the core material (see section 2.3, the derivation of eq. 2.20) and d_{sample}[13] is the distance between the top and bottom electrode. The amplitude of the electrical function ($A_2^{electric}\sin(\omega t + \theta_2)$) is measured using a lock-in amplifier (see fig. 3.14). The AC amplifier enhances $A_2^{electric}$ to approximately $400V_{P-P}$ in a typical measurement. Doing so the amplifier delays the signal compared to the signal it receives from the signal generator. The electrical phase (θ_2) is therefore in the starting point *not* equal to the phase (θ_1) of the electrical signal on the $LiNbO_3$ phase modulator.

Kerr material.

When the sample is a Kerr material, the change in refractive index is (see eq. 2.15)

$$\Delta n(E) = \frac{3\chi^{(3)}_{av}}{2n_{\phi,eff,0}} \cdot E^2. \tag{3.38}$$

The electrical field is a combination of three fields. A poled in DC-field ($E_{frozen-in}$), an applied DC-field (V_{DC}/d_{sample}) and an applied AC-field

[13]The voltage applied ($A_2^{electric}$) is divided by the electrode-electrode distance (d_{sample}) to determine the electric field. Doing this is correct when there are no free charges between the top and bottom electrodes, that can shield the applied voltage.

$(A_2^{electric}/d_{sample}\sin(\omega t+\theta_2))$. The phase modulation in the lower arm is therefore

$$\begin{aligned}\phi_2^{Kerr}(A_2^{electric},V_{DC}) &= \frac{2l_{sample}\pi}{\lambda}\frac{3}{2}\frac{\chi_{av}^{(3)}}{n_{\phi,eff,0}}\left(\frac{A_2^{electric}}{d_{sample}}\sin(wt+\theta_2)\right.\\ &\quad\left.+\frac{V_{DC}}{d_{sample}}+E_{frozen-in}\right)^2\\ &= \frac{3l_{sample}\pi}{\lambda}\frac{\chi_{av}^{(3)}}{n_{\phi,eff,0}}\left[\underbrace{\left(\frac{A_2^{electric}}{d_{sample}}\sin(wt+\theta_2)\right)^2}_{\substack{\text{frequency } 2w\text{ and zero,}\\ \text{as } 2\sin^2(x)=1-\cos(2x)}}\right.\\ &\quad+\underbrace{\left(\frac{V_{DC}}{d_{sample}}+E_{frozen-in}\right)^2}_{\text{frequency zero}}\\ &\quad\left.+\underbrace{2\frac{A_2^{electric}}{d_{sample}}\sin(wt+\theta_2)\left(\frac{V_{DC}}{d_{sample}}+E_{frozen-in}\right)}_{\text{frequency } w}\right],\end{aligned} \tag{3.39}$$

where V_{DC} is the DC voltage applied, $\chi_{av}^{(3)}$ is the average third-order nonlinear coefficient[14] and $E_{frozen-in}$ is the frozen-in electric field (possibly due to poling, see section 2.4).

[14]The average $\chi^{(3)}$ is confinement factor weighted, see section 2.3.

3.5 Method for measuring $\chi^{(2)}$, $\chi^{(3)}$ and $E_{frozen-in}$.

3.5.1 Detection using a lock-in amplifier.

The signal detected by the photo diode is (see eq. 3.14)

$$\begin{aligned} I &= I_1 \sin^2(Cl_c) + I_2 \cos^2(Cl_c) + 2\sqrt{I_1 I_2}\sin(Cl_c)\cos(Cl_c) \\ &\quad \cdot \sin\left[\varphi^{noise}(t) + \phi_1 - \phi_2\right]. \end{aligned} \tag{3.40}$$

where ϕ_1 is the phase change induced by the $LiNbO_3$ modulator (eq. 3.33) and ϕ_2 is the phase induced by the sample (eq. 3.37 or eq. 3.39). The signal is detected by a lock-in amplifier that also receives a reference TTL signal from the signal generator. From the reference signal, the lock-in amplifier generates an internal $\sin(\omega t + \theta_3)$ function and an internal $\cos(\omega t + \theta_3)$ function with the same frequency as the reference function but with a different phase (θ_3). The phase (θ_3) can be adjusted on the signal generator.

The function of the lock-in amplifier is described in section 3.3.3. *In this experiment the integration time slot on the lock-in amplifier is always chosen to be equal to one period of the signal from the signal generator.* That is, when the frequency of the signal from the signal generator is $33.333kHz$, the time slot is chosen to $30\mu s$ and when the frequency of the signal from the signal generator is $200kHz$, the time slot is chosen to $5\mu s$. As the time slots are much shorter than the oscillation of the noise, $\varphi^{noise}(t)$ is replaced by a constant c_φ^{noise}, that is *different* from measurement to measurement. This approximation was justified after the derivation of eq. (3.28) in section (3.3.3).

3.5.2 Measurement scheme used.

Overview.

The lock-in amplifier phase (θ_3) is adjusted by modulating the phase by the sample only (i.e. the electric field at the $LiNbO_3$ modulator is set to 0). The absolute value of the lock-in output Lock-in$_{\cos(x+\theta_3)}$ is averaged over a long time. This value (Lock-in$^{abs,average}_{\cos(x+\theta_3)}$) is minimized by adjusting

the lock-in phase (θ_3). Eq. (3.48) shows that the value is minimized when $\theta_3 = \theta_2$ or $\theta_3 = \theta_2 + \pi$.

The phase (θ_1) for the electric function for the $LiNbO_3$ modulator is then chosen by applying a modulation to both arms using the sample and the $LiNbO_3$ modulator. The value Lock-in$^{abs,average}_{\cos(x)}$ is again minimized and just after eq. (3.53) it is shown that the value is minimized when $\theta_1 = \theta_2$ or $\theta_1 = \theta_2 + \pi$.

The amplitude (a_1^u) and sign (s_{inv}) of the phase modulation from the $LiNbO_3$ modulator is then adjusted so the time average of the absolute value of the other lock-in output Lock-in$_{\sin(x)}$ is minimized. As shown in section (3.5.2) the value Lock-in$^{abs,average}_{\sin(x)}$ is minimized, when the $\chi^{(2)}$-type phase modulations in the two arms are exactly equal. This equality is used in section (3.5.3) to determine the non-linearity coefficient ($\chi^{(2)}$) and ($\chi^{(3)}$) and the frozen-in field ($E_{frozen-in}$).

Choosing the phase θ_3.

To adjust the internal phase (θ_3) of the lock-in amplifier, the modulation from the sample is maximized by adjusting the DC level on the sample and the modulation from the $LiNbO_3$ modulator is set to 0. The general phase modulation (ϕ_2) in the lower arm is $a_0^l + a_1^l \sin(x) + a_2^l \sin(2x)$, where $x = \omega t + \theta_2$. The phase modulation is either due to modulation on a Pockels (see eq. 3.37) or a Kerr material (see eq. 3.39). Substituting θ_3 with $\theta_3' = \theta_3 - \theta_2$ the output (Lock-in$_{\sin(x+\theta_3')}$) from the lock-in amplifier is[15]

$$\begin{aligned}
\text{Lock-in}_{\sin(x+\theta_3')} &= \int_{-\pi}^{\pi} \left(I_1 \sin^2(Cl_c) + I_2 \cos^2(Cl_c)\right) \sin(x+\theta_3')/(2\pi) dx \\
&\quad + \eta \int_{-\pi}^{\pi} \left[\sin\left(-\phi_2(x) + c_\varphi^{noise}(t)\right)\right. \\
&\quad \left. \sin(x+\theta_3')/(2\pi)\right] dx \\
&= \eta \int_{-\pi}^{\pi} \left[\sin\left(-a_1^l \sin(x) - a_2^l \sin(2x)\right.\right. \\
&\quad \left.\left. + c_\varphi^{noise}(t) - a_0^l\right) \sin(x+\theta_3')/(2\pi)\right] dx
\end{aligned}$$

[15] In the equation derivation there is made extensively use of the two formulas $\sin(A+B) = \sin(A)\cos(B) + \cos(B)\sin(A)$ and $\cos(A+B) = \cos(A)\cos(B) - \sin(B)\sin(A)$.

$$
\begin{aligned}
= \quad & \eta \sin(c_\varphi^{noise}(t) - a_0^l) \\
& \int_{-\pi}^{\pi} \Bigg[\underbrace{\cos\Bigg(\underbrace{-a_1^l \sin(x) - a_2^l \sin(2x)}_{\text{odd}}\Bigg)}_{\text{even}} \\
& \Bigg(\underbrace{\sin(x)\cos(\theta_3')}_{\text{odd}} + \underbrace{\cos(x)\sin(\theta_3')}_{\text{even}}\Bigg)/(2\pi)\Bigg] dx \\
& + \eta \cos(c_\varphi^{noise}(t) - a_0^l) \\
& \int_{-\pi}^{\pi} \Bigg[\underbrace{\sin\Bigg(\underbrace{-a_1^l \sin(x) - a_2^l \sin(2x)}_{\text{odd}}\Bigg)}_{\text{odd}} \\
& \Bigg(\underbrace{\sin(x)\cos(\theta_3')}_{\text{odd}} + \underbrace{\cos(x)\sin(\theta_3')}_{\text{even}}\Bigg)/(2\pi)\Bigg] dx.
\end{aligned}
\tag{3.41}
$$

The integrals limits are symmetrical around zero. The value of a symmetrical integral of an odd integrant is 0. This observation simplifies the equation for the lock-in output to

$$
\begin{aligned}
\text{Lock-in}_{\sin(x+\theta_3')} \quad = \quad & \eta \sin(c_\varphi^{noise}(t) - a_0^l)\sin(\theta_3') \\
& \int_{-\pi}^{\pi} \cos\left(-a_1^l \sin(x) - a_2^l \sin(2x)\right) \frac{\cos(x)}{2\pi} dx \\
& + \eta \cos(c_\varphi^{noise}(t) - a_0^l)\cos(\theta_3') \\
& \int_{-\pi}^{\pi} \sin\left(-a_1^l \sin(x) - a_2^l \sin(2x)\right) \frac{\sin(x)}{2\pi} dx.
\end{aligned}
\tag{3.42}
$$

The two integrals in eq. (3.42) are not analytically solvable, but the size of the integral can be estimated. The constants a_0^l, a_1^l and a_2^l all arise from a phase modulation from the sample. As the phase modulation

a_1^l [16] is no more than $\pi/10$ in the experiments, it is assumed the Taylor expansion of $\sin(x) = x$ and $\cos(x) = 1 - x^2/2$ can be used to compare the size of the integrals. That is

$$\begin{aligned} I_{2\cos}(a_1^l, a_2^l) &\equiv \int_{-\pi}^{\pi} \cos\left(-a_1^l \sin(x) - a_2^l \sin(2x)\right) \frac{\cos(x)}{2\pi} dx \\ &\approx \int_{-\pi}^{\pi} \left(1 - (a_1^l \sin(x) - a_2^l \sin(2x))^2/2\right) \frac{\cos(x)}{2\pi} dx \\ &= -a_1^l a_2^l/4 \qquad (3.43) \\ I_{2\sin}(a_1^l, a_2^l) &\equiv \int_{-\pi}^{\pi} \sin\left(-a_1^l \sin(x) - a_2^l \sin(2x)\right) \frac{\sin(x)}{2\pi} dx \\ &\approx \int_{-\pi}^{\pi} \left(a_1^l \sin(x) - a_2^l \sin(2x)\right) \frac{\sin(x)}{2\pi} dx \\ &= a_1^l/2. \qquad (3.44) \end{aligned}$$

As $a_2^l < \pi/100$ in the measurements, $|I_{2\cos}(a_1^l, a_2^l)| \ll |I_{2\sin}(a_1^l, a_2^l)|$. The absolute value of the measured output from the lock-in amplifier is averaged over the large timespan T, that is

$$\begin{aligned} \text{Lock-in}_{\sin(x+\theta_3')}^{abs,average} &= |\eta| \int_0^T \Big| \sin(c_\varphi^{noise}(t) - a_0^l) \sin(\theta_3') I_{2\cos}(a_1^l, a_2^l) \\ &\quad + \cos(c_\varphi^{noise}(t) - a_0^l) \cos(\theta_3') I_{2\sin}(a_1^l, a_2^l) \Big| \, dt/T. \end{aligned} \qquad (3.45)$$

The noise term $(c_\varphi^{noise}(t))$ is uniformly distributed between 0 and 2π modules 2π and the integral is therefore

$$\begin{aligned} \text{Lock-in}_{\sin(x+\theta_3')}^{abs,average} &= |\eta| \int_0^{2\pi} \Big| \sin(\tau) \sin(\theta_3') I_{2\cos}(a_1^l, a_2^l) \\ &\quad + \cos(\tau) \cos(\theta_3') I_{2\sin}(a_1^l, a_2^l) \Big| \, d\tau/(2\pi) \\ &= 2/\pi |\eta| \left(|\sin(\theta_3')| |I_{2\cos}(a_1^l, a_2^l)| + |\cos(\theta_3')| |I_{2\sin}(a_1^l, a_2^l)| \right). \end{aligned} \qquad (3.46)$$

[16] By inspecting eq. (3.39) it is seen a_2^l is smaller than a_1^l, as $a_1^l/a_2^l = 4(V_{DC} + E_{frozen-in} d_{sample})/A_2^{electric}$.

The size of the absolute value of the other lock-in output (Lock-in$_{\sin(x+\theta_3')}$) averaged over time is found in a similar way. That is

$$\text{Lock-in}^{abs,average}_{\cos(x+\theta_3')} = 2/\pi|\eta|\left(|\cos(\theta_3')||I_{2\cos}(a_1^l, a_2^l)| + |\sin(\theta_3')||I_{2\sin}(a_1^l, a_2^l)|\right). \tag{3.47}$$

The phase $\theta_3' = \theta_3 - \theta_2$ is chosen so Lock-in$^{abs,average}_{\cos(x+\theta_3')}$ is minimized. As $|I_{2\cos}(a_1^l, a_2^l)| \ll |I_{2\sin}(a_1^l, a_2^l)|$, the value of Lock-in$^{abs,average}_{\cos(x+\theta_3')}$ is minimized when $|\sin(\theta_3')| = 0$. Minimizing the value of Lock-in$^{abs,average}_{\cos(x+\theta_3')}$ maximizes the value of Lock-in$^{abs,average}_{\sin(x+\theta_3')}$. That is

$$\theta_3' = 0 \text{ or } \theta_3' = \pi \quad \Rightarrow \quad \begin{cases} \text{Lock-in}^{abs,average}_{\cos(x+\theta_3')} \text{ is minimal} \\ \text{Lock-in}^{abs,average}_{\sin(x+\theta_3')} \text{ is maximal.} \end{cases} \tag{3.48}$$

Choosing the phase θ_1.

To adjust the phase (θ_1) of the electrical signal for the $LiNbO_3$ modulator, the electrical signal for the sample is maintained (i.e. it is still maximized) and the lock-in phase θ_3' is maintained as 0 or π(i.e. Lock-in$^{abs,average}_{\cos(x+\theta_3')}$ is minimized). The only difference between $\theta_3' = 0$ and $\theta_3' = \pi$ is the sign of the output (Lock-in$_{\cos(x+\theta_3')}$) from the lock-in amplifier. As it is the time average of the *absolute value* of (Lock-in$_{\cos(x+\theta_3')}$), that is minimized, the sign of (Lock-in$_{\cos(x+\theta_3')}$) is irrelevant. The value for θ_3' therefore chosen to be 0.

The amplitude of the electrical signal for the $LiNbO_3$ modulator is set to $\approx 100mV$. Looking in table (3.1) of $V_\pi(\lambda)$, this corresponds to a phase modulation amplitude of $\approx \pi/10$, i.e. a modulation smaller than 1. The phase modulation from the $LiNbO_3$ modulator is $a_1^u \sin(x + \theta_1)$. Substituting the phase θ_1 with $\theta_1' = \theta_1 - \theta_2$, the output (Lock-in$_{\cos(x)}$)

from the lock-in amplifier is

$$
\begin{aligned}
\text{Lock-in}_{\cos(x)} &= \eta \int_{-\pi}^{\pi} \Big[\sin\Big(-a_1^l \sin(x) - a_2^l \sin(2x) + a_1^u \sin(x+\theta_1') \\
&\quad + c_\varphi^{noise}(t) - a_0^l \Big) \cos(x)/(2\pi) \Big] \, dx \\
&= \eta \sin(c_\varphi^{noise}(t) - a_0^l) \\
&\quad \int_{-\pi}^{\pi} \Bigg[\underbrace{\cos\Bigg(\underbrace{(a_1^u \cos(\theta_1') - a_1^l)\sin(x) - a_2^l \sin(2x)}_{\text{odd}} \Bigg)}_{\text{even}} \\
&\quad \underbrace{\cos\Bigg(\underbrace{(a_1^u \sin(\theta_1'))\cos(x)}_{\text{even}} \Bigg)}_{\text{even}} \underbrace{\cos(x)}_{\text{even}} /(2\pi) \Bigg] \, dx
\end{aligned}
$$

Continued on next page. (3.49)

$$
\begin{aligned}
&-\eta \sin(c_{\varphi}^{noise}(t) - a_0^l) \\
&\int_{-\pi}^{\pi} \Bigg[\underbrace{\sin\left(\underbrace{(a_1^u \cos(\theta_1') - a_1^l)\sin(x) - a_2^l \sin(2x)}_{\text{odd}} \right)}_{\text{odd}} \\
&\underbrace{\sin\left(\underbrace{(a_1^u \sin(\theta_1'))\cos(x)}_{\text{even}} \right)}_{\text{even}} \underbrace{\cos(x)}_{\text{even}} /(2\pi) \Bigg] \, dx \\
&+\eta \cos(c_{\varphi}^{noise}(t) - a_0^l) \\
&\int_{-\pi}^{\pi} \Bigg[\underbrace{\sin\left(\underbrace{(a_1^u \cos(\theta_1') - a_1^l)\sin(x) - a_2^l \sin(2x)}_{\text{odd}} \right)}_{\text{odd}} \\
&\underbrace{\cos\left(\underbrace{(a_1^u \sin(\theta_1'))\cos(x)}_{\text{even}} \right)}_{\text{even}} \underbrace{\cos(x)}_{\text{even}} /(2\pi) \Bigg] \, dx \\
&+\eta \cos(c_{\varphi}^{noise}(t) - a_0^l) \\
&\int_{-\pi}^{\pi} \Bigg[\underbrace{\cos\left(\underbrace{(a_1^u \cos(\theta_1') - a_1^l)\sin(x) - a_2^l \sin(2x)}_{\text{odd}} \right)}_{\text{even}} \\
&\underbrace{\sin\left(\underbrace{(a_1^u \sin(\theta_1'))\cos(x)}_{\text{even}} \right)}_{\text{even}} \underbrace{\cos(x)}_{\text{even}} /(2\pi) \Bigg] \, dx \Rightarrow
\end{aligned}
$$

$$\begin{aligned}
\text{Lock-in}_{\cos(x)} &= \eta \sin(c_{\varphi}^{noise}(t) - a_0^l) \\
&\int_{-\pi}^{\pi} \left[\cos\left((a_1^u \cos(\theta_1') - a_1^l) \sin(x) - a_2^l \sin(2x) \right) \right. \\
&\left. \cos\left((a_1^u \sin(\theta_1')) \cos(x) \right) \frac{\cos(x)}{2\pi} \right] dx \\
&+\eta \cos(c_{\varphi}^{noise}(t) - a_0^l) \\
&\int_{-\pi}^{\pi} \left[\cos\left((a_1^u \cos(\theta_1') - a_1^l) \sin(x) - a_2^l \sin(2x) \right) \right. \\
&\left. \sin\left((a_1^u \sin(\theta_1')) \cos(x) \right) \frac{\cos(x)}{2\pi} \right] dx. \qquad (3.50)
\end{aligned}$$

To determine the size of the two integrals in eq. (3.50), it is noted that the constants a_1^l, a_1^u and a_2^l are small. Sinus and cosine are therefore Taylor expanded, which results in

$$\begin{aligned}
I_{3\cos}(a_1^l, a_1^u, a_2^l) &= \int_{-\pi}^{\pi} \left[\cos\left((a_1^u \cos(\theta_1') - a_1^l) \sin(x) - a_2^l \sin(2x) \right) \right. \\
&\left. \cos\left((a_1^u \sin(\theta_1')) \cos(x) \right) \frac{\cos(x)}{2\pi} \right] dx \\
&\approx \int_{-\pi}^{\pi} \left[\left(1 - \left((a_1^u \cos(\theta_1') - a_1^l) \sin(x) - a_2^l \sin(2x) \right)^2 /2 \right) \right. \\
&\left. \left(1 - \left(a_1^u \sin(\theta_1') \cos(x) \right)^2 /2 \right) \frac{\cos(x)}{2\pi} \right] dx \\
&= 1/2 (a_1^u \cos(\theta_1') - a_1^l) a_2^l \underbrace{\left(1 - \left(a_1^u \sin(\theta_1')/4 \right)^2 \right)}_{\approx 1} \pi \\
&\approx 1/2 (a_1^u \cos(\theta_1') - a_1^l) a_2^l \pi \qquad (3.51)
\end{aligned}$$

$$
\begin{aligned}
I_{\cos,\sin,\cos}(a_1^l, a_1^u, a_2^l) &= \int_{-\pi}^{\pi} \Big[\cos\Big((a_1^u\cos(\theta_1') - a_1^l)\sin(x) - a_2^l\sin(2x)\Big) \\
&\quad \sin\big((a_1^u\sin(\theta_1'))\cos(x)\big)\frac{\cos(x)}{2\pi}\Big]\,dx. \\
&\approx \int_{-\pi}^{\pi} \Big[\Big(1 - \Big((a_1^u\cos(\theta_1') - a_1^l)\sin(x) - a_2^l\sin(2x)\Big)^2/2\Big) \\
&\quad \big(\big(a_1^u\sin(\theta_1')\cos(x)\big)\big)\frac{\cos(x)}{2\pi}\Big]\,dx \\
&= \underbrace{\Big(1 - \Big(a_1^u\cos(\theta_1') - a_1^l\Big)^2/8 + (a_2^l)^2/8\Big)}_{\approx 1} a_1^u\sin(\theta_1')\pi \\
&\approx a_1^u\sin(\theta_1')\pi \qquad (3.52)
\end{aligned}
$$

The absolute value of the lock-in output (Lock-in$_{\cos(x)}$) is averaged over a long timespan, as done from eq. (3.42) to eq. (3.46). That is

$$
\begin{aligned}
\text{Lock-in}_{\cos(x)}^{abs,average} &= 2/\pi|\eta|\left(|I_{3\cos}(a_1^l, a_1^u, a_2^l)| + |I_{\cos,\sin,\cos}(a_1^l, a_1^u, a_2^l)|\right). \\
&\approx |\eta|\left(|a_1^u\cos(\theta_1') - a_1^l||a_2^l| + |a_1^u\sin(\theta_1')|\right) \qquad (3.53)
\end{aligned}
$$

As $a_1^u > a_1^l \gg a_2^l$, the size of Lock-in$_{\cos(x)}^{abs,average}$ is minimized when $\sin(\theta_1') = 0$. That is when $(\theta_1 = \theta_2)$ or $(\theta_1 = \theta_2 + \pi)$. The phase delay between the signal reaching the sample and the signal from the signal generator is as previously noted due to the AC-amplifier (see fig 3.14). The approximate size of the phase delay (θ_2) has been measured and (θ_2) is small. Choosing the phase θ_1 close to 0 (i.e. close to the phase of the signal from the signal generator) ensures $(\theta_1 = \theta_2)$.

Adjusting the amplitude a_1^l.

With the phases θ_1' and θ_3' adjusted to 0, the size of the phase modulation on the $LiNbO_3$ modulator is adjusted until the absolute value of the lock-in output (Lock-in$_{\cos(x)}$) averaged over a long timespan is minimal. The

other output (Lock-in$_{\cos(x)}$) from the lock-in amplifier is then

$$\begin{aligned}
\text{Lock-in}_{\sin(x)} &= \eta \int_{-\pi}^{\pi} \Big[\sin\Big((a_1^u - a_1^l)\sin(x) - a_2^l \sin(2x) \\
&\quad + c_\varphi^{noise}(t) - a_0^l \Big) \sin(x)/(2\pi) \Big]\, dx \\
&= \eta \sin(c_\varphi^{noise}(t) - a_0^l) \\
&\quad \int_{-\pi}^{\pi} \Bigg[\underbrace{\cos\Bigg(\underbrace{(a_1^u - a_1^l)\sin(x) - a_2^l \sin(2x)}_{\text{odd}} \Bigg)}_{\text{even}} \underbrace{\frac{\sin(x)}{2\pi}}_{\text{odd}} \Bigg]\, dx \\
&\quad + \eta \cos(c_\varphi^{noise}(t) - a_0^l) \\
&\quad \int_{-\pi}^{\pi} \Bigg[\underbrace{\sin\Bigg(\underbrace{(a_1^u - a_1^l)\sin(x) - a_2^l \sin(2x)}_{\text{odd}} \Bigg)}_{\text{odd}} \underbrace{\frac{\sin(x)}{2\pi}}_{\text{odd}} \Bigg]\, dx \\
&= \eta \cos(c_\varphi^{noise}(t) - a_0^l) \\
&\quad \int_{-\pi}^{\pi} \Big[\sin\Big((a_1^u - a_1^l)\sin(x) - a_2^l \sin(2x) \Big) \frac{\sin(x)}{2\pi} \Big]\, dx
\end{aligned} \tag{3.54}$$

The absolute value of (Lock-in$_{\sin(x)}$) is averaged over a long timespan. That is

$$\text{Lock-in}_{\sin(x)}^{abs,average} = 2/\pi|\eta| \left| \int_{-\pi}^{\pi} \Big[\sin\Big((a_1^u - a_1^l)\sin(x) - a_2^l \sin(2x) \Big) \frac{\sin(x)}{2\pi} \Big]\, dx \right| \tag{3.55}$$

For small values of $(a_1^u - a_1^l)$ and a_2^l, the integral can be solved by Taylor expanding $\sin(x)$. That is

$$\begin{aligned}
\text{Lock-in}_{\sin(x)}^{abs,average} &\approx 2/\pi|\eta| \int_{-\pi}^{\pi} \Big[\Big((a_1^u - a_1^l)\sin(x) - a_2^l \sin(2x) \Big) \frac{\sin(x)}{2\pi} \Big]\, dx \\
&= |\eta||a_1^u - a_1^l|/\pi
\end{aligned} \tag{3.56}$$

Equation (3.56) shows that the measured value Lock-in$^{abs,average}_{\sin(x)}$ is minimal and equal, to 0, when $a_1^u = a_1^l$ [17]. The absolute value of a_1^u is adjusted on the electrical attenuator and the sign of a_1^u is chosen on the inverter (see fig. 3.14).

To show the solution is unambiguity a little more care must be taken, as the integral in eq. (3.55) is only solvable when $(a_1^u - a_1^l)$ and a_2^l are small. Strictly speaking, a_2^l is always small, as it is the 2-harmonic signal from the sample. The value of $(a_1^u - a_1^l)$ is *not* always small, as a_1^u is the signal from the $LiNbO_3$ modulator. To show the unambiguous numerical value of the integral has been calculated for $-\pi < (a_1^u - a_1^l) < \pi$ and $-\pi/2 < (a_2) < \pi/2$. The result is shown in fig. (3.16). The figure demonstrates the unambiguously of the determined value of a_1^u.

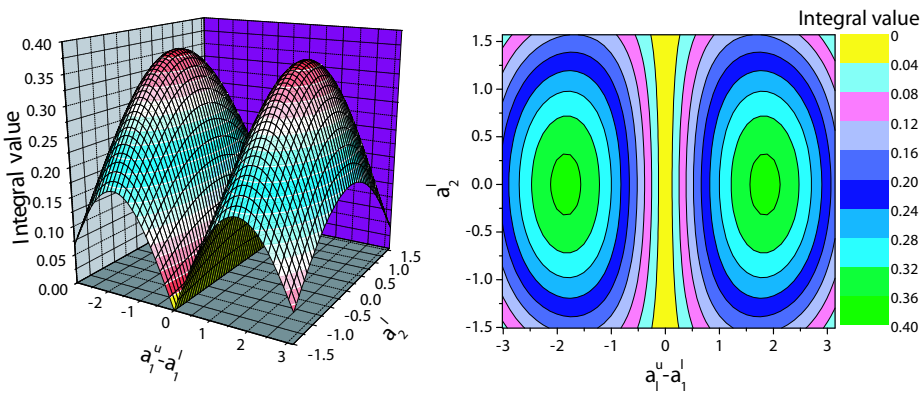

Figure 3.16: The absolute value of the integral in eq. (3.55). The integral value is only 0, when $(a_1^u - a_1^l)$ is 0. Unambiguously is therefore ensured.

3.5.3 Equations for $\chi^{(2)}$, $\chi^{(3)}$ and $E_{frozen-in}$.

Doing the phase adjustments described in section (3.5.2) and (3.5.2) and the amplitude adjustment described in section (3.5.2), an unambiguous

[17] As Lock-in$^{abs,average}_{\sin(x)}$ is the *absolute* value of Lock-in$_{\sin(x)}$ averaged over time, it is positive. The smallest possible value for a positive value is 0.

minimization has been made, that ensures

$$a_1^u = a_1^l, \tag{3.57}$$

where a_1^u and a_1^l are the phase change amplitude at the fundamental frequency in the upper arm and lower arm, respectively. The phase change in the upper arm is known (see eq. (3.33) in section (3.4.2)). For a **Pockels material**, the phase change is given by eq. (3.37). Eq. (3.57) is fulfilled when and only when

$$\begin{aligned} -s_{inv}\pi \cdot \frac{A_1^{electric}}{V_\pi} &= \frac{2l_{sample}\pi\Gamma_{core}\chi_{core}^{(2)}}{\lambda n_{\phi,bulk,0,core}} \cdot A_2^{electric}\varsigma/d_{sample} \Rightarrow \\ \chi_{core}^{(2)} &= -s_{inv}\frac{\lambda d_{sample} n_{\phi,bulk,0,core} A_1^{electric}}{2l_{sample}\Gamma_{core}V_\pi A_2^{electric}\varsigma}. \end{aligned} \tag{3.58}$$

All the parameters on the right hand side of eq. (3.58) are measured values and $\chi_{core}^{(2)}$ is then determined

For a **Kerr material**, the phase change is given by eq. (3.39). a_1^l is the amplitude of the fundamental part of the phase oscillation. Eq. (3.57) is fulfilled when and only when

$$\begin{aligned} -s_{inv}\pi \cdot \frac{A_1^{electric}}{V_\pi} &= \frac{3l_{sample}\pi}{\lambda}\frac{\chi_{av}^{(3)}}{n_{\phi,eff,0}} 2\frac{A_2^{electric}}{d_{sample}}\left(\frac{V_{DC}}{d_{sample}} + E_{frozen-in}\right) \Rightarrow \\ \underbrace{3\chi_{av}^{(3)}\left(\frac{V_{DC}}{d_{sample}} + E_{frozen-in}\right)}_{=\chi_{eff}^{(2)}} &= -s_{inv}\frac{\lambda d_{sample} n_{\phi,eff,0} A_1^{electric}}{2l_{sample}V_\pi A_2^{electric}}. \end{aligned} \tag{3.59}$$

All the parameters on the right hand side of eq. (3.59) are measured for multiple values of V_{DC}. The phases (θ_3) and (θ_1) are adjusted for the first measurement[18] and a_1^u is adjusted for each V_{DC}-value.

The determined values of the right hand side of eq. (3.59) vs. V_{DC}/d_{sample} is a straight line with slope $3\chi_{av}^{(3)}$. The measured line crosses the x-axis $(y = 0)$, when $V_{DC}/d_{sample} = -E_{frozen-in}$. An example of a measurement is plotted in fig. (3.18).

[18] It is only necessary to make the phase adjustments described in section (3.5.2) and (3.5.2) for the first amplitude (a_1^u) adjustment, as the optimal phase values for θ_3 and θ_1 are independent of V_{DC}. The optimal phase condition is $(\theta_3 = \theta_1 = \theta_2)$.

3.5.4 Sign of $LiNbO_3$ phase modulation.

To determine the sign in eq.(3.32) two measurements where made on the same sample. The non-linear coefficient ($\chi^{(2)}$) and ($\chi^{(3)}$) and the frozen-in field ($E_{frozen-in}$) where measured by both the Bragg grating method (see appendix C) and by the DC shifted MZI method. Even though the Bragg grating method is not extremely accurate, the sign of $\chi^{(3)}_{av}$ is trustworthy. The sign of $\chi^{(3)}_{av}$ for the sample was measured to be *positive*, i.e. the refractive index increases when an external field is applied. The measurement of the Bragg wavelength ($\lambda_{\text{Bragg}}(V) = \Lambda n(V)$) vs. external applied DC-field is shown in fig.(3.17). The pitch (Λ) is the period of the phase mask. As the period is a distance, Λ is a positive value.

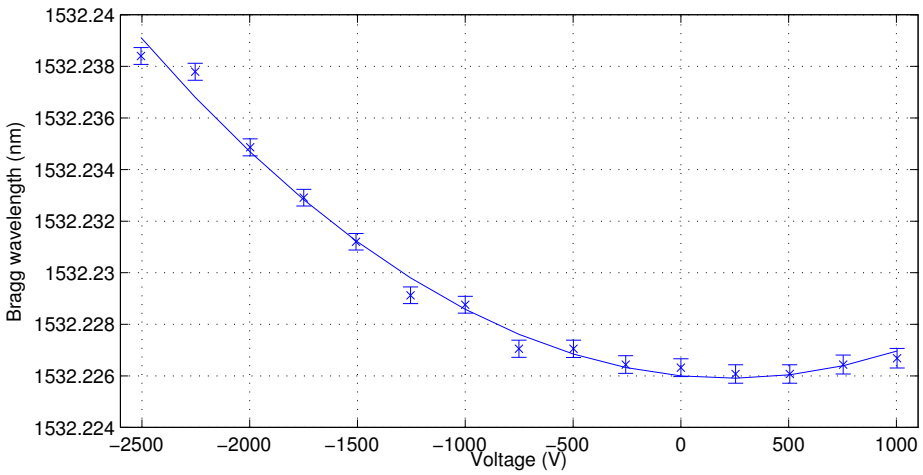

Figure 3.17: Plot of Bragg measurement results. The Bragg wavelength and thereby the refractive index clearly increases when a DC-field is applied. The $\chi^{(3)}_{av}$ is therefore *positive*. The measurement is for TE-polarized light.

The DC shifted MZI method was used for measuring on the same sample. The result is in fig.(3.18).
The chosen negative sign in eq.(3.32) is in the derivation brought all the way to negative sign on the right hand side of eq. (3.59). When the measured slope for the right hand side of eq. (3.59) is positive, the determined $\chi^{(3)}_{av}$ value is *positive*. This demonstrates that the negative sign in eq.(3.32) is correct.

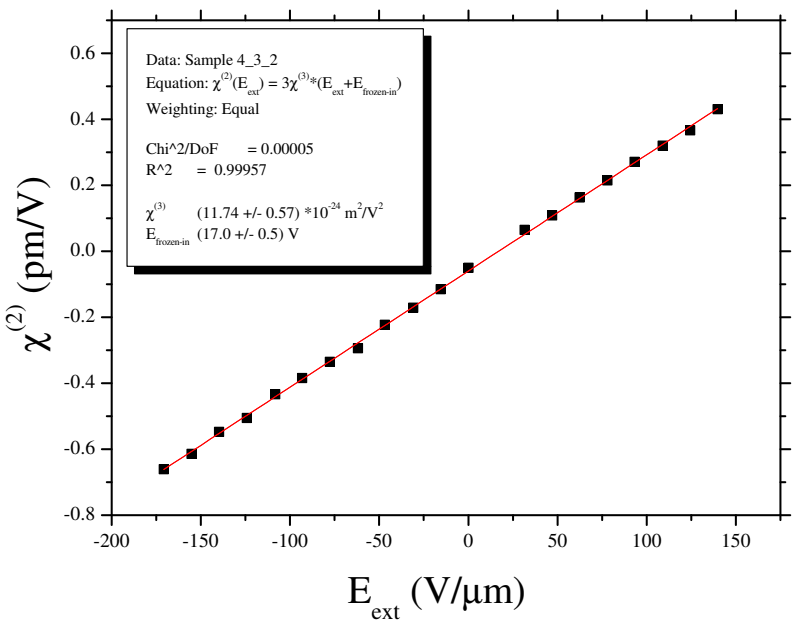

Figure 3.18: Plot of DC-shifter MZI measurement results. The slope of the line is clearly positive. The measurement is for TE-polarized light.

3.6 Accuracy of developed methods.

There are always two distinct types of errors connected to a measurement method. The first type is systematic error due to finite good calibration of the applied measurement instruments. The second error type is the reproducibility error, i.e. the derivation between repeated measurements that should be totally identical. Both error types are investigated in appendix B. The results found are summarized in table (3.2).
To make absolutely sure, that the measurement method works correctly and that no factors have been forgotten in the mathematical derivation a measurement was made on a pre-caracterized poled fiber. The fiber was made and characterized by Niklas Myrén [8]. The results measured by Niklas Myrén is shown in fig. (3.19).

Accuracy of developed methods.

Measurement type.	Wavelength systematic error. **x-axis**	Systematic error. **y-axis**	Reproducibility error. **y-axis**
V_π	10ppm	6.1‰	< 5.5‰
$\chi^{(2)}$	10ppm	4.6%	5.3%
$\chi^{(3)}$	10ppm	4.3%	3.1%

Table 3.2: The errors are determined in appendix B. Both the systematic and the reproducibility errors for the measurement of V_π are hard to reduce. The systematic error of the $\chi^{(2)}$ and $\chi^{(3)}$ measurements can be reduced by using a more accurate voltmeter. To reduce the reproducibility error for the $\chi^{(2)}$ measurement, the optical loss in the samples must be reduced. The reproducibility error for the $\chi^{(3)}$ measurement can be reduced by applying an interferometric measurement method for determining the sample thickness. Such a method would also decrease the reproducibility error for the $\chi^{(2)}$ measurement. **The DC-shifted MZI methods** detection limit for samples with a reasonable optical loss ($< 10dB$) is $< V_\pi/100$.

To compare the results measured by Niklas Myrén with the measurement made with **the DC shifted MZI method**, the measured curve for the phase shift in fig. (3.19) is rewritten to obtain the $\chi^{(3)}$ value. The equation for the phase shift ($\Delta\phi$) is

$$\Delta\phi(V) = a * (\frac{V + pol}{1.0322})^2, \tag{3.60}$$

where the constant a and pol are determined from the fit to the measurement points in fig. (3.19). The factor of 1.0322 corrects for an adjustment of a voltage probe measured after fig. (3.19) was made. The origin of the phase shift is a refractive index change in the waveguide of length l_{fiber}. The phase is shifted by π, when

$$\Delta n_{\phi,eff}(E) l_{fiber} = \lambda/2, \tag{3.61}$$

where λ is the wavelength of the incident light. The change in phase is linear with the change in refractive index and eq. (3.60) can therefore be written as[19]

$$\Delta n_{\phi,eff}(E) l_{fiber} 2/\lambda = a * (\frac{V + pol}{1.0322})^2. \tag{3.62}$$

[19]The phase shift in eq. (3.60) is measured in radians, i.e. in units of π.

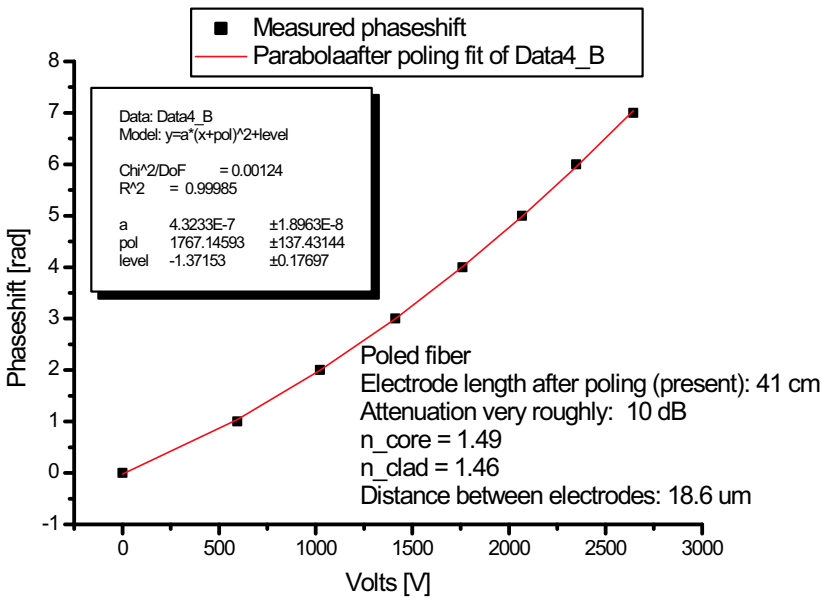

Figure 3.19: Measured phase change vs. external applied voltage. The phase change is measured in the unit of radians (= $\lambda/2$). After Niklas made the measurement, he calibrated the voltage probe and found that the real voltage is 3.22% higher than plotted on the graph.

The refractive index change ($\Delta n_{\phi,eff}(E)$) due to a third order non-linearity is known from eq. (2.15). Substituting $\Delta n_{\phi,eff}(E)$ gives

$$\frac{3\chi^{(3)}_{av}}{2n_{\phi,eff,0}}(V/d + E_{frozen-in})^2 l_{fiber} 2/\lambda = a * (\frac{V + pol}{1.0322})^2 \Rightarrow$$

$$\chi^{(3)}_{av} = \frac{a * d^2 \lambda n_{\phi,eff,0}}{3 l_{fiber} 1.0322^2} \quad \text{and} \qquad (3.63)$$

$$\chi^{(2)}_{eff} = \frac{a * pol * d^2 \lambda n_{\phi,eff,0}}{l_{fiber} 1.0322} \qquad (3.64)$$

where the electric field is interchanged with $V/d + E_{frozen-in}$. The equation was split into a linear part (the eq. for $\chi^{(2)}_{eff}$) and a quadratic term (the eq. for $\chi^{(3)}$). The first row of values in table (3.3) are found by inserting the values measured by Niklas measured numbers (see fig. 3.19)

into eq. (3.63) and eq. (3.64).

Comparison of obtained non-linear values.

Measurement	$\chi^{(2)}_{eff}$ (pm/V)	$\chi^{(3)}$ $10^{-24}m^2/V^2$	$E_{frozen-in}$ $V/\mu m$
Niklas (Polarization unknown)	0.0728 ± 0.0065	2.63 ± 0.12	92.0 ± 7.2
DC-shifted MZI (TE)	0.0606 ± 0.0025	2.218 ± 0.092	-91.07 ± 0.39
DC-shifted MZI (TM)	0.0602 ± 0.0025	2.415 ± 0.10	-83.07 ± 0.37

Table 3.3: The polarization of the light was *not* controlled in the measurement made by Niklas Myrén. The loss is lower for TE polarized light, which means Niklas Myrén measurements is probably for TE polarized light. The measured frozen-in fields are very comparable, but the non-linear coefficients deviates more than the uncertainties can justify. This could be due to the difference in frequency for the applied E-field in the two types of measurements. Niklas uses a DC-field, while **the DC-shifted MZI method** uses an AC-field with the frequency 33.333 kHz. The uncertainties in the table do *not* include the uncertainties for l_{fiber}, d and $n_{\phi,eff}$ as the exact same values are used when evaluating all three measurement series. The uncertainty of Niklas measurement only includes the error due to the parable fitting in fig. (3.19). The difference of the sign for $E_{frozen-in}$ is because the electrodes where interchanged in the DC-shifted MZI measurement compared to the measurement performed by Niklas.

Measurements where performed on the fiber using the DC-shifted MZI method. The non-linearity was determined for both polarizations and the measured non-linearities are plotted in fig. (3.20) and in fig. (3.21). The difference in the obtained non-linearity values (see table 3.3) is probably due to the different frequency of the applied fields. Niklas uses a pure DC-field, while the DC-shifted MZI method measures on a combination of a DC-field and a 33.333 kHz AC-field[20]. This comparison demonstrates that the derived equations are correct and that the principles of the DC shifted MZI method is correct.

[20]In the DC-shifted MZI method, the DC-field takes the role of the poled in field and the AC-field assembles the modulation field. The combination of a DC-field and an AC-field gives good predictions for device performance.

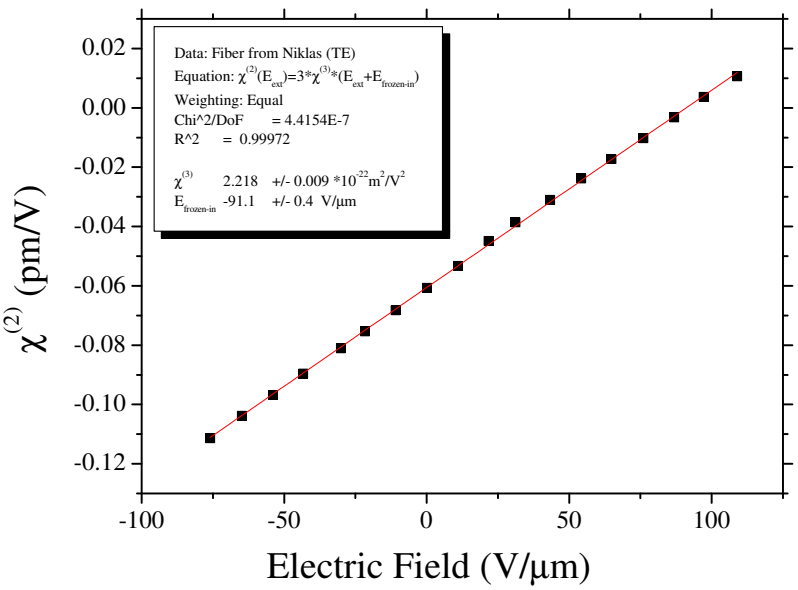

Figure 3.20: Measured second-order non-linearity vs. external applied field. The measurement is made on the fiber made by Niklas Myrén [8] for TE polarized light.

3.7 DC-shifted MZI method summary.

This chapter and two appendices A and B have been devoted to a detailed description of the measurement method developed in this project: **The DC-shifted MZI method**. To determine if the new method is worth the trouble, its advantages and possible disadvantages must be compared to the already established method. Before development of the DC-shifted MZI method, there were two methods for measuring non-linearities in the group, a method based on measuring the shift of wavelength for a Bragg grating inscribed in the sample and a method based on a fiber MZI.

The developed method is based on the old MZI method and the only real difference, besides the electrical measurement equipment starting with the lock-in amplifier, is the combination of the externally applied DC-field with the modulating AC-field. The old MZI method relied on

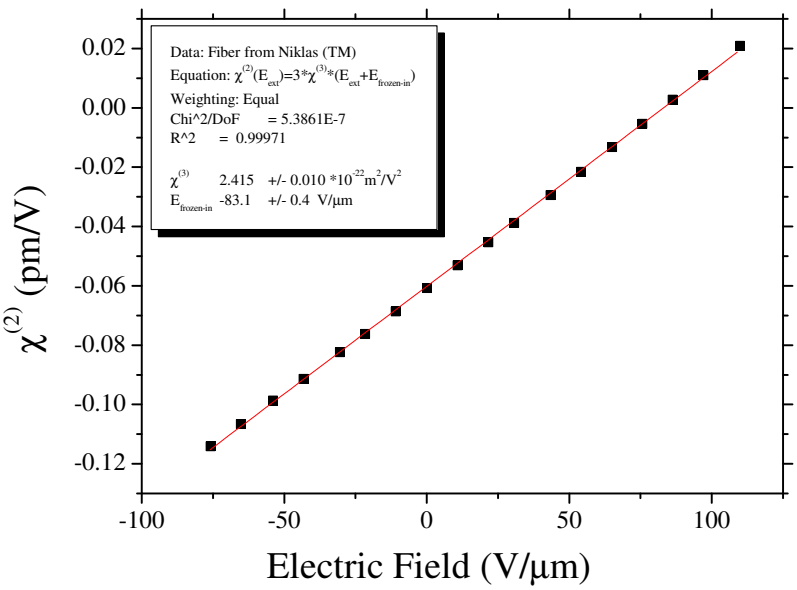

Figure 3.21: Measured second-order non-linearity vs. external applied field. The measurement is made on the fiber made by Niklas Myrén [8] for TM polarized light.

an internal DC field in the sample, i.e. a poled in field. In principle the old MZI method is identical to measuring only one point on the curve in fig. (3.18), where the frozen-in field would determine the position on the x-axis. The position on the x-axis was not measured and the measurement therefore only revealed the obtained $\chi^{(2)}_{eff}$ value, not $\chi^{(3)}_{av}$ and not $E_{frozen-in}$. However the old MZI method assumed a constant phase difference of $\pi/2$ between the two arms and as was shown in fig. (3.6) and fig. (3.7) this assumption is *not* correct, not even in the *simple* case where the sample is interchanged with a pigtailed fiber. The newly developed method takes the oscillation of the phase into account and the introduction of lock-in amplifier and all the complicated math originates back to the oscillation of the phase. Unfortunately re-measurements on samples characterized by the old MZI method could not be performed, as a previous group member put all samples characterized by the old MZI

method into the garbage can. The approximate size of the systematic error due to the wrongful assumption of constant phase difference can therefore not be determined.

When comparing the newly developed method and the Bragg grating method four aspects must be considered.

- The accuracy of the two methods.
- How versatile the methods are.
- How directly the measured result determine the size of interest.
- The stability of the methods[21]

The accuracy is easy to compare, as the error for fitting a measurement of Bragg wavelengths vs. electric field was around 8.5% [9]. This should be compared to the error when fitting measured data points acquired with the new method, where the error is 1% (see fig. B.17 in appendix B). This is however an unfair comparison for the Bragg grating method, as it is the total errors that should be compared. The thickness of the grown layers varies a couple of percent over each sample and the new method is therefore, strictly speaking, overprecise, as the error is now dominated by other sources. The accuracy is therefore improved from around 8.5%[22] for the Bragg grating method to 5.3%[23] for the DC-shifted MZI method. The great improvement of the new method is *not* the reduced error but the greatly improved stability of the method. It was observed that results measured with the Bragg grating method could vary by a factor of 1.5 when repeated. This is probably due to a communication problem between the laser and the optical spectrum analyzer. In contrast to this there are *no* stability problems for the DC-shifted MZI method.

The idea behind the Bragg grating method was originally to make a switchable Bragg grating, where an applied DC-voltage would position

[21] Stability here refers to reproducibility when a sample is characterized again after having lied in the drawer for a couple of day.

[22] The error of 8.5% is obtained from the fitting of the parabola. It does not contain all the other errors, but as both the systematic and the reproducibility errors found in appendix B are roughly identical to the errors expected for the Bragg grating method, the error of 8.5% will be the only dominant contribution

[23] The error of 5.3% is obtained by adding the systematic and the reproducibility errors from table (3.2).

the grating at the desired wavelength. Measuring the Bragg wavelength vs. applied field was the perfect way for determining if the Bragg grating was moving enough. I.e. the result determined by the Bragg grating method was directly usable for the original idea behind the method. The goal of this project was not to realize a switchable Bragg grating, but to make a switch based on a MZI. The trouble with the results determined by the Bragg grating method when used to make predictions for a MZI device, is the frequency of the applied field. In the Bragg grating method the field has to be DC, as it takes minutes to make a measurement scan determining the Bragg wavelength. There can be a difference between the material non-linearity for a DC-field and the non-linearity for an AC-field. As such derivation can limit the bandwidth of a device, it is better to measure the effect of an AC-field, when the objective is to make a switch. As the DC-shifted MZI method measures the phase change for an applied AC-field, the method directly measures the size of interest for the scope of this project. In chapter (6) there was observed a difference between low frequency and higher frequency modulation, a difference that the Bragg grating method could not have detected.

The developed method is capable of measuring on all types of single mode samples[24]. If a single mode sample guides light and if electrodes can be placed, the method can determine the induced phase shift. The Bragg grating method can only be used if it is possible to make a Bragg grating in the sample. This was again not a problem for the original purpose of the Bragg grating method, but to require UV-sensivitity[25] limits the number of usable samples. The breakthrough made in this project was made in a material (see chapter 6) that is not UV-sensitive and the versatility of the developed method therefore prooved crucial.

The goal with the development of **The DC-shifted MZI method** was to get a working characterization setup in our laboratory. Perhaps the same goal could have been reached by purchasing some equipment, e.g. a phase-locked loop could perhaps remove the observed phase noise [4], but due to the financial situation, the setup had to be made with equipment already available in the laboratory. The goal of making a working

[24]The Bragg grating method is capable of measuring on multimode waveguides and is hence more versatile with respect to the physical dimensions of the core.

[25]The Bragg grating is made by changing the index of the sample permanently by shining very intense patterned UV-light onto the sample (see appendix C).

setup with all sources of error known was reached. The limiting factors on the accuracy of the developed method is not the non-linear measurement method, but the experimental equipment applied. In particular a more accurate voltmeter would reduce the uncertainty. As the thickness is known to vary a couple of percents across the sample, a smaller uncertainty also requires multiple measurements of the thickness in order to make a 3D-thickness chart of the sample. As the limits of the accuracy is not directly due to the non-linear measurement method, there has *not* been made a comparison with other methods known from the literature [2, 4].

References to Chapter 3

[1] C. Marckmann, Y. Ren, G. Genty, and M. Kristensen. "Strength and symmetry of the third-order nonlinearity during poling of glass waveguides", *IEEE Photon. Technol. Lett.*, vol. 14, no. 9, pp. 1294–1296, 2002.

[2] M. Janos, W. Xu, D. Wong, H. Inglis, , and S. Fleming. "Growth and decay of the electrooptic effect in thermally poled b/ge codoped fiber", *Jour. of Lightwave Tech.*, vol. 17, no. 6, pp. 1037–1041, 1999.

[3] Y. Ren, C. Marckmann, J. Arentoft, and M. Kristensen. "Thermally poled channel waveguides with polarization independent electro-optic effect", *IEEE Photon. Technol. Lett.*, vol. 14, no. 5, pp. 639–641, 2002.

[4] A. C. Liu, M. J. Digonnet, and G. S. Kino. "Measurement of the dc kerr and electrostrictive phase modulation in silica", *Journal of the Optical Society of America B: Optical Physics*, vol. 18, no. 2, pp. 187–194, 2001.

[5] B. Saleh and M. Teich. *Fundamentals of Photonics.* Wiley, 1991. ISBN 0-471-83965-5.

[6] "http://www.photox.co.uk/linbo3.htm". Company selling LiNbO3 wafers.

[7] R. Syms and J. Cozens. *Optical guided waves and devices.* McGraw-Hill, 1992. ISBN 0-07-707425-4.

[8] N. Myrén. *Poled fiber devices.* Ph.D. thesis, Department of Physics and Quantum Optics, Royal institute of technolegy, Roslagstullsbacken 21, SE-106 91 Stockholm, Sweden., 2005. ISBN 91-7178-053-x.

[9] C. J. Marckmann. *Switchable Bragg gratings.* Ph.D. thesis, Research Center COM, Technical University of Denmark, Kgs. Lyngby, Denmark, 2003.

Chapter 4

Sample Fabrication.

This chapter contains an overview of the sample fabrication technique. The aim with the chapter is *only* to give a short introduction to the different fabrication processes used and to introduce the nomenclature. This is used in chapter (5) where the different samples and there characteristics are described. The interested reader can look in [1] for comprehensive information about thin film fabrication.

The samples used in this project have been fabricated or post processed in the Danchip cleanroom. To make a normal sample, the silicon wafer is oxidized thermally to obtain a thin glass film. Fig. (4.1) shows a wafer and a cleaved out sample.
The produced glass film is normally very pure and it is known as thermal oxide (TOX). A layer of high index glass is then grown on top of the TOX in a plasma-enhanced-chemical-vapor-deposition (PECVD) chamber (see fig. 4.2), where reaction gases are mixed and ionized. The high index glass is normally used to as the waveguide core.

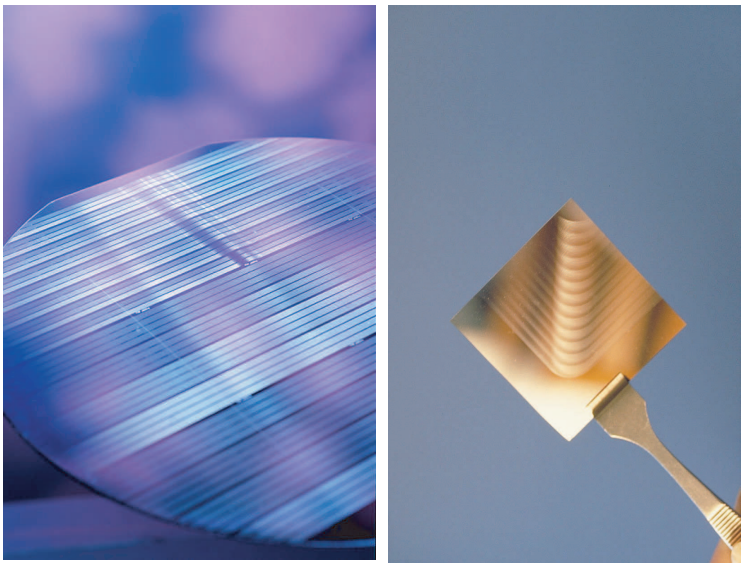

Figure 4.1: The left picture shows part of a 4 inch wafer with a structure made on top. The right picture shows a sample cleaved out of a wafer. Pictures made available by the COM photographer Lasse Rusborg.

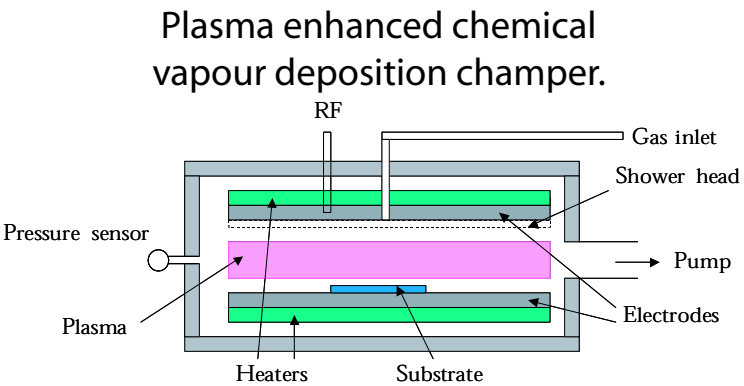

Figure 4.2: Plasma enhanced chemical vapor deposition chamber. Reaction gases enter a high-voltage radio frequency (RF) field where the molecules are ionized. The reacting vapor deposits glass at the wafer and other reaction products are pumped out. The controlled parameters are gas flows, RF frequency and power, temperature and pressure. Figure is made by Karin Andersen.

The grown glass can be doped with different elements to obtain the desired refractive index. The index can for example be doped with Germanium and/or Nitrogen. Both of these dopants raise the material refractive index. The reaction equations for the glass production are

$$SiH_4(g) + N_2O(g) \rightarrow SiO_2(s) + N_2(g) + H_2(g) \quad (4.1)$$

$$GeH_4(g) + N_2O(g) \rightarrow GeO_2(s) + N_2(g) + H_2(g) \quad (4.2)$$

$$SiH_4(g) + N_2O(g) + NH_3(g) \rightarrow SiON(s) + H_2O(g) + N_2(g) + H_2(g). \quad (4.3)$$

The reaction equations are *not* balanced and they should only be used as guidelines due to the complexity of the plasma reaction. The reaction speed would under normal chemical circumstances be extremely slow, but the gases are ionized in the PECVD chamber. The physical properties of the produced glass depend on various chamber parameters including pressure, electric effect and frequency and the obvious parameters like the gas mixture composition. All relevant controllable parameters are collected in the glass recipe that controls the PECVD while the glass is made. The reproducibility of the glass layers depends strongly on the applied recipe and reproducibility is high for the developed standard recipes. Experimental recipes are normally made by varying the parameters in a standard recipe to some extent as the reproducibility can be reduced dramatically. To compact and stabilize the glass, it is annealed by heating it to for example 1000°C in a controlled atmosphere and baked in the anneal chamber for a couple of hours (see fig. 4.3)
The waveguiding structure is made by spinning[1] a photoresist onto the core glass layer. The photoresist is then illuminated through a mask and the pattern on the mask is transferred to the photoresist at development. The wafer is then etched in a reactive ion etching (RIE) chamber where glass underneath the photoresist is etched away. In this way the pattern on the mask is transferred to the deposited glass (see fig 4.4).

[1] Spinning of photoresist is done by dripping or spraying photoresist onto a spinning wafer. The thickness of the applied photoresist layer depends on the rotation speed of the wafer and on how diluted the photoresist is.

Figure 4.3: Silicon wafers being transferred into an anneal oven. The wafers are usually backed in the oven for 4 hours. The temperature and the atmosphere are controllable. Picture is made available by the COM photographer Lasse Rusborg.

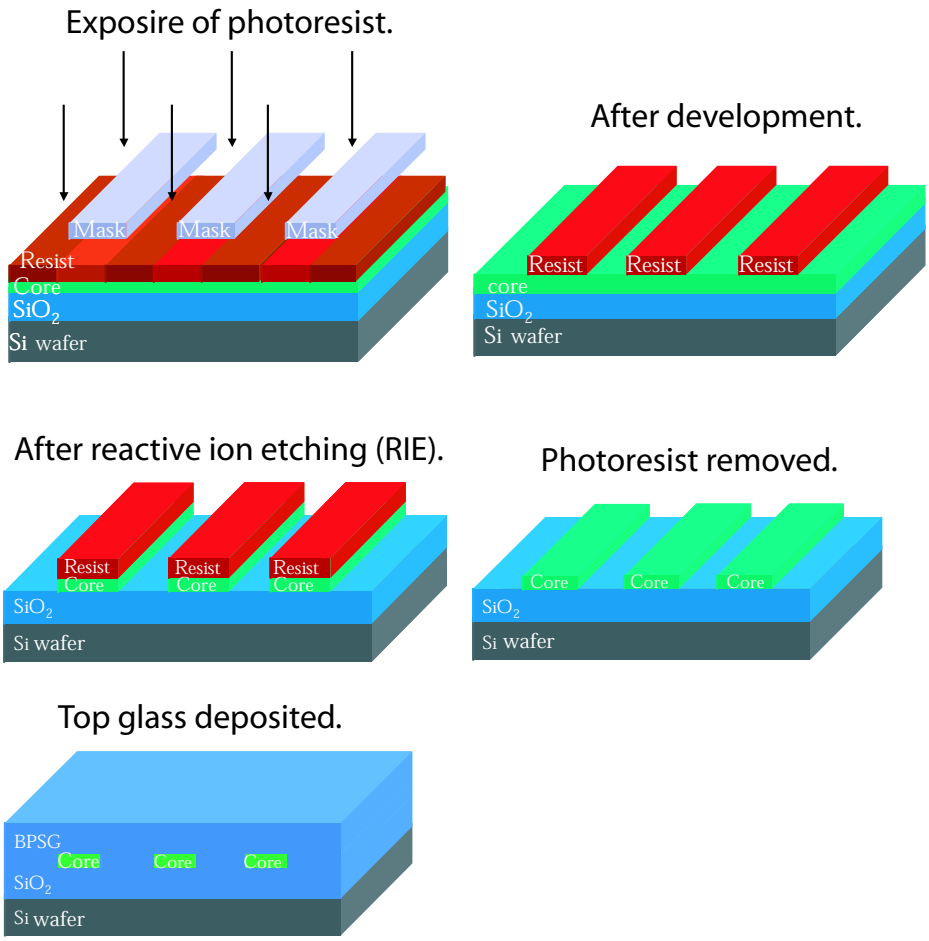

Figure 4.4: Fabrication process for making buried waveguides. Photolithography is used to transfer the pattern from a mask to a photosensitive layer (the photoresist). The pattern is then transferred to the core by RIE and the structure is finally covered by a topcladding. This figure is made by Karin Andersen.

The optical loss in the waveguide depends on both the deposition of the glass waveguide (the PECVD process) and on the sidewall roughness (governed by the RIE process). A whole Ph.D. project can be dedicated to make good lowloss components in a special glass [2]. Finally a top glass is PECVD grown on top of the waveguide. The top glass is normally either pure SiO_2 (hard topcladding) or doped with boron and phosphorus (soft topcladding). The soft topcladding can flow during anneal and hence cover the core in a more uniform low loss manor. The hard topcladding does not float during anneal, but it is better for freezing in an electric field during poling [3].

Different methods than RIE of the core structure can be applied to make a waveguiding structure, e.g. the index in the core layer can be raised by intense UV-light. For UV-written waveguides, the etching step is avoided and the horizontal index step is introduced after deposition of the top cladding. The waveguides can either be normal UV written, where aluminum on top of the waveguide shields the sample except in the places where index increase is desired. The waveguides are then made by flow exposure with intense UV light[2] as shown in fig. (4.5) after the sample was deuterium loading at ~ 200 bar to increase the UV-sensitivity.

An alternative way of increasing the core index is direct UV-writing [4] where a laser beam[3] is focused on the sample and then scanned over the place where a waveguide is wanted (see fig. 4.5). Waveguides made by direct UV-writing can ultimately have lower optical propagation loss [5] than normal UV-written waveguides due to degradation of the aluminum mask during exposure in the normal process [6].

[2]In this project an Eximer laser was used to make the flood exposure. The laser emits pulsed $248nm$ light with a duration of 20 ns and a repetition rate of $\sim$ 50Hz. The pulse energy is between 100 and 300 mJ and there was normally used $3kJ/cm^2$ to make the permanent index step.

[3]The laser wavelength is $257nm$ cw with a power of 50 mW.

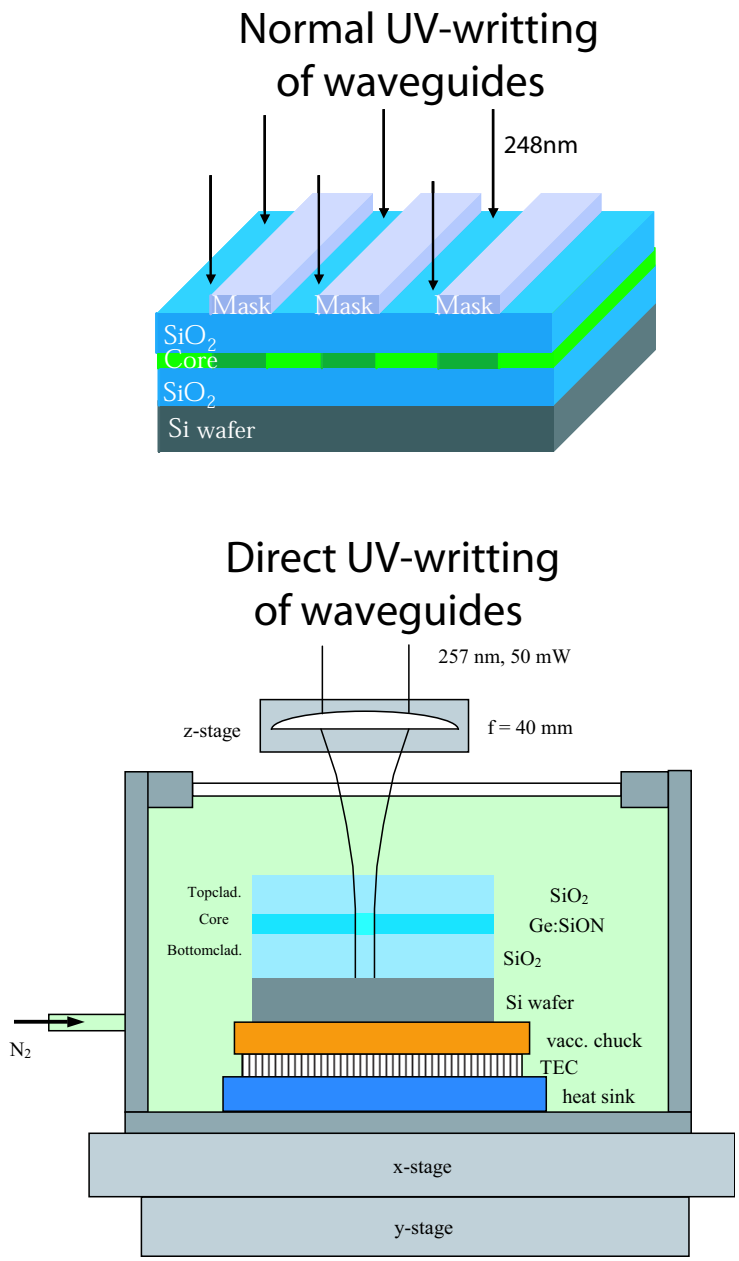

Figure 4.5: UV-writing of waveguides. The top figure shows normal UV-writing, where $248nm$ pulsed laser light is used to illuminate the core. The index is raised permanently at the exposed areas. The bottom figure shows direct UV-writing, where a laser beam is focused down on the sample. The waveguide is then written by translating the sample at $20-1000\mu m/s$. The sample temperature is kept at $-35°$C during direct UV-writing to avoid outdiffusion of deuterium. The spot size on the sample can be adjusted down to $2.5\mu m$ FWHM. The figure is made by Michael Svalgaard.

The horizontal waveguiding property can also be achieved by a photonic crystal structure [7], where periodicity of the cladding material prohibits propagation of certain wavelength intervals. The photonic crystal (PhC) waveguide requires very small structures in the cladding, structures so small, that they cannot be made using normal photolithography due to the wavelength of the light. The photoresist is instead exposed by an electron beam (by e-beam writing). An example of a PhC waveguide is shown in fig. (4.6) together with a simulated transmission diagram for TE polarized light. The distance between the centers of the holes (known as the pitch, Λ) is $425nm$ in the physical waveguides studied. The hole diameter is normally given relative to the pitch and the samples have a relative hole diameter of $272nm$.

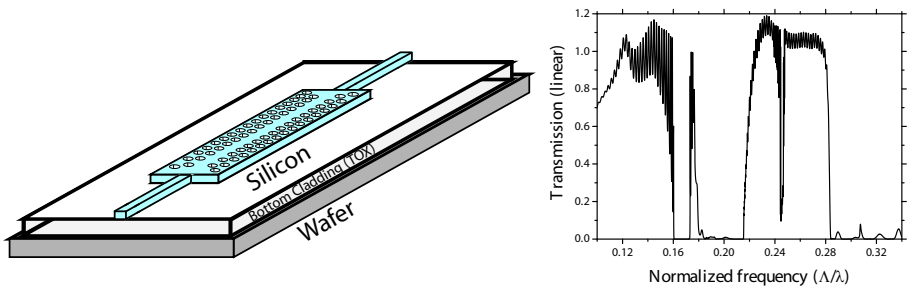

Figure 4.6: A 2D photonic crystal waveguide is made by etching small holes in a high index material like silicon ($n = 3.407$). The periodicity forbids propagation of certain wavelength regions. This is illustrated with the transmission spectrum calculated by 2D finite-difference-time-domain (FDTD). The transmission calculations where made by Andrei Lavrinenko.

The final waveguiding mechanism investigated in this project is guiding by Long-Range Surface Plasmon Polaritons (LRSPP), where the light is guided as a surface wave on the border between a metal and a dielectric [8]. The metal is a very thin ($\sim 10nm$) gold strip, that is $10\mu m$ wide. The mode is a combination of two surface modes, one on each side of the metal strip (see fig. 4.7).

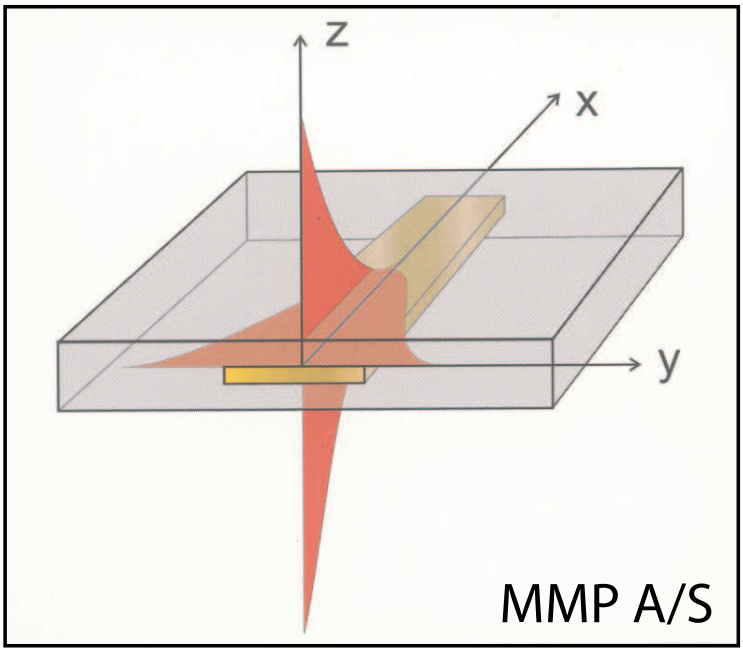

Figure 4.7: Light can be guided as Long-Range Surface Plasmon Polaritons (LRSPP) in the interface between a metal and a dielectric. The figure is made by Alexandra Boltasseva.

References to Chapter 4

[1] M. J. Madou. *Fundamentals of Microfabrication.* CRC press. ISBN 0849308267.

[2] K. Andersen. *Optical components based on high index materials.* Ph.D. thesis, Research Center COM, Technical University of Denmark, Kgs. Lyngby, Denmark, 2005.

[3] C. J. Marckmann. *Switchable Bragg gratings.* Ph.D. thesis, Research Center COM, Technical University of Denmark, Kgs. Lyngby, Denmark, 2003.

[4] M. Svalgaard, C. Poulsen, A. Bjarklev, and O. Poulsen. "Direct uv writing of buried singlemode channel waveguides in ge-doped silica films", *Electronics Letters*, vol. 30, no. 17, pp. 1401–1403, 1994.

[5] D. Zauner, K. Kulstad, J. Rathje, and M. Svalgaard. "Directly uv-written silica-on-silicon planar waveguides with low insertion loss", *Electronics Letters*, vol. 34, no. 16, pp. 1582–1584, 1998.

[6] P. Marques, J. Bonar, A. Leite, and J. Aitchison. "Simultaneous uv direct writing of channel waveguides and bragg gratings in germanium-doped planar silica", *Selected Topics in Quantum Electronics, IEEE Journal on*, vol. 8, no. 6, pp. 1316–1322, 2002.

[7] J. D. Joannopoulos, R. D. Meade, and J. N. Winn. *Photonic Crystals, Molding the flow of light.* Princeton University Press, 1995.

[8] A. Boltasseva. *Integrated-Optics Components Utilizing Long-Range Surface Plasmon Polaritons.* Ph.D. thesis, Research Center COM, Technical University of Denmark, Kgs. Lyngby, Denmark, 2004.

Chapter 5

Experimental results.

5.1 Introduction

This section presents the results for samples with a $\chi^{(3)}_{av}$ value. The aim with poling of glass is first discussed to make a frame for evaluating the obtained results. After looking at the disappointing results for poling of the normal core glass (Ge:SiON), a possible explanation for the very large second-order non-linearities reported in the literature [1, 2] is given based on results obtained for sample 3_5_1. The explanation shows that it is only possible to reach an interesting $\chi^{(2)}_{eff}$ value by increasing the material $\chi^{(3)}_{av}$ with a factor of 10. The possibilities for changing $\chi^{(3)}_{av}$ are described and a number of them are investigated. The most interesting result is found for silicon rich nitride (SRN), that has a 5 times higher $\chi^{(3)}_{av}$ than was obtained for Ge:SiON. It was however decided that *not* even an increase by a factor of 5 was enough to make a device usable.

5.2 The goal with the experiments.

The aim with this project was to realize a switch in poled glass, i.e. in a $\chi^{(3)}$ material where the EO coefficient is obtained by poling. The switch should be made on a 4 inch wafer and the switching voltage should be less than 300V. During the project, it was realized that even if the aim was reached, would there be no interest for such device. To make an interesting device, the switching voltage should be lowered even further,

as fast 300 volt electrical drivers are hard to make. It is hard to quantify exactly what requirements would make a switch in poled glass interesting, but a switching voltage swing less than 100V is a realistic limit. As described in section (2.3) the voltage can be reduced by using more than one electrode (see fig. 2.12). Two of the suggested methods can be applied directly, but applying electrodes on both side of the waveguide is *not* realistic as the mechanical properties of an unsupported waveguide are questionable. As the method of applying a $\lambda/4$ shift in one waveguide only reduces the absolute voltage and not the voltage swing, the reduction due to the applied electrode is only a factor of 2 compared to eq. (2.21), i.e. the voltage swing is reduced by modulating both arms. The lengths of the two affected waveguides are limited to $\sim 5cm$ each by the wafer size of 4 inches giving a total affected length of $\sim 10cm$. Inserting numbers together with the reduction factor of 2 due to the dual electrodes into eq. (2.21) gives

$$V_\pi = \frac{1550nm * 12\mu m * n_{\phi,bulk,0,eff}}{3 * 0.1m * \chi^{(3)}_{av} E_p} = 3.1 * 10^{-11} m \frac{n_{\phi,bulk,0,eff}}{\chi^{(3)}_{av} E_p}, \quad (5.1)$$

where the electrode-electrode distance has been set to $12\mu m$, This distance is a little low for the normal core glass used (Ge:SiON), as the tail of the mode will be lost to the wafer and to the top electrode. The equation can however be used to evaluate if a switching voltage of 100V is realistic. The frozen-in field obtained by poling in the investigated samples is $100 - 200V/\mu m$. This field could probably be increased but it is limited by the breakdown field of glass, that is $850V/\mu m$ at room temperature [3].

Assuming a normal index of glass ($n_{\phi,bulk,0,eff} = 1.5$) and an optimal frozen-in field of $850V/\mu m$ combined with a switching voltage of 100V requires a non-linear $\chi^{(3)}_{av}$ coefficient of

$$\chi^{(3)}_{av} = 5.5 * 10^{-22} m^2/V^2. \quad (5.2)$$

The non-linear value is for the poled glass, but we have never seen significant changes in the non-linearity due to poling, i.e. the same $\chi^{(3)}_{av}$ coefficient is measured before and after poling [4, 5]. The measured $\chi^{(3)}_{av}$ value for non-poled samples can therefore be compared with the value in eq. (5.2) to see if a switch is realisable with the investigated material.

5.3 Increasing the poling field by a charge trapping layer.

This first attempt made for reducing the switching voltage in this project aimed at realizing a larger frozen-in field[1]. The idea was to include a charge trapping layer in the structure in an optimal distance from the core. The glass $SiON$ with a relative high nitrogen dopant level was chosen as the charge trapping layer. The refractive index of the charge trapping layer was higher than the core refractive index, but by making the charge trapping layer thin ($\sim 0.3\mu m$), the light is still guided in the core (see fig. 5.1).

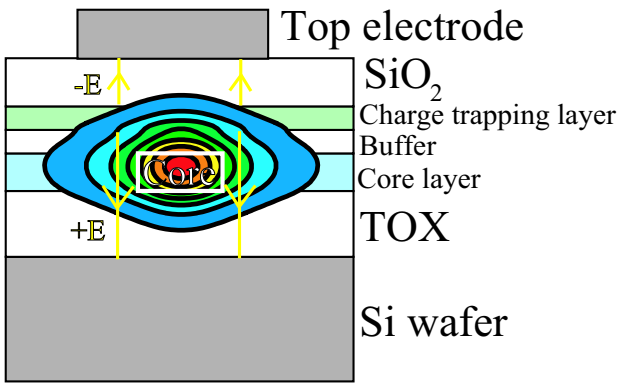

Figure 5.1: Sample with a charge trapping layer. The charge trapping ($0.3\mu m$) layer is separated from the core by a buffer ($0.6\mu m$). The figure is *not* to scale.

The distance was optimized to ensure the largest effect from the trapped charges, as the part of the optical mode, that is below the charge trapping layer sees the electric field E, while the part above the layer sees the field $-E$ as shown in fig. (5.1). Because the charges are trapped close to the guided mode, part of the mode will be affected by an opposite electric field. The effective second-order non-linearity is therefore the

[1] The author made the simulations of the waveguiding structure. The samples where fabricated together with the coworkers Carl-Johan Marckmann and Yetao Ren. The measurements made with the old MZI setup where made by Yetao Ren and the measurements with the Bragg grating method was made together with Carl-Johan Marckmann

large contribution from the optical field underneath the charge trapping layer *minus* the contribution from the optical mode above the charge trapping layer.

The size of the field depends on the poling conditions, but assuming it is possible to trap a fixed amount of charge per unit volume of the charge trapping layer, the thickness of the buffer layer can be optimized. It was found that a distance of $0.6\mu m$ was optimal. The waveguides were made by normal UV-writing and then characterized using both the old MZI method[2], and the Bragg grating method [6]. It was found that the charge trapping layer could increase the yield of the poling field by $\sim$ 20% and a $\mathfrak{r}$ value of $0.093 \pm 0.001 pm/V$ corresponding to $\chi^{(2)}_{eff} = 0.230 \pm 0.003 pm/V$ was obtained. The switching voltage possible with the obtained non-linearity is $\sim 820V$, and the $\chi^{(3)}_{av}$ value in the samples was $\sim 3.5 * 10^{-22} m^2/V^2$. The optimal poling conditions was determined by systematic adjustments of the poling temperature [6] and the result is shown in fig. (5.2).
Even though the charge trapping layer does increase the frozen-in field ($E_{frozen-in}$) it is limited by the small third-order non-linearity ($\chi^{(3)}_{av}$) of glass. In the theoretical case where the frozen-in field is equal to the breakdown field of glass ($850V/\mu m$) the switching voltage would still be $\sim 160V$ (obtained from eq. 5.2), which is unacceptably high.

5.4 The apparently large non-linear effect.

5.4.1 The original promise of silica poling.

The third-order non-linearity in the samples containing a charge trapping layer is higher than for pure silica due to the Germanium doping of the core. The doping makes the core UV-sensitive and also increases ($\chi^{(3)}_{av}$) from the literature value [7] for silica of $1.9 * 10^{-22} m^2/V^2$ to $\sim 3.5 * 10^{-22} m^2/V^2$. The non-linearity is still approximately a factor of 2 too low for making an interesting switch (see eq. 5.2), even when the poling field equals the breakdown field. As such a high poling field is *only* possible in theory, the real factor is more like 4-8. This factor is needed

[2]The measurement methods applied are *not* accurate, as noted in section (3.7). The old measurement methods are however reliable enough to determine that the possible switching voltage is to high to be interesting.

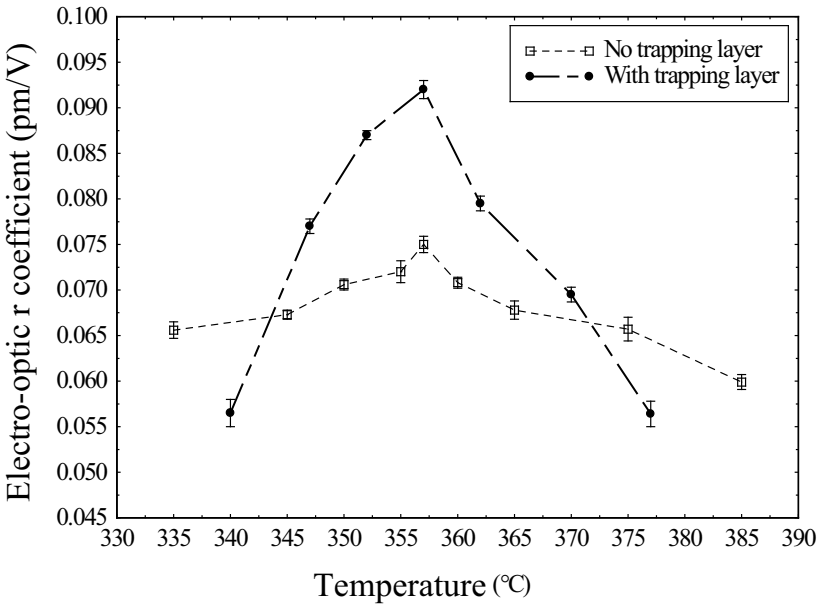

Figure 5.2: Obtained electro-optic coefficient (r) for different poling temperatures [6] for a sample with and without a charge trapping layer.

to reach the interesting regime, where there might be applications for a switch. This could also be interpreted as a need for a factor of 10 and the normal reaction to such a need is to change something dramatically, e.g. like changing the type of glass used for the waveguide. This aim of this project was however to realize a switch in silica. The project aim can be understood by forgetting silica's low non-linear coefficient for a moment. Then it makes sense to make a switch in silica due to the good properties of silica such as a low optical propagation loss, a very high breakdown field and ease of fabrication. The prospect of a glass based modulator with the same switching voltage as $LiNbO_3$ is huge, as glass is much cheaper and can moreover be integrated with silicon. A glass based modulator would open for fast optical chip to chip interconnects and the market could therefore become enormous. The only question remaining is how the low non-linear coefficient of silica could be forgotten. To understand this, one must look at the results published in the literature during

the nineties (1990-2000). Very large effective second-order non-linearities almost comparable to $LiNbO_3$ was reported in for example [1,2], but as reported by [8] the induced non-linear effect normally decayed rapidly.

5.4.2 Sample 3_5_1.

A possible explanation for the very large but decaying effective second-order non-linearities was found [9], when measurements where made on sample 3_5_1[3]. Measurements were performed on this sample and also on a reference sample 17_1. The two samples are distinguished from each other by the glass used as topcladding. The topcladding used for sample 3_5_1 is hard glass (see fig. 5.3), while it was soft glass (see fig. 5.4) for sample 17_1. There are cracks in the hard topcladding, while the soft topcladding is free of cracks (see fig. 5.3 and fig. 5.4).

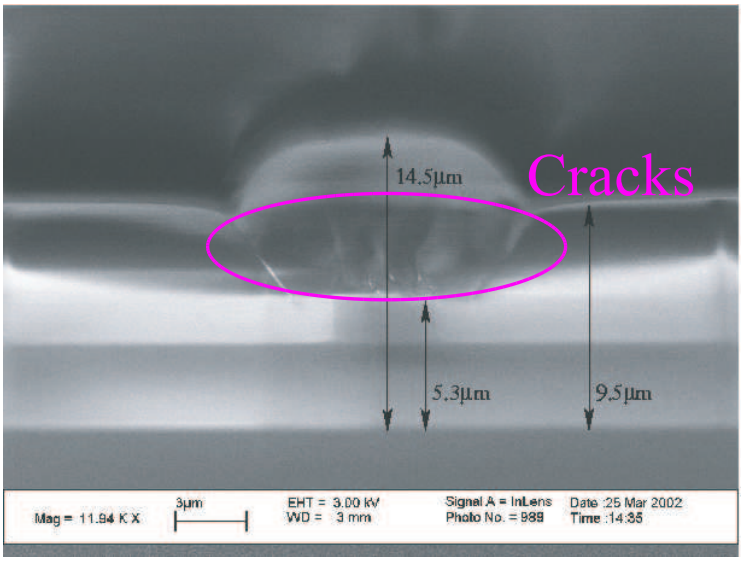

Figure 5.3: SEM picture of sample 3_5_1. Cracks are clearly visible.

[3]The sample fabrication and measurements where made by Carl-Johan Marckmann and the present author was only involved in the data intepretation process

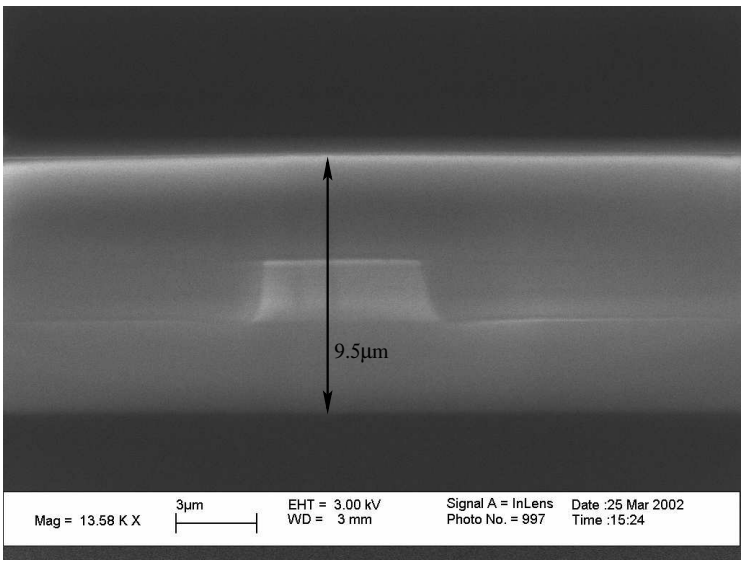

Figure 5.4: SEM picture of sample 17_1. Cracks are not observed. A $4\mu m$ waveguide was used for the measurements.

As the electric field used to measure λ_{Bragg} and hence the non-linearity is stronger than the breakdown field in air ($\approx 3V/\mu m$) [3], the airholes/cracks in sample 3_5_1 will act as short circuits. An applied voltage will therefore only drop over the part of the sample below the cracks, which means the electric field strength over the core is stronger than expected. The curvature of the parabola describing λ_{Bragg} as function of applied voltage will therefore be larger for the sample with cracks compared to the sample without cracks even though the core glasses are similar. The larger curvature of the parable due to cracks will naively be interpreted as a larger $\chi^{(3)}_{av}$ value, as $\chi^{(3)}_{av}$ is a measure for the curvature of the index parable (see table 5.1).

Moreover it is possible to pole the sample with cracks at room temperature, most likely because charges are accelerated through the cracks when voltage is applied (see fig. 5.5). A similar effect is not observed for sample 17_1 (see fig. 5.6) without cracks in the topcladding.

Thermal poling of sample 1 at 357°C for 20 minutes at -2.5kV yields a lin-

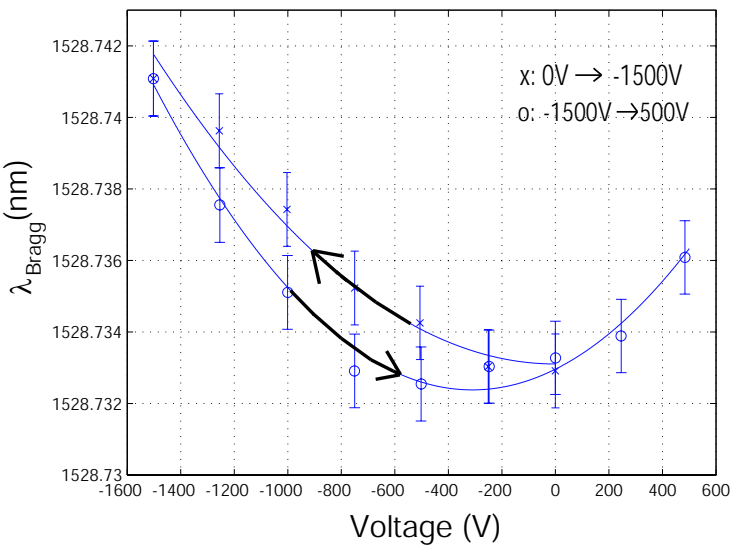

Figure 5.5: Sample 3_5_1, TE polarization, measured from 0 to -1.5kV and from -1.5 to 0.5kV. An internal field E_{int} of $21.4 \pm 3.3 V/\mu m$ is built into the glass during the first sweep. E_{int} is calculated assuming the effective electrode distance is $14.5 V/\mu m$, for other distances see table (5.1).

ear electro-optic coefficient $\left(\mathfrak{r} = 2\chi^{(2)}_{eff}/n^4\right)$ between 0.02 and $0.05 pm/V$ measured right after poling using the old MZI method. One day after poling, $\mathfrak{r}$ has decreased with between 60% and 80% of the initially induced value and one week after poling, $\mathfrak{r}$ was measured to zero within the measurement error.

The effective electrode distance is reduced because of the cracks. If this is not taken into account when $\chi^{(3)}_{av}$ is calculated from eq. (C.2), a very high nonlinearity is obtained. To show that cracks can explain the measurement for sample 3_5_1, $\chi^{(3)}_{av}$ is calculated assuming four different effective electrode distances (see table 5.1).
Three of the four distances are chosen according to distances marked on the SEM picture of the sample (see fig. 5.3). The last distance ($7.8\mu m$) illustrates how big the effective electrode distance is, if the material constant $\chi^{(3)}_{av}$ is exactly the same for sample 17_1 and for the sample in [4].

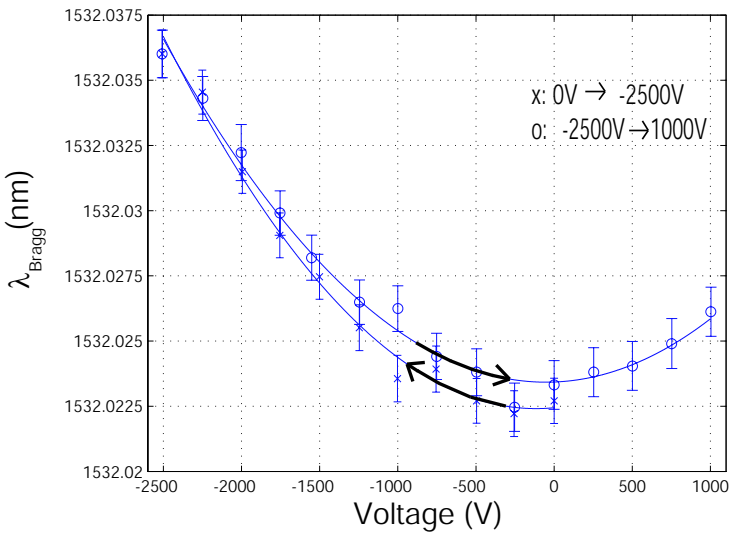

Figure 5.6: Sample 17_1, TE polarization, measured from 0 to -2.5kV and from -2.5 to 1.0kV. No internal field is built into the sample during the two sweeps.

The value of $\chi^{(3)}_{av}$ calculated for different effective electrode distances

	3_5_1 ($14.5\mu m$)	3_5_1 ($9.5\mu m$)	3_5_1 ($7.8\mu m$)	3_5_1 ($5.3\mu m$)	17_1
$\chi^{(3)}_{av}(10^{-22}\frac{m^2}{V^2})$	9.22 ± 0.28	3.96 ± 0.18	2.67 ± 0.08	1.23 ± 0.04	2.46 ± 0.16
$E_{frozen-in}(\frac{V}{\mu m})$	44.0 ± 1.7	67.2 ± 2.6	79.8 ± 3.1	120.4 ± 4.6	9.8 ± 3.9

Table 5.1: The measured values of $\chi^{(3)}_{av}$ and $E_{frozen-in}$ for sample 3_5_1 (assuming different effective electrode distances) and for sample 17_1.

The same recipe was used to make the core glass for these two samples and the $\chi^{(3)}_{av}$ values should therefore be similar.

The instability of the poling induced internal field can also be a result of the cracks, since charges trapped at the interfaces can escape through the cracks. The lifetime of the poling at 357°C might very well exceed the lifetime of the room temperature poling since the charges can be trapped temporarily at the ends of the cracks.

In [8] both a high nonlinearity and a short lifetime of E_{int} have been measured. Under the assumption of cracks all the way from the electrodes to the core in [8], the naive corrected $\mathfrak{r}$ value is reduced from 0.4 to $0.15pm/V$.

5.4.3 Conclusion for the apparently large non-linear effect.

Cracks in the investigated glass can explain many of the observed phenomenas for the samples with a high induced second-order non-linearity like the decay of the non-linearity and the possibility of room poling. The downside to this conclusion is that one should not expect manufacturing reproducibility of silica samples with a high second-order non-linearity. Moreover the very high $\chi^{(3)}_{av}$ value observed is only due to an effective shorter electrode-electrode distance, which is not usable in an actual device.

5.5 Changing $\chi^{(3)}_{av}$

5.5.1 Doping the core.

With the understanding from section (5.4.2) for the previously reported [1, 2] high effective second-order non-linearities, and with the need for reducing the switching voltage from $\sim 820V$ to below $100V$ (see discussion in section 5.3), the only possible solution is to increase $\chi^{(3)}_{av}$. This is only possibly by changing the waveguiding material or possible by changing the waveguiding method. In the PECVD chamber glass can be doped with several elements, like Germanium, Nitrogen, Boron and Prosporus.

Glass can be doped with Germanium and it raises the non-linearity of the glass [10]. Glass with a high Germanium content does however flow at room temperature as it reacts with water vapor from the air. I.e. even though $\chi^{(3)}_{av}$ can be increased by Germanium doping, $\chi^{(3)}_{av}$ is still limited to an uninterestingly low level. Glass doped with Boron and Phosphorus was used as topcladding for samples in previous work done within the group [5]. These samples did not show an increase in $\chi^{(3)}_{av}$.

5.5.2 Nitrogen doping.

The last possible dopant in the available PECVD chamber was nitrogen[4]. It was hence tried to change the material $\chi^{(3)}_{av}$ by producing samples with a core layer of Ge:SiON with different nitrogen doping levels[5]. The amount of nitrogen in the core can be increased by increasing the relative concentration of $NH_3(g)$ in the PECVD reaction (see reaction eq. 4.3). The flowrate of $NH_3(g)$ was varied from 0 sccm (standard cubic centimeters) to 250 sccm. Due to the complexity of the PECVD reaction, the nitrogen concentration in the deposited glass is *not* necessarily linear with the flow rate $NH_3(g)$. An indirect way of determining the nitrogen concentration in the deposited core glass is to measure the index of the deposited glass. The index is shown in fig. (5.7). As the index increases linearly with the $NH_3(g)$ flow, it is assumed that the incorporated nitrogen also increases linearly with $NH_3(g)$ flow.
The aim with the nitrogen doped samples was to investigate the change in $\chi^{(3)}_{av}$ and the samples where therefore made with a soft topcladding to avoid cracks like in fig. (5.3). Due to the soft top cladding, poling of the produced samples was not performed, as previous work in the group [5] had demonstrated that poling of samples with soft topcladding does not incorporate a significant electric field. The DC-shifted MZI method was used to measure $\chi^{(3)}_{av}$ for the 4 different samples and the result is shown in fig. (5.8). To make a fair comparison between the samples, the width of the waveguides was chosen different for the four samples to get the same confinement factor (~ 0.75) to the core material.
When the oxygen in SiO_2 is substituted with nitrogen, the glass will at some point make a spatial transition, as the ratio of silicon to oxygen is 1:2 in silica and the ratio of silicon to nitrogen is 3:4 in nitride glass (Si_3N_4). The spatial transition changes the local lattice around each silicon atom. The turn in the curve in fig. (5.8) could be caused by a transition which indicates that nitride glass could have a high $\chi^{(3)}$ value.

It is not easy to make a recipe for nitride glass and a RIE etching procedure, but luckily another group at COM investigated nitride glass.

[4]The nitrogen doped samples where made and characterized together with Carl-Johan Marckmann

[5]At the time where the samples were made, the Bragg grating method was still used for characterization. The samples therefore had to be UV-sensitive and they were hence co-doped with Germanium.

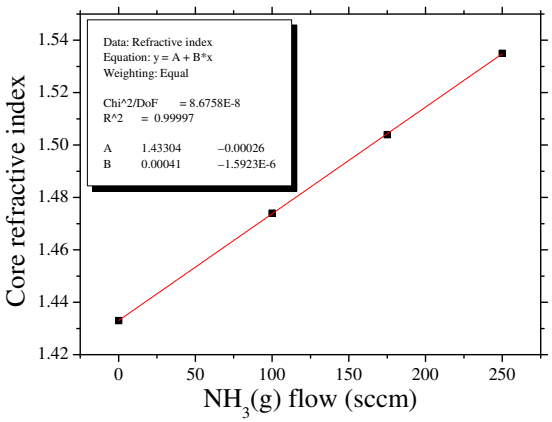

Figure 5.7: The refractive index of samples doped with nitrogen. As the refractive index is linear with the flow rate $NH_3(g)$, the nitrogen is properly also linear with the flow rate.

A silicon rich[6] nitride (SRN) sample was kindly provided by Karin Andersen [11] and $\chi^{(3)}_{av}$ was measured (see fig. 5.9 and table 5.2). The core size was $0.6 * 0.6\mu m$ as this core size made the waveguide single mode. The confinement factor to the core is 0.6 witch is a little lower than for the nitrogen samples.

The third-order non-linearity $\chi^{(3)}_{av}$ found in SRN is a factor of 9 larger than for silica. If the sample could be poled to reach a frozen-in field of $200V/\mu m$, the switching voltage for a dual electrode (see eq. 5.1) MZI would be $188V$, where the bulk index of 2.06 has been used for the SRN material. The high index step between the core and the cladding gives a very small mode size and hence could the electrode-electrode distance probably be reduced to $5\mu m$ without a significant increase in the optical loss. This would reduce the switching voltage to $78V$. However, this

[6]Silicon rich nitride is nitride glass with more silicon than the 3:4 ratio for pure nitride (Si_3N_4). A comprehensive description of SRN glass fabrication and investigation can be found in [11].

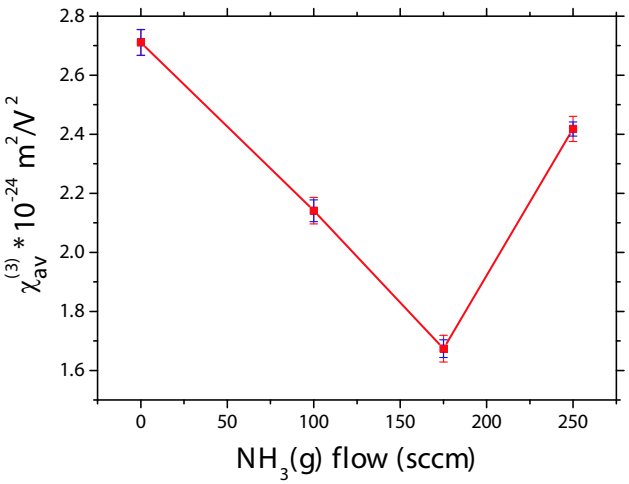

Figure 5.8: Measured $\chi^{(3)}_{av}$ values for samples with different nitrogen contains in the core glass measured for TE polarized light. The blue error bars marks the relative uncertainties, while the red error bars marks the total uncertainty including systematic errors. Uncertainties are discussed in appendix B. The confinement factor to the core was for all the samples was around 0.75.

$\chi^{(3)}_{av}$ **for SRN.**		
Measurement	$\chi^{(3)}$ $10^{-22}m^2/V^2$	$E_{frozen-in}$ $V/\mu m$
TE	10.62 ± 0.48	4.92 ± 0.28
TM	17.37 ± 0.78	-3.83 ± 0.46

Table 5.2: The $\chi^{(3)}_{av}$ values measured with the DC-shifted MZI setup for a silicon rich nitride (SRN) sample made by Karin Andersen [11]. The confinement factor to the core was ~ 0.6. The uncertainties includes all contributions (see appendix B).

switching voltage was judged to high to be of interest, and *no* poling attempts were therefore made on SRN waveguides.

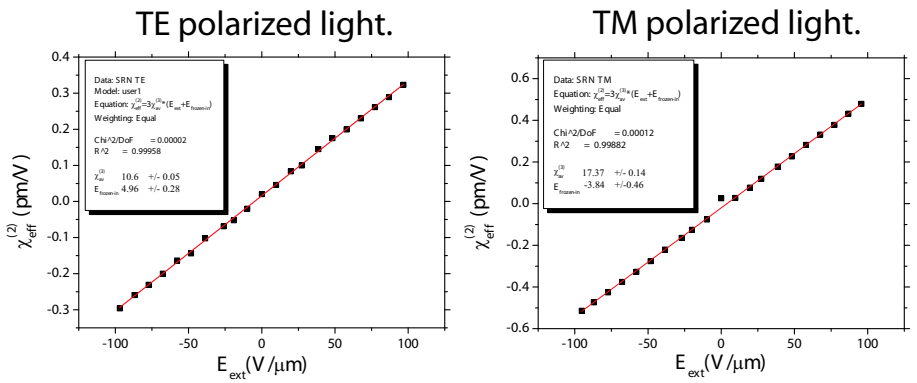

Figure 5.9: Measurement of the second-order non-linearity $\chi^{(2)}_{eff}$ vs. external applied field (E_{ext}) for silicon rich nitride (SRN) samples. The confinement factor to the core was $\sim$ 0.6. The non-linearity was measured using the DC-shifted MZI method. The samples were fabricate by Karin Andersen. The uncertainty is only the root mean square obtained by the fitting procedure.

5.5.3 Direct UV-writing.

After having investigated nitrogen doping, attention was paid to direct UV-writing. As described in chapter (4), the horizontal index step can be made by direct UV-writing of the waveguide. During the UV-writing, the sample is exposed to a focus laser beam with a FWHM of 2.5μm. The conditions during exposure is rather extreme in the sense of local temperature and this does introduce a permanent index increase in the material. The exposure could possibly also change the material $\chi^{(3)}$ value and measurements where made on a sample containing a charge trapping layer (see section 5.3). There was, however, *not* measured any difference in the obtained $\chi^{(3)}$ value.

5.5.4 Ion Implantation.

After having tried to dope the core with nitrogen there were no other easy dopants available. One method for trying other dopands is ion implantation, where the core glass should be bombarded with the ion in investigation. The challenges with this approach were twofold. Ion implantation is too expensive for mass production and if an interesting ion

was found, other ways for incorporating the ion into the glass should have been found. The other challenge was the lack of ion implantation equipment at DTU perimeters and in the end the idea was *not* pursued due to the lack of equipment.

5.6 Changing the waveguiding method.

5.6.1 The concept.

To increase the material non-linearity without changing material might seem like a contradiction in terms, but an attempt was never the less made. All the samples investigated so far were based on the principle of total internal reflection, where light is guided in a high index core surrounded by a lower index cladding. This is not the only way to guide light. There are two other methods known to the author. The first possibility is to guide light as a surface wave at the interface between a metal and a dielectrica (see section 5.6.2). The second possibility is to guide light by surrounding a waveguide with a micro-structured cladding in which the structure forbids propagation of certain wavelength intervals. This kind of guidance is known as photonic bandgap guidance and such samples are investigated in chapter (6).

5.6.2 Long-Range Surface Plasmon Polaritons.

Light can be guided as a surface wave in the boundary between a metal an a dielectric. When a thin metal strip is placed inside a dielectrica, light can be guided as two coupled surface modes with a reasonable low optical loss $\sim 2dB/cm$ [12]. Fig. (5.10) shows the mode guided by a thin metal strip.
There are two differences between light guided by normal index difference and light guided by a metal strip. The mode profile of light guided by a metal strip is exponential all the way into the metal [12], while light guided in a conventional waveguide to a good approximation is Gaussian in the core region. The other difference is the light propagating in the metal. Due to these two differences, a Long-Range surface plasmon polariton (LRSPP) waveguide was kindly provided by MMP A/S for investigation of the third-order non-linearity $\chi^{(3)}_{av}$. The DC-shifted MZI

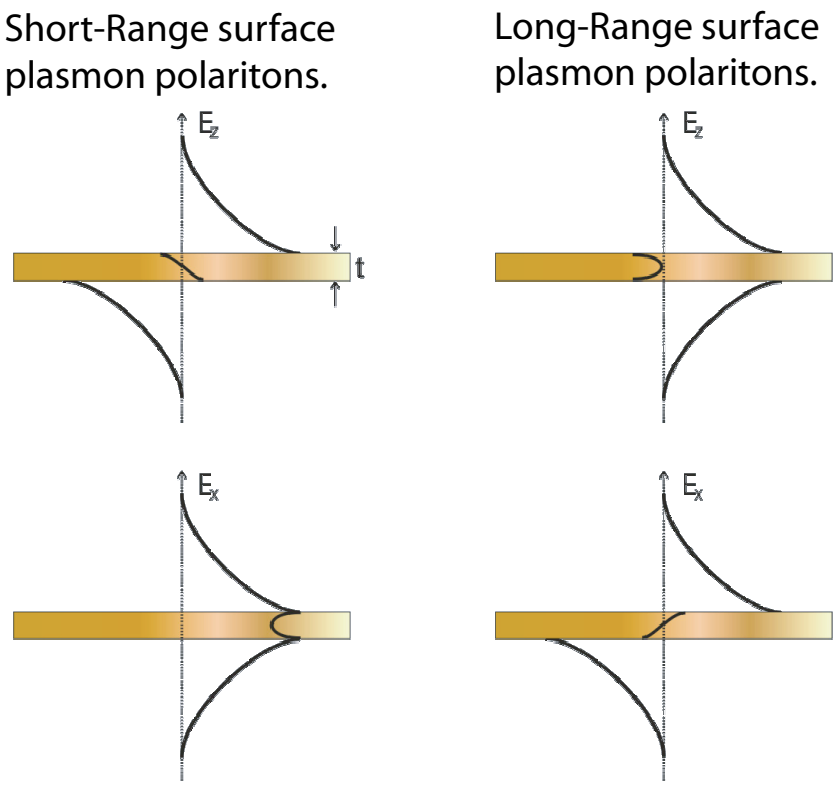

Figure 5.10: Light can be guided as Short-Range (SRSPP) or Long-Range Surface Plasmon Polaritons (LRSPP) in the interface between a metal and a dielectric. The SRSPP has high intensity inside the metal and will hence be attenuated by the large absorption in the metal. For LRSPP the intensity of light inside the metal is almost zero, and the attenuation is acceptable. The figure is made by Alexandra Boltasseva.

measurement results are shown in fig. (5.11) and the results are listed in table (5.3).

Even though the determined $\chi^{(3)}$ value is large $(60.6 \pm 2.7) * 10^{-22} m^2/V^2$, it is not surprisingly large as the cladding material used by MMP is a polymer and polymers are known to exhibit large $\chi^{(3)}$ values. I.e. the increased effect is properly due to a change in material *not* to a change in waveguiding method. As poling of polymers is not as straightforward as glass poling due to the lower breakdown field in polymers, the ap-

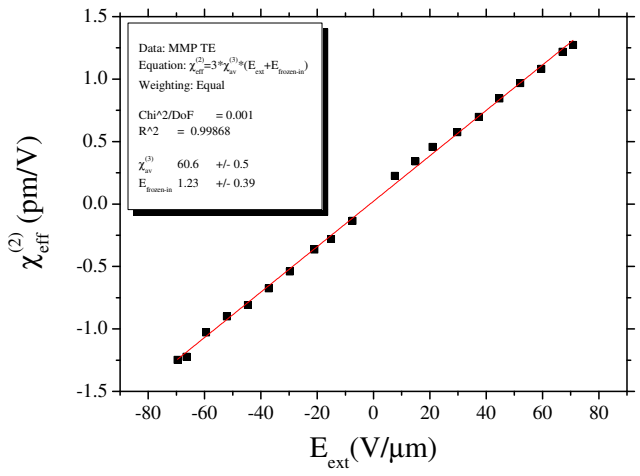

Figure 5.11: Measurement of the second-order non-linearity $\chi_{eff}^{(2)}$ vs. external applied field (E_{ext}) for a Long-Range Surface Plasmon Polariton guided by a thin ($10nm$) gold strip. The sample was kindly provided by the company MMP A/S. The uncertainty is only the root mean square (RMS) obtained by the fitting procedure.

$\chi_{av}^{(3)}$ for LRSPP.

Measurement	$\chi^{(3)}$ $10^{-22}m^2/V^2$	$E_{frozen-in}$ $V/\mu m$
TE	60.6 ± 2.7	1.23 ± 0.39

Table 5.3: The $\chi_{av}^{(3)}$ values measured with the DC-shifted MZI setup for a Long-Range Surface Plasmon Polariton guided by a thin ($10nm$) gold strip. The sample was kindly provided by the company MMP A/S. The uncertainties includes all contributions (see appendix B).

proach with LRSPP was discarded. An influencing factor for stopping the LRSPP investigation was the guided mode size. The mode size of the Long-Range Surface Plasmon Polariton is equivalent to the mode in a standard fiber, and the electrode-electrode distance must therefore be large ($\sim 15\mu m$) to avoid a significant propagation loss. The increase in

$\chi^{(3)}$ value should therefore be weighted against the increase in sample thickness.

5.7 Conclusion.

In this chapter all results concerning third-order non-linearities have been presented. The discussion of the obtained results demonstrated that: *The third-order non-linearity of silica is a factor of 10 too small to be of any interest for making a poling based MZI switch on a 4 inch wafer.* The interest in poling originated from very large $\chi^{(2)}_{eff}$ values being reported in the nineties [1,2]. A possible explanation for the large results reported has been proposed (see section 5.5.2 about cracks) and hence there are no mysteries left in poling of silica that can justify further research with the goal of making an electro-optic integrated switch in silica.

A method for realizing a poling based MZI switch in silica is to apply a poled fiber [13] where the electrode length can be significantly longer. The switching voltage is still high ($\sim 220V$) [14].

Higher $\chi^{(3)}_{av}$ values can be obtained by changing the core glass and it has been shown that a switching voltage of $\sim 80V$ is within reach presuming that silicon rich nitride and silica behave similarly during poling. *Even the obtained increase in $\chi^{(3)}_{av}$ by a factor of 5 was judged to be insufficient for realizing an interesting switch on a 4 inch wafer.*

References to Chapter 5

[1] R. Myers, N. Mukherjee, and S. Brueck. "Large second-order nonlinearity in poled fused silica", *Optics Letters*, vol. 16, no. 22, pp. 1732–4, 1991.

[2] T. Fujiwara, D. Wong, Y. Zhao, S. Fleming, S. Poole, and M. Sceats. "Electro-optic modulation in germanosilicate fibre with uv-excited poling", *Electronics Letters*, vol. 31, no. 7, pp. 573–575, 1995.

[3] D. K. Cheng. *Fundamentals of engineering electromagnetics.* Addison-Wesley, 1992. ISBN 0201566117.

[4] C. Marckmann, Y. Ren, G. Genty, and M. Kristensen. "Strength and symmetry of the third-order nonlinearity during poling of glass

waveguides", *IEEE Photon. Technol. Lett.*, vol. 14, no. 9, pp. 1294–1296, 2002.

[5] C. J. Marckmann. *Switchable Bragg gratings.* Ph.D. thesis, Research Center COM, Technical University of Denmark, Kgs. Lyngby, Denmark, 2003.

[6] Y. Ren, C. Marckmann, R. Jacobsen, and M. Kristensen. "Poling effect of a charge-trapping layer in glass waveguides", *Applied Physics B*, vol. 78, no. 3-4, pp. 371–375, 2004.

[7] A. C. Liu, M. J. Digonnet, and G. S. Kino. "Measurement of the dc kerr and electrostrictive phase modulation in silica", *Journal of the Optical Society of America B: Optical Physics*, vol. 18, no. 2, pp. 187–194, 2001.

[8] M. Janos, W. Xu, D. Wong, H. Inglis, , and S. Fleming. "Growth and decay of the electrooptic effect in thermally poled b/ge codoped fiber", *Jour. of Lightwave Tech.*, vol. 17, no. 6, pp. 1037–1041, 1999.

[9] C. Marckmann, R. Shim, Y. Ren, and M. Kristensen. "Interpretation of high poling effects with short lifetimes", *11th European Conference on Integrated Optics. Proceedings*, pp. 301–4 vol.1, 2003.

[10] K. Kim, R. Stolen, W. Reed, and K. Quoi. "Measuremnt of the nonlinear index of silica-core and dispersion-shifted fibers", *Optics Letters*, vol. 19, no. 4, pp. 257–259, 1994.

[11] K. Andersen. *Optical components based on high index materials.* Ph.D. thesis, Research Center COM, Technical University of Denmark, Kgs. Lyngby, Denmark, 2005.

[12] A. Boltasseva. *Integrated-Optics Components Utilizing Long-Range Surface Plasmon Polaritons.* Ph.D. thesis, Research Center COM, Technical University of Denmark, Kgs. Lyngby, Denmark, 2004.

[13] N. Myrén. *Poled fiber devices.* Ph.D. thesis, Department of Physics and Quantum Optics, Royal institute of technolegy, Roslagstullsbacken 21, SE-106 91 Stockholm, Sweden., 2005. ISBN 91-7178-053-x.

[14] "www.glamorous-eu.com/counter/download.asp?file=/download/final.pdf". The final report from the glamorous project.

Chapter 6

The photonic crystal samples.

6.1 Introduction.

The last waveguiding principle investigated[1] during this Ph.D. project was 2D photonic bandgap guidance [1]. The basic concept of bandgap guidance is to make a micro-structured material in which light in certain wavelength intervals cannot propagate. This is obtained by etching small holes in a periodic manor in a high index material like silicon. By designing the structure properly, the periodic changes in the refractive index between the silicon and the holes will prohibit propagation of the desired wavelength interval (an example of such structure is shown in fig. 6.1). To guide light in such a structure, a defect in the periodic structure is introduced by removing a line of holes (see fig. 6.1). The resulting solid silicon line then acts as a waveguide, as light incident into the line defect cannot propagate into the surrounding structure and hence is guided. The theoretical transmission diagram for a photonic bandgab structure is shown in fig. (6.2).

It is known from the literature [2], that the effect of a material nonlinearity should be enhanced linearly with the group index (see eq. 2.11) and very high group indexes have been reported [3] for light guided in

[1] The author does not know of any other waveguiding methods, that has been realized for integrated devices.

a photonic crystal (PhC) waveguide[2]. The investigation of PhC samples started with the hope of enhancing the effect of a material third-order non-linearity in the glass surrounding the 2D PhC structure (see fig. 6.4).

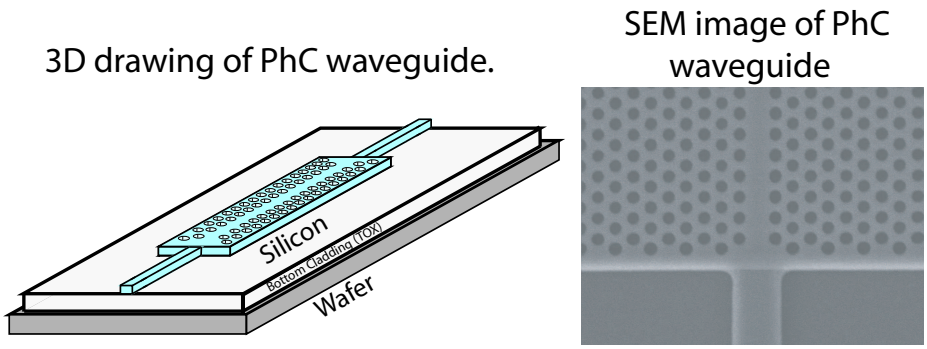

Figure 6.1: The left figure is of drawing of a PhC silicon structure supported by a silica layer. The light is guided to the PhC part by a ridge waveguide. The figure is *not* to scale. The right SEM image is of an etched structure in silicon.

6.2 Expected a $\chi^{(3)}$ and found a $\chi^{(2)}$.

6.2.1 Preparing sample for $\chi^{(3)}$ investigation.

The PhC waveguide samples were kindly supplied by Lars Frandsen and coworkers. The PhC waveguides were all designed for TE polarized light and hence only TE polarized light was investigated. All experimental and theoretical plots are made for TE polarized light. In the experiments the polarization was changed until a clear bandgap was observed. The first sample $r2c5$ had its original cut-off at 1610nm (see transmission spectrum in fig. 6.3). To move the cut-off down in wavelength, the sample was oxidized by backing it at 1050°C in a dry oxygen atmosphere. The cut-off was moved down to 1528nm after oxidation. A $\sim 2\mu m$ hard SiO_2

[2] Micro-structured materials are in general called photonic crystals, and photonic bandgap structures is a subset of PhC's.

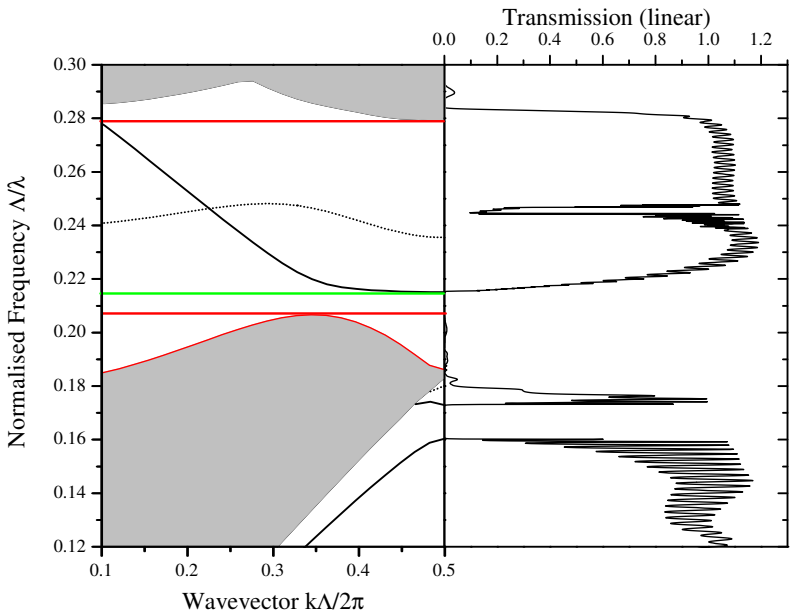

Figure 6.2: The left graph shows the bandgab diagram for the studied photonic crystal (PhC) waveguide determined by calculations using the software package MBP [4]. The gray areas represents a continuum of cladding modes and the two red lines indicate the bandgab, where no modes are allowed in the cladding. The two black lines are dispersion curves for the photonic bandgab modes guided in the silicon defect line. The green line shows the cut-off for transmission through the PhC waveguide. The MPB calculation results where kindly provided by Lars Frandsen. The right graph shows the transmission through the PhC waveguide determined by 2D finite-difference-time-domain (FDTD) calculations. The transmission is high in the bandgab region where the mode is present. The 2D FDTD calculations results where kindly provided by Andrei Lavrinenko.

topcladding was then deposited in the PECVD to confine the guided light inside the sample. After the glass was deposited, the cut-off had moved up to 1545nm (see fig. 6.3).
An electrode was painted on top of the sample, and the non-linearity was measured using the DC-shifted MZI setup. It was expected that the sample would have a $\chi^{(3)}$ value due to the tail of the mode propagating

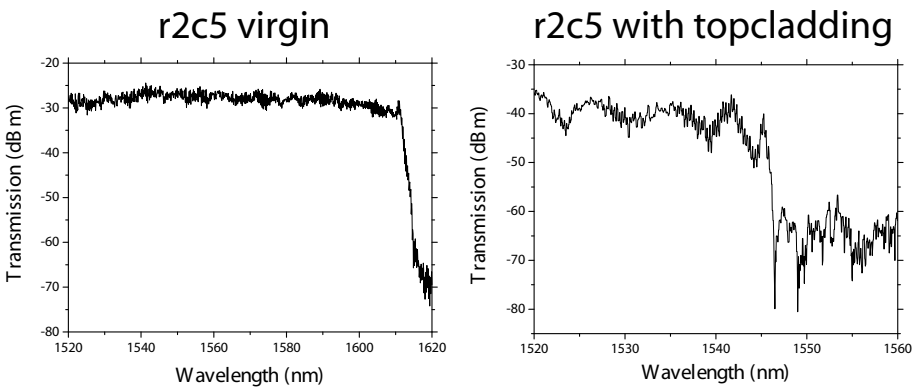

Figure 6.3: Transmission spectrum for the virgin sample r2c5 and for the sample after oxidation and after PECVD deposition of the topcladding. The measurement were made for a $20\mu m$ long PhC waveguide. The cut-off was 1610nm for the virgin sample and 1545nm after oxidation and growth of topcladding.

in the glass cladding surrounding the silicon layer (see fig. 6.4).

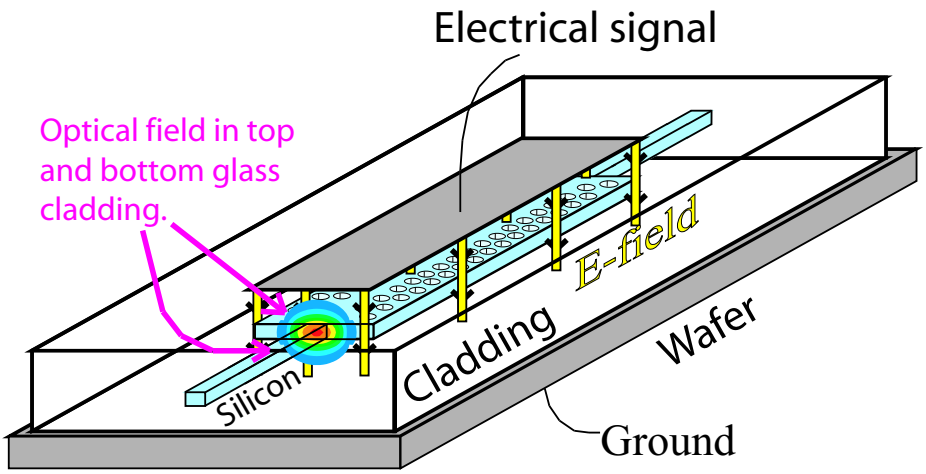

Figure 6.4: The drawing illustrates the PhC sample after it has been processed to measure $\chi^{(3)}$ by oxidation followed by growth of hard PECVD topcladding. There is applied an electrode on top of the PhC waveguide. In reality the electrode does also cover part of the buried waveguide. The original idea with the measurement was to measure the $\chi^{(3)}$ non-linearity due to light in the top and bottom glass claddings. When measurements where made, it was a surprise to observe, that the contribution from $\chi^{(3)}$ was not detectable compared to a discovered pure $\chi^{(2)}$ non-linearity.

6.2.2 Puzzling observations.

When measuring the non-linearity with the DC-shifted MZI method several observations where puzzling. The observations are listed below. The original experiments where made at an AC-frequency of 33.333kHz and with the top electrode covering both the PhC waveguide and also a couple of millimeters of the buried waveguides leading light to and from the PhC waveguide.

- A significant $\chi^{(2)}$ value was found but *no* detectable $\chi^{(3)}$ value was observed.
- The electrical phases θ_1 and θ_3 were wavelength dependent (see section 3.5 for a description of the phases θ_1 and θ_3).
- The measured $\chi^{(2)}$ value depended on the applied AC-voltage.
- The electrical phases θ_1 and θ_3 depended on applied AC-voltage.
- $\chi^{(2)}$ oscillated strongly with the wavelength.

It was determined that the measured $\chi^{(2)}$ was *not* due to $\chi^{(3)}$ combined with a frozen-in electric field ($E_{frozen-in}$) by measuring $\chi^{(2)}$ vs. applied external field (E_{ext}). The measured $\chi^{(2)}$ value was independent of the applied DC-field, as shown in fig. (6.5).

When changing wavelength, the electrical phases θ_1 and θ_3 had to be changed. These phases should only depend on the electrical equipment and they should be totally independent of the optical signal, i.e. both of optical power and optical wavelength. This was not the case for the first measurements at 33.333kHz as shown in fig. (6.5). This could indicate that the measured $\chi^{(2)}$ effect consisted of multiple contributions, and that the weight between the contributions varies with wavelength.
The measured $\chi^{(2)}$ value did *not* depend on the applied DC-field (see fig. 6.1), but it depended on the applied AC-field (see fig. 6.6). I.e. the phase change induced was *not* linear with the applied AC-field. The electrical angles θ_1 and θ_3 also depended on the applied field, as shown in fig. (6.6).

The last unexpected observation, was large oscillations in the measured $\chi^{(2)}$ value vs. wavelength. A monotone variation was expected, when the wavelength was tuned towards the cut-off frequency due to an increase

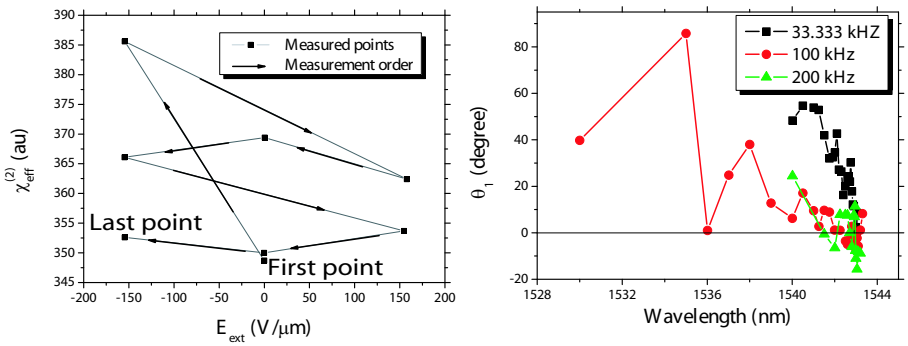

Figure 6.5: The left graph shows the measured $\chi^{(2)}$ value for different external applied fields. There is *not* observed any change in $\chi^{(2)}$ beyond measurement uncertainty when a DC-field is applied. This corresponds to a pure $\chi^{(2)}$ effect, *not* a $\chi^{(3)}$ effect. The right graph shows the change in the angle θ_1 vs. the wavelength of the incident light. The angle should *not* change but for the original 33.333kHz measurement θ_1 showed a significant wavelength dependence. Later the frequency was changed first to $100kHz$ and then to $200kHz$. There could still be a wavelength dependence for θ_1 at 100 kHz, but for $200kHz$ the dependence is *not* observed.

in the group velocity, but not the oscillating behavior shown in fig. (6.7).

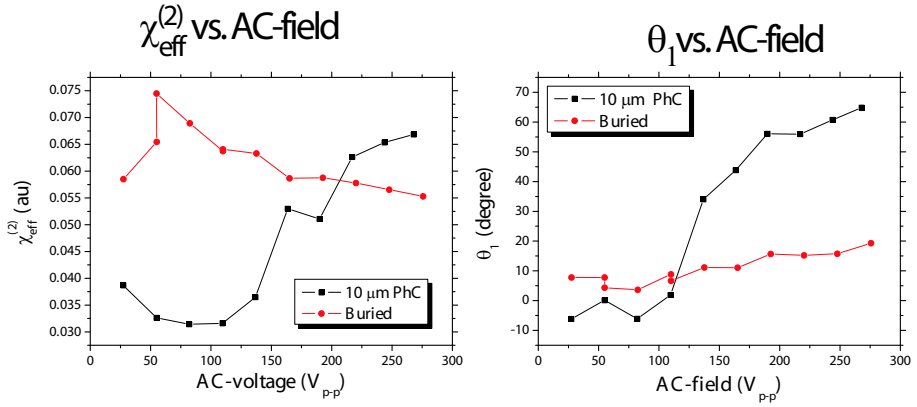

Figure 6.6: The left graph shows the measured $\chi^{(2)}$ vs. strength of the 33.333kHz AC-field. The measured effect should be constant, like the measured effect for the buried waveguide. For the PhC waveguide $\chi^{(2)}$ was however observed to depend on the AC-field. The right graph shows the electrical angle θ_1 vs. AC-field. θ_1 can depend on the AC-field due to phase delay from the AC-amplifier, *but* θ_1 should behave identical for a buried waveguide and for a waveguide with a PhC segment, which is clearly *not* observed here.

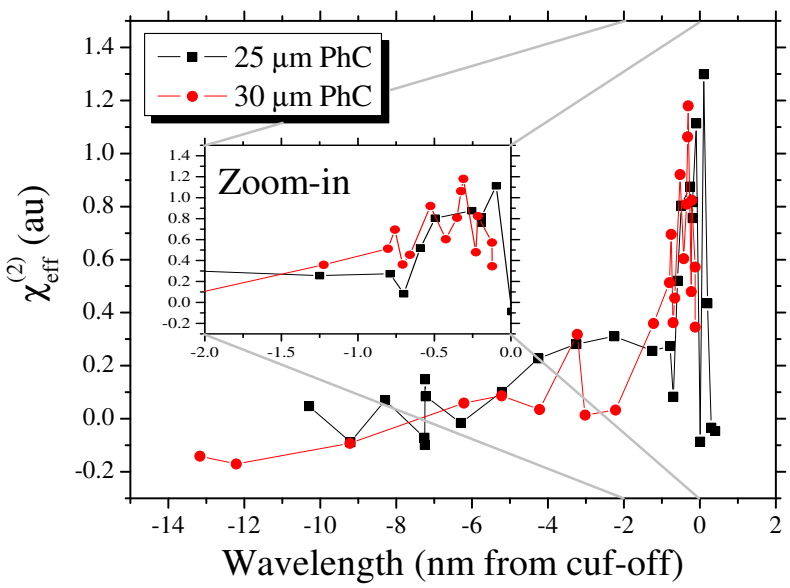

Figure 6.7: The measured $\chi^{(2)}$ value for $25\mu m$ and for $30\mu m$ PhC waveguide. The oscillations are much larger than what is explainable by the noise of $\sim 4\%$ (see appendix C).

6.2.3 Clearing out in the puzzling observations.

To explain the observed behavior, the difference between the sample with the PhC waveguide and the normal glass samples presented in chapter (5) with a $\chi^{(3)}$ non-linearity was investigated. One obvious difference was the semiconductor layer in which the PhC structure is etched. The normal glass samples consisted of electric isolating layers and hence there was no electron movement possible inside the sample. In contrast, it is possible to move charges in the horizontal direction inside the silicon layer (see fig. 6.8). It was determined[3] that the cut-off frequency for moving electrons in the silicon layer was $\sim 100kHz$.

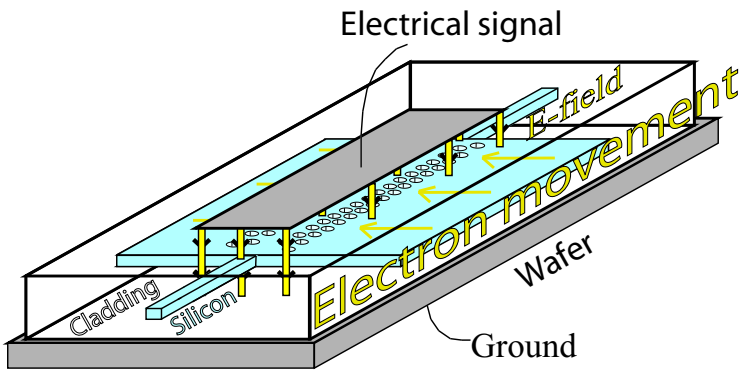

Figure 6.8: Drawing of a PhC waveguide, where electrons are being moved from the surrounding silica to a position underneath the electrode ($E_{ext} > 0$). Movement in the horizontal direction is caused by top electrode shape, that only covers part of the silicon structure. Due to resistance in the silicon, this electron movement will cut-off for frequencies faster than 100 kHz [5].

It was confirmed experimentally, that changing the AC-frequency to $200kHz$ removed some of the weird behaviors observed at first. It was also discovered that the buried waveguide contributed significantly to the first $\chi^{(2)}$ measurements performed. The only weird behaviors left when measuring at $200kHz$ with a short electrode (see fig. 6.9) was

- The significant $\chi^{(2)}$ value found.

[3] Ole Hansen at MIC (DTU) made a theoretical investigation on the movement of charges inside the silicon layer and determined that the cut-off frequency was $\sim 100kHz$.

- $\chi^{(2)}$ oscillates strongly with the wavelength.

After having increased the frequency to $200kHz$, refined measurements where made on sample $r2c5$. The result is shown in fig. (6.9). It was expected that the $\chi^{(2)}_{core}$ value[4] should be enhanced with the group index, but the group index was expected to increase in a monotonous manner when the wavelength approached the cut-off frequency. To determine the group index, a method based on the time of flight (ToF) principle was developed as described in section (6.3).

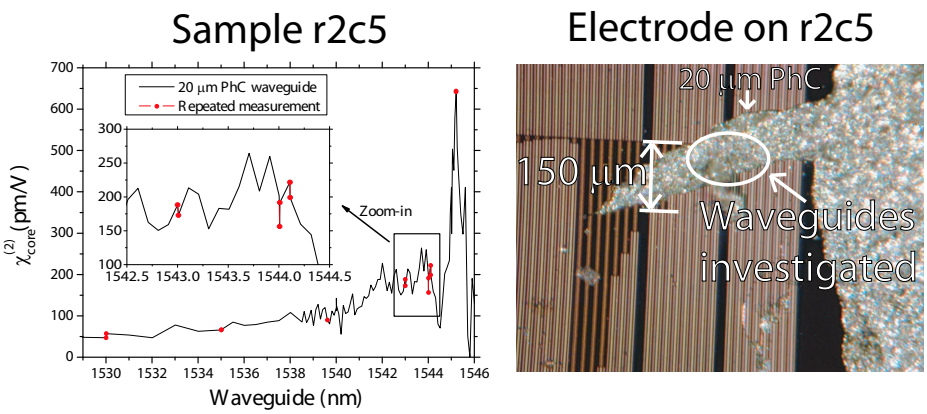

Figure 6.9: The left graph shows the measured $\chi^{(2)}_{core}$ value for a $20\mu m$ PhC waveguide at $200kHz$. The oscillations are much larger than explainable by the noise of $\sim 4\%$ (see appendix C). The right image shows the top electrode used for the measurements. The width of the hand painted electrode is around $150\mu m$ for the investigated $20\mu m$ waveguide.

[4]To determine the $\chi^{(2)}_{core}$ value from the measured $\chi^{(2)}_{eff}$ value, the confinement factor to the silicon was determined by calculation. The results can be found in appendix E.

6.3 Group index measurements.

6.3.1 Group index and enhancement of the non-linear effect.

The group index ($n_{g,eff}$) of light guided in photonic crystal (PhC) waveguides can reach much higher values [6] than observed in ordinary index guiding waveguides. Values up to $n_{g,eff} = 1000$ have been reported [3]. The effect of a material non-linearity is enhanced linearly with the high group index according to eq. (2.11). This has been derived theoretically [2], but until now experimental results have shown an enhancement effect [7] but the simple linear correlation have *not* been demonstrated. To show that the change in non-linearity measured for the PhC waveguides investigated is due to a change in the group index, a method for measuring $\Delta n_{g,eff}(\lambda)$ for the PhC waveguides is developed.

Experimental method.

The basic concept of measuring $\Delta n_{g,eff}(\lambda)$ using the time of flight (ToF) principle, is to measure the phase delay of a transmitted signal vs. wavelength. The transmitted signal is an envelope function for the amplitude of the light and the phase velocity of the signal is hence identical to the group index of the light. In the experiments, amplitude modulated light is sent through the PhC waveguide and the phase of the transmitted signal is recorded vs. wavelength. The phase of the modulation function is then used to calculate the group index of the light.

6.3.2 Experimental setup.

The phase of the envelope function is measured using a network analyzer, that both modulates the light and detects it after the PhC waveguide. This is sketched in fig. (6.10).
To measure $\Delta n_{g,eff}(\lambda)$ for a PhC waveguide, cw light with intensity (I) emitted from a laser is amplitude modulated by a $LiNbO_3$ MZI based modulator. The modulator changes the output amplitude due to an electrical sinus signal ($V_{amp}\sin(\omega t)$) with amplitude (V_{amp}) generated by the network analyzer. The intensity oscillation (I_{osc}) after the modulator is

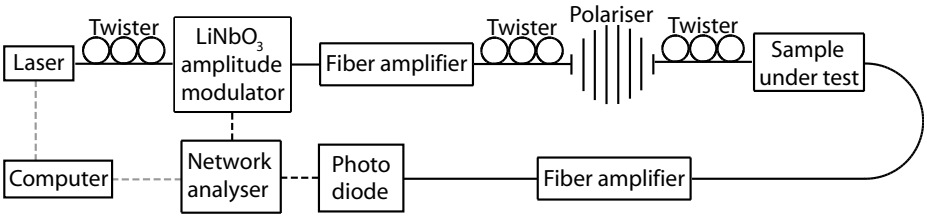

Figure 6.10: Continuous waves (cw) laser light is small signal modulated and then transmitted through the PhC waveguide. The phase of the modulation is measured by the network analyzer after detection at the photo diode. The computer controls the laser wavelength and records the phase detected by the network analyzer.

(see eq. 3.14).

$$I_{osc} = I \sin\left(c_{LiNbO3} V_{amp} \sin(\omega t)\right), \tag{6.1}$$

where c_{LiNbO3} is the linear factor between the voltage applied to the $LiNbO_3$ modulator and the phase change for the light. The equation is greatly simplified when compared to the output of a fiber based modulator (see eq. 3.14), as the difference in optical path length between the two arms in the MZI always[5] is $\lambda/2$. The modulation of the light affects the lights spectrum, as power is transferred to sidebands as illustrated in fig. (6.11). The sidebands are only detectable in the spectrum, when the amplitude of the modulation is large. The signal is always carried in the sidebands, and the spectral width of the probe pulse is therefore approximately $0.4nm$ also for the small amplitude modulations used in the actual experiment.
The amplitude V_{amp} of the applied electrical signal is small, and the intensity oscillation (eq. 6.1) therefore simplifies to

$$I_{osc} = I c_{LiNbO3} V_{amp} \sin(\omega t). \tag{6.2}$$

The oscillating wave is transmitted through the sample and detected by the photo detector. The phase of the received signal is then measured by the network analyzer. The obtained phase for TE polarized light sent through a $20\mu m$ symmetric W1 PhC waveguide[6] is shown in fig. (6.12).

[5] It is due to the integration of the interferometer on a chip, that it is possible to have a constant phase difference between the two arms.

[6] A symmetric W1 PhC waveguide is a photonic crystal, where the waveguide is made by removing a single row of holes. The SEM picture in fig. (6.1) is of a symmetric W1

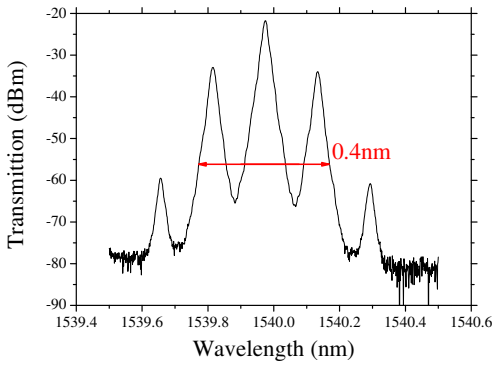

Figure 6.11: The spectrum of the laser modulated by large 20GHz amplitude oscillations. The modulation gives sidebands at $\lambda \pm 20GHz$ and the spectral width is therefore $0.4nm$. The sidebands are much smaller (actually not detectable using an optical spectrum analyzer) for the small amplitude modulation applied in the experiments. The position of the sidebands is independent of the modulation amplitude and the probes spectral width is therefore $0.4nm$.

6.3.3 Polarization control.

To ensure the right polarization of the light in the PhC waveguide, another laser is used to transmit light into the twister before the polarizer and the signal after the sample is detected by an optical spectrum analyzer (see fig. 6.13).
The twister just before the sample is adjusted until the desired polarization is obtained, while the twister in front of the polarizer is adjusted to get maximum transmission. It is ensured that the desired polarization is obtained by investigating the transmission spectrum, as the spectral transmission features of PhC waveguides are very different for TE and TM polarized light. When the setup with the network analyzer is reconnected like fig. (6.10), the polarization of the light reaching the sample is not changed because of the polarizer. The twister in front of the polarizer

waveguide.

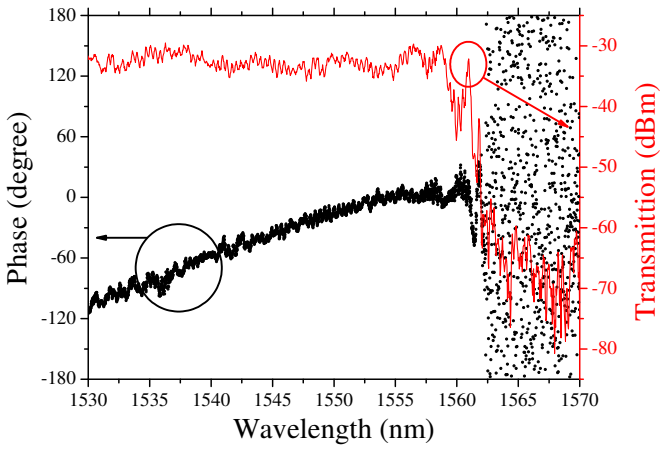

Figure 6.12: Measured points for phase vs. λ for a $20\mu m$ symmetric W1 PhC waveguide for TE polarized light.

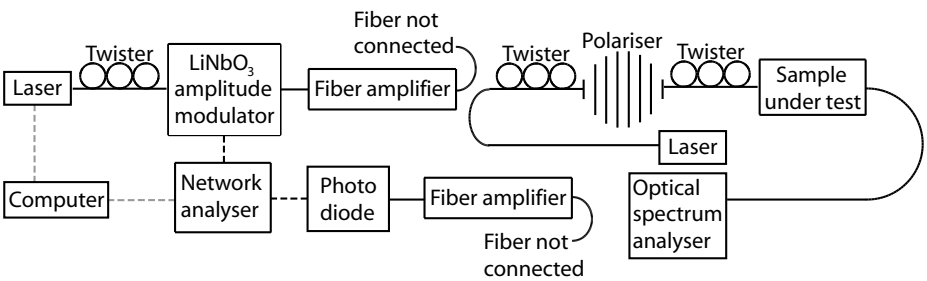

Figure 6.13: The desired polarization is obtained by measuring the transmission spectrum through the sample. After the desired polarization is obtained by adjusting the twister in front of the sample, the setup in fig. (6.10) is reconnected.

is again adjusted for maximal transmission.

6.3.4 Calculating the group index.

To obtain the group index from the measured phase, the points in fig. (6.12) must first be adjusted, as the result of a phase measurement is a number between $-180°$ and $180°$, i.e. the phase is measured modulos $360°$. As the phase is a continuous function, the recorded discontinuous of $360°$ are removed, as demonstrated in fig. (6.14).

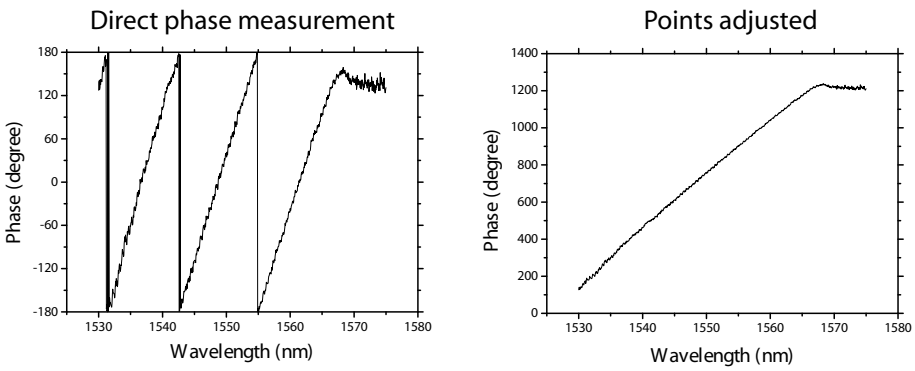

Figure 6.14: The left graph shows measured points for phase vs. λ for a buried waveguide. The large dispersion of the phase is due to the applied fiber amplifiers. The measurement is adjusted by adding $360°k$ to the points, where k is an integer. The integer is chosen such that the resulting line has no discontinuities. The result of the adjustment is shown in the right graph.

To find the phase change due to the PhC waveguide, a similar phase measurement like the one shown in fig. (6.12) is made on another waveguide on the sample. This new waveguide is similar to the waveguide containing the $20\mu m$ PhC, except that it does *not* contain a PhC part. The measured points are adjusted according to fig. (6.14) and then fitted with a 3-order polynomial as shown in fig. (6.15).
The polynomial from fig. (6.15) describing the phase change in the buried waveguide is subtracted from the phase points measured for the $20\mu m$ symmetric W1 PhC waveguide. The result is the phase change originating from the difference between the waveguide with the PhC part and the waveguide without a PhC part. This phase is plotted in fig. (6.16).

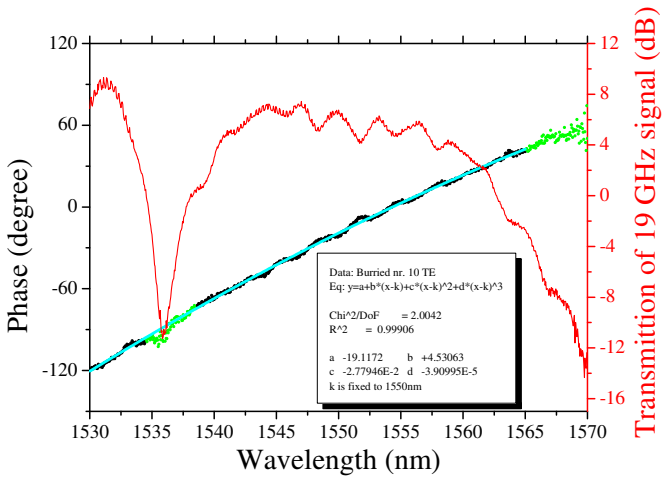

Figure 6.15: The phase measured for a buried waveguide. The points are fitted with a 3-order polynomial (the cyan line) and this fitted curve is used to calibrate the points measured for the 20μm PhC waveguide. The transmission spectrum (red curve) is for the 19GHz envelop function signal. The green points are *not* used when determining the polynomial, due to the low transmission of the 19 GHz signal. The transmission spectrum of the 19 GHz function is due to the carracteristics of the applied fiber amplifiers.

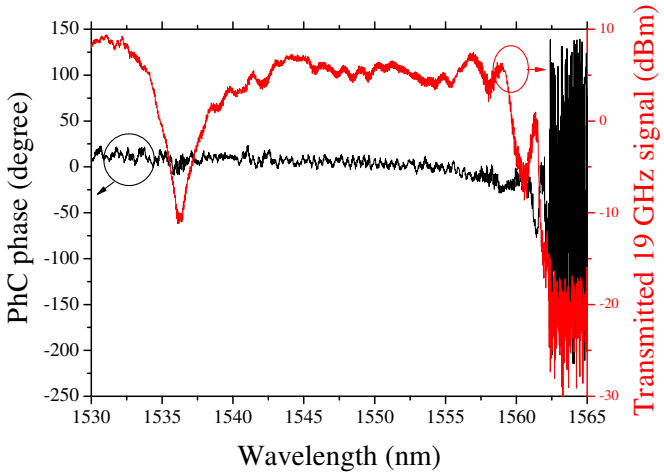

Figure 6.16: The phase change corrected for 360° discontinuities (see fig. 6.14) and calibrated to obtain only the PhC waveguide phase change by subtracting the polynomial from fig. (6.15)

To determine the group index ($n_{g,eff}$) from the phase delay ($\phi_{electric}$) of the PhC waveguide, it is noted that the phase is changed by 360° when the path length for the signal is increased by a wavelength ($\lambda_{electric}$). That is

$$\Delta\phi_{electric} = 360^\circ \quad \Leftrightarrow \quad \Delta n_{g,eff} l_{PhC} = \lambda_{electric}, \tag{6.3}$$

where l_{PhC} is the length of the PhC waveguide. Here it was used that the group index of the light equals the phase index of the envelope function (the electric function). As the phase shift is linear with $\Delta n_{g,eff}$, eq. (6.3) transforms into

$$\Delta n_{g,eff} = -\frac{\Delta\phi_{electric} c}{360^\circ l_{PhC} f_{electric}}, \tag{6.4}$$

where c is the vacuum speed of light and $f_{electric}$ is the frequency of the electrical modulation function. The negative sign is chosen because a larger phase delay (negative $\Delta\phi_{electric}$) is equivalent to a larger group index. The points in fig. (6.16) are used to calculate the group index of the PhC waveguide using eq. (6.4). The result is plotted in fig. (6.17). Part of the noise in fig. (6.17) is due to F-P oscillations in the waveguides leading light to and from the PhC waveguide. These two waveguide acts as F-P cavities. The optical path length for a F-P cavity is wavelength dependent and this change in optical path length is not removed from fig. (6.17). The F-P contribution can be removed by averaging over a F-P period, as this average optical part length is constant. The two F-P periods are determined to $0.14nm$ and $0.7nm$ from a cw transmission spectrum (see fig. 6.18). As the curve for $\Delta n_{g,eff}$ has interesting spectral features smaller than $0.7nm$, only the contribution from the physical long F-P cavity (equivalent to the spectral width of $0.14nm$) is removed by averaging. To determine the group index instead of only the *change* in group index, the experimental curve is compared with 2D finite-difference-time-domain (FDTD) calculations made by Andrei Lavrinenko after the change in group index was measured. The final curve for $n_{g,eff}(\lambda)$ is shown in fig. (6.19).

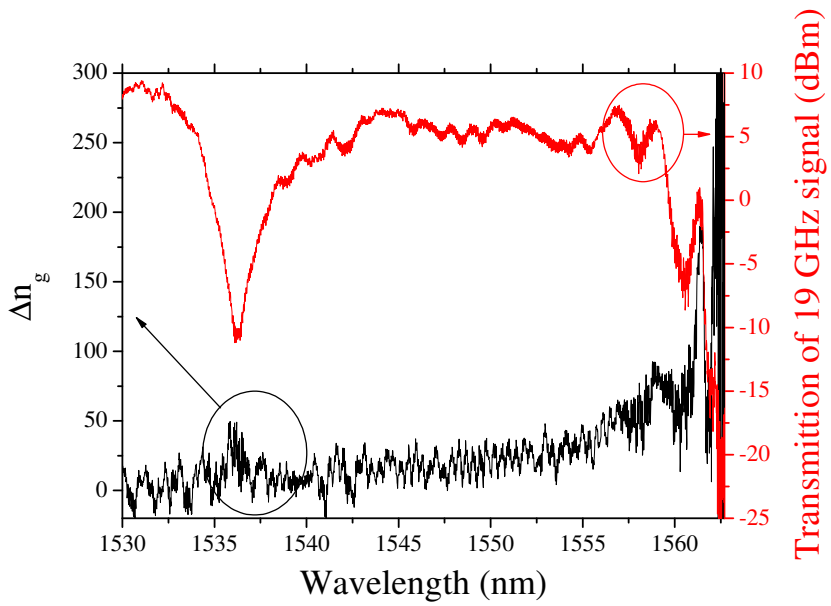

Figure 6.17: The determined group index for a $20\mu m$ symmetric W1 PhC waveguide. The noise part in fig. (6.16) due to the low transmission after the cut-off wavelength is partly omitted in this graph. As only the *change* in group index ($\Delta n_{g,eff}(\lambda)$) is measured, the left part of the curve is adjusted to oscillate around 0.

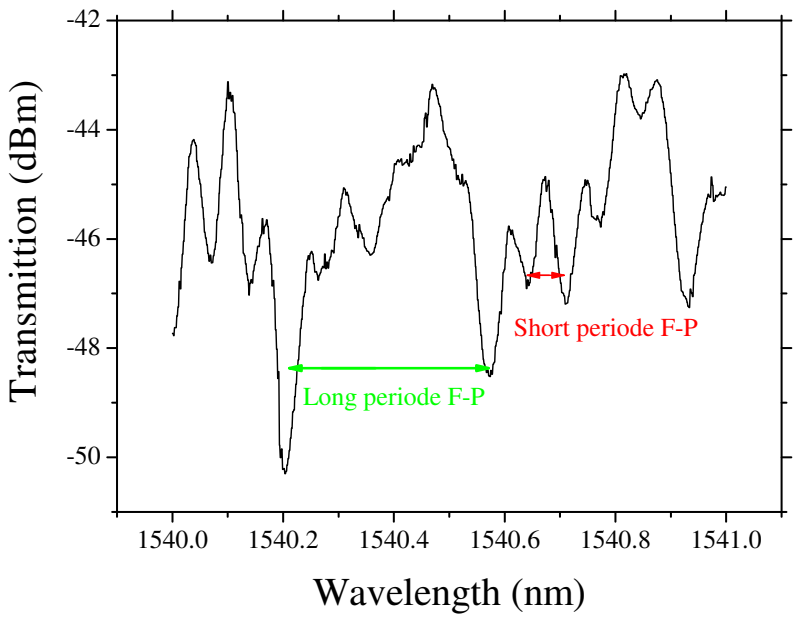

Figure 6.18: High resolution scan for the transmission spectrum of the waveguide containing a PhC part. The two periodic amplitude oscillations originate from each of the waveguides leading the light to and from the PhC part. The short period (long waveguide) is $0.14nm$ while the long period (short waveguide) is $0.7nm$.

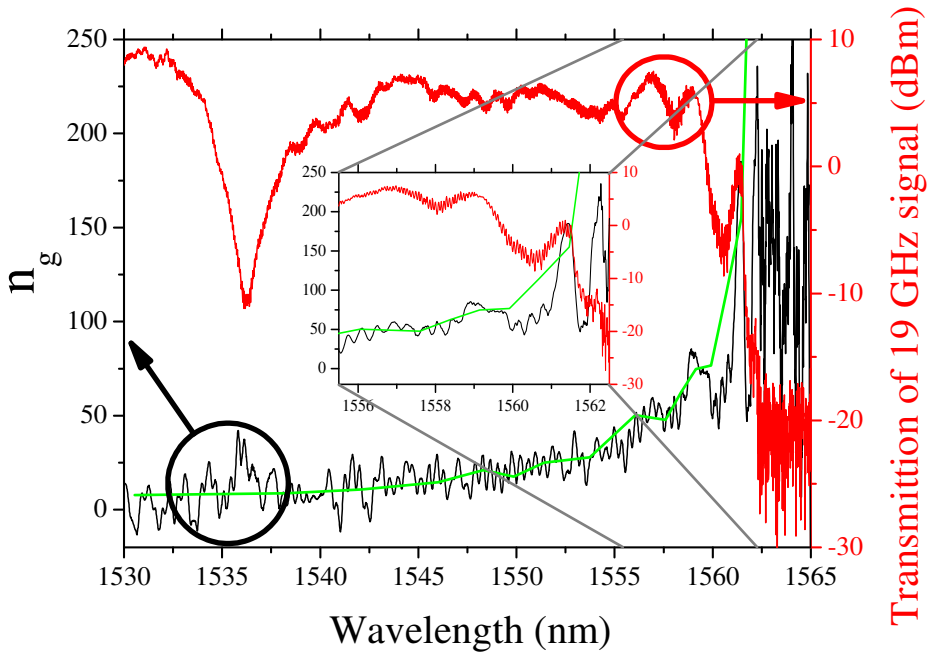

Figure 6.19: $n_{g,eff}$ for a $20\mu m$ symmetric W1 PhC waveguide, where the curve is averaged over $0.14nm$ to remove the contribution from a physical long F-P cavity (see fig. 6.18). The green curve is the group index determined by calculating ToF using the 2D finite-difference-time-domain (FDTD) metode [8]. The group index calculations where made by Andrei Lavrinenko after the change in group index was measured.

The measured group index (see fig. 6.19) does *not* increase uniformly towards the bandgap. The measured oscillations were yet another surprise and they are not seen in the 2D FDTD calculations. The group velocity of the light is equal to the slope of the dispersion curve. The form of the dispersion curve needed to give the measured group velocity is drawn in fig. (6.20) together with a calculated dispersion curve made with the MPB [4] software package by Lars Frandsen.

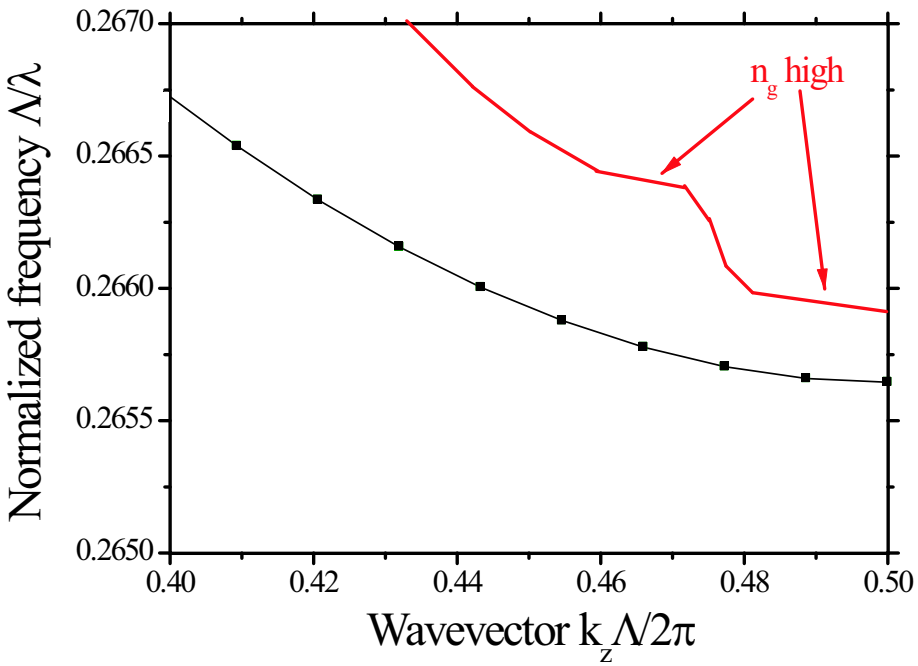

Figure 6.20: A zoom-in of the dispersion diagram that shows the cut-off for the guided mode. The points are 3D calculations made using MPB [4], kindly provided by Lars Frandsen. The red curve is a schematic drawing that demonstrates the needed behavior of the dispersion curve to assemble the measured group index behavior. The transition between the two flat regions corresponds to the measured low group index in between the two peaks on fig. (6.19).

The oscillating behavior is not observed in the 2D FDTD calculations and not even in the 3D calculations made using MPB. As described in appendix E, the calculations made with MPB does not correspond to the expected when the dispersion curve crosses a cladding mode from the sil-

ica surrounding the silicon PhC. This is probably due to the continuous boundary conditions applied in MPB (see appendix E). In 3D FDTD calculations Andrei Lavrinenko found a group index behavior similar to the measured [9], as shown in fig. (6.21). The measured oscillations in the group index are therefore *not* sample specific, but very advanced calculation methods like 3D FDTD are needed to see the group index oscillations theoretically.

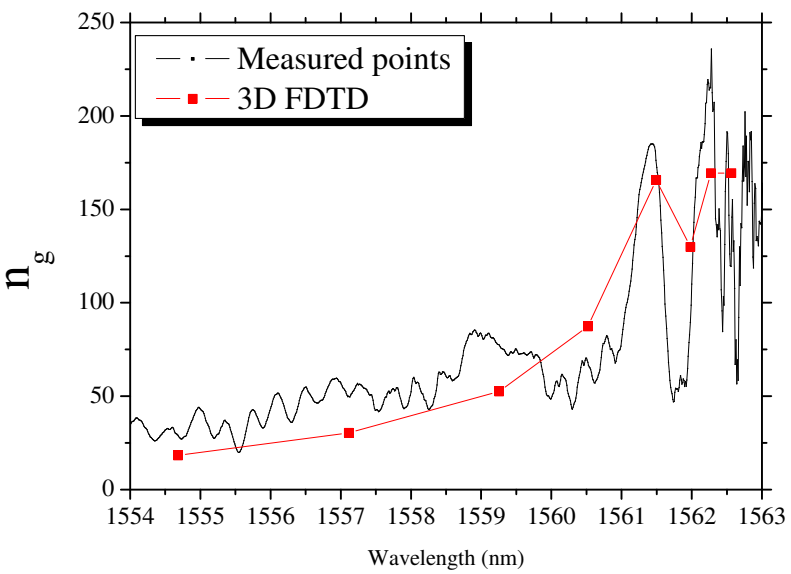

Figure 6.21: $n_{g,eff}$ for a $20\mu m$ symmetric W1 PhC waveguide, where the curve is averaged over $0.14nm$ to remove the contribution from a physically long F-P cavity (see fig. 6.18). The red curve is group index determined by calculations of ToF using the 3D finite-difference-time-domain (FDTD) metode [9]. The group index calculation was made by Andrei Lavrinenko after the change in group index was measured.

6.4 The $\chi^{(2)}_{core}$ in Ph.C. waveguides compared to the group index.

The oscillations in the group index explains the oscillations in the measured non-linearity, which is clearly seen when the second-order non-linearity[7] is plotted together with the group index (see fig. 6.22).

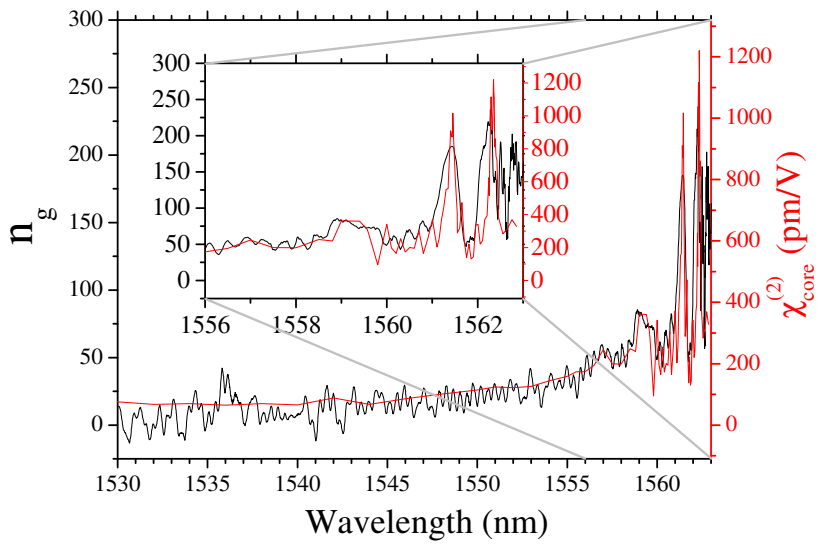

Figure 6.22: $n_{g,eff}$ and $\chi^{(2)}_{core}$ measured for a $20\mu m$ symmetric W1 PhC waveguide. The $n_{g,eff}$ curve is averaged over $0.14nm$ to remove the contribution from a physical long F-P cavity (see fig 6.18). The behavior of the curves are identical for the whole measurement range. This graph demonstrates for the first time experimentally, that $\chi^{(2)}_{core}$ scales linearly with the group index as predicted theoretically [2].

As the oscillations in the measured $\chi^{(2)}_{core}$ value are due to oscillations in the group index, the only remaining weird observation is the non-zero

[7] It is strictly speaking *not* correct to call the measured effect $\chi^{(2)}_{core}$, as the material $\chi^{(2)}_{core}$ is the measured effect divided by the group index. As discussed in section (2.3) the measured size is still called $\chi^{(2)}_{core}$ due to normal nomenclature.

$\chi^{(2)}_{core}$ value in silica. An experimental explanation for the $\chi^{(2)}_{core}$ value was found when producing sample $r2c4$. After deposition of hard topcladding there was only measured a negligible $\chi^{(2)}_{core}$ value (see fig. 6.23). There was then deposited a layer of Si_3N_4 on top of the structure (see fig. 6.24). The growth conditions were chosen according to [10] to obtain a high stress in the Si_3N_4 layer. A significant non-linearity was measured after applying the stressing layer, as shown in fig. (6.23).

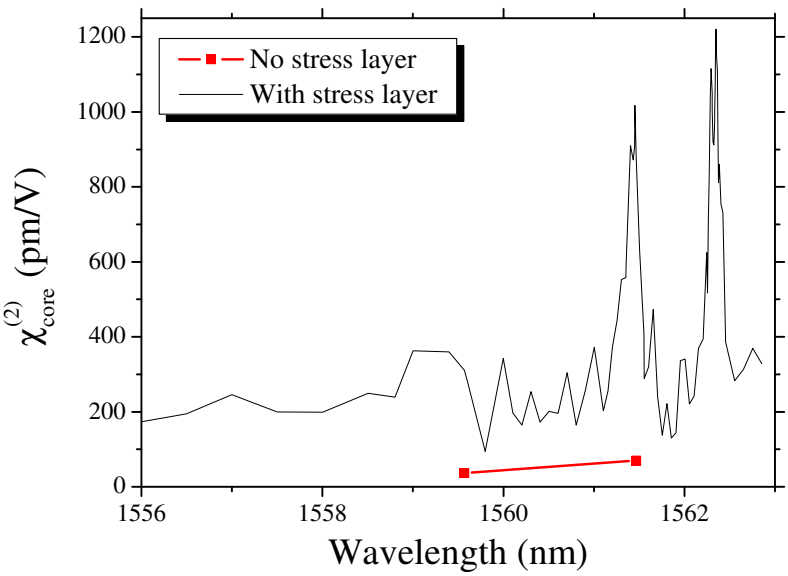

Figure 6.23: $\chi^{(2)}_{core}$ measured for a $20\mu m$ symmetric W1 PhC waveguide before and after applying a stressing layer to the structure. The non-linearity is almost 0 before the stress layer was deposited and it is significant afterwards. The optical field does not penetrate into the stressing layer, and the affect of the layer is purely mechanical.

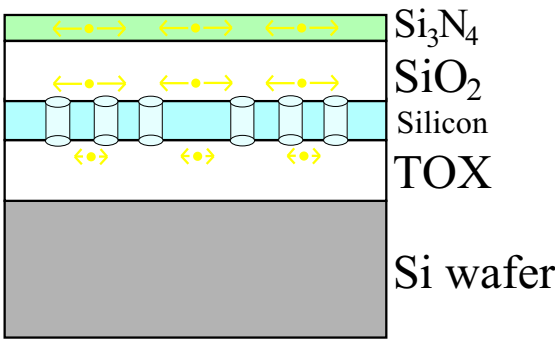

Figure 6.24: The Si_3N_4 would like to expand in the horizontal direction at all points, but the rest of the structure prohibits a significant expansion. The Si_3N_4 therefore stresses the structure. The stress is transmitted through the top cladding, which cannot expand in any significant degree. The experimental results from the buried waveguide can be explained if the stress partially released by deformation of the holes in the PhC waveguide.

The original non-linearity in sample $r2c5$ was probably due to a stress from the topcladding. When the topcladding for sample $r2c5$ was grown, a mass controller in the PECVD chamber for $SiH_4(g)$ was defect. The result of the defect mass controller was a faster growth rate and hence there was deposited $2\mu m$ hard topcladding instead of only $1\mu m$, as was intended. The difference in growth conditions would probably also induce stress in the layer, as the normal recipe used, is developed to obtain a low stress level. I.e. the discovery of a stress induced $\chi^{(2)}_{core}$ was made possible by chance.

The mass controller was replaced before topcladding was grown on sample $r2c4$ and the stress in the topcladding was therefore significantly lower. The optical light is confined below the hard topcladding first applied and a significant non-linearity was first measured after applying the stress. The origin of the non-linearity is therefore the stress and its effect on the silicon. Thinking back, it is not totally surprising, that stressed silicon has a non-zero $\chi^{(2)}$ value, as stress induced second harmonic generation (SHG) has been observed [11] in silicon.

6.5 Outlook for non-linear Silicon.

As discussed in section (2.3), there are numerous ways for reporting the non-linear value obtained. In the material development process, $\chi^{(2)}$ is the most interesting size. To evaluate if a device made of the developed material is interesting the phase change induced per unit length is the size of interest. I.e. the value for $V_\pi * l$ must be compared with the obtained value for other known material. For $LiNbO_3$ the value of $V_\pi * l$ is $10 - 12V * cm$ [12,13] for an actual device. In the devices, all parameters have been optimized, and the desire for a short electrode-electrode distance has been weighted against the optical loss due to optical leakage to the electrodes. For sample $r2c4$ the $V_\pi * l$ value is plotted in fig. (6.25).
As the optical loss in PhC waveguides is quite high it will at this point in the PhC development state *not* be interesting to make a MZI based modulator that incorporates a PhC structure to enhance the non-linear effect due to a high group index. The interesting value is therefore the non-enhanced value $V_\pi * l$ obtained in silicon. It has been shown, that the enhancement is equal to the group index, and by assuming a group index of 3 in a normal waveguide, it is found that

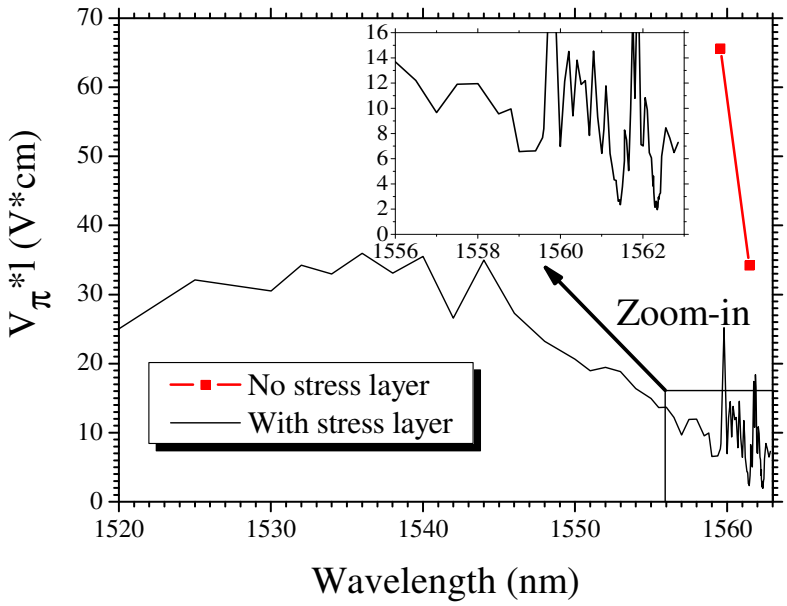

Figure 6.25: The measured value of $V_\pi * l$ for sample $r2c4$ before and after growing the Si_3N_4 stress layer. The voltage is low as a consequence of three parameter, the short electrode-electrode distance of $\sim 2.6\mu m$, the high group index of ~ 200 and as the material non-linearity is $\sim 130V * cm$. The short electrode-electrode distance does *not* cause a measurable optical leaking loss to the wafer and to the top electrode due to the high index step between silicon and silica. The electrode-electrode distance can possibly even be reduced without an increase in the optical loss.

- $V_\pi * l \sim 130V * cm$ with a normal group index of 3.

The non-linearity was measured for TE polarized light. If stressed silicon is comparable to normal glass (an isotropic material) the $\chi^{(2)}$ effect for TM polarized light should be 3 times higher (see appendix D). To measure the non-linear value for TM polarized light, single mode samples were fabricated using normal lithography techniques. The waveguide was made single mode by making it $1\mu m$ in width and only etching 30 nm down in the silicon layer (the height was measured using an atomic force

microscope), as shown in fig. (6.26). A hard topcladding was then grown on top of the waveguide and finally a stressing layer was also added. The measured $\chi^{(2)}$ value was negligible, even though a $1cm$ long waveguide was underneath the top electrode. I.e. even though the length of the affected waveguide was ~ 500 times longer than the $20\mu m$ PhC waveguide investigated.

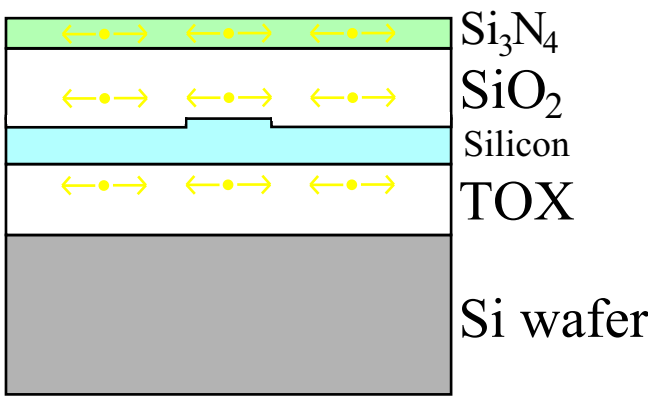

Figure 6.26: A buried waveguide made by etching a 30nm step down in the silicon layer. The with of the waveguide was $1\mu m$ and it is single mode. There was not detected any $\chi^{(2)}$ value in the samples fabricated. The possible explanation is that the stress does not relax when transmitted through the solid core layer and hence is symmetrically seen from the core layers perspective.

The difference between the buried waveguide and the PhC waveguide is from a stress perspective the holes in the silicon layer. These holes probably contains air even after the topcladding has been deposited and the silicon can therefore expand into the holes. This is not possible for the fabricated buried structures. As a PhC waveguide is somewhere between a buried and a ridge waveguide, the discovered effect will probably be much higher in a ridge structure, as drawn in fig. (6.27). The silicon waveguide will become very asymmetric when a stressing layer is applied on top, as the stress can be relieved by expansion of the top of the silicon waveguide. The bottom of the silicon waveguide cannot expand, as the wafer underneath is non-expandable (due to its thickness of $500\mu m$).
The structure in fig. (6.27) has not yet been fabricated and it remains to be seen how high a non-linear coefficient that can be obtained in stressed

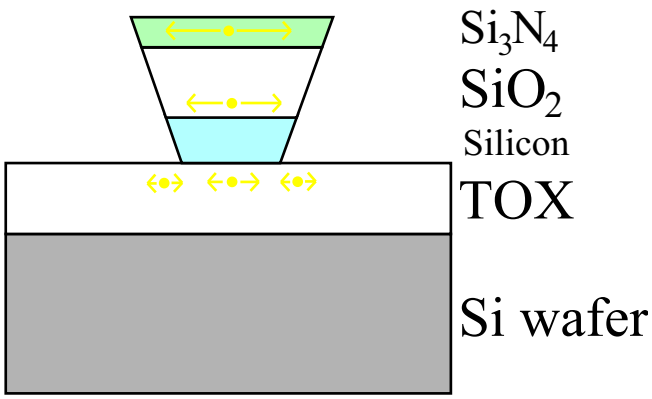

Figure 6.27: A ridge waveguide made with a stress layer on top. *This structure has not yet been fabricated.* It is expected that the $\chi^{(2)}$ value found in stressed PhC waveguides originate from deformation of the holes. A ridge waveguide should therefore exhibit a larger $\chi^{(2)}$ value than a PhC waveguide (when comparing non-enhanced $\chi^{(2)}$ values), as stress releasing over the core region should be more pronounced for a ridge waveguide.

silicon. The waveguide can be made single-mode by careful design, as described in [14, 15]. It also remains to measure the effect at higher frequencies than $500kHz$. The AC-amplifier used in the DC-shifted MZI setup does not deliver a high enough signal for frequencies higher than $500kHz$. Even with a faster AC-amplifier, the measurement frequency is limited by the lock-in amplifier (signal recovery 7280/98), which cannot measure beyond 2MHz. This is the fastest commercial lock-in amplifier found, that can also measure for short integration times (an integration time of one period is necessary, as described in section 3.5). To measure the effect at higher frequencies, there must be fabricated a sample where a larger phase swing is induced by a lower voltage. This is only possible by increasing the affected waveguide length from $20\mu m$ to a couple of centimeters. I.e. a normal waveguide is needed, as the loss in the PhC waveguides limits the propagation length below $50\mu m$ in the fabricated samples.

6.6 Conclusion.

The first measurements on PhC waveguides did result in several unexpected observations. By increasing the modulation frequency and by reducing the electrode length, only two observations lacked a proper explanation. The existence of a pure $\chi^{(2)}$ value in silicon and the wavelength dependent oscillations of the $\chi^{(2)}$ value.

To explain the oscillations of $\chi^{(2)}$ vs wavelength, a measurement method was developed to determine the group index in a $20\mu m$ long PhC waveguide. The measured group index corresponds to the calculated group index obtained afterwards, and the oscillations in the group index does explain the oscillations in the measured $\chi^{(2)}$ value.

The origin of the unexpected $\chi^{(2)}$ value was determined by fabricating a sample without a $\chi^{(2)}$ value and then inducing a $\chi^{(2)}$ value by applying a stress layer on top of the sample.

Steps where taken to fabricate a sample with a $\chi^{(2)}$ value in a normal index guiding waveguide. The first attempt was not successful but did point towards an explanation on how stress induces a $\chi^{(2)}$ value in silicon.

Plans have been made for making another index guiding silicon structure, that should posses an even higher material (non-enhanced) $\chi^{(2)}$ value, than found in the PhC structure. Such a waveguide can also be investigated for TM polarized light, which can lead to the discovery of an even higher $\chi^{(2)}$ value.

When the effect has been transferred to a normal index guiding waveguide, the effect should immediately be investigated for a possible cut-off frequency. The big remaining open question is the cause of the effect on an atomic level, and it could turn out that there is a cut-off frequency for the effect. The author and coworkers have tried to come up with an explanation for the effect that does not rely on perturbation of atomic orbitals but *no* other theoretical explanations have been found. Perturbation of atomic orbitals is an instantaneous effect for all practical applications. But to quote Jens Martin Knudsen: *It is the experiment that rules.* For $\chi^{(2)}$ in stressed silicon more experiments must be made before opening the champagne.

References to Chapter 6

[1] J. D. Joannopoulos, R. D. Meade, and J. N. Winn. *Photonic Crystals, Molding the flow of light*. Princeton University Press, 1995.

[2] M. Soljačić, S. Johnson, S. Fan, M. Ibanescu, E. Ippen, and J. Joannopoulos. "Photonic-crystal slow-light enhancement of nonlinear phase sensitivity", *J. Opt. Soc. Am. B.*, vol. 19, no. 9, 2002.

[3] H. Gersen, T. Karle, R. Engelen, W. Bogaerts, J. Korterik, N. Van Hulst, T. Krauss, and L. Kuipers. "Real-space observation of ultraslow light in photonlc crystal waveguides", *Physical Review Letters*, vol. 94, no. 7, pp. 1–4, 2005.

[4] S. G. Johnson and J. D. Joannopoulos. "Block-iterative frequency-domain methods for maxwell's equations in a planewave basis", *Opt. Exp.*, vol. 8, no. 3, pp. 173–190, 2001.

[5] "Private communication with ole hansen from the department mic at the danich technical university."

[6] M. Notomi, K. Yamada, A. Shinya, J. Takahashi, C. Takahashi, and I. Yokohama. "Extremely large group-velocity dispersion of line-defect waveguides in photonic crystal slabs", *Physical Review Letters*, vol. 87, no. 25, pp. 253902/1–253902/4, 2001.

[7] H. Nakamura, Y. Sugimoto, K. Kanamoto, N. Ikeda, Y. Tanaka, Y. Nakamura, S. Ohkouchi, Y. Watanabe, K. Inoue, H. Ishikawa, and K. Asakawa. "Ultra-fast photonic crystal/quantum dot all-optical switch for future photonic networks", *Optics Express*, vol. 12, no. 26, 2004.

[8] A. V. Lavrinenko, R. S. Jacobsen, J. Fage-Pedersen, B. Zsigri, C. Peucheret, L. H. Frandsen, M. Kristensen, and P. I. Borel. "Direct numerical and experimental determination of group index dispersion in photonic crystal waveguides.", *Spie, vol 5950, nr 15*, 2005.

[9] A. V. Lavrinenko, R. S. Jacobsen, J. Fage-Pedersen, L. H. Frandsen, B. Zsigri, C. Peucheret, and P. I. Borel. "Extreme group index measured and calculated in 2d soi-based photonic crystal waveguides.", *LEOS, TuR4*, 2005.

[10] F. E. Rasmussen, B. Geilman, M. Heschel, O. Hansen, and A. M. Jorgensen. "Development and characterisation of koh resistant pecvd silicon nitride for microsystems applications.", *ECS april27-maj2 Abstract no. 367*, 2003.

[11] T. V. Dolgova, V. Bessonov, A. I. Maidykovski, and O. A. Aktsipetrov. "Strain-induced second-harmonic generation in silicon.", *ICONO/LAT, IThC5, Hall4 Thursday 10:30*, 2005.

[12] G. Gopalakrishnan, R. Esman, C. Bulmer, and W. Burns. "Broadband drive voltage measurements in linbo3 traveling wave modulators", *Broadband Analog and Digital Optoelectronics, Optical Multiple Access Networks, Integrated Optoelectronics, Smart Pixels, LEOS 1992 Summer Topical Meeting Digest on*, pp. 5–6, 1992.

[13] J. Kondo, A. Kondo, K. Aoki, S. Takatsuji, O. Mitomi, M. Imaeda, Y. Kozuka, and M. Minakata. "High-speed and low-driving-voltage x-cut linbo/sub 3/ optical modulator with two step backside slot", *Electronics Letters*, vol. 38, no. 10, pp. 472–473, 2002.

[14] R. Soref, J. Schmidtchen, and K. Petermann. "Large single-mode rib waveguides in gesi-si and si-on-sio/sub 2/", *Quantum Electronics, IEEE Journal of*, vol. 27, no. 8, pp. 1971–1974, 1991.

[15] S. Pogossian, L. Vescan, and A. Vonsovici. "The single-mode condition for semiconductor rib waveguides with large cross section", *Lightwave Technology, Journal of*, vol. 16, no. 10, pp. 1851–1853, 1998.

Chapter 7

Conclusion.

This goal of this project was to realize a switch in poled silica with a switching voltage less than 300V. This goal was *not* accomplished. Actually the author has never poled a sample, as the lower limit for the switching voltage is governed by the third-order non-linearity $\chi^{(3)}$ of the investigated material. Numerous attempts where made for increasing $\chi^{(3)}$ and the best result was obtained for silicon rich nitride (SRN), which is 5 times more non-linear than the Ge:SiON samples investigated at first. It should be possible to make a switch in SRN that has a switching voltage below 250V, but at the time, even this switching voltage was judged to high for any device applications.

During the investigation of $\chi^{(3)}$ materials, a possible explanation for the very high non-linearities reported through the nineties [1,2] was found. This explanation shows that the only possible way for lowering the switching voltage is to increase the material non-linearity $\chi^{(3)}$. Actually $\chi^{(3)}$ must be increased by a factor of 10 to reach a level where a device with an interesting switching voltage could be possible. Material doping and change of the waveguiding method are tried but without success. From the investigation, it is concluded that: *There are no mysteries left in poling of silica that can justify further research with the goal of making an electro-optic integrated switch in silica.*

To measure the non-linearity a precision method was developed due to reproducibility problems experienced with the Bragg grating method applied in the author's research group. After developing the new method called **The DC-shifted MZI method** the dominant measurement un-

certainty is due to thickness variations of the investigated samples. To reduce the uncertainty further, a new method must be developed for determining the sample thickness. There is not observed any reproducibility problems with the DC-shifted MZI method, which is also more versatile than the Bragg grating method. The DC-shifted MZI method can measure on all waveguides usable for a switch, i.e. on all single mode waveguides. The total uncertainty for a determined $\chi^{(3)}$ value is $\sim 5\%$ including all error contributions.

When photonic crystal (PhC) waveguides where investigated a discovery was made. After careful designed experiments and the development of a method for measuring the group index of PhC waveguides this discovery was clarified to be:

- Stressed silicon possesses a significant $\chi^{(2)}$ non-linearity.

The investigation of the PhC waveguide also led to a collection of impressive results. That is

- The current record for a direct measured group index ($n_g = 220$).
- The linear enhancement of the $\chi^{(2)}$ effect with the group index predicted theoretically in [3] is experimentally verified for the first time.
- The current non-linearity corresponds to $V_\pi * l < 2V * cm$ for the high group index case
- By dividing the obtained results with the determined group index, a non-linearity corresponding to $V_\pi * l = 130V * cm$ is predicted as the non-enhanced value.

Measurement with the aim of making a device that exploits the discovered effect are planned. The most crucial question that still lacks an answer is the frequency behavior of the stress induced $\chi^{(2)}$. If the effect diminishes for fast modulations, then it cannot be used in practice. I.e. from the application point of view, it is still to early to guarantee success.

References to Chapter 7

[1] R. Myers, N. Mukherjee, and S. Brueck. "Large second-order nonlinearity in poled fused silica", *Optics Letters*, vol. 16, no. 22, pp. 1732–4, 1991.

[2] T. Fujiwara, D. Wong, Y. Zhao, S. Fleming, S. Poole, and M. Sceats. "Electro-optic modulation in germanosilicate fibre with uv-excited poling", *Electronics Letters*, vol. 31, no. 7, pp. 573–575, 1995.

[3] M. Soljačić, S. Johnson, S. Fan, M. Ibanescu, E. Ippen, and J. Joannopoulos. "Photonic-crystal slow-light enhancement of nonlinear phase sensitivity", *J. Opt. Soc. Am. B.*, vol. 19, no. 9, 2002.

Appendices

Appendix A

Fitting an ellipse.

A.1 Introduction of the challenges.

In chapter (3.3) ellipsoids are fitted to measurement points. The fitting is not trivial and the procedure is gone through in this appendix. Basically the ellipses consists of measurement points, where the x-coordinate and the y-coordinate are sizes of the fundamental 33.333 kHz function and the second harmonic 66.666 kHz function, respectively. There are two complications, that distinguish the measured ellipses from a mathematical ellipse. To illustrate the two complications, an "ugly" measured ellipse is plotted in fig. (A.1). The ellipse is measured for $\lambda = 1550nm$ when $V_{P-P} = 200mV$ at the $LiNbO_3$ modulator, i.e. when the lowest modulation voltage was used. This is expected to be the most error encumbered ellipse.
The deviation in the x-direction is smaller, than the deviation in the y-direction. The other problem is the non-uniform angular distribution of the points.

A.2 Determination of the X and Y standard deviations.

To fit the ellipse, the size of the Gaussian deviation in the x and y directions must be determined. Luckily this information can be extracted

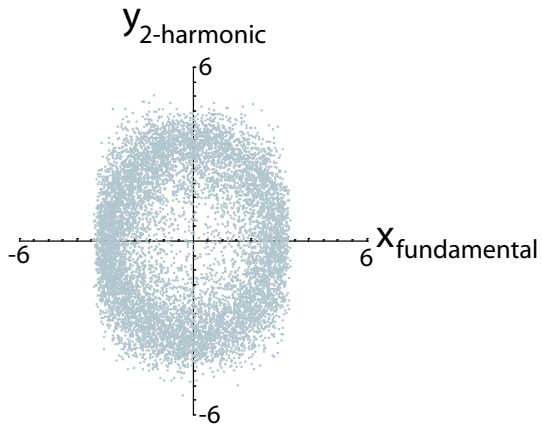

Figure A.1: A measured ellipse for $\lambda = 1550nm$ when $V_{P-P} = 200mV$ at the $LiNbO_3$ modulator. The angular distribution of points is non-uniform and the deviation in the x and y direction is non-equal ($\sigma_x < \sigma_y$).

from the measurements. The ellipse x and y coordinates are determined by measuring integral values as derived in eq. (3.20) and fitting the two sets of measured points with two straight lines. An example of such a line is given in fig. (A.2).
The projection of corresponding fundamental and 2-harmonic points onto the fitted lines is the ellipse x and y coordinates. Each measured point (x_1^f, y_1^f) and (x_1^s, y_1^s) on the right and left plot (A.2),respectively, are encumbered with measurement error. As the points are non-datatreated, the deviation from the true value is Gaussian. There is no difference between the two measured coordinates in the left plot (A.2), and it is therefore assumed that the standard deviation is the same for x_1^f and y_1^f and for x_1^s and y_1^s. This is illustrated with error circles around two corresponding points on fig. (A.3).
The measurement error can be determined from the plot (A.3), by rotating the coordinate system, so the determined line is the x-axis. Calling the new coordinates (x_2^f, y_2^f) and (x_2^s, y_2^s) , the rotated plot is shown in fig. (A.4).
The deviation from 0 in the $y_2^{f/s}$-direction is solely due to measurement

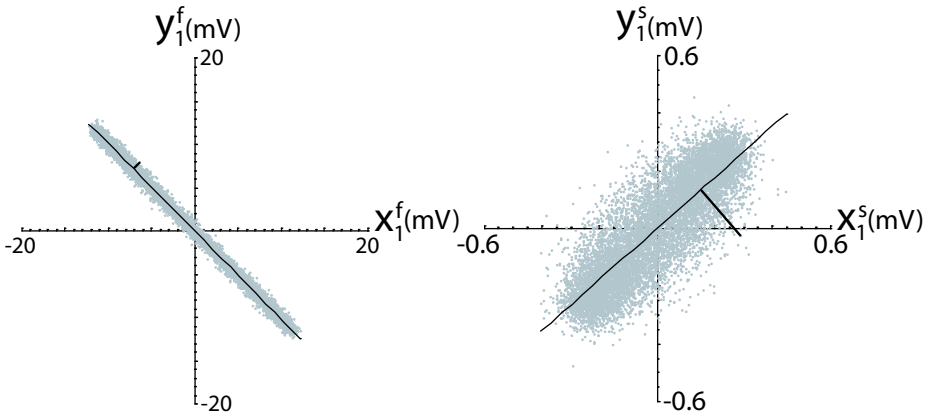

Figure A.2: Integrals values measured for the fundamental and 2-harmonic functions using a lock-in amplifier as described in chapter (3.3). The ellipse x-value for each point is found by projecting the point onto the fitted line (left fit) for the fundamental measurement. The ellipse y-value (for the determined x-value) is found by projecting the corresponding 2-harmonic point onto the line (right fit).

error[1]. The error in the $x_2^{f/s}$-direction is equal to the error in the $y_2^{f/s}$-direction, as the errors for $x_1^{f/s}$ and $y_1^{f/s}$ are equal. The plotted density of the point distribution in the $y_2^{f/s}$-direction, gives a Gaussian curve as shown in fig (A.5).
The standard deviation $\sigma_{y_2^{f/s}}$ for $y_2^{f/s}$ are found by the normal standard deviation formula using 0 as the measured true value.

$$\sigma_{y_2^{f/s}} = \sqrt{\frac{1}{N-1}\sum (y_{2,i}^{f/s} - 0)^2}. \tag{A.1}$$

This deviation is as argued equal to $\sigma_{x_2^{f/s}}$. The value $\sigma_{x_2^f}$ is the standard deviation in the ellipses x-coordinate and the value $\sigma_{x_2^f}$ is the standard deviation in the ellipses y-coordinate.

[1] This is only true, if the determined line on fig. (A.2) is without error, as the rotation of the coordinate system is otherwise incorrect. If there are enough measurement points, the determined line will be without errors. With 10000 measured points it is assumed that the line is the true error-free line.

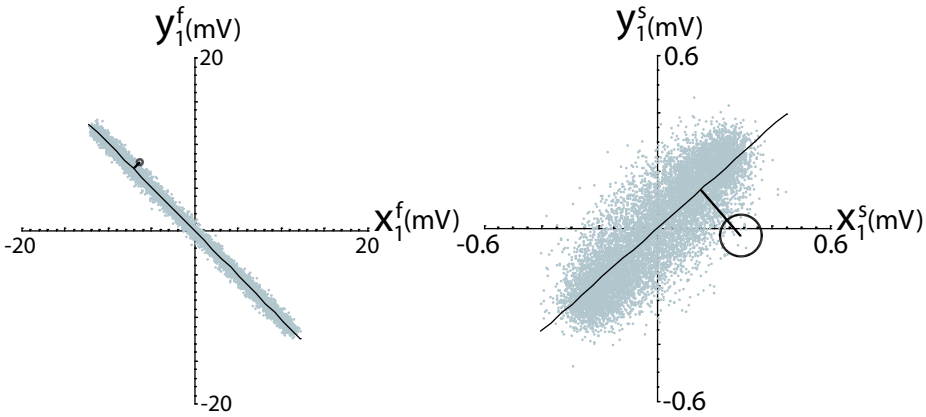

Figure A.3: Integral values measured for the fundamental and 2-harmonic functions using a lock-in amplifier as described in chapter (3.3). The two circles illustrate the standard deviation for two corresponding measured points.

A.3 Fitting an ellipse.

The value at interest is b/a, where the eccentricity of the ellipse is $\epsilon = \sqrt{1^2 + (b/a)^2}$. The equation for the ellipse in cartesian coordinates is

$$\frac{x^2}{a^2} + \frac{y^2}{b^2} = 1. \tag{A.2}$$

A mathematical ellipse is plotted in fig. (A.6).
To fit the ellipse, with known x and y uncertainties, the points are shifted to polar coordinates (illustrated in fig. A.7).
The equation for an ellipse in polar coordinates is

$$r(\theta)^2 = \frac{a^2 b^2}{a^2 \sin^2(\theta) + b^2 \cos^2(\theta)}. \tag{A.3}$$

The advantages of shifting to polar coordinates is that the ellipse function $r(\theta)$ is a function (there is one and only one value for $r(\theta)$ for each value of (θ)). The points can be fitted using normal least square fitting procedure. Transforming the ellipse points to polar coordinates and then making a fit using the normal least square method is called **the polar fitting procedure**.

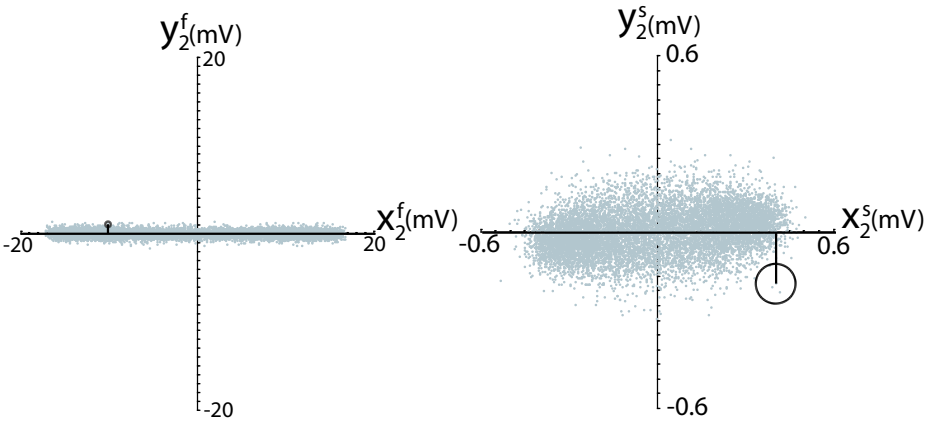

Figure A.4: Integrals values measured for the fundamental and 2-harmonic functions using a lock-in amplifier as described in chapter (3.3) in a rotated coordinate system. The two circle illustrates the standard deviation for the two corresponding measured points.

A.4 Investigation of non-equal deviation effect.

When the points on a measured ellipse are fitted in polar coordinates, a systematic error is introduced. The measurement error for the points in cartesian coordinates was Gaussian, but when a 2D-Gaussian error is transformed into polar coordinates, the error is no longer Gaussian (see fig. A.8). Normal statistical methods will therefore *not* give correct results.

A MonteCarlo[2]approach is used to determine the systematic error due to the fitting procedure. To illustrate the concept of a Montecarlo method imagine the value of π was unknown, but the formula for the area A_c of a circle ($A_c = \pi * r_c^2$) was known. Here r_c is the radius of the circle. To find π a 2D set (x_c, y_c) of random numbers with values in the range $[-1, 1]$ is made. A set with 10000 points together with a circle of radius 1 is plotted in fig. (A.9).

Dividing the area of the circle with the area of the square is $2^2 = 4$ gives $\pi/4$. This is equal to the probability for a point lying inside the circle.

[2]Any method that relies on the use of many random numbers is called a MontCarlo method.

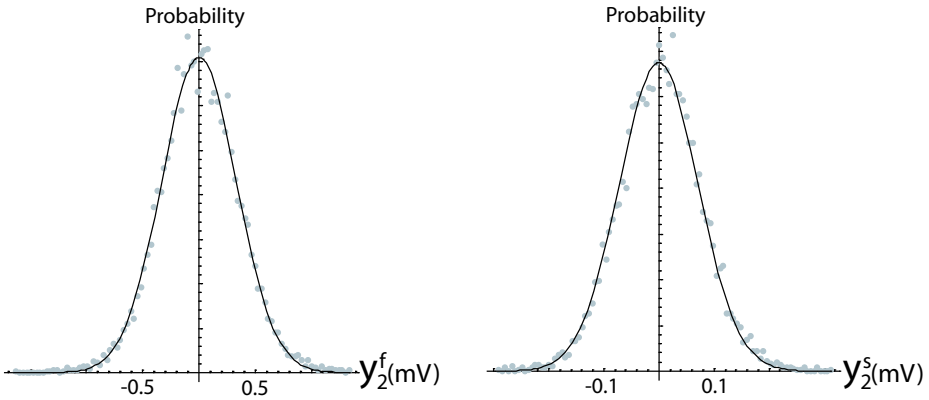

Figure A.5: Distribution of points in the y_2^f(right) and in the y_2^s(left) directions. A Gaussian fit corresponds nicely to the points. This demonstrates the measurement error is Gaussian distributed.

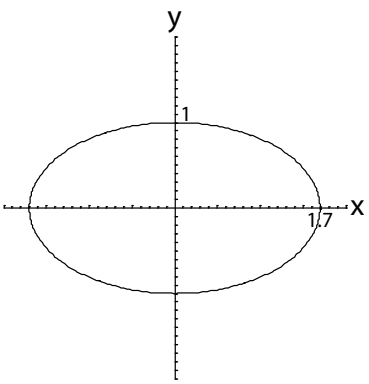

Figure A.6: Mathematical ellipse with $a = 1.7 * b$. Mathematical means the ellipse is generated from a formula (A.2).

Point i lies inside the circle when $x_{c,i}^2 + y_{c,i}^2 \leq 1$. Using this formula it is found that 7869 of the 10000 points lie inside the circle. That is, the probability P_{inside} of lying inside the circle is 0.7869. As the probability is equal to $\pi/4$, the value of π has now been determined to 3.1476. The real value of π is 3.14159.

Whenever a Montecarlo approach is used, the random number gen-

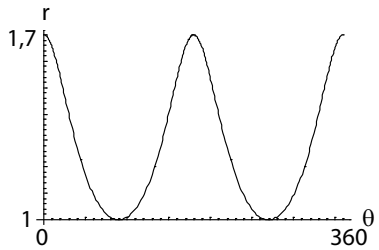

Figure A.7: Mathematical ellipse with $a = 1.7 * b$ in polar coordinates. The same ellipse in cartesian coordinates is shown in fig. (A.6)

erator must be investigated. The random number generator is used to give a Gaussian distribution and to investigate it, a plot of the random number density and a Gaussian fit is made in fig. (A.10).
As the random number density corresponds to the Gaussian curve (see fig. A.10), the random number generator can be trusted.

A set of points on a mathematical circle with radius 1 and with two Gaussian errors added is made. One Gaussian error with $\sigma_x = 0.1$ is added in the x-direction and the other Gaussian error of $\sigma_y = 0.2$ is added in the y-direction. The circle with the added error is plotted in fig. (A.11).
The points are transformed to polar coordinates and the function for the polar ellipse is fitted to the points. This is shown in fig. (A.12). If the fitting procedure was without systematic error due to the non-Gaussian distribution in polar coordinates, the fit in fig. (A.12) would be a constant function with value 1 ($y = 1$).

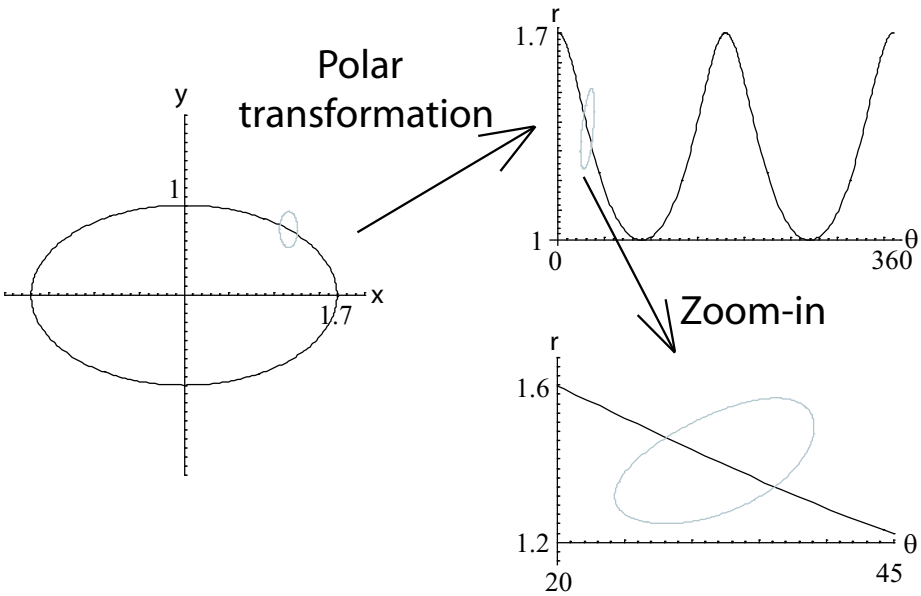

Figure A.8: Mathematical ellipse with $a = 1.7 * b$ with an uncertainty ellipse for a point. The ellipse is transformed to polar coordinates and the close-up view shows the uncertainty is no more Gaussian. Normal statistical methods will *not* give the correct result due to the non-Gaussian error distribution.

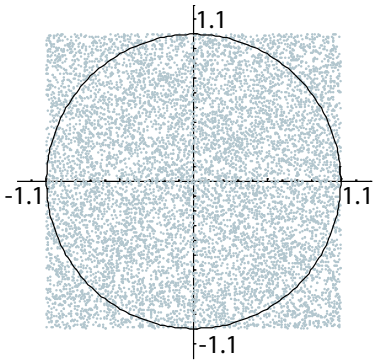

Figure A.9: Demonstration of the Montecarlo method. The points are uniform random distributed between -1 and 1 in both the x and y direction. The circle has radius 1. Determining the ratio of points inside the circle ($= P_{inside}$), π is determined to 3.1476. The correct value of π is 3.1416.

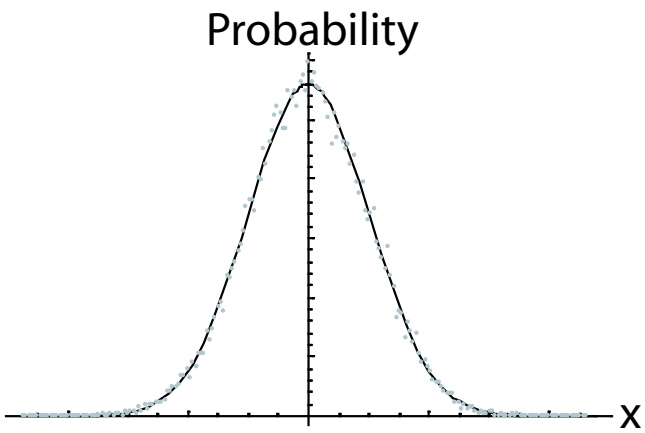

Figure A.10: The points is the distribution of the random number generator and the curve is a fitted normal distribution. As the points and the curve correspond nicely, the random number generator is trustworthy.

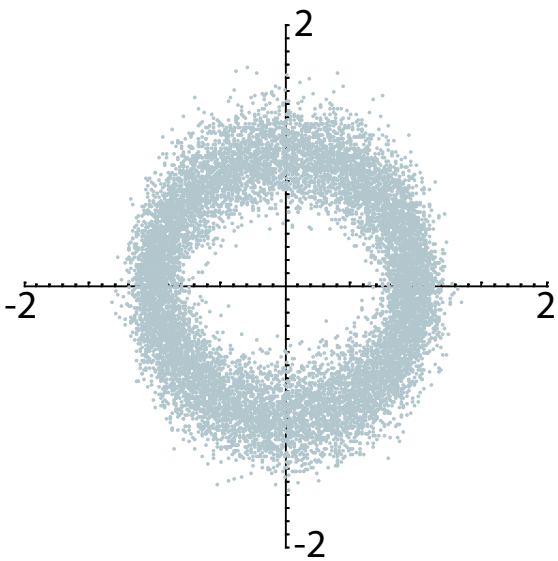

Figure A.11: Points on a mathematical circle with added errors in the x and y directions with $\sigma_x = 0.1$ and $\sigma_y = 0.2$, respectively.

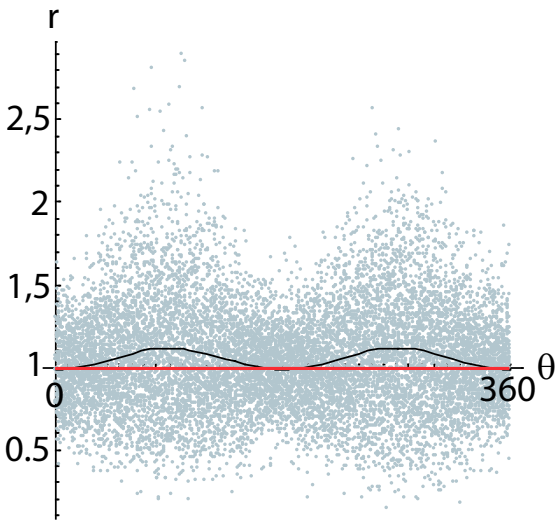

Figure A.12: The circle in fig. (A.11) in polar coordinates. The black curve is fitted using the normal least square fitting criteria. The correct fit is a constant function with value 1 (red line).

The result of the fit is the parameters of the ellipse and especially the value of b/a. The value should be 1, as a circle was used, i.e. an ellipse with eccentricity 0. This is repeated for different values of the standard deviation in the x and y directions. The value of b/a is plotted in a 2D plot (see fig. A.13) as function of the absolute uncertainty σ_x and of the absolute uncertainty σ_y.

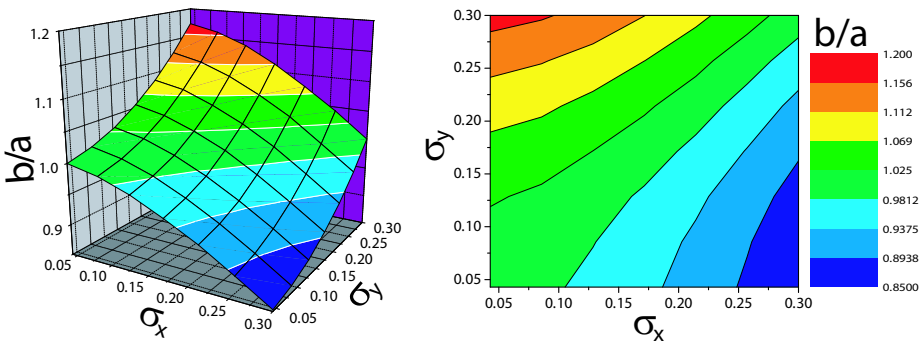

Figure A.13: The value of b/a vs. σ_x and σ_y for a circle (correct value $b/a = 1$) determined by the polar fitting procedure. As the determined value depends systematically on σ_x and σ_y, action must be taken to remove the systematic error from the fitting procedure. This is done in section (A.4).

The plot of b/a vs. σ_x and σ_y shows that action must be taken to get around the introduced systematic error.

A.5 Investigation of non-uniform angular distribution.

The other problem with the measured ellipse is the non-uniformity of the angular distribution of the measurement points. To investigate if this non-uniformity introduces an error, a number of partial circles are made mathematically. To illustrate the angular filling factor three of these are shown in fig. (A.14).
The first partial circle is a half circle (filling factor 180°) and the last partial circle is a full circle (filling factor 360°). Gaussian errors are added to the circle points in cartesian coordinates using the Montecarlo method. The resulting circles are plotted in fig. (A.15).

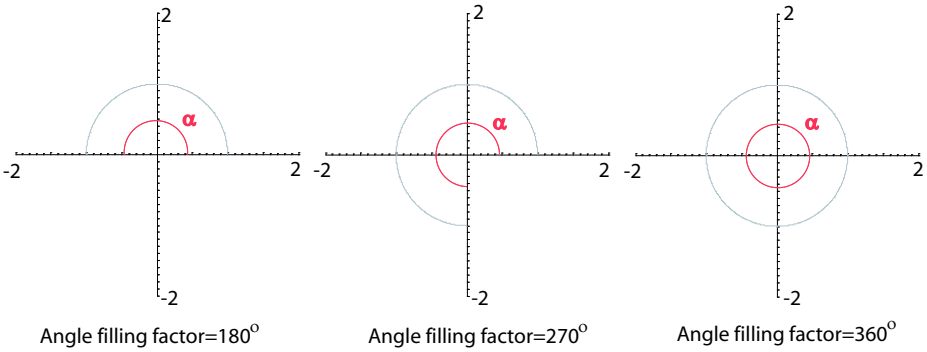

Figure A.14: Partial mathematical circles for different angle filling factor. The filling factor is the angle (α) (in red).

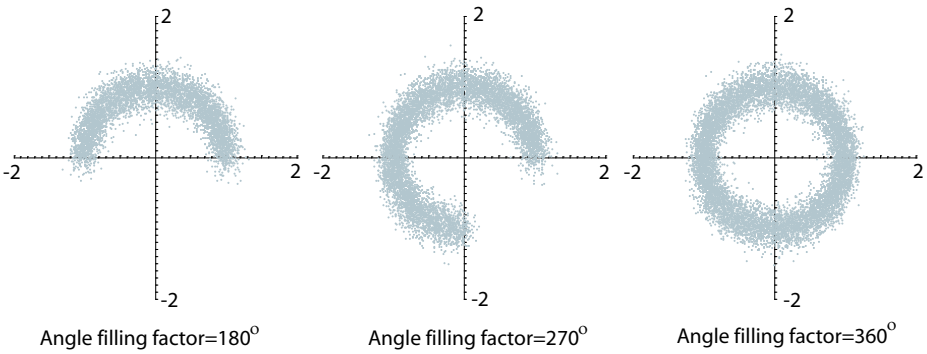

Figure A.15: Partial mathematical circles with added Gaussian uncertainty ($\sigma_x = 0.1$ and $\sigma_y = 0.15$) for different angle filling factor.

The Gaussian error is approximately equal to the worst measured ellipses deviation. The error in the x and y directions are $\sigma_x = 0.1$ and $\sigma_y = 0.15$, respectively. Using the polar fitting procedure introduces an error. A plot of b/a vs. the angular filling factor for the circle is shown in fig. (A.16). The figure shows both the problem with the non-uniform angular distribution (the oscillations) and the figure shows the systematic error due to the polar fitting procedure. The effect of the systematic error is that the mean value of b/a is *not* 1 but 1.0247.
The value of b/a in the plot (A.16) does depend on the angular filling

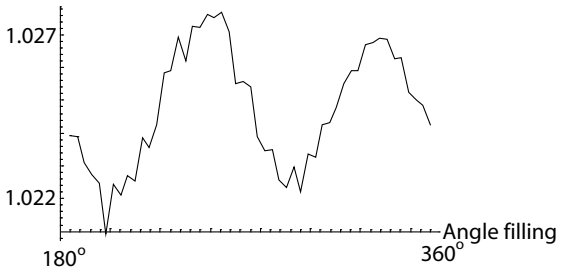

Figure A.16: Determined b/a value vs. filling angle for a circle of radius 1 and with $\sigma_x = 0.1$ and $\sigma_y = 0.15$. The oscillations are due to the change in filling factor. The roughness of the curve is due to the limited number of points used in each Montecarlo circle. The mean values deviation from 1 is because of the systematic error introduced by the polar fitting procedure.

factor. The plot shows the maximum deviation due to non-uniform angular distribution for the measured points is $2 - 3‰$. This is a worst case scenario both for the non-uniformity of the angular distribution and for the Gaussian error's. It is therefore assumed that the error due to the non-uniform angular distribution is less than $1‰$. An error of $1‰$ is added to the error of the final result because of this.

A.6 Solving the non-equal deviation problem.

In section (A.4), it was shown, that the polar fitting procedure introduced a systematic error, when the deviations in the x and y directions where non-equal. The size of the systematic error was determined using Montecarlo simulations.

If the normalized deviations σ_x/a and σ_y/b are known, the Montecarlo simulation can determine the exact systematic error $E_{polarfit}$ for the measured $b/a_{measured}$ value. The true value of b/a_{yrue} is then determined as.

$$b/a_{true} = b/a_{measured}/E_{polarfit}. \tag{A.4}$$

That is, if the polar fitting procedure overestimates b/a by 10 percent and the size of the overestimation is known, the true value is found by dividing b/a with the overestimation factor ($= 1.10$).

The trouble is that σ_x/a and σ_y/b are unknown for the measured ellipse. The deviations σ_x and σ_y are known (see section A.2), but the value of a and b are unknown.

To determine a and b an iterative process is used. The polar fitting procedure estimates a_1 and b_1 but the values are affected by a systematic error. Measured points together with a ellipse determined using the polar fitting procedure is shown in fig. (A.17).

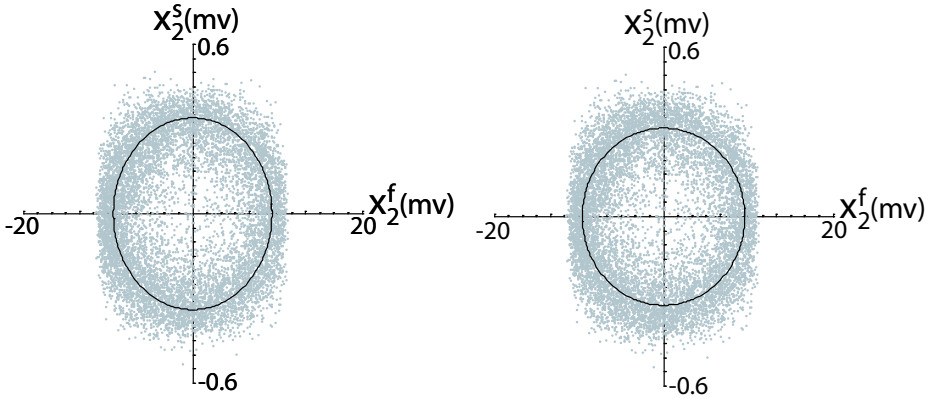

Figure A.17: A measured ellipse for $\lambda = 1550nm$ when $V_{P-P} = 200mV$ at the $LiNbO_3$ modulator with an ellipse fitted using the polar fitting method(left) and with an ellipse fitted using the iterative polar fitting method(right). The ellipse curve is encumbered with the systematic error.

To determine the systematic error, a Montecarlo circle with radius 1 and with deviations σ_x/a_1 and σ_y/b_1 in the x and y directions is made. The circle is plotted in fig. (A.18).
Fitting the circle using the polar method, correction factors ($a_{c,1}$, $b_{c,1}$) due to the fitting procedure for a and b are found. The new values for a and b are

$$\begin{aligned} a_2 &= a_1/a_{c,1} \\ b_2 &= b_1/b_{c,1}. \end{aligned} \tag{A.5}$$

This procedure is repeated until convergence is obtained. To demonstrate the procedure, a mathematical ellipse with $b/a = 0.5$ and with different errors in x and y directions is made with 628319 Montecarlo points. The

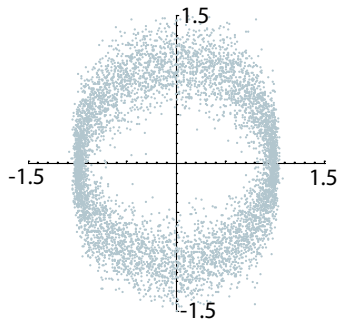

Figure A.18: A mathematical circle with radius 1 and with relative x and y error's equal to the errors of the measured ellipse in fig. (A.17).

high number of points ensures that the converged b/a value is 0.5. The same circle with a reduced number of points is plotted in fig. (A.19). The errors of $\sigma_x = 0.2$ and $\sigma_y = 0.15$ corresponds approximately to the error of the worst measured ellipse ($\sigma_x/a = 0.1$ and $\sigma_y/b = 0.15$).

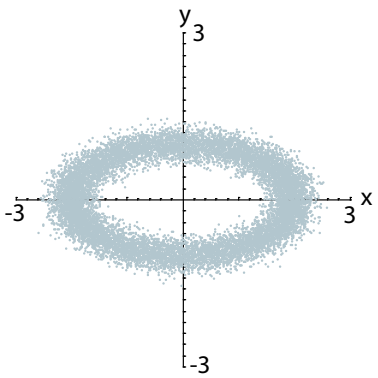

Figure A.19: A mathematical ellipse with $a = 2$, $b = 1$, $\sigma_x = 0.2$ and $\sigma_y = 0.15$.

Using the polar fitting procedure, the first b_1/a_1 value is determined. Then values for b_i/a_i are determined using the iterative process and the determined value of b_i/a_i is plotted in fig. (A.20).

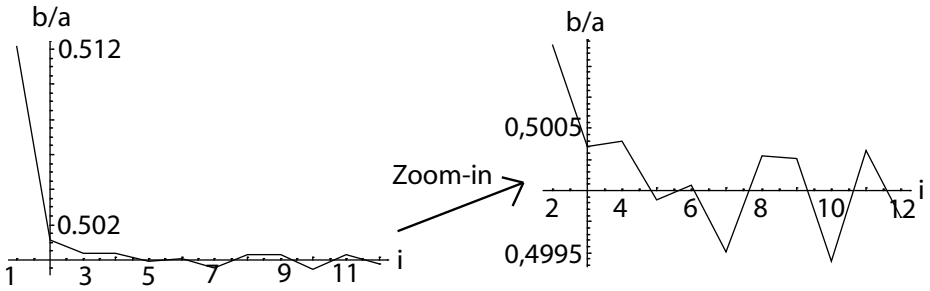

Figure A.20: The value of b_i/a_i determined for the ellipse in fig. (A.19) as function of iteration number(i). The true value is 0.5 and the first determined value using the polar fitting procedure is 0.512. The final determined value is 0.49979 after making 11 Montecarlo circles. Point 1 is before the value is corrected using a Montecarlo circle.

The criteria used for convergence is that the last result (n) should not differ more than 0.2‰ form the average of the two results ($n-1$) and ($n-2$). That is

$$\frac{b_n/a_n - \left(b_{n-1}/a_{n-1} + b_{n-2}/a_{n-2}\right)/2}{b_n/a_n} < 0.0002 \qquad \text{(A.6)}$$

This convergence criteria tries to avoid converging at a local extremum like point 8 and 9 in fig. (A.20) by including the three last points.

Test runs show, that the polar fitting error for the final result is reduced to less than 1‰ with this convergence criteria. As convergence is reached using a routine that oscillates around the end result, the left-over error is non-systematical. The final procedure including the iterative process is called **The iterative polar fitting procedure**.

Appendix B

Determining accuracy of measurements.

B.1 Introduction.

In all experiments there are two distinct error type, that must be considered. The systematic error due to the finite good calibration of the measurement instruments and the reproducibility error, i.e. the derivation between repeated "identical" measurements. This appendix contains a detailed description of both types of errors for the non-linear measurement setup developed in this Ph.D. project. There are numerously places where errors are introduced. Each error is investigated and a value for the error is determined (each error contribution is written in **bold** font). After the systematic error is determined, the reproducibility error for the experimental setup is investigated.

B.2 $LiNbO_3$ calibration.

In the experiment used to calibrate the $LiNbO_3$ phase modulator there are used two lock-in amplifiers, a voltmeter and an A/D-converter[1] to measure electrical signals (see section 3.3). The setup is shown schematicly in fig. (B.1).

[1] Four of the input ports on the analog to digital converter (A/D-converter) are used.

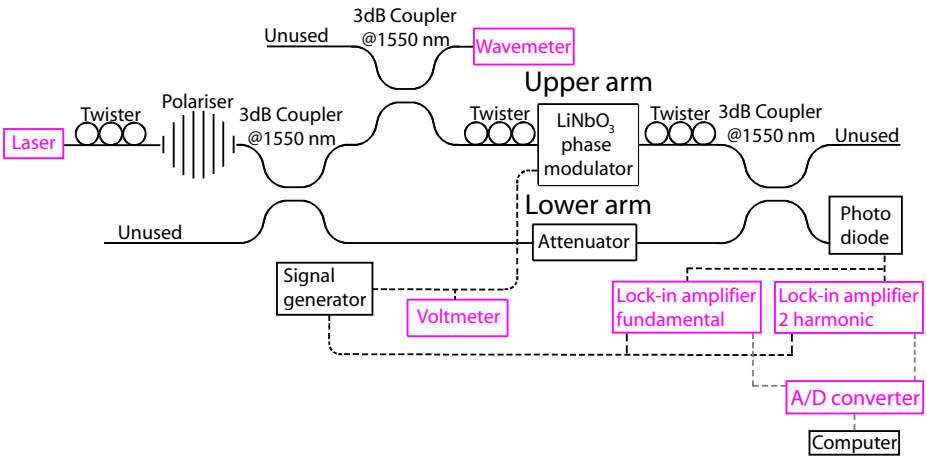

Figure B.1: The MZI setup used for measuring V_π. The 6 red boxes performs a measurement where systematic errors occurs.

The voltmeter is used to measure the amplitude ($A_{electric}$) of the electrical signal ($A_{electric}$*sin($\omega t+\theta$)) on the $LiNbO_3$ modulator. The voltmeter is a **Fluke 45 dual display multimeter**. The voltmeter is only guaranteed to be accurate within 4% at 33.333kHz. To decrease the uncertainty, a measurement is performed, where the same sinus signal is measured simultaneously by the voltmeter and by a **Signal recovery 7280/98 lock-in amplifier**. The lock-in amplifier is guaranteed to be accurate within 6‰. The result is plotted in fig. (B.2).
The results measured with the voltmeter and with the lock-in amplifier differ less than 2‰ (see fig B.2), and it is therefore assumed that the corrected result $V_{rms}^{fluke,corrected}$ is within **6**‰[2] of the true value.

The second systematic error is introduced by the two lock-in amplifiers used to measure the electrical signal from the photo diode. The value in search is V_π, that is found by solving the equation below(see eq. 3.28)

$$\frac{b}{a} = \frac{J_2(A)}{J_1(A)}, \tag{B.1}$$

as function of $A_{electric}$. The values of a and b are measured by the

[2]The 6‰ is the guaranteed accuracy for the lock-in amplifier. The lock-in amplifier should normally be accurate within 3‰.

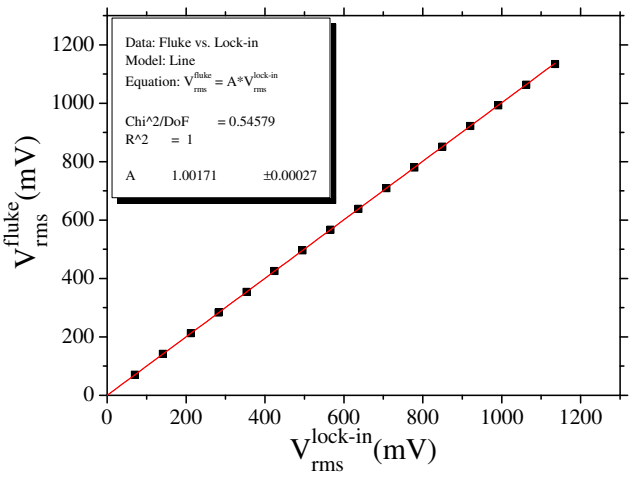

Figure B.2: The V_{rms}^{fluke} measured on the **Fluke 45 dual display multimeter** as function of the $V_{rms}^{lock-in}$ measured on the more accurate **Signal recovery 7280/98 lock-in amplifier** at 33.333kHz. The linear correction factor for the fluke multimeter is $V_{rms}^{fluke,corrected} = 0.9983 * V_{rms}^{fluke}$.

two lock-in amplifiers, as the fundamental (a) and 2-harmonic (b) signal, respectively. As the used value is the ratio b/a, the systematic error is the ratio of errors from the two lock-in amplifiers. To determine the ratio error, A is measured 10 times for a chosen $A_{electric}$-value ($V_{rms}^{fluke,corrected} = 704.9mV$) and then remeasured 9 times after the two lock-in amplifiers have been interchanged. The measured results are plotted in fig. (B.3).
As shown in fig. (B.3) the difference between the average V_π-value before and after interchange of the lock-in amplifiers is **0.5**‰.

An error also occur from the A/D converter used to measure the output from the lock-in amplifiers. The 4 outputs from the lock-in amplifiers are the fundamental x-value (x_f), the fundamental y-value (y_f), the 2-harmonic x-value (x_{2-H}) and finally the 2-harmonic y-value (y_{2-H}). The

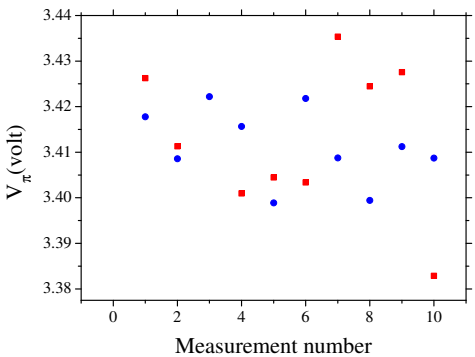

Figure B.3: The points are measured values of V_π for repeated measurements for the same modulation voltage ($V_{rms}^{fluke,corrected} = 704.9mV$). The blue points are measured before interchanging the lock-in amplifiers and the red points are measured after interchanging the lock-in amplifiers. The difference between the average value of the measured V_π-values before and after interchange of the two lock-in amplifiers is 0.5‰. As there is no systematic derivation between the blue and red points it is expected that the difference in average value would approach zero if enough measurements where compared, but the derivation of 0.5‰ is still used to be on the save side.

corresponding[3] values of (x_f) and of (y_f) are plotted as points $\{x_f, y_f\}$ in fig. (3.8). To determine the error introduced by the A/D converter, the four outputs $(x_f, y_f, x_{2-H}, y_{2-H})$ from the two lock-in amplifiers are connected to the four A/D-converter inputs (I_1, I_2, I_3, I_4) in 3 different ways. That is

$$\begin{aligned}
&\text{1 connection:} \quad x_f \to I_1,\ y_f \to I_2,\ x_{2-H} \to I_3 \text{ and } y_{2-H} \to I_4 \\
&\text{2 connection:} \quad x_f \to I_2,\ y_f \to I_1,\ x_{2-H} \to I_4 \text{ and } y_{2-H} \to I_3 \\
&\text{3 connection:} \quad x_f \to I_3,\ y_f \to I_4,\ x_{2-H} \to I_1 \text{ and } y_{2-H} \to I_2
\end{aligned} \tag{B.2}$$

The value of V_π is measured for the same $A_{electric}$-value ($V_{rms}^{fluke,corrected} = 704.1mV$) 10 times for each of the 3 connections. The measured results are plotted in fig. (B.4).

[3] Corresponding values are measured simultaneously.

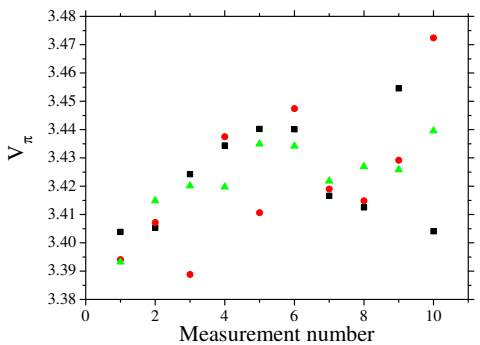

Figure B.4: The points are measured values of V_π for repeated measurements for the same modulation voltage ($V_{rms}^{fluke,corrected} = 704.1mV$). The blue points are measured for the 1 connection, the red for the 2 connection and the green for the 3 connection (see eq. B.2). The largest difference between the average measured V_π-values is 0.44‰. There is not observed any systematic derivation between the 3 measurement series and it is likely that the derivation between the 3 average values would approach zero if enough measurements where made. To be on the save side, the derivation of 0.44‰ is still applied.

As shown in fig. (B.4), the largest difference in average V_π-value when interchanging the A/D-converter inputs is less than **0.44‰**. **The iterative polar fitting procedure** introduces a systematic error smaller than **1‰** (see section A.5). The total systematic error for the determined V_π-value is

$$\sigma_s(V_\pi) = \sqrt{\underbrace{(6‰)^2}_{voltmeter} + \underbrace{(0.5‰)^2}_{lock-in} + \underbrace{(0.44‰)^2}_{A/D-converter} + \underbrace{(1‰)^2}_{Ellipsoid_{fit}}} = 6.1‰. \quad \text{(B.3)}$$

The largest error is introduced by measuring the amplitude of the electrical sinus signal on the $LiNbO_3$ modulator. The voltmeter used for the measurement is calibrated against a lock-in amplifier. The **Signal recovery 7280/98 lock-in amplifier** is a precision instrument and it is therefore not easy to decrease this error. The systematic error (eq. B.3) and the reproducibility error (see the last column in table 3.1 in section 3.3.3) are both around 5‰. I.e. it is not easy to decrease the error further as both the systematic and the reproducibility errors should be decreased simultaneously to obtain a better result.

The value of V_π is measured as function of laser wavelength. The center wavelength of the laser light is measured using a **HP 86120B multi-wavemeter**. The instrument is guaranteed to measure the center wavelength within **±3ppm**. The linewidth of the laser is measured using an optical spectrum analyzer (OSA). A typical result is shown in fig. (B.5).
The uncertainty of the wavelength is chosen as halve width for a 10dB[4] drop of the intensity. The typical wavelength uncertainty is **±10ppm**. The laser wavelength error is therefore

$$\sigma_s(\lambda) = \sqrt{\underbrace{(3ppm)^2}_{HP86120B} + \underbrace{(10ppm)^2}_{fig.(B.5)}} = 10.0ppm. \quad \text{(B.4)}$$

There is no reproducibility error for the laser wavelength determination, as the wavemeter is guaranteed to be accurate within $3ppm$ and this error includes all kind of errors. For the $LiNbO_3$ measurement experiment, the uncertainties are

[4]The choice of 10 dB is arbitrary, but the resulting wavelength uncertainty is large enough to ensure the "true" result is within the uncertainty bar.

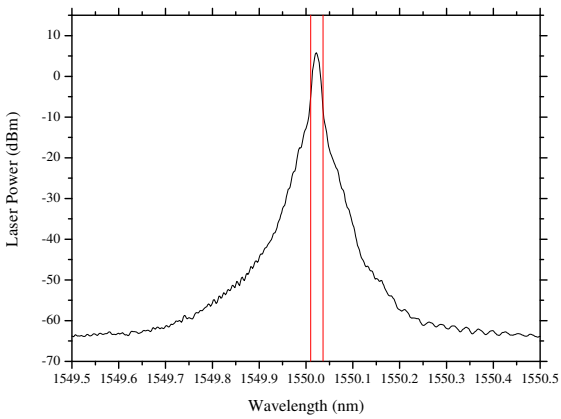

Figure B.5: Spectrum of the an Ando 4321A laser, when the laser emits at 1550 nm. The halve width at 10 dB attenuation is 0.015nm, which is equal to an error of $\pm 10ppm$. Due to the limited spectral resolution of the optical spectrum analyzer (0.01nm) the measured linewidth could therefore be artificial broaden, i.e. the real error is probably even smaller than $\pm 10ppm$.

Uncertainty for experimental measurement of V_π for $LiNbO_3$ modulator

Wavelength systematic error	V_π systematic error	V_π reproducibility error
$10ppm$	6.1‰	< 5.5‰

Table B.1: The error of the determined V_π value for the $LiNbO_3$ modulator is quite low and to get more accurate results, the systematic error and the reproducibility error must be reduced simultaneously. There exists, to the authors knowledge, no easy way for obtaining such error reduction.

B.3 $\chi^{(2)}$ measurements.

The setup used to measure $\chi^{(2)}_{Si}$ is shown in fig. (B.6). Uncertainty is introduced by the 5 red components.
The voltmeter used is a **Fluke 45 dual display multimeter**. It is not

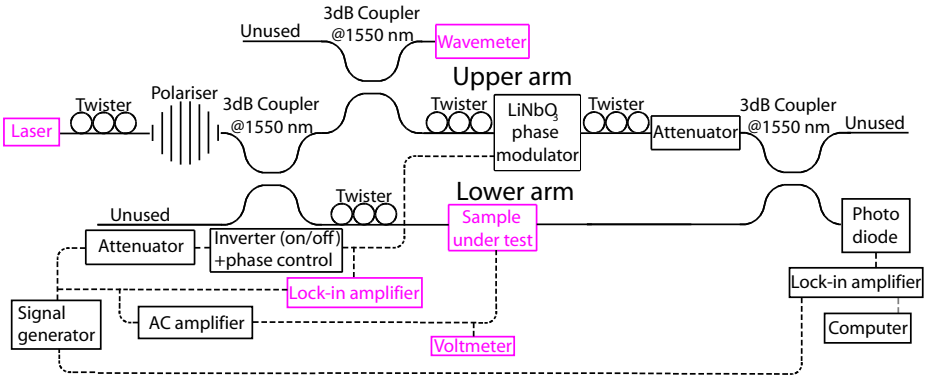

Figure B.6: The MZI used for measuring $\chi^{(2)}$. The 5 red components introduces a systematic error.

specified to work beyond 100 kHz, but the applied modulation frequency is 200 kHz. The modulation voltage on the sample is always roughly the same (the maximum $\sim 110 V_{rms}^{HP34401A}$). To establish the uncertainty of the **Fluke 45 dual display multimeter** at 200 kHz, simultaneous measurements on a high AC-voltage are made with two voltmeters. That is with the **Fluke 45 dual display multimeter** and with a **HP 34401A multimeter**. The HP multimeter is guaranteed to be accurate within 4% at 200 kHz. The result of the measurement is shown in fig. (B.7). After correcting the fluke voltmeter readout, the measurement error is

$$\sigma(fluke, 200kHz) = \sqrt{\underbrace{(4\%)^2}_{HP34401A} + \underbrace{(0.06‰)^2}_{fig.(B.7)}} = \mathbf{4.0\%}. \tag{B.5}$$

The **Fluke 45 dual display multimeter** is used in the MZI setup (see fig. B.6), as the **HP 34401A multimeter** was borrowed from a different DTU department.

The uncertainty of the lock-in amplifier is guaranteed to be less than **6**‰ and the wavelength uncertainty is **10ppm** (see eq. B.4). To determine $\chi_{Si}^{(2)}$, the length (l_{sample}), the height (d_{sample}) and the bulk phase refractive index ($n_{\phi,bulk}$) must also be determined, as $\chi_{Si}^{(2)}$ is (see eq. 3.58)

$$\chi_{Si}^{(2)} = -s_{inv} \frac{\lambda d_{sample} n_{\phi,bulk,0,Si} A_1^{electric}}{2 l_{sample} V_{\pi} \varsigma A_2^{electric} \Gamma_{Si}}. \tag{B.6}$$

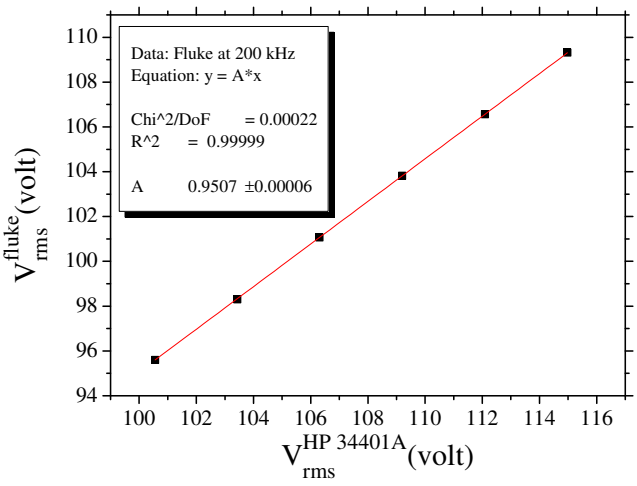

Figure B.7: V_{rms}^{fluke} measured on the **Fluke 45 dual display multimeter** vs. $V_{rms}^{HP34401A}$ measured on a **HP 34401A multimeter** at 200 kHz. The corrected value is found by multiplying the fluke readout with 1.052.

As the only sample type investigated with a pure $\chi^{(2)}$-value are photonic crystal (PhC) waveguides, the length (l_{sample}) is determined by the fabrication process. The sample is fabricated by CMOS technique and the design lengths are therefore replicated in a quasi perfect manner. The derivation is around $1\mu m$ for the whole sample (length 3 cm). The uncertainty for the sample length due to fabrication is therefore less than 0.1‰. The origin of the length uncertainty is therefore not fabrication, but the trouble of defining how fast the waveguide changes characteristics from a normal buried waveguide to a PhC waveguide. On fig. (B.8) it is demonstrated, that the absolute length uncertainty equals halve the pitch ($\Delta/2$). For a $20\mu m$ PhC waveguide with 425nm pitch, the systematic uncertainty is **2.1**%.
The refractive index ($n_{\phi,bulk,0,Si}$) in eq. (B.6) is the bulk index of the nonlinear material. In this project the only material type having a pure $\chi^{(2)}$ value is silicon. The index of single crystalline silicon in the commer-

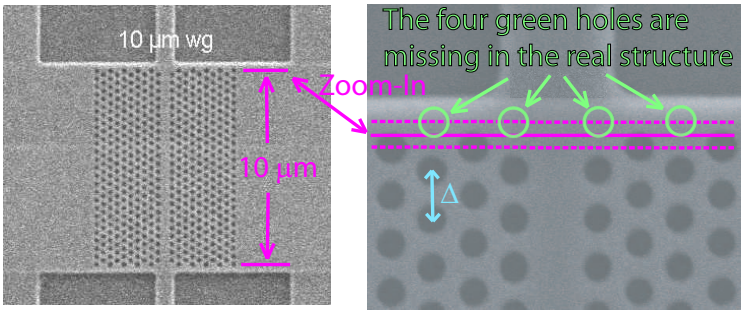

Figure B.8: Picture of a $10\mu m$ PhC waveguide. There is $10\mu m$ from the center of the first row of holes to the center of the last row of holes. The problem with the length definition is to point at the correct beginning of the PhC waveguide. On the zoom-in at the beginning of a waveguide, the definition problem is better illustrated. The buried waveguide ends in a slab structure, where the light propagates until it enters the PhC waveguide. The photonic crystal waveguide starts at the horizontal line where the horizontal periodic structure begins. This line is however ill-defined, as the periodic structure begins somewhere between the center of the 4 green holes (the missing hole) and the center of the first row of holes. These two lines are marked with a dotted red line. The middle in between the two possibly beginnings marked with a solid red line is here defined as the start of the PhC waveguide. The uncertainty of this definition equals the distance between the solid red line and the dotted red line, which equals a quarter of the pitch ($\Delta/4$). There is the same uncertainty at the other end of the waveguide, and the total uncertainty therefore equals halve the pitch ($\Delta/2$).

cial SOI wafers used is $3.478 \pm \mathbf{1}‰$. The refractive index of silicon is not measured for the specific sample, but a smooth curve approximation (see fig. B.9) to reported [1] measurements for the bulk phase refractive index of silicon gives this value. The uncertainty is determined by comparing the determined result with other ($n_{\phi,bulk,0,Si} = 3.476$) reported [2] index values of silicon.

The sample thickness (d_{sample}) is determined by a microscope picture of the samples end facet, as shown in fig. (B.10).

The distance in pixels is converted to μm using a converting factor. There is both a systematic error and a reproducibility error in connection with the thickness measurement. The systematic error is due to uncertainty of the conversion factor ($32.23nm/pixel \pm \mathbf{4}‰$). The repeatability error for a single measurement is determined to 6%, by measuring the height of a sample 10 times. To reduce the uncertainty, the height is measured at

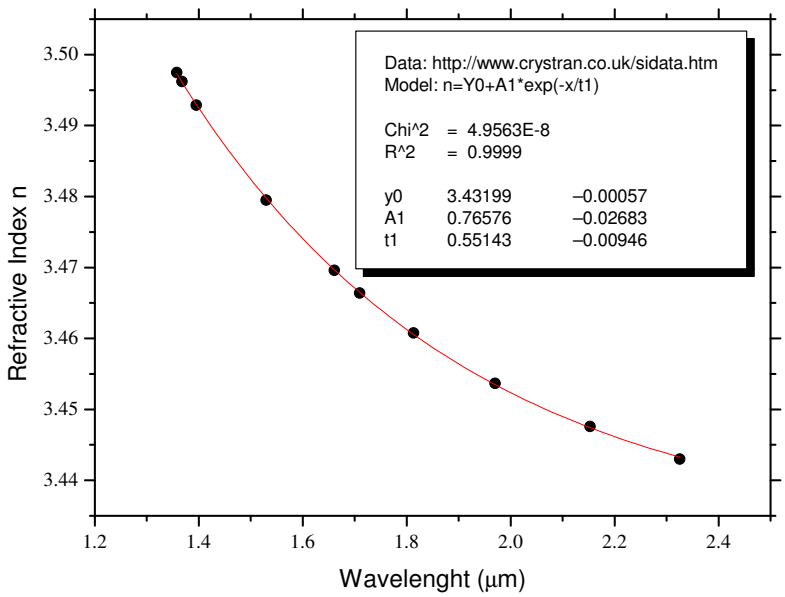

Figure B.9: The points are measured values of the refractive index of crystalline silicon from [1]. The red curve is a smooth curve approximation without any physical origin. The refractive index of silicon is found to 3.478 using this method, while it is evaluated to 3.476 using the Sellmeier type equation in [2]. The uncertainty of the number is therefore around 1‰.

least 3 times for each sample and the measurement uncertainty is therefore **3.5**%. The total systematic error for a $\chi^{(2)}$ measurement is

$$\sigma_s(\chi^{(2)}) = \left(\underbrace{(4\%)^2}_{voltmeter} + \underbrace{(6‰)^2}_{lock-in} + \underbrace{(10ppm)^2}_{\lambda-width} + \underbrace{(2.1\%)^2}_{l_{sample}} + \underbrace{(4‰)^2}_{d_{sample}} + \underbrace{(1‰)^2}_{n_{sample}} + \underbrace{(6.1‰)^2}_{V_\pi} \right)^{1/2} = 4.6\%. \quad \text{(B.7)}$$

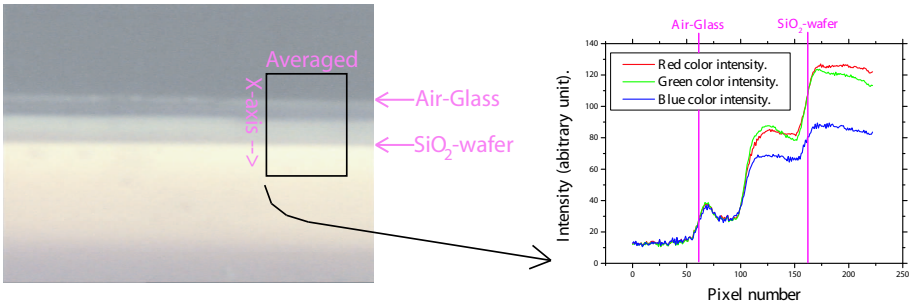

Figure B.10: The left picture is a microscope image of the end facet of sample $c2r4$. The sample thickness (d_{sample}) is determined by averaging the intensity over the box along the direction called **Average**. The result of the averaging is shown in the right figure, where the intensity of the colors are plotted. The first vertical line marks the boarder between air and the sample. The other vertical line marks the boarder between the bottom glass and the silicon wafer.

The total reproducibility error is due to the electrode-electrode distance (d_{sample}) measurement as already discussed and to the reproducibility error of the $\chi^{(2)}$ measurement. The reproducibility error for the $\chi^{(2)}$ measurement is around **4%** (see fig. B.11).
The total reproducibility error is therefore

$$\sigma_r(\chi^{(2)}) = \sqrt{\underbrace{(3.5\%)^2}_{d_{sample}} + \underbrace{(4\%)^2}_{(fig.(B.11)}} = 5.3\%. \tag{B.8}$$

Both the systematic and the reproducibility error for the $\chi^{(2)}$ measurement has been described. The dominant systematic error is due to the voltmeter used for calibrating the **Fluke 45 dual display multimeter**. To reduce this uncertainty, it would be advisable to permanently use a more accurate voltmeter (e.g. **Fluke 8508A** with uncertainty $< 5‰$), as a more accurate calibration of the **Fluke 45 dual display multimeter** could be compromised by drift.

To reduce the repeatability error, the optical loss in the sample must be reduced. The repeatability error would then approach the error for the repeated $\chi^{(3)}$ measurement of 1% (see fig. B.17 later in this appendix).

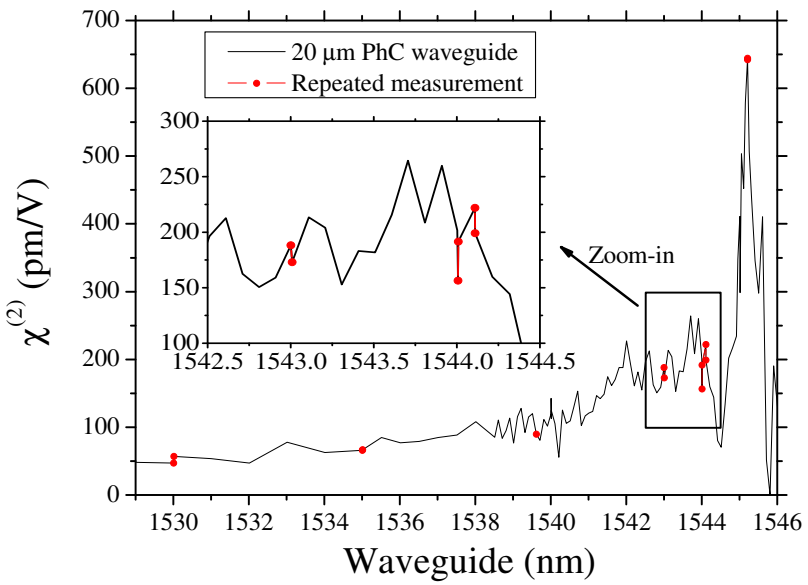

Figure B.11: Measurement of $\chi^{(2)}_{Si}$ for a $20\mu m$ PhC. waveguide. The length is chosen as close as possible to $20\mu m$ for the applied pitch of 425nm. The length is in reality $20.19\mu m$. The red points are remeasured to determine the accuracy of the measurement. The average error is less than 4%.

Uncertainty for experimental measurement of $\chi^{(2)}$		
Wavelength systematic error	$\chi^{(2)}$ systematic error	$\chi^{(2)}$ reproducibility error
$10ppm$	4.6%	5.3%

Table B.2: The error for determination of $\chi^{(2)}$ is dominated by the reproducibility error due to a high optical loss in the PhC. waveguides. The systematic error could be reduced by using a more accurate voltmeter.

B.4 $\chi^{(3)}$ measurements.

The setup used to measure $\chi^{(3)}$ is shown in fig. (B.12). Uncertainty is introduced by the 8 red components.

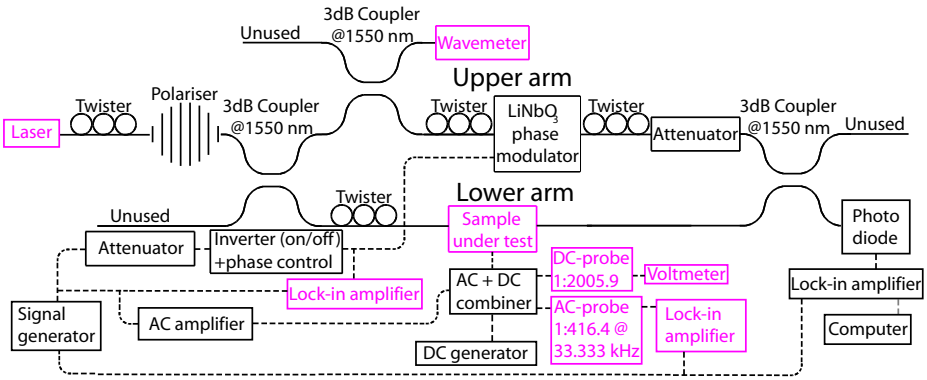

Figure B.12: The MZI used for measuring $\chi^{(2)}$. The 6 red boxes introduces systematic errors.

The probe values have been determined by simultaneously measuring the voltage before and after the probe. The DC-probe value was measured using the **Fluke 45 dual display multimeter** before the probe and the **HP 34401A multimeter** after the probe. The measurement is shown in fig. (B.13).
The uncertainty of the **Fluke 45 dual display multimeter** at DC is guaranteed to be less than 0.25‰ and the uncertainty of the **HP 34401 A multimeter** at DC is guaranteed to be less than 0.1‰. The accuracy of the DC-probe value is therefore better than **0.3**‰ (see eq. B.9).

$$\sqrt{\underbrace{(0.25‰)^2}_{Fluke} + \underbrace{(0.1‰)^2}_{HP34401A} + \underbrace{(0.04‰)^2}_{fig.(B.13)}} = 0.27‰ \tag{B.9}$$

The AC-probe is measured using the **HP 34401 A multimeter** to measure the high voltage AC before the probe and using the **Signal recovery 7280/98 lock-in amplifier** to measure after the probe. The result is shown in fig. (B.14)
The uncertainty of the **HP 34401 A multimeter** at 33.333kHz is guaranteed to be less than 4% and the uncertainty of the **Signal recovery**

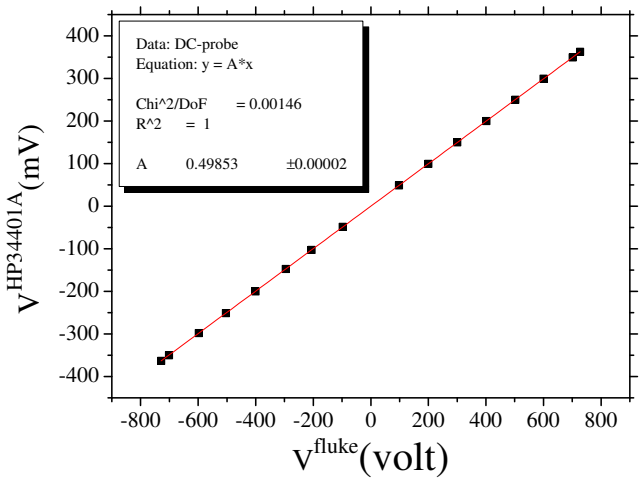

Figure B.13: DC-voltage after the DC-probe vs. the input DC-voltage. The DC-probe is 1:2005.9.

7280/98 lock-in amplifier is guaranteed to be less than 6‰. The accuracy of the measured value for the AC-probe is therefore better than **4.1**% (see eq. B.10).

$$\sqrt{\underbrace{(4\%)^2}_{HP34401A} + \underbrace{(6‰)^2}_{Lock-in} + \underbrace{(0.025‰)^2}_{fig.(B.14)}} = 4.04\% \tag{B.10}$$

The uncertainty of the **Signal recovery 7280/98 lock-in amplifier** used to measure the electrical signal at the $LiNbO_3$ modulator and used for measuring the AC-voltage after the AC-probe is guaranteed to be less than **6**‰. The uncertainty of the **Fluke 45 dual display multimeter** used to measure on the DC-voltage after the DC-probe is guaranteed to be less than **0.25**‰ and the accuracy of the laser wavelength is **10ppm** (see eq. B.4).

To determine $\chi^{(3)}$, the length (l_{sample}), height (d_{sample}) and refractive

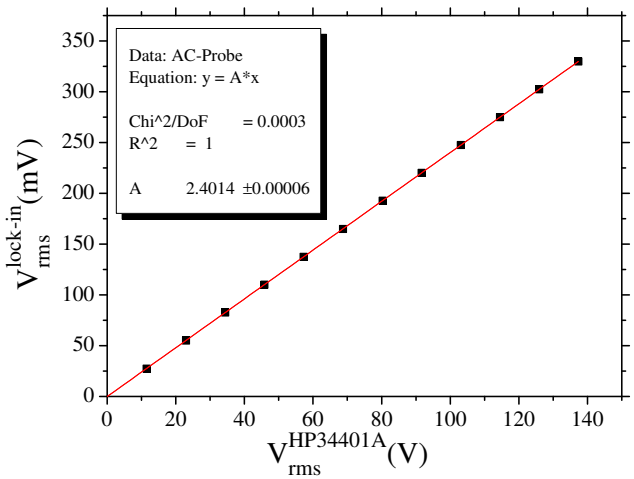

Figure B.14: AC-voltage after the AC-probe vs. the input voltage at 33.333kHz. The AC-probe is 1:416.4 at 33.333kHz.

index (n_{sample}) must also be measured, as $\chi^{(3)}$ is

$$\underbrace{3\chi_{av}^{(3)}\left(\frac{V_{DC}}{d_{sample}}+E_{frozen-in}\right)}_{=\chi_{eff}^{(2)}} = -s_{inv}\frac{\lambda d_{sample} n_{\phi,eff,0} A_1^{electric}}{2 l_{sample} V_\pi A_2^{electric}} \quad \text{(B.11)}$$

As noted in section (2.3), the effective $\chi_{av}^{(3)}$ is the weighted sum of the different material contributions. The weighting factor is the confinement factor to the material. As only the effective $\chi_{av}^{(3)}$ is measured, the effective phase refractive index ($n_{\phi,eff,0}$) is used instead of the materials bulk phase refractive indexes as a good approximation of the confinement factor weighted refractive index. $n_{\phi,eff,0}$ is either determined using the Bragg wavelength (see appendix C) or calculated from the measured material refractive indexes using the finite difference approximation[5]. The

[5] Calculations of the group index was made using the commercial software TempSelene.

error connected with the Bragg determination of $n_{\phi,eff}$ is as noted in appendix (C) negligible due to the fabrication procedure. The error of the calculated $n_{\phi,eff,0}$ is estimated to be less than 1% by calculating $n_{\phi,eff,0}$ for a sample (127_1) containing a Bragg grating and then comparing calculations with measurements. The length (l_{sample}) is measured by looking at the electrode edge through a microscope and then translating the sample with a micrometer screw until the other end of the electrode is seen in the center of the microscope. This is illustrated in fig. (B.15). There are two kinds of uncertainties connected with the length measurement, the systematic uncertainty due to the calibration error of the micrometer screw ($< \mathbf{0.5}‰$) and the repeatability uncertainty. The typical repeatability uncertainty for a single measurement is $\mathbf{1.5}‰$ and it is found by repeating a length measurement 10 times.
The sample thickness d_{sample} is measured using a microscope picture, as shown in fig. (B.16).
The distance in pixels is converted to μm using a converting factor. There is both a systematic error and a reproducibility error in connection with the thickness measurement. The systematic error is due to uncertainty of the conversion factor ($32.23 nm/pixel \pm \mathbf{4}‰$). The repeatability error is determined to 1.5%, by measuring the height of a sample 10 times. To improve the accuracy, each height measurement is repeated 3 times and the standard derivation of the measured mean value is therefore $< \mathbf{1}\%$. The total systematic error for a $\chi^{(3)}$ measurement is

$$\sigma_s(\chi^{(3)}) = \left(\underbrace{(4.1\%)^2}_{AC-probe} + \underbrace{(0.5‰)^2}_{DC-probe} + \underbrace{(0.25‰)^2}_{fluke} + \underbrace{(10ppm)^2}_{\lambda-width} + \underbrace{(0.5‰)^2}_{l_{sample}} + \underbrace{(2*4‰)^2}_{d_{sample}} + \underbrace{(1\%)^2}_{n_{\phi,eff}} + \underbrace{(6.1‰)^2}_{V_\pi} \right)^{1/2} = 4.3\%. \quad \text{(B.12)}$$

The same lock-in amplifier is used to measure both $A_1^{electric}$ and $A_2^{electric}$. The ratio of the values is used for determination of $\chi_{av}^{(3)}$ and the systematic error from the lock-in amplifier is therefore cancelled out.

The repeatability error is due to the length measurement, the height measurement and the $\chi_{av}^{(3)}$ measurement. In principle, the uncertainty for

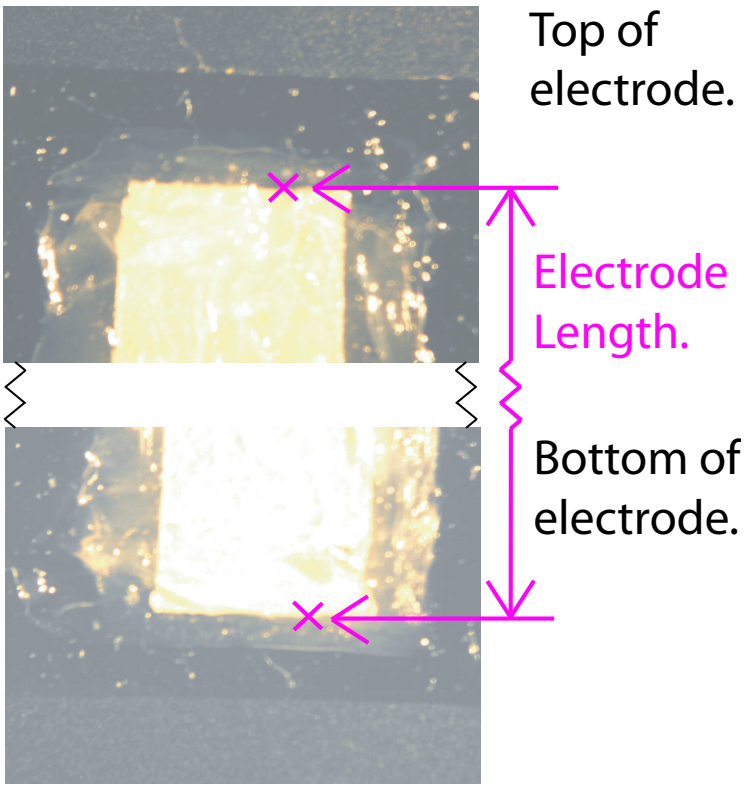

Figure B.15: The length of the electrode is measured by moving the top electrode into the center of the microscope picture. The sample is then translated using a micrometerscrew until the bottom of the electrode is in the center of the electrode. The electrode length then equals the translation distance on the micrometerscrew.

$n_{\phi,eff,0}$ should also be included, but it is negligible when measured using a Bragg grating. The reproducibility error of a $\chi^{(3)}_{av}$ measurement is less than **1**% (see fig. B.17).
The total reproducibility error is

$$\sigma_r(\chi^{(3)}) = \sqrt{\underbrace{(3\%)^2}_{d_{sample}} + \underbrace{(1.5‰)^2}_{l_{sample}} + \underbrace{(1\%)^2}_{(fig.(B.17))}} = 3.1\%. \qquad \text{(B.13)}$$

The reproducibility error is only approximate, as the $\chi^{(3)}$ contribution is evaluated separately each time. The uncertainty in connection with the

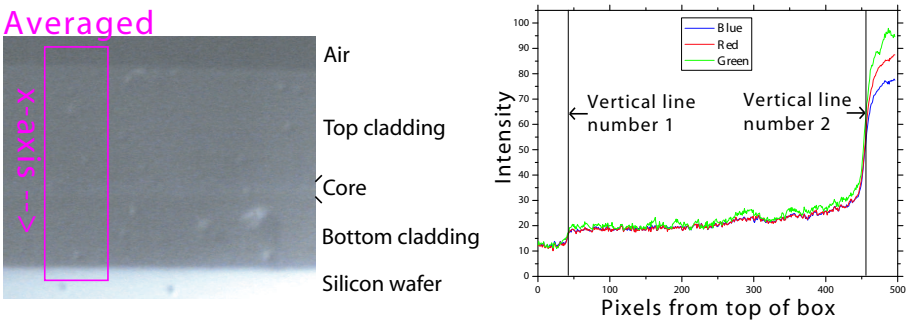

Figure B.16: The left picture is a microscope picture of the end facet of sample 125_1. The sample thickness (d_{sample}) is determined by averaging the intensity over the red box. The result of the averaging is shown in the right figure, where the intensity of the colors are plotted. The first vertical line (number 1) marks the boarder between air and the sample. The other vertical line (number 2) marks the boarder between the bottom glass and the silicon wafer.

$\chi^{(3)}$ measurement is summarized in table (B.3).

Uncertainty for experimental measurement of $\chi^{(3)}$		
Wavelength systematic error	$\chi^{(3)}$ systematic error	$\chi^{(3)}$ reproducibility error
$10ppm$	4.3%	3.1%

Table B.3: The systematic error and the reproducibility error are approximately equal. To reduce the error further, both error types must be reduces simultaneously. The dominating term for the systematic error is the AC-probe value, which can be improved by using a more accurate voltmeter (e.g. the voltmeter **Fluke 8508A** uncertainty $< 1‰$) instead of the **HP 34401 A multimeter**. The reproducibility error is dominated by the measurement of the electrode-electrode distance (d_{sample}). This could be improved by using a measurement technique based on interferometric, but the uncertainty is ultimately limited by the fact that d_{sample} varies on the sample. It is therefore unlikely, that the error can be reduced significantly.

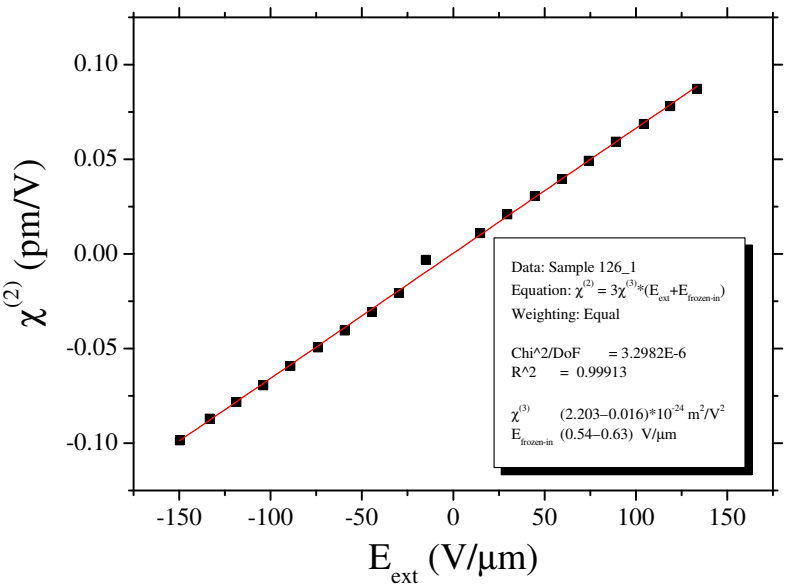

Figure B.17: The induced E-O coefficient ($\chi^{(2)}_{eff}$) is measured as function of external applied electric field. The ($\chi^{(3)}_{av}$) value is found by fitting the experimental data with a straight line. The uncertainty of the determined ($\chi^{(3)}_{av}$) value is only due to the measured points derivation from the theoretical straight line. The uncertainty is less than 1%.

References to Appendix B

[1] "http://www.crystran.co.uk/sidata.htm". Homepage with crystal information.

[2] "Optical functions of intrinsic si: Region of near transparency", 1987. EMIS datareview RN=17803.

Appendix C

The Bragg grating measurement method.

C.1 Introduction.

The Bragg grating measurement method was used to characterize samples early in this project. A more reliable and easier method was develop during the project and the Bragg grating method was then abandoned. The Bragg grating method measures the obtained shift of Bragg wavelength, when the effective index ($n_{\phi,eff}$) is changed due to an applied electric field. In this appendix, the production of a Bragg grating is shown and the connection between Bragg wavelength and applied field is derived.

C.2 Making a Bragg grating.

When very intense laser light is shined onto UV-sensitive glass, the index of refraction is changed permanently in the glass. This phenomenon can be used to change the index of refraction in a periodic manor along the waveguide by shining light onto the sample through a phase mask, as shown in fig. (C.1) below.
There is etched small grooves into the phase mask. The etching deep is adjusted in such a way, that the difference in optical path length between the light propagating inside the glass and light propagating in the etched grooves (in air) equals $\lambda/2$ on exit from the phase mask (λ is the

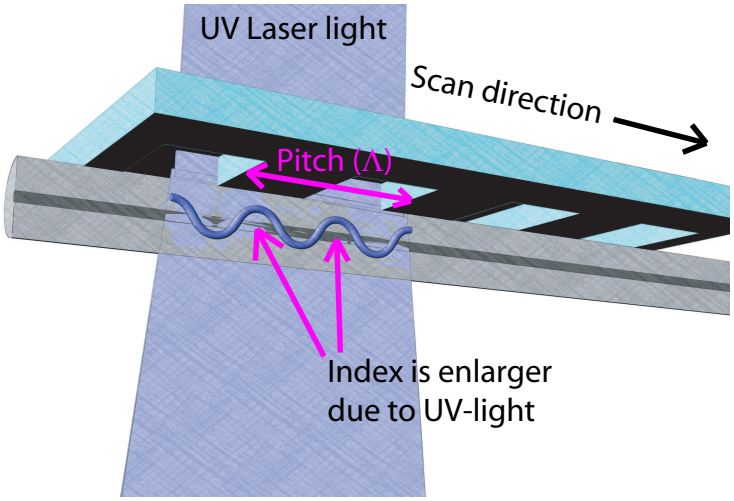

Figure C.1: Picture of a Bragg grating being made in a fiber. The phase mask lying on top of the fiber creates an interference pattern with the period $\Lambda/2$. The fiber core is UV-sensitive and its refractive index is raised permanently, at the places where the intensity of the UV-light is high. Due to the periodicity of the phase mask, the index varies periodically along the fiber core. The laser beam is scanned over the length of the phase mask, when the grating is made. There was typical used $1kJ/cm^2$ to write the grating with a pulsed Eximer laser (see section 4).

wavelength of the UV laser light). The periodic length of the phase mask is called the pitch (Λ). The interference pattern from the light gives a varying intensity along the waveguide and the index of the waveguide is enlarge periodically.

The inscribed periodic index contrast is called a Bragg grating. When light is sent into the waveguide, it is reflected when the backwards scattering light adds up in phase. The first order reflection is for light with a wavelength λ_m in the material such that light is reflected at every interface between high and low index material, that is $\lambda_m = \Lambda$. It is more convenient to write the equation in terms of vacuum wavelength, i.e.

$$\lambda_{Bragg} = n_{\phi,eff}\Lambda \tag{C.1}$$

Light with a slightly different wavelength is also reflected and the reflection coefficient vs. wavelength can be derived mathematically using coupled wave theory [1]. A transmission spectrum of a typical grating is

shown in fig. (C.2), and the curve is approximated with a Gauss function. The center wavelength is determined from the fitted Gauss.

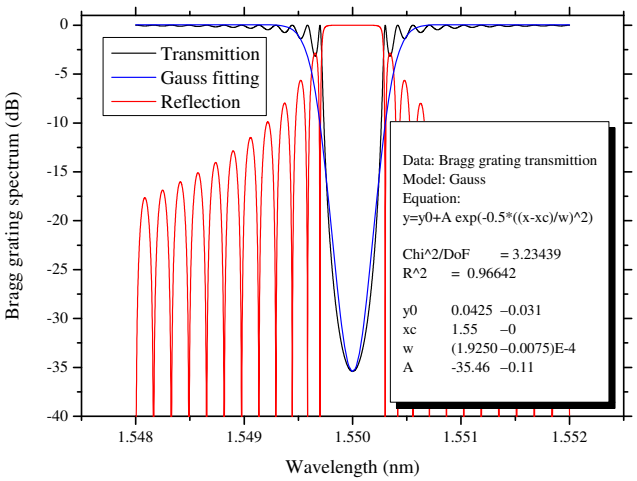

Figure C.2: Bragg grating for a 5mm long grating in a fiber core with a permanent index modulation of 0.001. The Bragg wavelength is determined by fitting the transmission spectrum with a Gauss function.

The uncertainty of the measured Bragg wavelength is around 2ppm and as the pitch Λ of the phase mask is known with 6 digits (for example 1050.59nm), the refractive index is determined with 5 figures of accuracy from the Bragg wavelength. Combining eq. (C.1) with eq. (2.15) describing the wavelength change due to third order non-linearity gives

$$\Delta\lambda_{Bragg} = \Lambda \frac{3\chi^{(3)}_{av}}{2n_{\phi,eff,0}} E^2. \tag{C.2}$$

The quadratic increase in λ_{Bragg} is exactly what is observed in measurements of the Bragg wavelength vs. external applied electric field (see fig. 2.16).

References to Appendix C

[1] "Fiber lasers", 2002. Notes - contact jhp@com.dtu.dk.

Appendix D

Derivation of $\Delta n_{\phi,bulk}(E)$ for a $\chi^{(3)}$ material.

The Maxwell equations in matter are (in SI units)

$$\nabla \cdot \mathbf{D} = \rho_f \tag{D.1}$$

$$\nabla \times \mathbf{E} = -\frac{\partial \mathbf{B}}{\partial t} \tag{D.2}$$

$$\nabla \cdot \mathbf{B} = 0 \tag{D.3}$$

$$\nabla \times \mathbf{H} = \mathbf{J}_f + \frac{\partial \mathbf{D}}{\partial t}, \tag{D.4}$$

where ρ_f are the free charges and $\mathbf{J}_f$ are the free currents. Glass is magnetic linear and the magnetic susceptibility is approximately zero, that is

$$\mathbf{B} = \mu_0 \mathbf{H} \tag{D.5}$$

In our experiment, it is assumed that there are no free charges and no free currents inside the sample. This assumption is correct for materials with a $\chi^{(3)}$ value as the sample is made out of electric isolating material (glass). In the case of samples with a silicon core, there are some free charges, but the number of free charges does not affect the results, as shown in fig. (6.5). That is

$$\rho_f = 0 \tag{D.6}$$

$$\mathbf{J}_f = 0. \tag{D.7}$$

With these assumptions the Maxwell equations can be written

$$\nabla \cdot \mathbf{D} = 0 \tag{D.8}$$

$$\nabla \times \mathbf{E} = -\frac{\partial \mathbf{B}}{\partial t} \tag{D.9}$$

$$\nabla \cdot \mathbf{B} = 0 \tag{D.10}$$

$$\nabla \times \mathbf{B} = \mu_0 \frac{\partial \mathbf{D}}{\partial t}. \tag{D.11}$$

Using the curl operator ($\nabla\times$) on eq. (D.9) and then substituting using eq. (D.11), gives

$$\nabla \times \nabla \times \mathbf{E} = -\nabla \times \frac{\partial \mathbf{B}}{\partial t} = -\frac{\partial}{\partial t}\nabla \times \mathbf{B} = -\mu_0 \frac{\partial^2 \mathbf{D}}{\partial t^2} \tag{D.12}$$

As glass is not electrical linear, the general relation between the $\mathbf{D}$ field and the $\mathbf{E}$ field must be used, that is

$$\mathbf{D} = \epsilon_0 \mathbf{E} + \mathscr{P}, \tag{D.13}$$

where $\mathscr{P}$ is the polarization density vector. Using this relation and the operator relation $\left(\nabla \times \nabla \times \mathbf{A} = \nabla(\nabla \cdot \mathbf{A}) - \nabla^2 \mathbf{A}\right)$ in eq. (D.12), gives

$$\nabla(\nabla \cdot \mathbf{E}) - \nabla^2 \mathbf{E} = -\mu_0 \epsilon_0 \frac{\partial^2 \mathbf{E}}{\partial t^2} - \mu_0 \frac{\partial^2 \mathscr{P}}{\partial t^2} \tag{D.14}$$

The weakly guided approximation gives $\nabla(\nabla \cdot \mathbf{E}) = 0$ which in turn gives the propagation equation

$$\nabla^2 \mathbf{E} - \mu_0 \epsilon_0 \frac{\partial^2 \mathbf{E}}{\partial t^2} = \mu_0 \frac{\partial^2 \mathscr{P}}{\partial t^2} \tag{D.15}$$

The polarization density is a function of the electric field, that is

$$\mathscr{P}_i = \epsilon_0 \left(\chi_{ij} E_j + \chi^{(2)}_{ijk} E_j E_k + \chi^{(3)}_{ijkl} E_j E_k E_l + \ldots \right), \tag{D.16}$$

where Einstein's notation for summation has been used. As glass is isotropic $\underline{\underline{\chi}} = \chi * \underline{\underline{I}}$, $\chi^{(2)}_{ijk} = 0 \, \forall i,j,k$ and the only nonzero elements of the $\chi^{(3)}$ tensor are listed in table (D.1).

Elements of $\chi^{(3)}$.
$\chi^{(3)}_{1111} = \chi^{(3)}_{2222} = \chi^{(3)}_{3333}$
$\chi^{(3)}_{1122} = \chi^{(3)}_{1133} = \chi^{(3)}_{2211} = \chi^{(3)}_{2233} = \chi^{(3)}_{3311} = \chi^{(3)}_{3322}$
$\chi^{(3)}_{1212} = \chi^{(3)}_{1313} = \chi^{(3)}_{2121} = \chi^{(3)}_{2323} = \chi^{(3)}_{3131} = \chi^{(3)}_{3232}$
$\chi^{(3)}_{1221} = \chi^{(3)}_{1331} = \chi^{(3)}_{2112} = \chi^{(3)}_{2332} = \chi^{(3)}_{3113} = \chi^{(3)}_{3223}$
$\chi^{(3)}_{1111} = \chi^{(3)}_{1122} + \chi^{(3)}_{1212} + \chi^{(3)}_{1221}$

Table D.1: The non-vanishing elements of the $\chi^{(3)}$ tensor and the relations between these elements for isotropic symmetry [1].

For an isotropic material, the polarization density matrix can be split into a linear $\mathscr{P}^L$ and a non-linear $\mathscr{P}^{NL}$ part, that is

$$\mathscr{P}_i = \underbrace{\epsilon_0 \chi E_i}_{\mathscr{P}_i^L} + \underbrace{\epsilon_0 \chi^{(3)}_{ijkl} E_j E_k E_l}_{\mathscr{P}_i^{NL}}, \tag{D.17}$$

where terms of order higher than three are set to zero. The propagation equation (D.15) can be written as

$$\nabla^2 \mathbf{E} - \frac{1+\chi}{c_0^2} \frac{\partial^2 \mathbf{E}}{\partial t^2} = \mu_0 \frac{\partial^2 \mathscr{P}^{NL}}{\partial t^2}, \tag{D.18}$$

where the relation $(1+\chi)\epsilon_0\mu_0 = \frac{1+\chi}{c_0^2}$ has been used. To solve this differential equation approximately for light propagating in the x-direction subjected to an electric DC field in the z-direction, guesses for two solutions are made. That is a TE polarized solution

$$\mathbf{E} = \begin{pmatrix} 0 \\ E_{op} \\ E_{DC} \end{pmatrix} \tag{D.19}$$

and the TM polarized solution

$$\mathbf{E} = \begin{pmatrix} 0 \\ 0 \\ E_{op} + E_{DC} \end{pmatrix}, \tag{D.20}$$

where $E_{op} = Re(E(\omega)e^{i\omega t})$. To find the TE solution, $\mu_0 \frac{\partial^2 \mathscr{P}^{NL}}{\partial t^2}$ for TE is derived

$$\begin{aligned}
\mu_0 \left(\frac{\partial^2 \mathscr{P}^{NL}}{\partial t^2}\right)_1 &= \frac{1}{c_0^2}\frac{\partial^2}{\partial t^2}\Big(\chi^{(3)}_{1,2,2,2}E_{op}E_{op}E_{op} + \chi^{(3)}_{1,2,2,3}E_{op}E_{op}E_{DC} \\
&\quad + \chi^{(3)}_{1,2,3,2}E_{op}E_{DC}E_{op} + \chi^{(3)}_{1,2,3,3}E_{op}E_{DC}E_{DC} \\
&\quad + \chi^{(3)}_{1,3,2,2}E_{DC}E_{op}E_{op} + \chi^{(3)}_{1,3,2,3}E_{DC}E_{op}E_{DC} \\
&\quad + \chi^{(3)}_{1,3,3,2}E_{DC}E_{DC}E_{op} + \chi^{(3)}_{1,3,3,3}E_{DC}E_{DC}E_{DC}\Big) \\
&= 0 \qquad \text{(D.21)} \\
\mu_0 \left(\frac{\partial^2 \mathscr{P}^{NL}}{\partial t^2}\right)_2 &= \frac{1}{c_0^2}\frac{\partial^2}{\partial t^2}\Big(\chi^{(3)}_{2,2,2,2}E_{op}E_{op}E_{op} + \chi^{(3)}_{2,2,2,3}E_{op}E_{op}E_{DC} \\
&\quad + \chi^{(3)}_{2,2,3,2}E_{op}E_{DC}E_{op} + \chi^{(3)}_{2,2,3,3}E_{op}E_{DC}E_{DC} \\
&\quad + \chi^{(3)}_{2,3,2,2}E_{DC}E_{op}E_{op} + \chi^{(3)}_{2,3,2,3}E_{DC}E_{op}E_{DC} \\
&\quad + \chi^{(3)}_{2,3,3,2}E_{DC}E_{DC}E_{op} + \chi^{(3)}_{2,3,3,3}E_{DC}E_{DC}E_{DC}\Big) \\
&= \frac{1}{c_0^2}\frac{\partial^2}{\partial t^2}\Big(\chi^{(3)}_{2,2,2,2}E_{op}^3 + \chi^{(3)}_{2,2,3,3}E_{op}E_{DC}^2 \\
&\quad + \chi^{(3)}_{2,3,2,3}E_{op}E_{DC}^2 + \chi^{(3)}_{2,3,3,2}E_{op}E_{DC}^2\Big) \\
&= \frac{1}{c_0^2}\frac{\partial^2}{\partial t^2}\Big(\chi^{(3)}_{2,2,2,2}E_{op}^3 + 3\chi^{(3)}_{2,2,3,3}E_{op}E_{DC}^2\Big) \qquad \text{(D.22)} \\
\mu_0 \left(\frac{\partial^2 \mathscr{P}^{NL}}{\partial t^2}\right)_3 &= \frac{1}{c_0^2}\frac{\partial^2}{\partial t^2}\Big(\chi^{(3)}_{3,2,2,2}E_{op}E_{op}E_{op} + \chi^{(3)}_{3,2,2,3}E_{op}E_{op}E_{DC} \\
&\quad + \chi^{(3)}_{3,2,3,2}E_{op}E_{DC}E_{op} + \chi^{(3)}_{3,2,3,3}E_{op}E_{DC}E_{DC} \\
&\quad + \chi^{(3)}_{3,3,2,2}E_{DC}E_{op}E_{op} + \chi^{(3)}_{3,3,2,3}E_{DC}E_{op}E_{DC} \\
&\quad + \chi^{(3)}_{3,3,3,2}E_{DC}E_{DC}E_{op} + \chi^{(3)}_{3,3,3,3}E_{DC}E_{DC}E_{DC}\Big) \\
&= \frac{1}{c_0^2}\frac{\partial^2}{\partial t^2}\Big(\chi^{(3)}_{3,2,2,3}E_{op}^2E_{DC} + \chi^{(3)}_{3,2,3,2}E_{op}^2E_{DC} \\
&\quad + \chi^{(3)}_{3,3,2,2}E_{op}^2E_{DC} + \chi^{(3)}_{3,3,3,3}E_{DC}^3\Big) \\
&= \frac{1}{c_0^2}\frac{\partial^2}{\partial t^2}\Big(3\chi^{(3)}_{2,2,3,3}E_{op}^2E_{DC} + \chi^{(3)}_{3,3,3,3}E_{DC}^3\Big) \\
&= \frac{1}{c_0^2}\frac{\partial^2}{\partial t^2}\Big(3\chi^{(3)}_{2,2,3,3}E_{op}^2E_{DC}\Big), \qquad \text{(D.23)}
\end{aligned}$$

where the time differentiation removed all the terms, that are solely DC. All in all the $\mu_0\left(\frac{\partial^2 \mathscr{P}^{NL}}{\partial t^2}\right)$ vector field is

$$\mu_0\left(\frac{\partial^2 \mathscr{P}^{NL}}{\partial t^2}\right) = \frac{1}{c_0^2}\begin{pmatrix} 0 \\ \frac{\partial^2}{\partial t^2}\left(\chi^{(3)}_{2,2,2,2}E_{op}^3 + 3\chi^{(3)}_{2,2,3,3}E_{op}E_{DC}^2\right) \\ \frac{\partial^2}{\partial t^2}\left(3\chi^{(3)}_{2,2,3,3}E_{op}^2E_{DC}\right) \end{pmatrix}. \quad \text{(D.24)}$$

Ignoring terms involving E_{op}^2 (light with the double frequency) and E_{op}^3 (light with the triple frequency) simplifies the non-linear term further

$$\begin{aligned} \mu_0\left(\frac{\partial^2 \mathscr{P}^{NL}}{\partial t^2}\right) &= \frac{1}{c_0^2}\begin{pmatrix} 0 \\ \frac{\partial^2}{\partial t^2}\left(3\chi^{(3)}_{2,2,3,3}E_{op}E_{DC}^2\right) \\ 0 \end{pmatrix} \\ &= \frac{1}{c_0^2}3\chi^{(3)}_{2,2,3,3}E_{DC}^2\begin{pmatrix} 0 \\ \frac{\partial^2 E_{op}}{\partial t^2} \\ 0 \end{pmatrix}. \end{aligned} \quad \text{(D.25)}$$

Substituting this in the propagation equation gives

$$\begin{aligned} \nabla^2\left(\begin{pmatrix} 0 \\ E_{op} \\ 0 \end{pmatrix} + \begin{pmatrix} 0 \\ 0 \\ E_{DC} \end{pmatrix}\right) - \frac{1+\chi}{c_0^2}\frac{\partial^2}{\partial t^2}\left(\begin{pmatrix} 0 \\ E_{op} \\ 0 \end{pmatrix} + \begin{pmatrix} 0 \\ 0 \\ E_{DC} \end{pmatrix}\right) \\ = \frac{1}{c_0^2}3\chi^{(3)}_{2,2,3,3}E_{DC}^2\frac{\partial^2}{\partial t^2}\begin{pmatrix} 0 \\ E_{op} \\ 0 \end{pmatrix}. \end{aligned} \quad \text{(D.26)}$$

This equation can be split into two separate equations, that is a DC equation and an optical equation. The DC equation is not accurate because of the weakly guided approximation. The equation for the optical field is

$$\begin{aligned} &\nabla^2\begin{pmatrix} 0 \\ E_{op} \\ 0 \end{pmatrix} - \frac{1+\chi}{c_0^2}\frac{\partial^2}{\partial t^2}\begin{pmatrix} 0 \\ E_{op} \\ 0 \end{pmatrix} = \frac{1}{c_0^2}3\chi^{(3)}_{2,2,3,3}E_{DC}^2\frac{\partial^2}{\partial t^2}\begin{pmatrix} 0 \\ E_{op} \\ 0 \end{pmatrix} \Rightarrow \\ &\nabla^2\begin{pmatrix} 0 \\ E_{op} \\ 0 \end{pmatrix} - \frac{1+\chi+3\chi^{(3)}_{2,2,3,3}E_{DC}^2}{c_0^2}\frac{\partial^2}{\partial t^2}\begin{pmatrix} 0 \\ E_{op} \\ 0 \end{pmatrix} = 0 \end{aligned} \quad \text{(D.27)}$$

The solution to this differential equation is

$$\mathbf{E} = \begin{pmatrix} 0 \\ Re(E_0 e^{kx-i\omega t}) \\ 0 \end{pmatrix}, \tag{D.28}$$

where $k = nk_0$ and $n^2 = 1 + \chi + 3\chi^{(3)}_{2,2,3,3}E^2_{DC}$. I.e. the non-linear term alters the refractive index. The change in index $\Delta n_{TE}(E_{DC})$ is

$$\begin{aligned} \Delta n_{TE}(E_{DC}) &= \sqrt{1+\chi+3\chi^{(3)}_{2,2,3,3}E^2_{DC}} - \sqrt{1+\chi} \\ &= \sqrt{1+\chi}\left(\sqrt{1+\frac{3\chi^{(3)}_{2,2,3,3}E^2_{DC}}{1+\chi}} - 1\right) \end{aligned} \tag{D.29}$$

Power series development of $\sqrt{1+\chi}$ to first order gives

$$\Delta n_{TE}(E_{DC}) = \frac{3\chi^{(3)}_{2,2,3,3}E^2_{DC}}{2n_0}, \tag{D.30}$$

where the relation $n_0 = \sqrt{1+\chi}$ has been used. To find the TM solution, $\mu_0 \frac{\partial^2 \mathscr{P}^{NL}}{\partial t^2}$ for TM is derived

$$\begin{aligned} \mu_0\left(\frac{\partial^2 \mathscr{P}^{NL}}{\partial t^2}\right)_1 &= \frac{1}{c_0^2}\frac{\partial^2}{\partial t^2}\left(\chi^{(3)}_{1,3,3,3}(E_{op}+E_{DC})(E_{op}+E_{DC})(E_{op}+E_{DC})\right) \\ &= 0 \end{aligned} \tag{D.31}$$

$$\begin{aligned} \mu_0\left(\frac{\partial^2 \mathscr{P}^{NL}}{\partial t^2}\right)_2 &= \frac{1}{c_0^2}\frac{\partial^2}{\partial t^2}\left(\chi^{(3)}_{2,3,3,3}(E_{op}+E_{DC})(E_{op}+E_{DC})(E_{op}+E_{DC})\right) \\ &= 0 \end{aligned} \tag{D.32}$$

$$\begin{aligned} \mu_0\left(\frac{\partial^2 \mathscr{P}^{NL}}{\partial t^2}\right)_3 &= \frac{1}{c_0^2}\frac{\partial^2}{\partial t^2}\left(\chi^{(3)}_{3,3,3,3}(E_{op}+E_{DC})(E_{op}+E_{DC})(E_{op}+E_{DC})\right) \\ &= \frac{1}{c_0^2}\frac{\partial^2}{\partial t^2}\left(\chi^{(3)}_{3,3,3,3}(E^3_{op}+3E^2_{op}E_{DC}+3E_{op}E^2_{DC}+E^3_{DC})\right) \\ &= \frac{1}{c_0^2}\frac{\partial^2}{\partial t^2}\left(\chi^{(3)}_{3,3,3,3}(E^3_{op}+3E^2_{op}E_{DC}+3E_{op}E^2_{DC})\right) \end{aligned} \tag{D.33}$$

All in all the $\mu_0\left(\frac{\partial^2 \mathscr{P}^{NL}}{\partial t^2}\right)$ vector field is

$$\mu_0\left(\frac{\partial^2 \mathscr{P}^{NL}}{\partial t^2}\right) = \frac{1}{c_0^2}\begin{pmatrix} 0 \\ 0 \\ \frac{\partial^2}{\partial t^2}\left(\chi^{(3)}_{3,3,3,3}(E_{op}^3 + 3E_{op}^2 E_{DC} + 3E_{op}E_{DC}^2)\right) \end{pmatrix} \tag{D.34}$$

Ignoring terms involving E_{op}^2 and E_{op}^3 simplifies the non-linear term further

$$\begin{aligned} \mu_0\left(\frac{\partial^2 \mathscr{P}^{NL}}{\partial t^2}\right) &= \frac{1}{c_0^2}\begin{pmatrix} 0 \\ 0 \\ \frac{\partial^2}{\partial t^2}\left(\chi^{(3)}_{3,3,3,3} 3E_{op}E_{DC}^2\right) \end{pmatrix} \\ &= \frac{1}{c_0^2} 3\chi^{(3)}_{3,3,3,3} E_{DC}^2 \begin{pmatrix} 0 \\ 0 \\ \frac{\partial^2 E_{op}}{\partial t^2} \end{pmatrix}. \end{aligned} \tag{D.35}$$

Substituting this in the propagation equation gives

$$\begin{aligned} \nabla^2\left(\begin{pmatrix} 0 \\ 0 \\ E_{op} \end{pmatrix} + \begin{pmatrix} 0 \\ 0 \\ E_{DC} \end{pmatrix}\right) - \frac{1+\chi}{c_0^2}\frac{\partial^2}{\partial t^2}\left(\begin{pmatrix} 0 \\ 0 \\ E_{op} \end{pmatrix} + \begin{pmatrix} 0 \\ 0 \\ E_{DC} \end{pmatrix}\right) \\ = \frac{1}{c_0^2} 3\chi^{(3)}_{3,3,3,3} E_{DC}^2 \begin{pmatrix} 0 \\ 0 \\ \frac{\partial^2 E_{op}}{\partial t^2} \end{pmatrix} \end{aligned} \tag{D.36}$$

This equation can be split into two separate equations, that is a DC equation and an optical equation. The DC equation is not accurate because of the weakly guided approximation. The equation for the optical field is

$$\begin{aligned} &\nabla^2\begin{pmatrix} 0 \\ 0 \\ E_{op} \end{pmatrix} - \frac{1+\chi}{c_0^2}\frac{\partial^2}{\partial t^2}\begin{pmatrix} 0 \\ 0 \\ E_{op} \end{pmatrix} = \frac{1}{c_0^2} 3\chi^{(3)}_{3,3,3,3} E_{DC}^2 \begin{pmatrix} 0 \\ 0 \\ \frac{\partial^2 E_{op}}{\partial t^2} \end{pmatrix} \Rightarrow \\ &\nabla^2\begin{pmatrix} 0 \\ 0 \\ E_{op} \end{pmatrix} - \frac{1+\chi+3\chi^{(3)}_{3,3,3,3}E_{DC}^2}{c_0^2}\frac{\partial^2}{\partial t^2}\begin{pmatrix} 0 \\ 0 \\ E_{op} \end{pmatrix} = 0 \end{aligned} \tag{D.37}$$

The solution to this differential equation is

$$\mathbf{E} = \begin{pmatrix} 0 \\ 0 \\ Re(E_0 e^{kx-i\omega t}) \end{pmatrix}, \tag{D.38}$$

where $k = nk_0$ and $n^2 = 1 + \chi + 3\chi^{(3)}_{3,3,3,3}E^2_{DC}$. I.e. the non-linear term alters the refractive index. The change in index $\Delta n_{TM}(E_{DC})$ is

$$\begin{aligned} \Delta n_{TM}(E_{DC}) &= \sqrt{1+\chi+3\chi^{(3)}_{3,3,3,3}E^2_{DC}} - \sqrt{1+\chi} \\ &= \sqrt{1+\chi}\left(\sqrt{1+\frac{3\chi^{(3)}_{3,3,3,3}E^2_{DC}}{1+\chi}} - 1\right) \end{aligned} \tag{D.39}$$

Power series development of $\sqrt{1+x}$ to first order gives

$$\Delta n_{TM}(E_{DC}) = \frac{3\chi^{(3)}_{3,3,3,3}E^2_{DC}}{2n_0}, \tag{D.40}$$

where the relation $n_0 = \sqrt{1+x}$ has been used.

When a permanent electric field $E_{\text{frozen-in}}$ is frozen into the glass by poling, the combined effect of $\chi^{(3)}$ and $E_{\text{frozen-in}}$ is equivalent to a first order nonlinearity $\chi^{(2)}$. To derive an expression for $\chi^{(2)}$, the symmetry operations for the poled glass are considered. The electric field is in the 3 direction (the z-direction), and as the glass is otherwise isotropic, there is still inversion symmetry in both direction 1 and direction 2. The inversion operation is $R_{\alpha\beta} = -\delta_{\alpha\beta}$, where $\delta_{\alpha\beta}$ is the Kronecker delta. As $\chi^{(2)}$ must obey the symmetry of the glass

$$\begin{aligned} \chi^{(2)}_{ijk} &= R_{11}\chi^{(2)}_{ijk} = (-1)^{n_1}\chi^{(2)}_{ijk} \\ \chi^{(2)}_{ijk} &= R_{22}\chi^{(2)}_{ijk} = (-1)^{n_2}\chi^{(2)}_{ijk} \\ \chi^{(2)}_{ijk} &= R_{11}R_{22}\chi^{(2)}_{ijk} = (-1)^{n_1+n_2}\chi^{(2)}_{ijk}, \end{aligned} \tag{D.41}$$

where n_1 is the number of 1's among ijk and n_2 is the number of 2's among ijk. This for example means that

$$\begin{aligned} \chi^{(2)}_{111} = -1^3\chi^{(2)}_{111} &\Leftrightarrow \chi^{(2)}_{111} = 0 \\ \chi^{(2)}_{133} = -1\chi^{(2)}_{133} &\Leftrightarrow \chi^{(2)}_{133} = 0 \\ \chi^{(2)}_{123} = -1\chi^{(2)}_{133} &\Leftrightarrow \chi^{(2)}_{123} = 0. \end{aligned} \tag{D.42}$$

The only surviving terms are the ones where there is an even number of both 1's and of 2's. The is also rotation symmetry for any angle around the z-axis. There is especially 90° rotation symmetry. That is

$$\chi^{(2)}_{113} = C_4\chi^{(2)}_{113} = \chi^{(2)}_{223} \tag{D.43}$$

The only surviving elements are presented in the table below.

Elements of $\chi^{(2)}$.
$\chi^{(2)}_{113} = \chi^{(2)}_{131} = \chi^{(2)}_{311} = \chi^{(2)}_{223} = \chi^{(2)}_{232} = \chi^{(2)}_{322}$
$\chi^{(2)}_{333}$

Table D.2: The non-vanishing elements of the $\chi^{(2)}$ tensor and the relations between these elements for a medium that is isotropic in all xy cross sections.

To find the effect of $\chi^{(2)}$ the propagation equation (D.18) must be solved for TE and TM polarized light. That is a TE polarized solution

$$\mathbf{E} = \begin{pmatrix} 0 \\ E_{op} \\ E_{DC} \end{pmatrix} \tag{D.44}$$

and the TM polarized solution

$$\mathbf{E} = \begin{pmatrix} 0 \\ 0 \\ E_{op} + E_{DC} \end{pmatrix}, \tag{D.45}$$

To find the TE solution, $\mu_0 \frac{\partial^2 \mathscr{P}^{NL}}{\partial t^2}$ for TE is derived

$$\begin{aligned}
\mu_0 \left(\frac{\partial^2 \mathscr{P}^{NL}}{\partial t^2} \right)_1 &= \frac{1}{c_0^2} \frac{\partial^2}{\partial t^2} \left(\chi^{(2)}_{1,2,2} E_{op} E_{op} + \chi^{(2)}_{1,2,3} E_{op} E_{DC} \right. \\
&\quad \left. + \chi^{(2)}_{1,3,2} E_{DC} E_{op} + \chi^{(2)}_{1,3,3} E_{DC} E_{DC} \right) \\
&= 0 \qquad \text{(D.46)} \\
\mu_0 \left(\frac{\partial^2 \mathscr{P}^{NL}}{\partial t^2} \right)_2 &= \frac{1}{c_0^2} \frac{\partial^2}{\partial t^2} \left(\chi^{(2)}_{2,2,2} E_{op} E_{op} + \chi^{(2)}_{2,2,3} E_{op} E_{DC} \right. \\
&\quad \left. + \chi^{(2)}_{2,3,2} E_{DC} E_{op} + \chi^{(2)}_{2,3,3} E_{DC} E_{DC} \right) \\
&= \frac{1}{c_0^2} \frac{\partial^2}{\partial t^2} \left(2\chi^{(2)}_{2,2,3} E_{DC} E_{op} \right) \qquad \text{(D.47)} \\
\mu_0 \left(\frac{\partial^2 \mathscr{P}^{NL}}{\partial t^2} \right)_3 &= \frac{1}{c_0^2} \frac{\partial^2}{\partial t^2} \left(\chi^{(2)}_{3,2,2} E_{op} E_{op} + \chi^{(2)}_{3,2,3} E_{op} E_{DC} \right. \\
&\quad \left. + \chi^{(2)}_{3,3,2} E_{DC} E_{op} + \chi^{(2)}_{3,3,3} E_{DC} E_{DC} \right) \\
&= \frac{1}{c_0^2} \frac{\partial^2}{\partial t^2} \left(\chi^{(2)}_{3,2,2} E_{op}^2 + \chi^{(2)}_{3,3,3} E_{DC}^2 \right) \\
&= \frac{1}{c_0^2} \frac{\partial^2}{\partial t^2} \left(\chi^{(2)}_{3,2,2} E_{op}^2 \right) \qquad \text{(D.48)}
\end{aligned}$$

All in all the $\mu_0 \left(\frac{\partial^2 \mathscr{P}^{NL}}{\partial t^2} \right)$ vector field is

$$\mu_0 \left(\frac{\partial^2 \mathscr{P}^{NL}}{\partial t^2} \right) = \frac{1}{c_0^2} \begin{pmatrix} 0 \\ \frac{\partial^2}{\partial t^2} \left(2\chi^{(2)}_{2,2,3} E_{op} E_{DC} \right) \\ \frac{\partial^2}{\partial t^2} \left(\chi^{(2)}_{3,2,2} E_{op}^2 \right) \end{pmatrix}. \qquad \text{(D.49)}$$

Ignoring the term with E_{op}^2 (the double frequency), simplifies the nonlinear term further, that is

$$\mu_0 \left(\frac{\partial^2 \mathscr{P}^{NL}}{\partial t^2} \right) = \frac{1}{c_0^2} \begin{pmatrix} 0 \\ \frac{\partial^2}{\partial t^2} \left(2\chi^{(2)}_{2,2,3} E_{op} E_{DC} \right) \\ 0 \end{pmatrix}. \qquad \text{(D.50)}$$

Substituting this in the propagation equation gives

$$\nabla^2\left(\begin{pmatrix}0\\E_{op}\\0\end{pmatrix}+\begin{pmatrix}0\\0\\E_{DC}\end{pmatrix}\right) - \frac{1+\chi}{c_0^2}\frac{\partial^2}{\partial t^2}\left(\begin{pmatrix}0\\E_{op}\\0\end{pmatrix}+\begin{pmatrix}0\\0\\E_{DC}\end{pmatrix}\right) = \frac{1}{c_0^2}2\chi^{(2)}_{2,2,3}E_{DC}\frac{\partial^2}{\partial t^2}\begin{pmatrix}0\\E_{op}\\0\end{pmatrix}. \quad \text{(D.51)}$$

This equation can be split into two separate equations, that is a DC equation and an optical equation. The DC equation is not accurate because of the weakly guided approximation. The equation for the optical field is

$$\nabla^2\begin{pmatrix}0\\E_{op}\\0\end{pmatrix} - \frac{1+\chi}{c_0^2}\frac{\partial^2}{\partial t^2}\begin{pmatrix}0\\E_{op}\\0\end{pmatrix} = \frac{1}{c_0^2}2\chi^{(2)}_{2,2,3}E_{DC}\frac{\partial^2}{\partial t^2}\begin{pmatrix}0\\E_{op}\\0\end{pmatrix} \Rightarrow$$

$$\nabla^2\begin{pmatrix}0\\E_{op}\\0\end{pmatrix} - \frac{1+\chi+2\chi^{(2)}_{2,2,3}E_{DC}}{c_0^2}\frac{\partial^2}{\partial t^2}\begin{pmatrix}0\\E_{op}\\0\end{pmatrix} = 0 \quad \text{(D.52)}$$

The solution to this differential equation is

$$\mathbf{E} = \begin{pmatrix}0\\Re(E_0 e^{kx-i\omega t})\\0\end{pmatrix}, \quad \text{(D.53)}$$

where $k = nk_0$ and $n^2 = 1+\chi+2\chi^{(2)}_{2,2,3}E_{DC}$. I.e. the non-linear term alters the refractive index. The change in index $\Delta n_{TE}(E_{DC})$ is

$$\begin{aligned}\Delta n_{TE}(E_{DC}) &= \sqrt{1+\chi+2\chi^{(2)}_{2,2,3}E_{DC}} - \sqrt{1+\chi}\\ &= \sqrt{1+\chi}\left(\sqrt{1+\frac{2\chi^{(2)}_{2,2,3}E_{DC}}{1+\chi}}-1\right)\end{aligned} \quad \text{(D.54)}$$

Power series development of $\sqrt{1+x}$ to first order gives

$$\Delta n_{TE}(E_{DC}) = \frac{2\chi^{(2)}_{2,2,3}E_{DC}}{2n_0} = \frac{\chi^{(2)}_{TE,eff}E_{DC}}{n_0}, \quad \text{(D.55)}$$

where the relation $n_0 = \sqrt{1+\chi}$ has been used. As $\chi^{(2)}_{2,2,3}$ originates from an electric field frozen into the glass sample, it is called an effective first order nonlinearity $\chi^{(2)}_{TE,eff}$. To find a connection between $\chi^{(2)}_{TE,eff}$ and $\chi^{(3)}_{TE}$, the refractive index change caused by $\chi^{(3)}_{TE}$ and an electric field E_{DC} in the presence of a frozen-in electric field $E_{frozen-in}$ is investigated. Equation (D.30) gives

$$\begin{aligned} \Delta n_{TE}(E_{DC}) &= \frac{3\chi^{(3)}_{TE}(E_{DC}+E_{frozen-in})^2}{2n_0} \\ &= \frac{3\chi^{(3)}_{TE}(E^2_{DC}+E^2_{frozen-in}+2E_{DC}E_{frozen-in})}{2n_0} \end{aligned} \tag{D.56}$$

The linear part of the refractive index change is

$$\Delta n_{TE}(E_{DC})|_{linear} = \frac{3\chi^{(3)}_{TE}E_{DC}E_{frozen-in}}{n_0} \tag{D.57}$$

This is equal to the refractive index change caused by $\chi^{(2)}_{TE,eff}$, and by combining equation (D.55) with (D.57), the following relation between $\chi^{(2)}_{TE,eff}$ and $\chi^{(3)}_{TE}$ is derived

$$\chi^{(2)}_{TE,eff} = 3\chi^{(3)}_{TE}E_{frozen-in}. \tag{D.58}$$

To find the TM solution, $\mu_0\frac{\partial^2 \mathscr{P}^{NL}}{\partial t^2}$ for TM is derived

$$\begin{aligned} \mu_0\left(\frac{\partial^2\mathscr{P}^{NL}}{\partial t^2}\right)_1 &= \frac{1}{c_0^2}\frac{\partial^2}{\partial t^2}\left(\chi^{(2)}_{1,3,3}(E_{op}+E_{DC})(E_{op}+E_{DC})\right) \\ &= 0 \end{aligned} \tag{D.59}$$

$$\begin{aligned} \mu_0\left(\frac{\partial^2\mathscr{P}^{NL}}{\partial t^2}\right)_2 &= \frac{1}{c_0^2}\frac{\partial^2}{\partial t^2}\left(\chi^{(2)}_{2,3,3}(E_{op}+E_{DC})(E_{op}+E_{DC})\right) \\ &= 0 \end{aligned} \tag{D.60}$$

$$\begin{aligned} \mu_0\left(\frac{\partial^2\mathscr{P}^{NL}}{\partial t^2}\right)_3 &= \frac{1}{c_0^2}\frac{\partial^2}{\partial t^2}\left(\chi^{(2)}_{3,3,3}(E_{op}+E_{DC})(E_{op}+E_{DC})\right) \\ &= \frac{1}{c_0^2}\frac{\partial^2}{\partial t^2}\left(\chi^{(2)}_{3,3,3}(E^2_{op}+2E_{op}E_{DC}+E^2_{DC})\right) \\ &= \frac{1}{c_0^2}\frac{\partial^2}{\partial t^2}\left(\chi^{(2)}_{3,3,3}(E^2_{op}+2E_{op}E_{DC})\right) \end{aligned} \tag{D.61}$$

All in all the $\mu_0\left(\frac{\partial^2 \mathscr{P}^{NL}}{\partial t^2}\right)$ vector field is

$$\mu_0\left(\frac{\partial^2 \mathscr{P}^{NL}}{\partial t^2}\right) = \frac{1}{c_0^2}\begin{pmatrix} 0 \\ 0 \\ \frac{\partial^2}{\partial t^2}\left(\chi^{(2)}_{3,3,3}(E_{op}^2 + 2E_{op}E_{DC})\right) \end{pmatrix} \tag{D.62}$$

Ignoring terms involving E_{op}^2 simplifies the non-linear term further

$$\begin{aligned} \mu_0\left(\frac{\partial^2 \mathscr{P}^{NL}}{\partial t^2}\right) &= \frac{1}{c_0^2}\begin{pmatrix} 0 \\ 0 \\ \frac{\partial^2}{\partial t^2}\left(\chi^{(2)}_{3,3,3}2E_{op}E_{DC}\right) \end{pmatrix} \\ &= \frac{1}{c_0^2}2\chi^{(2)}_{3,3,3}E_{DC}\begin{pmatrix} 0 \\ 0 \\ \frac{\partial^2 E_{op}}{\partial t^2} \end{pmatrix}. \end{aligned} \tag{D.63}$$

Substituting this in the propagation equation gives

$$\begin{aligned} \nabla^2\left(\begin{pmatrix} 0 \\ 0 \\ E_{op} \end{pmatrix} + \begin{pmatrix} 0 \\ 0 \\ E_{DC} \end{pmatrix}\right) - \frac{1+\chi}{c_0^2}\frac{\partial^2}{\partial t^2}\left(\begin{pmatrix} 0 \\ 0 \\ E_{op} \end{pmatrix} + \begin{pmatrix} 0 \\ 0 \\ E_{DC} \end{pmatrix}\right) \\ = \frac{1}{c_0^2}2\chi^{(2)}_{3,3,3}E_{DC}\begin{pmatrix} 0 \\ 0 \\ \frac{\partial^2 E_{op}}{\partial t^2} \end{pmatrix} \end{aligned} \tag{D.64}$$

This equation can be split into two separate equations, that is a DC equation and an optical equation. The DC equation is not accurate because of the weakly guided approximation. The equation for the optical field is

$$\begin{aligned} &\nabla^2\begin{pmatrix} 0 \\ 0 \\ E_{op} \end{pmatrix} - \frac{1+\chi}{c_0^2}\frac{\partial^2}{\partial t^2}\begin{pmatrix} 0 \\ 0 \\ E_{op} \end{pmatrix} = \frac{1}{c_0^2}2\chi^{(2)}_{3,3,3}E_{DC}\begin{pmatrix} 0 \\ 0 \\ \frac{\partial^2 E_{op}}{\partial t^2} \end{pmatrix} \Rightarrow \\ &\nabla^2\begin{pmatrix} 0 \\ 0 \\ E_{op} \end{pmatrix} - \frac{1+\chi+2\chi^{(2)}_{3,3,3}E_{DC}}{c_0^2}\frac{\partial^2}{\partial t^2}\begin{pmatrix} 0 \\ 0 \\ E_{op} \end{pmatrix} = 0 \end{aligned} \tag{D.65}$$

The solution to this differential equation is

$$\mathbf{E} = \begin{pmatrix} 0 \\ 0 \\ Re(E_0 e^{kx - i\omega t}) \end{pmatrix}, \tag{D.66}$$

where $k = nk_0$ and $n^2 = 1 + \chi + 2\chi^{(2)}_{3,3,3}E_{DC}$. I.e. the non-linear term alters the refractive index. The change in index $\Delta n_{TM}(E_{DC})$ is

$$\begin{aligned}\Delta n_{TM}(E_{DC}) &= \sqrt{1+\chi+2\chi^{(2)}_{3,3,3}E_{DC}} - \sqrt{1+\chi} \\ &= \sqrt{1+\chi}\left(\sqrt{1+\frac{2\chi^{(2)}_{3,3,3}E_{DC}}{1+\chi}} - 1\right)\end{aligned} \tag{D.67}$$

Power series development of $\sqrt{1+\chi}$ to first order gives

$$\Delta n_{TM}(E_{DC}) = \frac{2\chi^{(2)}_{3,3,3}E_{DC}}{2n_0} = \frac{\chi^{(2)}_{TM,eff}E_{DC}}{n_0}, \tag{D.68}$$

where the relation $n_0 = \sqrt{1+\chi}$ has been used. As $\chi^{(2)}_{3,3,3}$ originates from an electric field frozen into the glass sample, it is called an effective first order nonlinearity $\chi^{(2)}_{TM,eff}$. To find a connection between $\chi^{(2)}_{TM,eff}$ and $\chi^{(3)}_{TM}$, the refractive index change caused by $\chi^{(3)}_{TM}$ and an electric field E_{DC} in the presence of a frozen-in electric field $E_{frozen-in}$ is investigated. Equation (D.40) gives

$$\begin{aligned}\Delta n_{TM}(E_{DC}) &= \frac{3\chi^{(3)}_{TM}(E_{DC}+E_{frozen-in})^2}{2n_0} \\ &= \frac{3\chi^{(3)}_{TM}(E^2_{DC}+E^2_{frozen-in}+2E_{DC}E_{frozen-in})}{2n_0}\end{aligned} \tag{D.69}$$

The linear part of the refractive index change is

$$\Delta n_{TM}(E_{DC})|_{linear} = \frac{3\chi^{(3)}_{TM}E_{DC}E_{frozen-in}}{n_0} \tag{D.70}$$

This is equal to the refractive index change caused by $\chi^{(2)}_{TM,eff}$, and by combining equation (D.68) with (D.70), the following relation between $\chi^{(2)}_{TM,eff}$ and $\chi^{(3)}_{TM}$ is derived

$$\chi^{(2)}_{TM,eff} = 3\chi^{(3)}_{TM}E_{frozen-in}. \tag{D.71}$$

To summarize the results,it has been found that

$$\Delta n_{TE}(E_{DC}) = \frac{3\chi^{(3)}_{2,2,3,3}E^2_{DC}}{2n_0} = \frac{3\chi^{(3)}_{TE}E^2_{DC}}{2n_0} \quad (D.72)$$

$$\Delta n_{TM}(E_{DC}) = \frac{3\chi^{(3)}_{3,3,3,3}E^2_{DC}}{2n_0} = \frac{3\chi^{(3)}_{TM}E^2_{DC}}{2n_0} \quad (D.73)$$

$$\chi^{(2)}_{TE,eff} = 3\chi^{(3)}_{TE}E_{frozen-in} \quad (D.74)$$

$$\chi^{(2)}_{TM,eff} = 3\chi^{(3)}_{TM}E_{frozen-in}. \quad (D.75)$$

Instead of looking at the polarization density vector, a more phenomenology approach is often used. The refractive index is written as

$$n(E) = n_0 - \frac{1}{2}\mathfrak{r}n_0^3E - \frac{1}{2}\mathfrak{s}n_0^3E^2 + \ldots \quad (D.76)$$

This definition is more simple than inspecting of the polarization density vector, and there is no need for symmetry considerations. The physical refractive index is simply Taylor expanded around zero field. The drawback of this approach is that it contains less information about the coefficients $\mathfrak{r}$ and $\mathfrak{s}$. As the coefficients $\mathfrak{r}$ and $\mathfrak{s}$ are used in the literature, conversion equations between these coefficients and $\chi^{(2)}$ and $\chi^{(3)}$ are needed. By inspecting the equations (D.55, D.68, D.72 and D.73) together with (D.76) it is easily derived that

$$\mathfrak{r}_{TE,eff} = -\frac{2\chi^{(2)}_{TE,eff}}{n_0^4} \quad (D.77)$$

$$\mathfrak{r}_{TM,eff} = -\frac{2\chi^{(2)}_{TM,eff}}{n_0^4} \quad (D.78)$$

$$\mathfrak{s}_{TE} = -\frac{3\chi^{(3)}_{TE}}{n_0^4} \quad (D.79)$$

$$\mathfrak{s}_{TM} = -\frac{3\chi^{(3)}_{TM}}{n_0^4}. \quad (D.80)$$

References to Appendix D

[1] P. Butcher and D. Cotter. *The elements of nonlinear optics.* Cambridge University Press, 1990. ISBN 0-521-42424-0.

Appendix E

The confinement factor for a PhC waveguide.

The confinement factor was kindly determined by Lars Frandsen. It was calculated using the software package MPB [1] and for the mode of interest, the confinement factor is shown together with the bandgab diagram in fig. (E.1)
The non-physical fluctuations is due to mode crossing with cladding modes. The cladding modes only appear in 3D calculations and they are propagating in the silica above and below the silicon layer. They are not represented properly in the calculation due to the continuous boarder condition applied in MPB. The modes are better described in a FDTD calculation, where the boarder conditions are absorbing. The wrongful representation of the crossing with cladding modes also means that effects solely due to the third dimension will be ill represented. The oscillation found for the group index both by measurements and by 3D FDTD calculations will be very hard to find in MPB due to the different boarder conditions.

The calculated points for the confinement factor are sorted by the black modes distance to other modes and only the points on the green line in fig. (E.1) are considered trustworthy. The points on the green line corresponds to points on the black curve, which are long away from the places where the mode crosses with another mode (evaluated by eye). The green points are fitted with a parable as shown in fig. (E.2) and the parable is used for evaluating the confinement factor in the eq. (3.58) for

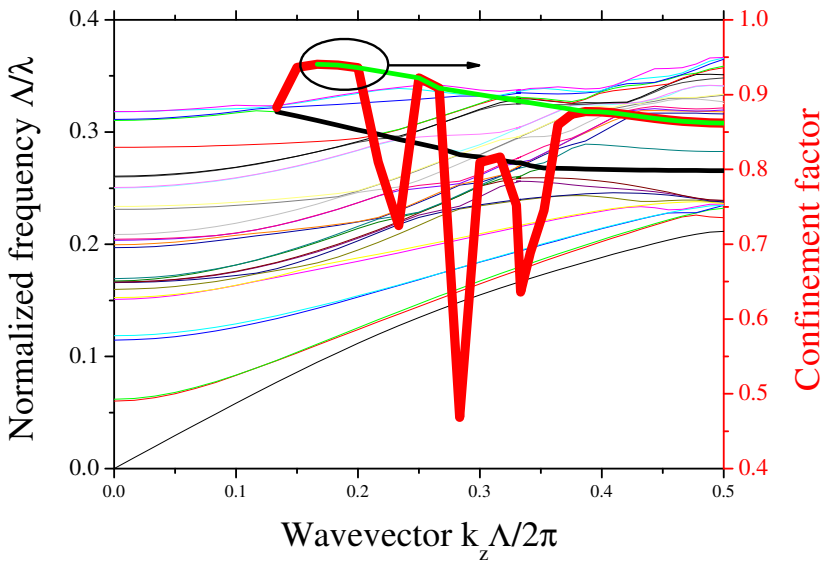

Figure E.1: The bandgap diagram for the PhC waveguide. The thick black line is the mode investigated and the thick red curve is the calculated confinement factor to the silicon. Due to mode crossing, the confinement factor makes non-physical fluctuations. The green line represents the trustworthy points.

determining the $\chi^{(2)}_{core}$ value.
The derivation due to the less than perfect determination of the confinement factor introduces a systematically and wavelength depended error. The size of the error is evaluated to 2% by looking at fig. (E.2). The confinement factor calculation will in the future be improved by using 3D FDTD calculations. This systematic error is *not* included in the error calculation in appendix B, as there are other dominant contributions. The problem with the confinement factor error is the wavelength dependency, which is not pronounced for the other error type discussed in appendix B. The error of 2% is probably not detectable on the plots of $\chi^{(2)}_{core}$ vs. wavelength but care must be taken when there exists a systematic error, which depends on a plotting parameter.

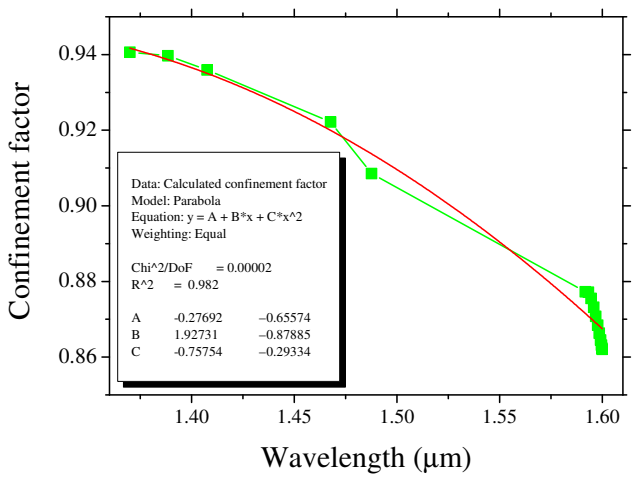

Figure E.2: The green line connects the trustworthy confinement factor points from fig. (E.1). The points are fitted with a parabola, i.e. with a smooth curve without to many fitting parameters.

References to Appendix E

[1] S. G. Johnson and J. D. Joannopoulos. "Block-iterative frequency-domain methods for maxwell's equations in a planewave basis", *Opt. Exp.*, vol. 8, no. 3, pp. 173–190, 2001.

Bibliography

[1] Butcher, P.N. and Cotter, D. **The elements of nonlinear optics**, Cambridge university press, 1990, ISBN 0-521-42424-0

[2] Syms, R. and Cozens, J. **Optical guide waves and devices**, McGraw-Hill, 1992, ISBN 0-07-707425-4

[3] Kittel, C. **Introduction to solid state physics**, Wiley, 1996, ISBN 0-471-11181-3

[4] Saleh, B.E.A. and Teich, M.C. **Fundamentals of Photonics**, Wiley, 1991, ISBN 0-471-83965-5

[5] Coldren, L.A. and Corzine, S.W. **Diode lasers and photonic integrated circuits**, Wiley, 1995, ISBN 0-471-11875-3

[6] Soljačić, M., Johnson, S.G., Fan, S., Ibanescu, M., Ippen, E. and Joannopoulos, J.D., Photonic-crystal slow-light enhancement of nonlinear phase sensitivity, J. Opt. Soc. Am. B., 19, 9(2002).

[7] Elbek, B. **Elektromagnetisme**, Niels Bohr Institutet, 1997, ISBN 87-87585-07-3

[8] Kazansky, P.G. and Russel, P.St.J., Thermally poled glass: Frozen-in electric field or oriented dipoles?, Opt. Commun., 110, pp. 611-614, 1994.

[9] Niklas Myrén, Doctoral thesis, Poled fiber devices, 2005, ISBN 91-7178-053-x

[10] Marckmann, C.J., Ren, Y., Genty G. and Kristensen M., Strength and symmetry of the third-order nonlinearity during poling of glass waveguides, IEEE Photon. Technol. Lett., 14, no. 9, pp. 1294-1296, 2002.

[11] Janos M., Xu W., Wong D., Inglis H., and Fleming S., Growth and Decay of the Electrooptic Effect in Thermally Poled B/Ge Codoped Fiber, Jour. of Lightwave Tech., 17, no. 6, pp. 1037-1041, 1999

[12] Ren Y., Marckmann C.J., Arentoft J., and Kristensen M., Thermally poled channel waveguides with polarization independent electro-optic effect, IEEE Photon. Technol. Lett., 14, no. 5, pp. 639-641, May 2002.

[13] **http://www.photox.co.uk/linbo3.htm**

[14] **http://www.crystran.co.uk/sidata.htm**

[15] Aspnes, D.E., Optical functions of intrinsic Si: Region of near transparency, EMIS datareview RN=17803, 1987.

[16] Povlsen, J.H. , Fiber lasers, Notes from 2002, contact jhp@com.dtu.dk.